CEA-R-6467

ISSN 0429 - 3460

COMMISSARIAT À L'ÉNERGIE ATOMIQUE
ET AUX ÉNERGIES ALTERNATIVES

ACTE DU WORKSHOP "ABSORBED DOSE IN WATER AND AIR" UN PROGRAMME DE RECHERCHE COMMUN DE EMPIR

par

Sorin BERCEA, Valentin BLIDEANU, Jean-Marc BORDY, Margarida Isabela CAMACHO CALDEIRA, Aurelia CELAREL, Constentin CENUSA, Ioan CENUSA, Marc DONOIS, Dorin DUSCIAC, Elena ILIESCU, Aimé OSTROWSKY, Benjamin RAPP, Vladimir SOCHOR, Andrea STEURER, TIEFENBÖCK

CEA SACLAY
DIRECTION DE LA RECHERCHE TECHNOLOGIQUE
LABORATOIRE D'INTÉGRATION DES SYSTÈMES
ET DES TECHNOLOGIES
DÉPARTEMENT MÉTROLOGIE, INSTRUMENTATION
ET INFORMATION
LABORATOIRE NATIONAL HENRI BECQUEREL

DIRECTION DE L'ÉNERGIE NUCLÉAIRE

2017

DIRECTION DES SYSTÈMES
D'INFORMATION
CEA / SACLAY 91191 GIF-SUR-YVETTE CEDEX FRANCE

RAPPORT

RAPPORT
CEA-R-6467

RAPPORT CEA-R-6467 – Bercea Sorin, Blideanu Valentin, Bordy Jean-Marc, Camacho Caldeira Margarida Isabela, Celarel Aurelia, Cenusa Constentin, Cenusa Ioan, Donois Marc, Dusciac Dorin, Iliescu Elena, Ostrowsky Aimé, Rapp Benjamin, Sochor Vladimir, Steurer Andrea, Tiefenböck.

«Acte du workshop "ABSORBED DOSE in WATER and AIR", un programme de recherche commun de EMPIR»

Résumé - Le projet "Absorbed dose in water and air" (Absorb) a pour objectif de partager et d'améliorer la connaissance dans la conception de dosimètres primaires (calorimètres, chambres d'ionisation de cavité, chambres d'ionisation à paroi d'air) pour des mesures de la « dose » en radiothérapie et radio diagnostique. Il vise aussi l'harmonisation de procédures d'étalonnage, la détermination et l'harmonisation des bilans d'incertitudes. Dans le cadre de ce projet un « workshop » a été organisé au LNE (Laboratoire national de métrologie et d'Essais) à Paris du 29 février au 2 mars 2016. Ce rapport représente les actes de ce workshop. Il inclut un état de l'art de deux collaborations bilatérales, établie pour poursuivre le travail au-delà du cadre de Absord, entre la LIST CEA (LNE) LNHB et d'une part l'IFIN-HH (Roumanie) et d'autre part l'IST-LPSR-LMRI (Portugal) pour construire des chambres d'ionisation primaires à cavité pour des photons émis par le cobalt 60 et le Césium 137. Absorb est un projet de recherche du Programme de Métrologie européen pour l'Innovation et la Recherche (EMPIR) qui est co-financé par le programme de recherche et d'innovation « Horizon 2020 » de l'Union européenne ainsi que par les états participants à EMPIR.

2017 – Commissariat à l'Énergie Atomique et aux Énergies Alternatives – France

---

RAPPORT CEA-R-6467 – Bercea Sorin, Blideanu Valentin, Bordy Jean-Marc, Camacho Caldeira Margarida Isabela, Celarel Aurelia, Cenusa Constentin, Cenusa Ioan, Donois Marc, Dusciac Dorin, Iliescu Elena, Ostrowsky Aimé, Rapp Benjamin, Sochor Vladimir, Steurer Andrea, Tiefenböck.

« Proceeding of the Workshop "ABSORBED DOSE in WATER and AIR", an EMPIR joint research project. »

Abstract - The project "Absorbed dose in water and air" (Absorb) is aimed at sharing and improving the knowledge on the design of Primary Standards (calorimeter, cavity ionization chambers, free air ionization chambers) for "dose" measurements in radiation therapy and diagnostic, the harmonization of calibration procedures, the determination of uncertainty and harmonization of uncertainty budgets. Within the framework of this project a workshop was organized at the LNE (Laboratoire National de métrologie et d'Essais) in Paris from February, 29th to March, 2nd 2016. This report is the proceeding of this workshop. It includes a state of the art of two bilateral collaborations, launched to go beyond the framework of Absorb, between CEA LIST (LNE) LNHB and in one hand IFIN-HH (Romania), and in the other hand IST-LPSR-LMRI (Portugal) to build primary cavity ionization chambers for photons emitted by cobalt-60 and Cesium-137. Absorb is a Joint Research Project of the European Metrology Programme for Innovation and Research (EMPIR) which is co-funded by the European Union's Horizon 2020 research and innovation programme and the EMPIR Participating States.

2017 – Commissariat à l'Énergie Atomique et aux Énergies Alternatives – France

- Rapport CEA-R-6467 -

CEA Saclay
Direction de la Recherche Technologique
Laboratoire d'Intégration des Systèmes et des Technologies
Département Métrologie, Instrumentation et Information
Laboratoire National Henri Becquerel

ACTE DU WORKSHOP "ABSORBED DOSE IN WATER AND AIR", UN PROGRAMME DE RECHERCHE COMMUN DE EMPIR

par

Bercea Sorin, Blideanu Valentin, Bordy Jean-Marc, Camacho Caldeira Margarida Isabela, Celarel Aurelia, Cenusa Constentin, Cenusa Ioan, Donois Marc, Dusciac Dorin, Iliescu Elena, Ostrowsky Aimé, Rapp Benjamin, Sochor Vladimir, Steurer Andrea, Tiefenböck

- Mai 2017 -

Table of contents

FOREWORD

A workshop was organized at the LNE (Laboratoire National de métrologie et d'Essais) in Paris from February, 29th to March, 2nd 2016 within the framework of the Joint Research Project (JRP) of the European Metrology Programme for Innovation and Research (EMPIR) named ”Absorbed dose in water and air” (ABSORB). This report is the proceeding of this workshop.

The aim of the ABSORB project is to share and improve the knowledge on the design of Primary Standards (calorimeter, cavity ionization chambers, free air ionization chambers) for dose measurements in radiation therapy and diagnostic, the harmonization of calibration procedures, the determination of uncertainty and harmonization of uncertainty budgets and finally – for each partner - an individual strategy for the long-term development of their research and calibration capability in radiation dosimetry including the establishment of appropriate quality schemes and accreditation. The workshop was organized to allow the exchange of information between the partners of the project, it was agreed that other members of EURAMET could attend the workshop even if they were not part of it. Therefore, in addition to the partners, one representative of the CIEMAT (National Metrology Institute in Spain) took part to the workshop.

The EMPIR initiative is co-funded by the European Union’s Horizon 2020 research and innovation programme and the EMPIR Participating States.

The manufacturing of the primary standard is not included in the Absorb Joint Research Project, therefore, CEA LIST (LNE) LNHB has launched bilateral collaborations with IFIN-HH (Romania) and IST-LPSR-LMRI (Portugal) to build these standard. With Romania, it is under the hospice of the COOPERATION AGREEMENT IN THE FIELD OF SCIENTIFIC RESEARCH between the Commissariat à l’énergie atomique et aux énergies alternatives (CEA) and the Institut de Fisica Atomica (IFA). Within this frame, CEA LIST (LNE) LNHB and the National Institute for Physics and Nuclear Engineering “Horia Hulubei” (IFIN-HH) launched the project CATRAS (Development of the traceability of the calibrations in radiotherapy, radiation protection and medical imaging in Romania) aimed at building a primary cavity ionization chamber. For Portugal the goal is the same, it is under the hospice of the PHD Thesis of the Universidade de Lisboa, instituto Superior Técnico entitled “Design, construction, characterization and bilateral comparison of an air-kerma cavity standard”. For both projects, the primary standard is based on the CEA LIST (LNE) LNHB design of cavity ionization chamber for photons emitted by cobalt-60 and Cesium-137. The first results of these collaborations were reported during the workshop and are included in this Proceeding.

Agenda of the Absorb Workshop

Paris LNE 29th of February start 13h30 to 2nd of March 17h00

Monday 29th of February

13h30 Welcome address – Maguelone Chambon Head of DRST LNE (French MNI)

1- Introduction to uncertainty budget GUM method – JM Bordy (CEA LNE LNHB)
2- Free air chamber CMI design - V. Sochor (CMI)

15h30 coffee break

3- Diagnostic facility and free air chamber at BEV – A Steurer (BEV)
4- Measurement calibration - A Steurer (BEV)

End 17h30

Tuesday 1st of March

9h00

5- Cavity chamber, method Principle form collected charges to air kerma – MI Camacho Caldeira (IST LMRI)
6- Electronic associated to IC - MI Camacho Caldeira (IST LMRI)

10h15 coffee break

7- Use of capacitor for collected charge measurement – JM Bordy (CEA LNE LNHB)
8- Cavity chamber manufacturing - MI Camacho Caldeira (IST LMRI)

12h15 Lunch at LNE

13h30

9- Calorimetry – water and graphite calorimeter pro and con - B. Rapp (CEA LNE LNHB)
10- Graphite calorimeter at BEV – A. Steurer (BEV)
11- Therapy X ray facility at BEV – A. Steurer (BEV)
12- Cavity chamber, correction factors measurement- MI Camacho Caldeira (IST LMRI)

15h30 coffee break

13- Cavity chamber, correction factors calculation - MI Camacho Caldeira (IST LMRI)
14- Measuring system and evaluation software – A Steurer (BEV)
15- Presentation of BEV laboratory - A. Steurer (BEV)
16- Presentation of CMI laboratory - V. Sochor (CMI)

End 17h30

Workshop diner 19h30

Wenesday 2nd of March

9h00

17- Accreditation ISO 17025, overview of the chapters 4 and 5 – JM Bordy (CEA LNE LNHB)
18- Presentation of IST LMRI laboratory - J. Alves (IST LMRI)

10h15 coffee break

19- Presentation of VINCA laboratory – O. Ciraj-Bjelac (VINCA)
20- Presentation of SCK-CEN laboratory – L.C. Mihailescu (SCK-CEN)

12h00 Lunch at LNE

13h15

21- Former poll of WG Health of IR TC – JM Bordy (CEA LNE LNHB)
22- Discussion on the first answer to the 4 polls launched by ABSORB

15h30 coffee break

23- Next steps for the Absorb project (Review of the tasks)
24- Other questions, next meeting (date, place), ….

End 17h00

List of participants

Names	country	institute
Alves João	Portugal	IST-LPSR-LMRI
Amra Sabeta	Bosnia and Herzegovia	IMBIH
Aviles Paz	Espagne	CIEMAT
Bercea Sorin	Roumanie	IFIN HH
Bernat Robert	Croatia	RBI
Bideanu valentin	France	LNE LNHB (CEA)
Bordy Jean-Marc	France	LNE LNHB (CEA)
Caldeira Camacho Margarida	Portugal	IST-LPSR-LMRI
Cardoso João	Portugal	IST-LPSR-LMRI
Chiriotti Alvarez sabina	Belgium	SCKCEN
Derlacinski Michal	Poland	GUM
Iliescu Elena	Roumanie	IFIN HH
Krzanovic Nikola	serbia	VINCA
Mihailescu Liviu-Cristian	Belgium	SCKCEN
Rapp Benjamin	France	LNE LNHB (CEA)
Sochor Vladimir	Czech Rep.	CMI
Steurer Andrea	Austria	BEV
Vojnić Kortmiš Maja	Croatia	RBI
Zivanovic Milos	Serbia	VINCA

List of the authors

V. Sochor

CMI - Czech Metrology Institute, Okružní 31/772, 638 00 Brno, Czech Republic

A Steurer, W. Tiefenböck

BEV – Bundesamt für Eich- und Vermessungswesen, 1160 Wien, Arltgasse 35, Austria

M.I. Camacho Caldeira,

IST LPSR LMRI - Istituto Superior Tècnico Laboratório de Protecção e Segurança Radiológica Laboratório de Metrologia das Radiações Ionizantes, Campus Tecnológico e Nuclear Estrada Nacional 10 2686-953 Sacavém Portugal

S. Bercea, A. Celarel, C. Cenusa, I. Cenusa, E. Iliescu,

“Horia Hulubei” National Institute for R&D in Physics and Nuclear Engineering (IFIN-HH), Str. Reactorului n ° 30, POBOX MG-6, Bucarest - Magurele, Roumanie

V. Blideanu, J.-M. Bordy, M. Donois, D. Dusciac, A. Ostrowsky, B. Rapp

CEA, LIST, Laboratoire National Henri Becquerel (LNE-LNHB), 91191 Gif-sur-Yvette, France

Free-air chamber

Principle of operation, basic design

Vladimír Sochor - CMI

1 Introduction

This short paper gives a brief simplified summary of working principle, design, corrections of free-air chamber based on CMI experiences with a low-energy FAC.

Building a FAC at CMI has been a rather long-term run: The decision was made in 2011 and the very first phase was then the information gathering, where the valuable sources of initial information were the publications [1] D.T.Burns and L. Buermann: Free-air ionization chambers, Metrologie 46 (2009), S9-S23, [2] Practical Course in Reference Dosimetry „kV X-ray Dosimetry at NPL“, National Physical Laboratory; http://www.npl.co.uk/upload/pdf/pcrd-9-notes.pdf, [3] C. Kessler, P. Roger, D. T. Burns: Establishment of reference radiation qualities for mammography, BIPM Rapport-2010/01, and personal visits at BIPM and LNHB and valuable private communication. Based on the information collected a physical design was created, which was then several times updated under consultations with the manufacturer, and the final drawings were prepared till end of the year. Mechanical parts were manufactured on the edge of 2011/2012, so in 2012 the wires, connectors and voltage divider could be connected. First measurements were performed in spring 2012, followed by determination of some of the correction factors. In October we have performed a performance test/comparison at BEV while still working on a refinement of correction factors. The information of FAC and its characteristics was presented in 2013 on a Prague conference and then an idle phase followed until 2014 when a paper describing the FAC was finally published. After that we could apply for key comparisons BIPM.RI(I)-K2 and BIPM.RI(I)-K7, which were then performed in December 2015. At present (in April 2016) both final reports were published in the Metrologia Tech. Suppl. Series.

Based on experiences with the low-energy FAC, CMI started to work on a medium-energy FAC in 2014. This second FAC is now (in April 2016) functioning, first measurements have been performed, however it is still under development.

2 Principle of operation

FAC is usually built as a plan-parallel ionization chamber. Beam of X-rays is entering the shielded metal box through an opening of an area A, then it is traveling between two plan-parallel electrodes and leaves the box through an opening on the opposite side without touching the structure of FAC. Between these electrodes an electric field exists, its homogeneity is maintained by a set of guarding bars/rings connected to equidistantly divided polarizing potential.

Main components of FAC [2]:

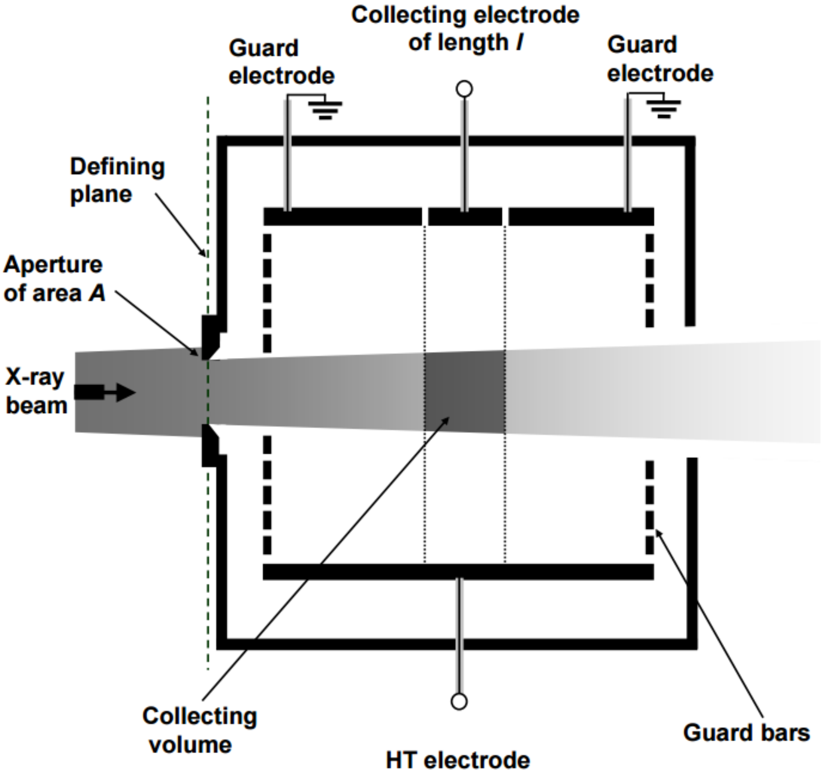

Air kerma is then determined by collecting and measurement of the charge created in the measuring/collecting volume:

$$K_{air} = \frac{Q}{m}\frac{W_{air}}{e}\frac{1}{(1-g)}$$

where
- Q - collected charge,
- m - air mass in the collecting volume,
- W_{air}/e - energy required to produce an ion pair in dry air (W_{air}/e = 33,97 J/C),
- g - fraction of energy loss to bremsstrahlung (for X rays from 8 to 300kV g is negligible (g = 0)),

Because the collecting volume is a section of air deep inside the FAC and its shape and dimensions are determined by the beam and the effective collector length, it is not possible to measure the actual measuring volume (i.e. the air mass) inside the FAC directly!
However, it can be shown [2] that the charge, Q, collected by a FAC is a measure of the exposure at the defining plane of the aperture, corrected for air attenuation between the aperture and collecting electrode:

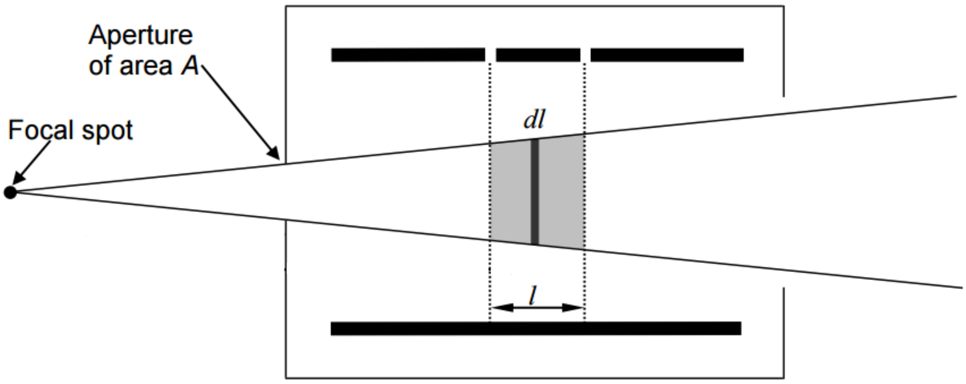

Beam cross-section at the aperture defining plane is equal to the aperture area, A, so then:

$$K_{A,air} = \frac{Q}{A.l.\rho}\frac{W_{air}}{e}\frac{\prod k_i}{(1-g)}$$

where
- Q – collected charge,
- A – aperture area,
- l – effective length of the collector (i.e. incl. half of the air gap),
- ρ - air density at a pressure of 101.325 kPa, a temperature of 20ºC and 50% relative humidity,
- Πk_i – product of several correction factors.

So, the task of air kerma measurement is divided into three separated sub-tasks: determination/measurement of the A and l parameters; determination of the correction factors values; and, measurement of the charge Q.

3 Realization

This chapter summarises the main considerations when working on the FAC design and on the above mentioned sub-tasks.

Dimensions:

- aperture diameter: ideally should be as small as possible, but larger then the X-ray tube focus. And, we need some measurable charge/current, so one should calculate the desired measuring volume based on expected air kerma rates;
- aperture thickness: simple solution: calculation of thickness sufficient to attenuate the primary photons (eg. 1 mm of tungsten for low energies up to 50 keV); more sophisticated approach: MC simulations of the aperture layout and optimisation of aperture influence corrections (useful for medium-energy FAC);
- aperture-to-collector distance: has to be larger than the electron range to achieve CPE;
- collector length: ideally should be as small as possible, because mainly for lower energies the attenuation in air is changing along the collector, but again, we need some measurable charge/current, so one should calculate the desired measuring volume based on expected air kerma rates; for medium energies it can be larger (smaller attenuation change along the collector);
- internal dimensions (distance of the internal parts from the beam): has to be larger than the electron range => for low energies: simple calculation based on the electron range, for medium energies: MC simulations and optimisation;

- outer radiation shielding thickness: has to ensure sufficient attenuation to minimise the wall transport.

High voltage:

- electric field strength of appr. 100-200V/cm required for sufficient charge collection => appr. 1-2kV for low-energy, 4-6kV for medium-energy. CMI decision for low-energy FAC: 1500V

Examples of several low-energy FACs:

Dimension [mm]	BIPM	LNHB	BEV	GUM	ENEA	ARPANSA	NIST	CMI
Aperture diameter	9.941	5.0085	8.0240	9.995	8.014	4.9879	10.0017	10.164
Air path length	100.0	71.95	63.64	102.2	65.12	85.0	127.4	100.007
Collecting length	15.466	20.445	40.822	20.273	40.738	20.197	70.03	14.498
Electrode separation	70	118.6	60	69.9	60	60	90	70
High voltage [V]	+1500	+3000	+1600	+4000	+1600	-3000	+5000	+1500

Examples of several medium-energy FACs:

Dimension [mm]	BIPM	LNHB	BEV	GUM	VSL	ARPANSA	NMIJ
Aperture diameter	10	10	20	10	10	8	10
Aperture to collector	282	318	465	393	520	297	372
Collector length	60	60	300	100	100	101	100
Electrode separation	180	180	326	240	300	200	240
High voltage [V]	4000	5000	6000	500	6000	5000	4000

Material and make:

- diaphragm: tungsten (stable shape, high density, high Z); precise aperture, dimensions measurement by CMM (Coordinate Measuring Machine) with an accuracy of few µm;
- electrodes: aluminium alloy; no need for special surface processing, smooth glossy surface is sufficient, however graphite layer on the base electrode and collector recommended by a BIPM [3]. CMM measurements of the collector length and air-gap dimensions, aperture-to-collector distance, mutual levelness of collector and base electrode;
- insulators (i.e. distance pieces between guard electrodes, collector holder): stable shape necessary, carefully cleaned surface to lower the leakage current: sapphire, glass, durable plastic;
- outer shell: e.g. stainless steel, lead for the front plate

Number of guard electrodes:

Ideally as many as possible to achieve homogenous electric field, however this is of course not practical. Preferably thicker electrodes, thinner air gap [1]. Electric field simulation made using the QuickField^{TM} (infinite-element simulation software). CMI: 17 electrodes for low-energy FAC (HV and base electrode separation 70mm), 35 electrodes for medium-energy FAC (HV and base electrode separation 300mm).

Voltage divider:

Resistances of 10MΩ placed outside the chamber to reduce heating.

Wires:

FAC is emg. shielded, nevertheless it is recommended to use shielded coaxial cables inside the chamber.

Connectors:

Measuring chain similar to that of secondary chamber, therefore: signal - BNC connector, HV - determined by the HV source (up to 5kV: SHV Kings1704-1, 5kV up to 20kV: Kings1764-1).

Measuring apparatus:

The same consideration is valid as for a secondary ionization chamber that the uncertainty of the charge (current) measurement directly influences the resulting air kerma uncertainty, so precise electrometer (eg. Keithley 6517A,B) and stable HV source (eg. Keithley 2290-5 or 2290-10) are necessary. Internal temperature sensor recommended.

Some pictures from the FAC design:

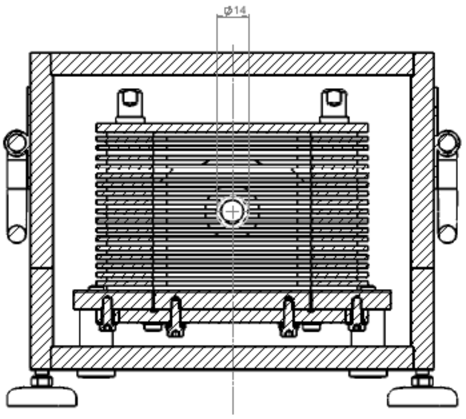

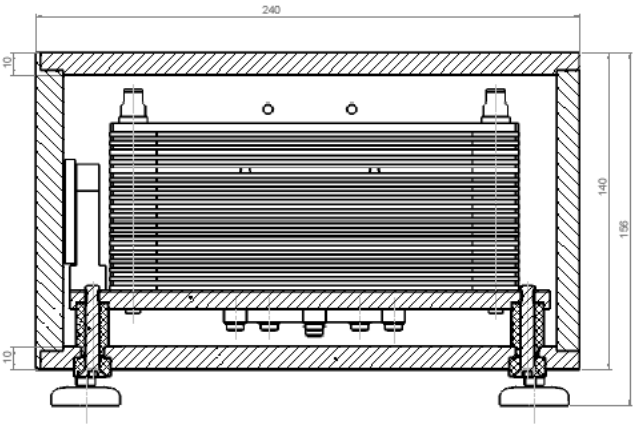

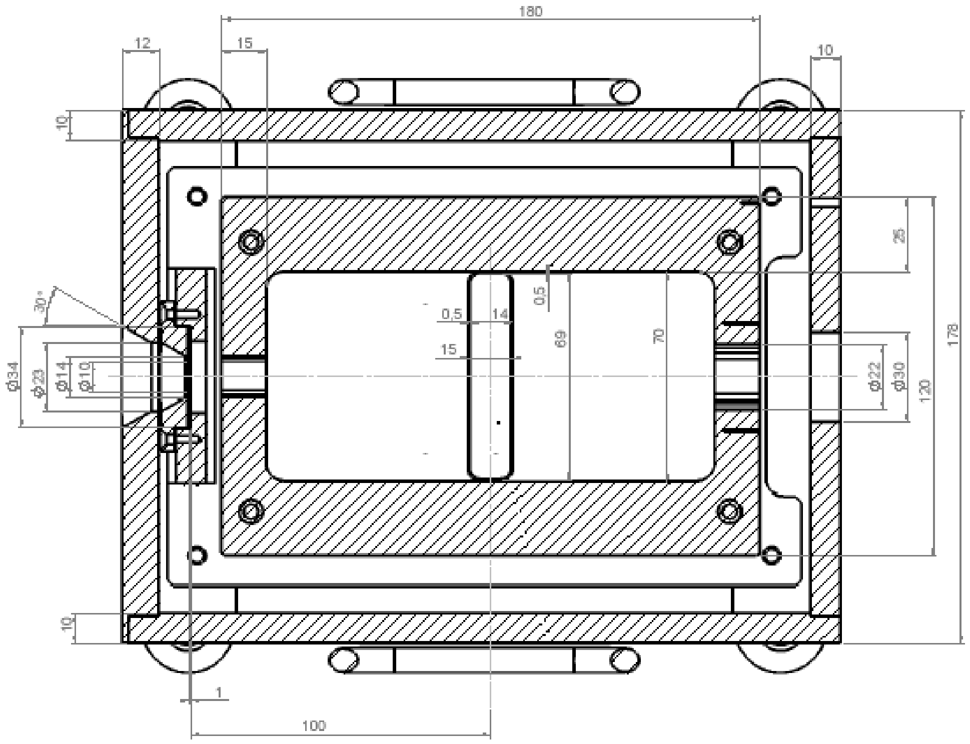

FAC drawings

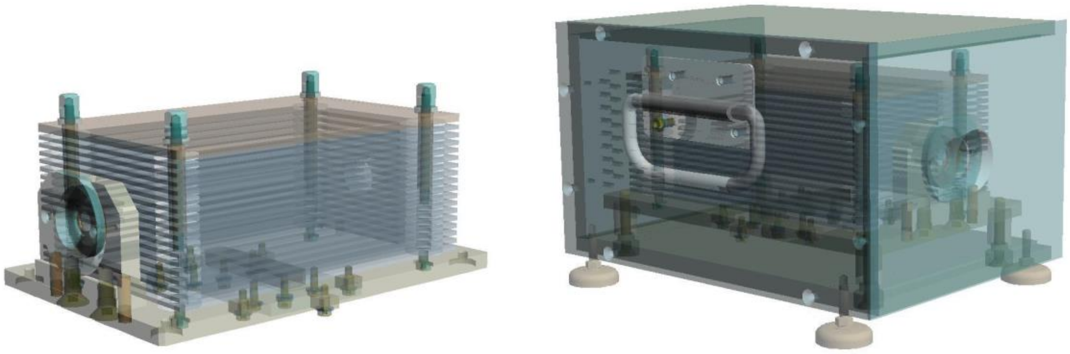

CAD visualisation, on the left FAC without outer shielding

FAC without outer shielding (on the left),
FAC with the HV electrode removed, collector visible (on the right)

CMM measurement of the aperture diameter (on the left),
voltage divider on the FAC rear wall (on the right)

4 Correction factors

With the parts carefully manufactured by a competent manufacturer, dimensions *A* and *l* determined by CMM measurements and the charge *Q* measured by stable and accurate measuring chain, the correction factors are the "tricky" part of FAC realization.

"usual", i.e. corrections which are the same as for a secondary ionization chamber: correction for humidity, k_h, air pressure and temperature, $k_{T,p}$, correction for HV polarity, k_{pol}, and saturation, k_s;

el. field distortion, k_d: the collecting volume is defined by "effective" collector length, i.e. actual collector length plus one half of the air gap on both sides of the collector. This assumes that the collected charge is evenly distributed between collector and base electrode. However, if the field is not homogenous, the charge is not collected as assumed, thus the collecting volume is not correctly defined. This can happen if the guarding bars are not correctly designed or working or if the collector is not flush with the base electrode (see BIPM [3]). Other reason could be a potential difference between collector and base electrode, but this influence is corrected already by the polarity correction. Field homogeneity is usually verified by simulations using finite element analysis system QuickField™ (Tera Analysis Ltd.). Correction is usually laid equal 1 influencing the uncertainty only.

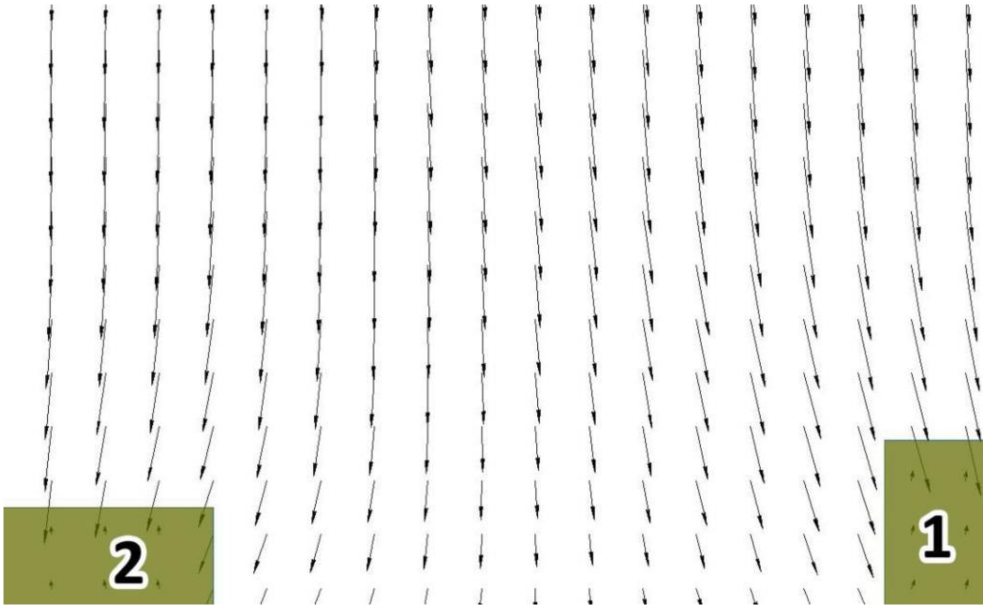

Influence of the electrode displacement to the electric field shape. One can see the field lines unevenly distributed between the collector (1) and the base electrode (2). Consequently, the effective collecting volume is enlarged towards the base electrode in this case.

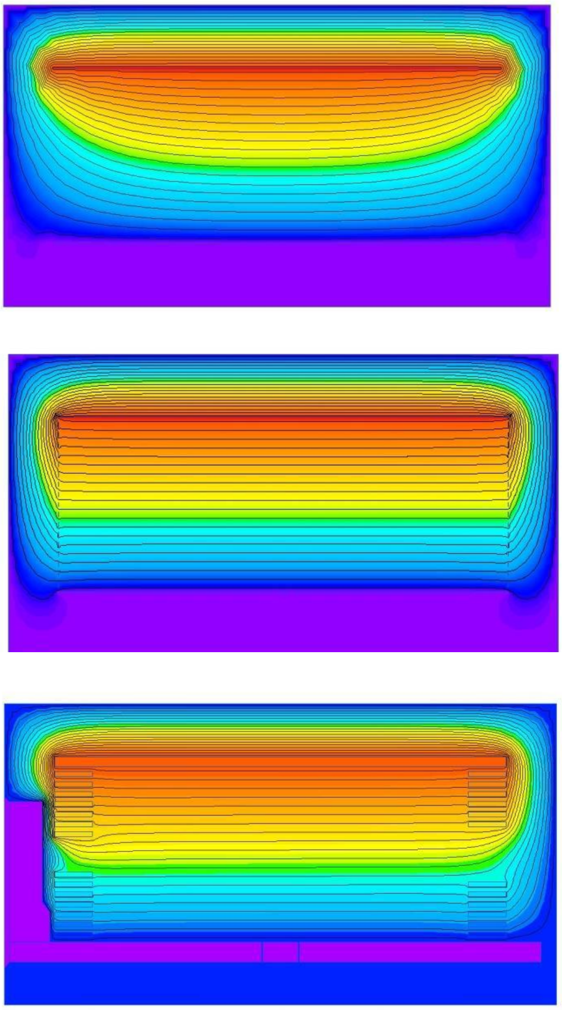

Simulation of electric field between the HV and base electrode (on the top), with the guarding bars added (in the middle) and in the realistic model of FAC (on the bottom)

attenuation, k_{att}: correction for the attenuation of primary photons between the aperture and collector; can be determined experimentally (several ways), calculated analytically using μen values or by MC simulations (solution adopted in CMI);

scattered photons, k_{sc}, and fluorescence photons from Ar, k_{fl}: correction for secondary photons contributing to the collected charge; can be determined experimentally (tube along the beam inside the chamber), in CMI calculated using MC simulations;

charge loss, k_e: correction for electrons impacting the internal parts of the chamber, thus not contributing to the collected charge; equals 1 for internal dimensions larger than the electron range, then increases. Calculated by MC simulations;

aperture influence: correction for transmission of photons through the aperture, kdtr, and for photons scattered on the aperture edge, kdsc - MC simulations;

outer wall, k_p: correction for photon transmission through the outer wall - MC simulations;

Monte Carlo simulations of correction factors at CMI using MCNPX [13]:

– performed in two steps: first, a simulation was used to generate a Particle Track output (PTRAC) file storing information necessary to distinguish photons and electrons contributing to different correction factors and for each correction factor a separate ASCII file was generated storing information about position, direction vector, energy and weight of each particle contributing to the given correction factor.

- then, second set of simulations – one simulation per each ASCII file used as particle source inputs. Results of these simulations were used to determine a numerical value of each correction factor utilizing formulae published by Kurosawa and Takata [8], [9] (kdtr and kdsc) and Laitano et al. [11] (ksc, kfl, ke).
- in addition, katt was determined as a ratio of air kerma at the aperture to that at the center of the collecting volume, and ktr was obtained using simulations with and without a diaphragm transmittable for photons.

Examples of MC simulations using MCNPX^{TM}

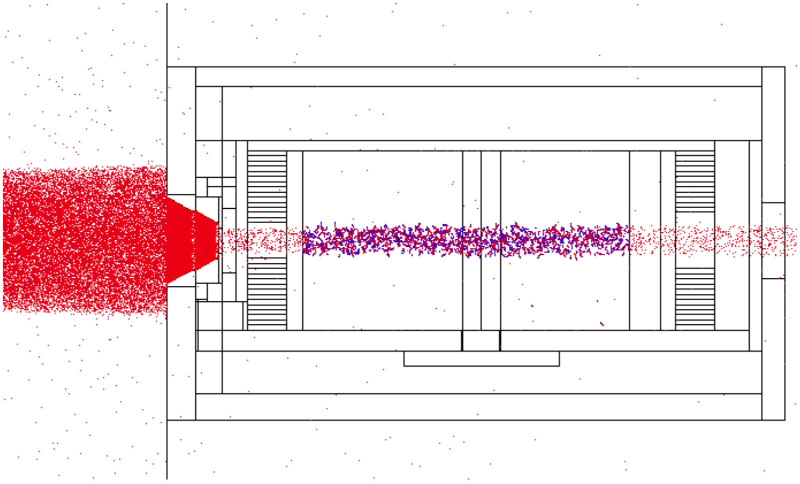

N10

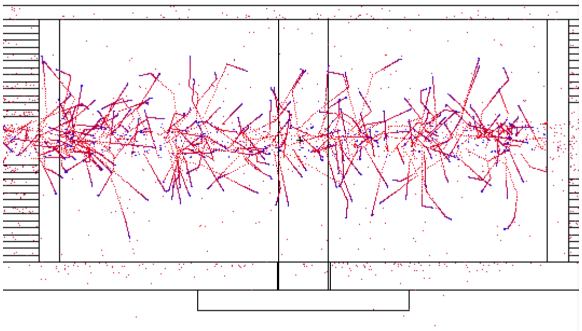

N40

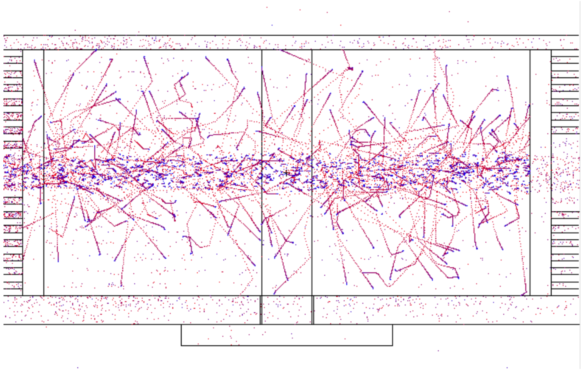

N60 (electrons impacting the internal parts are visible)

initial charge, k_{ii}: correction for additional charge of initial electron, which contributes to the collected charge, but it is not included in the air kerma definition; recommended by Buerman [1], not yet recommended by CCRI, therefore currently not implemented at CMI.

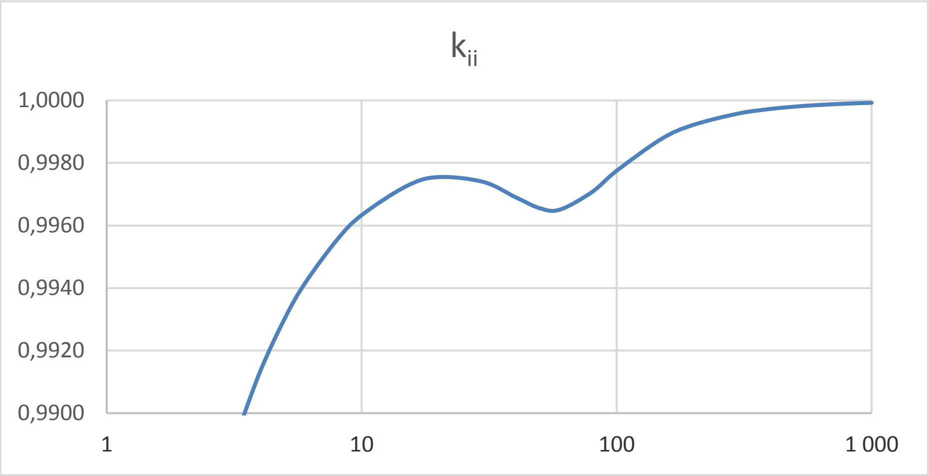

k_{ii} value as a function of photon energy (in keV)

Values of correction factors of the low-energy FAC at CMI

Radiation quality	**10kV**	**30kV**	**25kV**	**50kVb**	**50kVa**	u_{iA}	u_{iB}
Air attenuation k_{att}	1.1977	1.0442	1.0306	1.0083	1.0045	-	0.0030
Scattered radiation k_{sc}	0.9954	0.9973	0.9975	0.9981	0.9983	-	0.0010
Fluorescence k_{fl}	0.9947	0.9961	0.9964	0.9976	0.9981	-	0.0006
Electron loss k_e	1.0000	1.0000	1.0000	1.0000	1.0000	-	0.0002
Ion recombination k_s	1.0010	1.0010	1.0010	1.0010	1.0010	-	0.0003
Polarity k_{pol}	1.0006	1.0006	1.0006	1.0006	1.0006	-	0.0003
Field distortion k_d	1.0000	1.0000	1.0000	1.0000	1.0000	-	0.0010
Aperture transmission k_{dtr}	0.9997	0.9999	0.9999	0.9999	0.9999	-	0.0003
Aperture scatter k_{dsc}	0.9999	1.0000	1.0000	1.0000	1.0000	-	0.0003
Wall transmission k_p	1.0000	1.0000	1.0000	1.0000	1.0000	-	0.0001
Humidity k_h	0.9980	0.9980	0.9980	0.9980	0.9980	-	0.0003
$1 - g_{air}$	1.0000	1.0000	1.0000	1.0000	1.0000	-	0.0001

5 Uncertainty budget of the low-energy FAC at CMI

Relative standard uncertainty	u_{iA}	u_{iB}
Ionization current	0.0015	0.0023
Positioning	-	0.0007
Volume	-	0.0006
Correction factors (excl. kh)	-	0.0034
Humidity k_h	-	0.0003
Physical constants	-	0.0015
	0.0015	0.0045
	0.0047	

6 Conclusion

Prerequisities:

1) MC simulations
2) electric field analysis system (eg. QuickField)
3) competent manufacturer
4) CMM
5) suitable charge measurement apparatus

7 Literature

[1] D.T.Burns and L. Buermann: Free-air ionization chambers, Metrologia 46 (2009), S9-S23
[2] Practical Course in Reference Dosimetry „kV X-ray Dosimetry at NPL“, National Physical Laboratory; http://www.npl.co.uk/upload/pdf/pcrd-9-notes.pdf
[3] C. Kessler, P. Roger, D. T. Burns: Establishment of reference radiation qualities for mammography, BIPM Rapport-2010/01,
[4] ICRU (1980); International Commission on Radiological Units and Measurement, Radiation Quantities and Units, *ICRU Report 33*
[5] CCEMRI 1985 report of the 8th meeting of section I (Rayons X et γ, électrons), *Comité Consultatif pour les Étalons de Mesure des Rayonnements Ionisants, Rapport de la 11ème session* (Sèvres: BIPM) R157-166
[6] Correction d’Humidité Report of the 4th meeting of Section I (Rayons X et γ, électrons), Comité Consultatif pour les Étalons de Mesure des Rayonnements Ionisants, Rapport de la 4ème Réunion –1977 page R(I)6, Bureau International des Poids et Mesures (BIPM), Sèvres,1977
[7] D.T. Burns at all: Key comparison BIPM.RI(I)-K2 of the air kerma standards of ENEA-INMRI, Italy and the BIPM in low-energy X-rays, *Metrologia 48 (2011) Tech. Suppl. 06010*
[8] T. Kurosawa, N. Takata: Estimation of Electron-loss and Photon-scattering Corrections for Parallel-plate Free-air Chambers, Journal of Nuclear Science and Technology, Vol. 42, No. 12, pp. 1077-1080 (Dec. 2005)
[9] T. Kurosawa, N. Takata: Correction factors for free-air ionization chambers for X-rays transmitted through a diaphragm edge and scattered from the surface of diaphragm aperture, Report CCRI(I)/05-27
[10] K. Derikum, Correcting for ion recombination effects in ionization chambers consistently in continuous and pulsed radiation, IAEA-CN-96-30
[11] Laitano, R.F., Pimpinella, M., Toni, M.P., 2005. Re-determination of the k_{sc}, k_e, k_{fl} Correction Factors for Low and Medium Energy x-ray Air-kerma Measurement by the ENEA-INMRI Free-air Chambers. CCRI(I)/05-31
[12] Ulrike Ankerhold: Catalogue of X-ray spectra..., PTB-Dos-34, Braunschweig, April 2000
[13] Pelowitz, D.B., Durkee, J.W., Elson, J.S., Fensin, M.L, Hendricks, J.S., et al., 2011. MCNPX$^{\text{TM}}$ 2.7.E Extensions.

Free air chamber at BEV

Andreas Steurer, Wilhelm Tiefenböck

The paper presents the technical description of the Primary Standards for cobalt 60 and Cesium 137 photons based on cavity chamber including the identification and determination of correction factors.

1 Primary Standards – air kerma X-ray Radiation qualities: different Free air ionization Chamber

1.1 Principle

The air kerma rate measured with a free-air ionization chamber primary standard is determined by the relation

$$\dot{K}_{\mathrm{a}} = \frac{I}{\rho_a \cdot V} \cdot \left(\frac{W}{e}\right) \cdot \frac{1}{1-g_{\mathrm{a}}} \qquad (1) \qquad ; \quad \text{with} \qquad V = \frac{d_{\mathrm{ap}}^2 \cdot \pi}{4} \cdot l_{\mathrm{E}} \qquad (2)$$

Under real conditions correction factors must be used:

$$\dot{K}_a = I_+ \cdot k_{\mathrm{pol}} \cdot \left(\frac{k_{pT}}{\rho_a \cdot V}\right) \cdot \left(\frac{W}{e}\right) \cdot \frac{1}{1-g_{\mathrm{a}}} \cdot \frac{k_{\mathrm{a}}}{k_{\mathrm{a0}}} \cdot k_{\mathrm{s,vol}} \cdot \prod_i k_i \qquad (3)$$

with:

$$k_{\mathrm{pol}} = \frac{I_+ + I_-}{2 \cdot i_+} \qquad (4)$$

$$k_{pT} = \frac{p_0}{p} \cdot \frac{273{,}15 + T}{273{,}15 + T_0} \qquad (5)$$

$$\frac{k_{\mathrm{a}}}{k_{\mathrm{a0}}} = \mathrm{e}^{\left[\left(\frac{\mu}{\rho}\right)_0 \cdot \left(\frac{1}{k_{pT}} - 1\right) \cdot d_{\mathrm{a}} \cdot \rho_a + \left(\frac{\mu}{\rho}\right)_1 \cdot \frac{R \cdot d_{\mathrm{a}} \cdot \rho_{\mathrm{a}}^2}{k_{pT}^2}\right]} \qquad (6)$$

$$k_{\mathrm{s,vol}} = 1 + s \cdot I_+ \qquad (7)$$

The resulting calibration coefficient is defined by:

$$\dot{K}_a = I_{\mathrm{P}} \cdot N_{\dot{K}_a,\mathrm{P}} \qquad (8)$$

with:

$$I_P = I_+ \cdot k_{pT} \cdot \frac{k_{\mathrm{a}}}{k_{\mathrm{a0}}} \cdot k_{\mathrm{s,vol}} \qquad (9)$$

$$N_{\dot{K}_a,\mathrm{P}} = \frac{1}{\rho_a \cdot V} \cdot \left(\frac{W}{e}\right) \cdot \frac{1}{1-g_{\mathrm{a}}} \cdot k_{\mathrm{pol}} \cdot \prod_i k_i \qquad (10)$$

Every factor in this product is an input quantity to calculate calibration coefficient. The relative combined standard uncertainty of the calibration coefficient is calculated with:

$$u_{N_{\dot{K}_a}} = \sqrt{\sum_i \left(u_{i,\mathrm{A}}^2 + u_{i,\mathrm{B}}^2\right)} \qquad (11)$$

The meaning of the symbols is described in table 1.

Symbol	Meaning
$\dot{K}_\mathrm{a}$	Air kerma rate
I	Ionization current measured with the free-air ionization chamber
ρ_a	Density of dry air under reference conditions
V	Measuring volume of the free-air ionization chamber
(W_a / e)	Mean energy expended by an electron to produce an ion pair in air
g_a	Fraction of the initial electron energy lost through radiative processes in air
d_ap	Aperture diameter
l_E	Length of the collecting electrode(s)
I_+	Ionization current measured with positive polarity
I_-	Ionization current measured with negative polarity
k_pol	Correction factor with regard to polarity
k_pT	Correction factor with regard to air density for measurement conditions differing from reference conditions
p_0	Air pressure at reference conditions (p_0 = 101,325 kPa)
p	Air pressure during measurement
T_0	Air temperature at reference conditions (T_0 = 20 °C)
T	Air temperature during measurement
$\frac{k_\mathrm{a}}{k_{a0}}$	Correction factor to correct the influence of the air attenuation for measurement conditions differing from reference conditions for the air path length (distance between the reference point of the free-air ionization chamber and the effective point of ionzation current measurement in the middle of the measuring volume)
$(\mu / \rho)_0$	First order mass attenuation coefficient at reference conditions
$(\mu / \rho)_1$	Second order mass attenuation coefficient at reference conditions (only for 10 kV unequal 0)
d_a	Air attenuation distance between the reference point of the free-air ionization chamber and the geometric center of the collecting electrode(s)
R	Distance from the focus of the X-ray tube to the reference point of the free-air ionization chamber
$k_\mathrm{s,vol}$	Correction factor with regard to volume recombination
s	Volume recombination coefficient
I_P	Ionization current of the free-air ionization chamber primary standard corrected to reference conditions and with regard to volume recombination
$\prod_i k_i$	Product of energy depending correction factors which are independent of dose rate and air density
$N_{\dot{K}_a,\mathrm{P}}$	Calibration coefficient of the free-air ionization chamber primary standard to calculate the air kerma rate
$u_{N_{\dot{K}_a}}$	Relative combined standard uncertainty of the calibration coefficient
$u_{i,\mathrm{A}}$	Relative standard uncertainty of type A of the input quantity *i*
$u_{i,\mathrm{B}}$	Relative standard uncertainty of type B of the input quantity *i*

Table 1 Meaning of the symbols (to be continued on the next page)

The values for the physical constants used for the determination of air kerma are given in Table 2.

Symbol	Value	Uncertainty	
		$u_{i,\mathrm{A}}$	$u_{i,\mathrm{B}}$
ρ_a	0,001 204 5 g·cm^{-3}	-	0,01 %
$\left(\frac{W_\mathrm{a}}{e}\right)$	33,97 J·C^{-1}	-	0,15 %

Table 2 Physical constants used for the determination of the Air Kerma Rate

The product of correction factors is given by

$$\prod_i k_i = k_{\mathrm{a0}} \cdot k_{\mathrm{sc}} \cdot k_{\mathrm{sa}} \cdot k_{\mathrm{el}} \cdot k_{\mathrm{pe}} \cdot k_{\mathrm{fl}} \cdot k_{\mathrm{br}} \cdot k_{\mathrm{d}} \cdot k_{\mathrm{t}} \cdot k_{\mathrm{s,ini}} \cdot k_{\mathrm{h}} \qquad (12)$$

The Meaning of the corrections are given in Table 3.

Symbol	Meaning
k_{a0}	Air attenuation of the air path length for reference conditions
k_{sc}	Scatter
k_{sa}	Scatter in aperture
k_{el}	Electron loss
k_{pe}	Lip effect aperture
k_{fl}	Fluorescence
k_{br}	Bremsstrahlung reabsorbing
k_{d}	Field distortion
k_{t}	Wall transmission
$k_{\mathrm{s,ini}}$	Initial recombination
k_{h}	Humidity

Table 3 Correction factors for the determination of the Air Kerma Rate

The correction factors are caused by different effects, which can described as follows:

$$k_{\mathrm{sc}} = \frac{E_{\mathrm{ap}}}{E_{\mathrm{ap}} + E_{\mathrm{asc}}} \quad (13) \quad ; \quad k_{\mathrm{sa}} = \frac{E_{\mathrm{ap}}}{E_{\mathrm{ap}} + E_{\mathrm{asa}}} \quad (14) \quad ; \quad k_{\mathrm{el}} = \frac{E_{\mathrm{ap}} + E_{\mathrm{bp}}}{E_{\mathrm{ap}}} \qquad (15)$$

$$k_{\mathrm{pe}} = \frac{E_{\mathrm{ap}}}{E_{\mathrm{ap}} + E_{\mathrm{ape}}} \quad (16) \quad ; \quad k_{\mathrm{fl}} = \frac{E_{\mathrm{ap}}}{E_{\mathrm{ap}} + E_{\mathrm{afl}}} \quad (17) \quad ; \quad k_{\mathrm{br}} = \frac{E_{\mathrm{ap}}}{E_{\mathrm{ap}} + E_{\mathrm{abr}}} \qquad (18)$$

$$k_{\mathrm{t}} = \frac{E_{\mathrm{ap}}}{E_{\mathrm{ap}} + E_{\mathrm{at}}} \qquad (19)$$

Meaning of the symbols

E_{ap}	To the measuring volume A transferred energy by electrons (and following particles), which are generated by interaction with primary photons
E_{asc}	To the measuring volume A transferred energy by electrons (and following particles), which are generated by interaction with scattered photons
E_{asa}	To the measuring volume A transferred energy by electrons (and following particles), which are generated by interaction with the aperture
E_{bp}	Not to the measuring volume A but to the surrounding area B transferred energy by electrons (and following particles), which are generated by interaction with primary photons
E_{ape}	To the measuring volume A transferred energy by particles (and following particles) by transmission through the lead around the aperture
E_{afl}	To the measuring volume A transferred energy by electrons (and following particles), which are generated by interaction with fluorescence photons
E_{abr}	To the measuring volume A transferred energy by electrons (and following particles), which are generated by interaction with bremstrahlung photons
E_{at}	To the measuring volume A transferred energy by particles (and following particles) by transmission through the front wall auf the chamber

The Calibration Coefficient of the Ionization Chamber in terms of Air Kerma is given in Equation (10).

1.1.1 Free Air Ionization Chamber PKK

The characteristics (main dimensions, the measuring volume and polarizing voltage) of the free-air ionization chamber PKK (Parallelplatten Kammer Klein = small parallel plate chamber) are given in Table 4 and Figure 1.

	Symbol	Value	Uncertainty	
			$u_{i,\mathrm{A}}$	$u_{i,\mathrm{B}}$
Aperture diameter (aperature K6)	d_{ap}	0,802 40 cm	-	-
Air path length	d_{a}	6,364 cm	-	-
Electrode collecting length	l_{E}	4,082 2 cm	-	-
Electrodes separation	-	6 cm	-	-
Collector width	-	6 cm	-	-
Measuring volume	V	2,064 3 cm^3	-	0,10 %
Volume recombination coefficient	s	$0{,}002\,4 \cdot 10^9\ \mathrm{A}^{-1}$	0,02 %	0,05 %
Polarizing voltage	HV	+ 1 600 V	-	-

Table 4 Free-air ionization chamber PKK, main characteristics

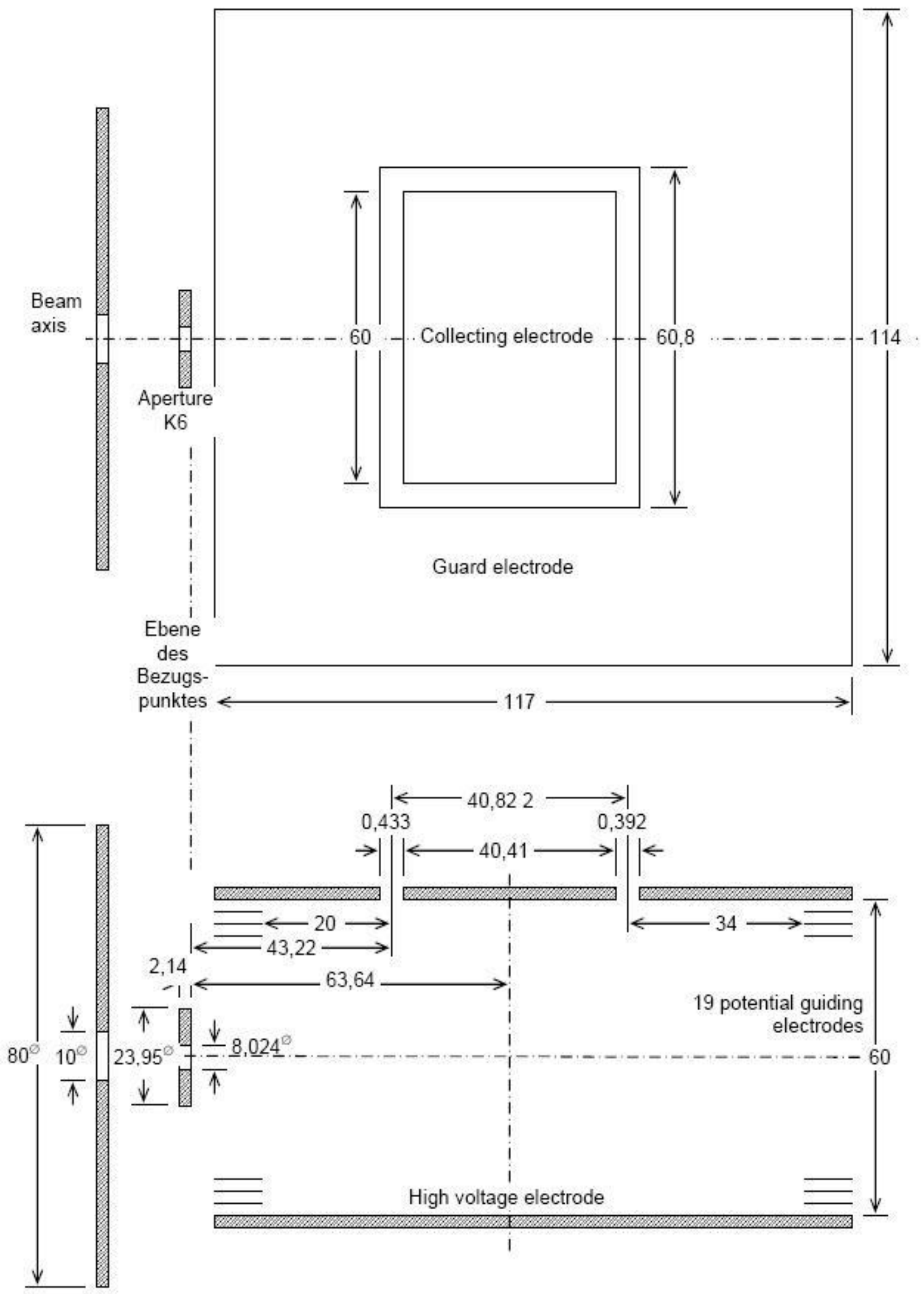

Figure 1 Free-air ionization chamber PKK, schematic drawing

The free-air ionization chamber PKK is the BEV Primary Standard for measurement of air kerma for low energy X-rays (radiation qualities TW10, TW25, TW30, TW50, SH50).

The main characteristics for these radiation qualities are described in Table 5. The corrections factors are given in Table 6.

	Symbol	Unit	Values for different radiation qualities				
			TW10	TW25	TW30	TW50	SH50
X-ray high voltage	U	kV	10	25	30	50	50
Filter (Al)	-	mm	-	0,400	0,225	1,150	4,120
Half value layer (Al)	HVL	mm	0,030	0,244	0,170	1,000	2,232
First order mass attenuation coefficient	$\left(\frac{\mu}{\rho}\right)_0$	$\frac{\text{cm}^2}{\text{g}}$	24,660	2,545	3,602	0,754	0,378
Second order mass attenuation coefficient	$\left(\frac{\mu}{\rho}\right)_1$	$\frac{\text{cm}^4}{\text{g}^2}$	-117,54	0	0	0	0

Table 5 Main characteristics for the free-air ionization chamber PKK for low energy X-rays (radiation qualities TW10, TW25, TW30, TW50, SH50)

Correction	Symbol	Uncertainty		Values for different radiation qualities				
		$u_{i,\text{A}}$	$u_{i,\text{B}}$	TW10	TW25	TW30	TW50	SH50
Fraction of the initial electron energy lost trough radiative processes in air	g_a	-	0,02 %	0,000 1	0,000 2	0,000 2	0,000 2	0,000 3
	$\frac{1}{1-g_\text{a}}$	-	0,02 %	1,000 1	1,000 2	1,000 2	1,000 2	1,000 3
Polarity	k_pol	0,02 %	0,05 %	1,000 0	1,000 0	1,000 0	1,000 0	1,000 0
Attenuation	k_a0	0,02 %	0,57 % (TW10) 0,30 % (other)	1,208 1	1,019 7	1,028 0	1,005 8	1,002 9
Scatter	k_sc	-	0,10 %	0,995 0	0,996 0	0,996 0	0,997 0	0,997 0
Scatter in aperture	k_sa	-	0,10 %	1,000 0	1,000 0	1,000 0	1,000 0	1,000 0
Electron loss	k_el	-	0,05 %	1,000 0	1,000 0	1,000 0	1,000 0	1,001 0
Lip effect aperture	k_pe	-	0,02 %	1,000 0	1,000 0	1,000 0	1,000 0	1,000 0
Fluorescence	k_fl	-	0,05 %	1,000 0	1,000 0	1,000 0	1,000 0	1,000 0
Bremsstrahlung reabsorbing	k_br	-	0,05 %	1,000 0	1,000 0	1,000 0	1,000 0	1,000 0
Field distortion	k_d	-	0,10 %	1,000 0	1,000 0	1,000 0	1,000 0	1,000 0
Wall transmission	k_t	0,02 %	0,02 %	1,000 0	1,000 0	1,000 0	1,000 0	1,000 0
Initial recombination	$k_\text{s,ini}$	0,02 %	0,03 %	1,000 6	1,000 6	1,000 6	1,000 6	1,000 6
Humidity	k_h	-	0,05 %	0,998 0	0,998 0	0,998 0	0,998 0	0,998 0

Table 6 Correction factors for the free-air ionization chamber PKK for low energy X-rays (radiation qualities TW10, TW25, TW30, TW50, SH50)

The calibration coefficients and the corresponding standard uncertainty are given in Table 7.

	Symbol	Unit	Values for different radiation qualities				
			TW10	TW25	TW30	TW50	SH50
Calibration coefficient	$N_{\dot{K}_a}$	$10^7 \frac{\text{Gy}}{\text{C}}$	1,640 1	1,385 9	1,397 2	1,368 4	1,365 9
Relative combined standard uncertainty	$u_{N_{\dot{K}_a}}$	-	0,58 %	0,30 %	0,30 %	0,30 %	0,30 %

Table 7 Calibration coefficients of the free-air ionization chamber PKK for low energy X-rays (radiation qualities TW10, TW25, TW30, TW50, SH50)

1.1.2 Free Air Ionization Chamber PKM

The caracteristics (main dimensions, the measuring volume and polarizing voltage) of the free-air ionization chamber PKM (Parallelplatten Kammer Mittel = medium parallel plate chamber) are given in Table 8 and Figure 2.

	Symbol	Value	Uncertainty	
			$u_{i,\mathrm{A}}$	$u_{i,\mathrm{B}}$
Aperture diameter (aperature G4)	d_{ap}	2,002 05 cm	-	-
Air path length	d_{a}	10,990 cm	-	-
Electrode collecting length (2 electrodes)	l_{E}	5,645 47 cm	-	-
Electrodes separation	-	11,496 5 cm	-	-
Collector width	-	13,05 cm	-	-
Measuring volume	V	17,773 1 cm^3	-	0,10 %
Volume recombination coefficient	s	$0{,}002\,5 \cdot 10^9\ \mathrm{A}^{-1}$	0,02 %	0,05 %
Polarizing voltage	HV	+ 2 500 V	-	-

Table 8 Free-air ionization chamber PKM, main characteristics

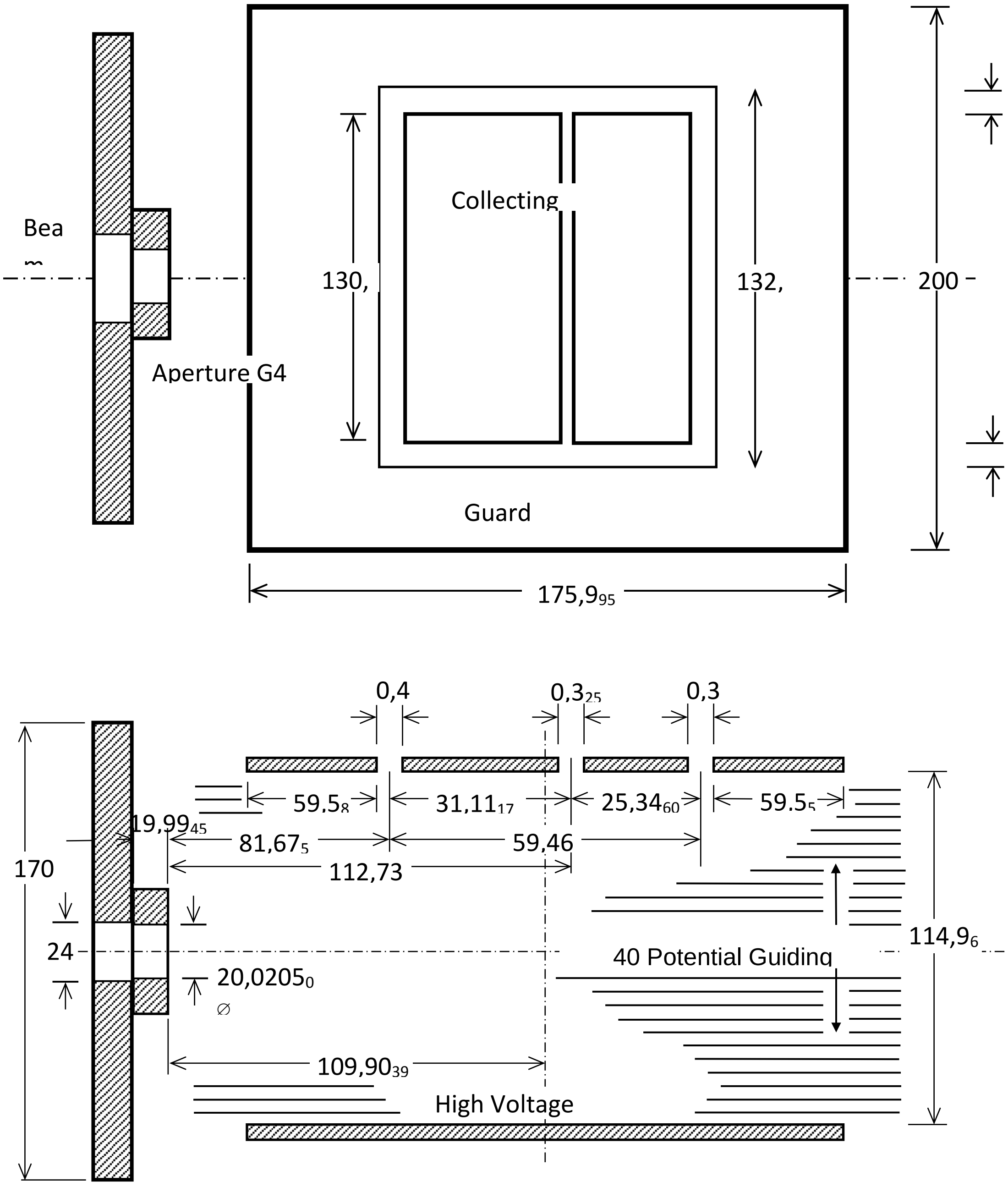

Figure 2 Free-air ionization chamber PKM, schematic drawing

The free-air ionization chamber PKM is the BEV Primary Standard for all diagnostic radiation qualities described in “Calibration and Verification at BEV” (this proceeding) section 2.1.3.1.

To give an example the data for the measurement of air kerma for mammograpy X-rays with Mo-tube and 30 µm Mo (radiation qualities MMV25, MMV28, MMV30, MMV35) are given.

The main characteristics for these radiation qualities are described in Table 9. The corrections factors are given in Table 10.

	Symbol	Unit	Values for different radiation qualities			
			MMV25	MMV28	MMV30	MMV35
X-ray high voltage	U	kV	25	28	30	35
Filter (Mo)	-	µm	30	30	30	30
Half value layer (Al)	*HVL*	mm	0,286	0,322	0,340	0,379
First order mass attenuation coefficient	$\left(\frac{\mu}{\rho}\right)_0$	$\frac{\mathrm{cm}^2}{\mathrm{g}}$	1,663	1,508	1,434	1,295

Table 9 Main characteristics for the free-air ionization chamber PKM for mammograpy X-rays with Mo-tube and 30 µm Mo (radiation qualities MMV25, MMV28, MMV30, MMV35)

Correction	Symbol	Uncertainty		Values for different radiation qualities			
		$u_{i,\mathrm{A}}$	$u_{i,\mathrm{B}}$	MMV25	MMV28	MMV30	MMV35
Fraction of the initial electron energy lost trough radiative processes in air	g_{a}	-	0,02 %	0,000 16	0,000 16	0,000 17	0,000 17
	$\frac{1}{1-g_{\mathrm{a}}}$	-	0,02 %	1,000 2	1,000 2	1,000 2	1,000 2
Polarity	k_{pol}	0,02 %	0,05 %	1,000 0	1,000 0	1,000 0	1,000 0
Attenuation	k_{a0}	0,02 %	0,10 %	1,022 3	1,020 2	1,019 2	1,017 3
Scatter	k_{sc}	-	0,10 %	0,994 6	0,994 8	0,994 9	0,995 1
Scatter in aperture	k_{sa}	-	0,20 %	0,998 9	0,998 9	0,998 8	0,998 7
Electron loss	k_{el}	-	0,05 %	1,000 0	1,000 0	1,000 0	1,000 0
Lip effect aperture	k_{pe}	-	0,05 %	1,000 0	1,000 0	1,000 0	1,000 0
Fluorescence	k_{fl}		0,05 %	0,996 8	0,996 9	0,996 9	0,997 0
Bremsstrahlung reabsorbing	k_{br}		0,05 %	0,999 9	0,999 9	0,999 9	0,999 9
Field distortion	k_{d}	-	0,10 %	1,000 0	1,000 0	1,000 0	1,000 0
Wall transmission	k_{t}	0,02 %	0,02 %	1,000 0	1,000 0	1,000 0	1,000 0
Initial recombination	$k_{\mathrm{s,ini}}$	0,02 %	0,03 %	1,000 5	1,000 5	1,000 5	1,000 5
Humidity	k_{h}	-	0,05 %	0,998 0	0,998 0	0,998 0	0,998 0

Table 10 Correction factors for the free-air ionization chamber PKM for Mammography X-rays with Mo-tube and 30 µm Mo (radiation qualities MMV25, MMV28, MMV30, MMV35)

Most of the data in Table 9 and Table 10 are calculated with mono energetic data and measured spectra as stated in “Calibration and Verification at BEV” (this proceeding) section 2.1.3.3 as mean value:

$$\left(\frac{\mu}{\rho}\right)_0 = \frac{\int \left(\frac{\mu}{\rho}\right)_0 (E) \cdot \Phi_E \cdot E \,\mathrm{d}E}{\int \Phi_E \cdot E \,\mathrm{d}E}, \; g_\mathrm{a} = \frac{\int g_\mathrm{a}(E) \cdot \Phi_E \cdot E \,\mathrm{d}E}{\int \Phi_E \cdot E \,\mathrm{d}E}, \; k_\mathrm{sc} = \frac{\int k_\mathrm{sc}(E) \cdot \Phi_E \cdot E \,\mathrm{d}E}{\int \Phi_E \cdot E \,\mathrm{d}E}, \ldots \tag{20}$$

Meaning of The symbols:

$\left(\frac{\mu}{\rho}\right)_0 (E)$	First order mass attenuation coefficient for photon energy E
$g_\mathrm{a}(E)$	Fraction of the initial electron energy lost trough radiative processes in for photon energy E
$k_\mathrm{sc}(E)$....................	Scattering correction factor for photon energy E
E..........................	Photon energy
Φ_E........................	Spectral Particle Fluence

The mono energetic data for the correction factors of the Free Air Ionization Chamber PKM were calculated with Monte Carlo methods. An example is given in Table 11.

Energy	k_sc	k_sa	k_el	k_pe	k_fl	k_br
5 keV	0,976060	0,999966	1,000000	0,999999	0,992938	0,999957
7 keV	0,977813	0,999905	1,000000	0,999996	0,994375	0,999946
10 keV	0,991077	0,999812	1,000000	0,999992	0,995617	0,999930
15 keV	0,994891	0,999065	1,000000	0,999993	0,996721	0,999919
20 keV	0,995887	0,998448	1,000000	0,999990	0,997377	0,999910
30 keV	0,996728	0,996893	1,000000	0,999943	0,998205	0,999910
40 keV	0,997023	0,995760	1,000000	0,999882	0,998688	0,999901
Spectrum	k_sc	k_sa	k_el	k_pe	k_fl	k_br
RQR-M2	0,99482	0,99886	1,00000	0,99999	0,99688	0,99992

Table 11 Calculated correction factors for the Mammograpy qualities MMV28 (RQR-M2)

The calibration coefficients and the corresponding standard uncertainty are given in Table 12.

	Symbol	Unit	Values for different radiation qualities			
			MMV25	MMV28	MMV30	MMV35
Calibration coefficient	$N_{\dot{K}_a}$	$10^5 \frac{\mathrm{Gy}}{\mathrm{C}}$	1,604 2	1,601 3	1,599 9	1,597 2
Relative combined standard uncertainty	$u_{N_{\dot{K}_a}}$	-	0,35 %	0,35 %	0,35 %	0,35 %

Table 12 Calibration coefficients of the free-air ionization chamber PKM for mammography X-rays with Mo-tube and 30 µm Mo (radiation qualities MMV25, MMV28, MMV30, MMV35)

1.1.3 Free Air Ionization Chamber PKG

The characteristics (main dimensions, the measuring volume and polarizing voltage) of the free-air ionization chamber PKG (Parallelplatten Kammer Gross = big parallel plate chamber) are given in Table 13 and Figure 3.

	Symbol	Value	Uncertainty	
			$u_{i,\mathrm{A}}$	$u_{i,\mathrm{B}}$
Aperture diameter (aperature G3)	d_{ap}	1,958 8 cm	-	-
Air path length	d_{a}	46,54 cm	-	-
Electrode collecting length (3 electrodes)	l_{E}	29,968 cm	-	-
Electrodes separation	-	32,6 cm	-	-
Collector width	-	31,9 cm	-	-
Measuring volume	V	90,308 cm^3	-	0,10 %
Volume recombination coefficient	s	0,000 8 · 10^9 A^{-1}	0,02 %	0,05 %
Polarizing voltage	HV	+ 6 000 V	-	-

Table 13 Free-air ionization chamber PKG, main characteristics

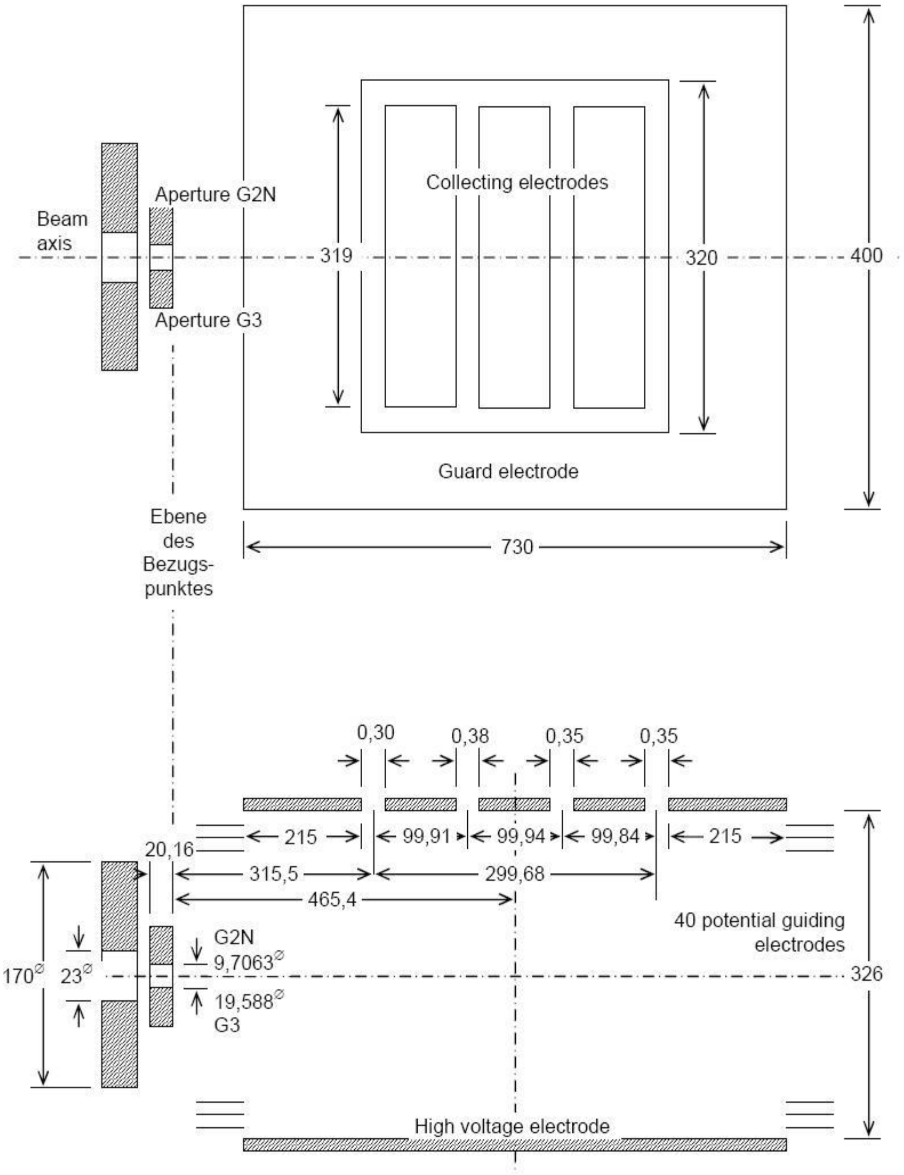

Figure 3 Free-air ionization chamber PKG, schematic drawing

The free-air ionization chamber PKG is the BEV Primary Standard for measurement of air kerma for medium energy X-rays (radiation qualities TW10, TW25, TW30, TW50, SH50).

The main characteristics for these radiation qualities are described in Table 14. The corrections factors are given in Table 15.

	Symbol	Unit	Values for different radiation qualities			
			TH100	TH135	TH180	TH250
X-ray high voltage	U	kV	100	135	180	250
Filter (Al)	-	mm	3,62	4,02	4,02	4,02
Filter (Cu)	-	mm	-	0,20	0,46	1,60
Half value layer (Al)	HVL	mm	3,99	-	-	-
Half value layer (Cu)	HVL	mm	-	0,49	0,99	2,51
First order mass attenuation coefficient	$\left(\frac{\mu}{\rho}\right)_0$	$\frac{\text{cm}^2}{\text{g}}$	0,285	0,211	0,177	0,153

Table 14 Main characteristics for the free-air ionization chamber PKG for medium energy X-rays (radiation qualities TH100, TH135, TH180, TH250)

Correction	Symbol	Uncertainty		Values for different radiation qualities			
		$u_{i,\text{A}}$	$u_{i,\text{B}}$	TH100	TH135	TH180	TH250
Fraction of the initial electron energy lost trough radiative processes in air	g_a	-	0,02 %	0,000 3	0,000 3	0,000 3	0,000 3
	$\frac{1}{1-g_\text{a}}$	-	0,02 %	1,000 3	1,000 3	1,000 3	1,000 3
Polarity	k_pol	0,02 %	0,05 %	1,000 0	1,000 0	1,000 0	1,000 0
Attenuation	k_a0	0,02 %	0,10 %	1,016 1	1,011 9	1,010 0	1,008 6
Scatter	k_sc	-	0,10 %	0,993 5	0,994 1	0,994 4	0,994 6
Scatter in aperture	k_sa	-	0,10 %	1,000 0	1,000 0	1,000 0	1,000 0
Electron loss	k_el	-	0,05 %	1,000 0	1,000 5	1,001 0	1,001 5
Lip effect aperture	k_pe	-	0,02 %	0,999 7	0,999 6	0,999 6	0,999 5
Fluorescence	k_fl	-	0,05 %	1,000 0	1,000 0	1,000 0	1,000 0
Bremsstrahlung reabsorbing	k_br	-	0,05 %	1,000 0	1,000 0	1,000 0	1,000 0
Field distortion	k_d	-	0,1 %	1,000 0	1,000 0	1,000 0	1,000 0
Wall transmission	k_t	0,02 %	0,02 %	1,000 0	1,000 0	1,000 0	1,000 0
Initial recombination	$k_\text{s,ini}$	0,02 %	0,03 %	1,001 0	1,001 0	1,001 0	1,001 0
Humidity	k_h	-	0,05 %	0,998 0	0,998 0	0,998 0	0,998 0

Table 15 Correction factors for the free-air ionization chamber PKG for medium energy X-rays (radiation qualities TH100, TH135, TH180, TH250)

2 BEV relating Literature

- D. T. Burns, C. Kessler, A. Steurer, W. Tiefenboeck, M. Bauer: “Key comparison BIPM.RI(I)-K7 of the air-kerma standards of the BEV, Austria and the BIPM in mammography x-rays” (Metrologia 52 (2015) Tech. Suppl. 06003)
- D. T. Burns, C. Kessler, A. Steurer, W. Tiefenboeck, M. Bauer: “Key comparison BIPM.RI(I)-K2 of the air-kerma standards of the BEV, Austria and the BIPM in low-energy x-rays” (Metrologia 52 (2015) Tech. Suppl. 06001)
- D. T. Burns, C. Kessler, A. Steurer, W. Tiefenboeck, M. Bauer: “Key comparison BIPM.RI(I)-K3 of the air-kerma standards of the BEV, Austria and the BIPM in medium-energy x-rays” (Metrologia 52 (2015) Tech. Suppl. 06004)

Cavity Chambers principles

From the collected charges to the air-kerma

Margarida Caldeira, IST-LPSR-LMRI

1. Introduction

Dosimeters are devices able to provide a reading that is a measure of the absorbed dose derived from the energy deposited by ionizing radiation in its sensitive volume *V.*
Cavity chambers are ionization chambers that are based in cavity theories, which provide a very useful way to interpret the dosimeter measurements and make it possible to relate the absorbed dose in a dosimeter and the absorbed dose in the medium containing it (Figure 1).

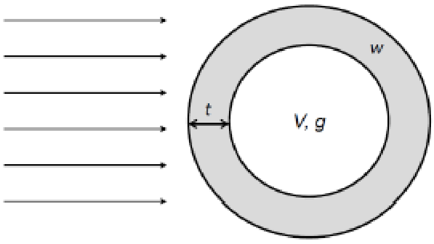

Figure 1: Considering that the volume *V* is filled with a medium *g* and that it is surrounded by a wall of another medium *w* with thickness *t*, we can interpret the dosimeter in terms of cavity theories, where the sensitive volume is identified as the cavity

If the mean energy required to create an ion pair in the filling gas, W_{gas}, is known, we can relate the measured charge per mass of gas to the absorbed dose to the gas cavity as:

$$D_{gas} = \frac{Q}{m_{gas}} \left(\frac{\overline{W}}{e} \right)_{gas} \tag{1}$$

where *e* is the charge of the electron.

The wall thickness must be chosen in order to minimize influence of scattered photons in the radiation field, which means that there must be charged particles equilibrium (CPE).

2. Important concept – Charged Particle Equilibrium (CPE)

In order to study the charged particle equilibrium, we must analyse the fluence of the secondary electrons as a function of the depth inside a given material.

In a very simplistic way, we can state that CPE exists in a given volume if the number of charged particles of a certain type, energy and direction exiting that volume is identical to the number of particles of the same type, energy and direction entering it, over the same period of time, as schematized in Figure 2.

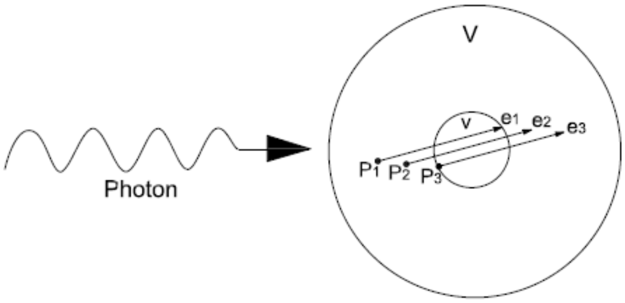

Figure 2: Simplified representation of Charged Particle Equilibrium

If the following conditions exist in the Volume *V*, then there is CPE in the volume of the cavity *v*:

– The volume is uniformly irradiated by photons, meaning that there is negligible photon attenuation
– The atomic composition and density of the medium is homogeneous
– There is no electric or magnetic fields responsible by changes in energy fluence across the volume
– The volume is small, but not so small that statistical fluctuations of interaction with the detector become important.

As long as the volume *v* is small enough as to allow the photons resulting from radiative losses to escape from it, for an infinitesimal volume *dv* containing a mass *dm* about the point of interest *P* we can state that the net energy transferred is equal to the energy imparted:

$$\frac{d\overline{\varepsilon}}{dm} = \frac{d\overline{\varepsilon}^{n}_{tr}}{dm} \tag{2}$$

This means that, directly from the definitions of Dose and kerma, the dose equals the collision kerma, as long as CPE holds:

$$D \overset{CPE}{=} K_{col} \tag{3}$$

where the collision kerma can be writen as:

$$K_{col} = K\left(1 - \overline{g}\right) \tag{4}$$

being $\bar{g}$ the mean fraction of the energy of the electrons liberated by photons lost in radiative processes.

In realistic situations, CPE does not usually occur, since we must take into account the photon attenuation and scattering in the medium. In this case, we can talk about a Transient Charged Particle Equilibrium – TCPE. The differences between CPE and TCPE are represented in Figure 3.

The collision kerma has its maximum at the surface of the irradiated material. Assuming that there is no attenuation of the radiation with depth, the collision kerma is constant for the incrementing depths. The charged particle fluence (and consequently, the absorbed dose) increases as a function of depth until it reaches the depth of maximal dose, zmax, establishing a stable electron spectrum. In this case, where there is no photon attenuation or scattering in the medium, but still electrons are produced, the buildup is followed by a region of CPE, where the absorbed dose equals the collision kerma (figure 3a).

In the realistic situation (figure 3b), however, there is photon attenuation and scattering in the medium. The collision kerma has its maximum at the surface of the medium, and decreases continuously with depth. There is a buildup region up to a maximum dose, until the increase in electron fluence is balanced by the attenuation of photons in deeper layers, since there are less electrons scattered back. The result is a decrease in the electron fluence and hence, in the absorbed dose.

In this case, we have a region where D is proportional to K_c. This is the transient charged particle equilibrium. The proportionality holds throughout the region because, in high energy photon beams, the average energy of the secondary electrons, and hence their range, does not suffer much change with depth in the medium.

In this scenario CPE exists at the depth of maximum dose in the medium, z_{max}. We can speak of a local equilibrium between the energy transferred to the kinetic energy of the electrons and the energy absorbed from the electrons.

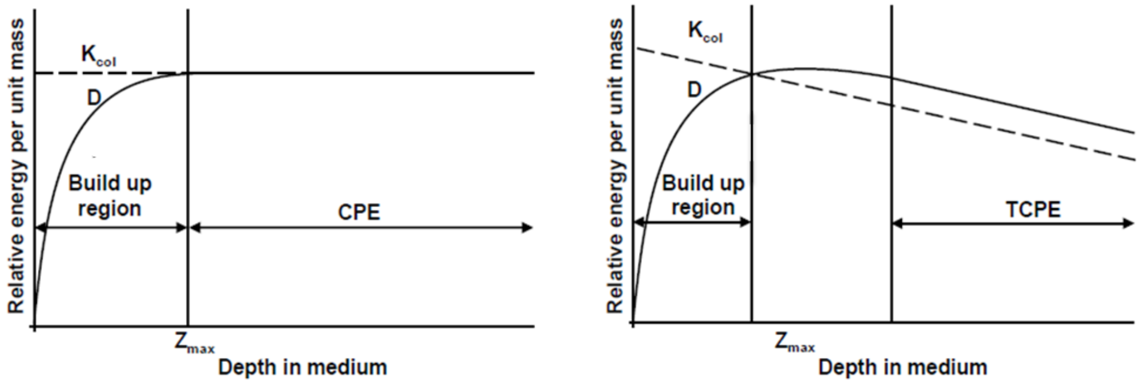

(a) Ideal Charged Particle Equilibrium

(b) Realistic Transient Charged Particle Equilibrium

Figure 3: Differences between CPE and TCPE for high energy photon beams hitting a surface

3. Cavity chambers – Working principles

In order to interpret the cavity chamber in terms of cavity theories, special attention should be given to the materials used to build the chamber, to the thickness of the wall and to the size of the cavity**.**

To understand the working principles of a cavity chamber, we start by considering an air-wall chamber, i.e, a sphere of air with an air cavity in the centre, uniformly irradiated with a photon beam, as sketched in Figure 4:

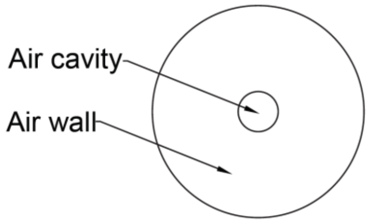

Figure 4: An air-wall chamber, where the range of secondary electrons in the wall is too large

Here, we assume that CPE exists and that the thickness of the outer layer is at least equal to the secondary electron range. This raises a difficulty, which is that, in air, this thickness is too large for ^{60}Co photons, which produce secondary electrons with a projected range of about 170 cm.

We can then consider an “air-equivalent” wall, with atomic number, Z, similar to the effective atomic number of air, Z_{air}, with a larger density, so that the thickness that allows CPE to exist is much thinner (Figure 5). The wall material is usually graphite.

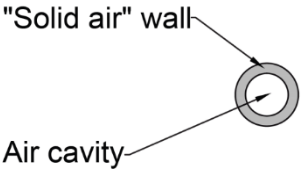

Figure 5: An air-equivalent wall chamber, where the wall material has an atomic number similar to air but higher density, so the range of secondary electrons is much smaller

The condition of air-equivalence ensures that the energy spectrum of electrons liberated in the chamber wall is similar to that in air. This can be achieved if the effective atomic number of the wall material is approximated to that of air.

Finally, in order to make charge measurements, the high voltage was applied to the outer electrode of the cavity chamber (the graphite wall) and a central electrode was placed inside the chamber so that it collects the charge created in the air cavity. This central electrode is preferentially made of the same material as the wall, in order to have a homogeneous cavity. Insulators are placed between the two electrodes and a guard ring is placed in order to prevent leakages (Figure 6).

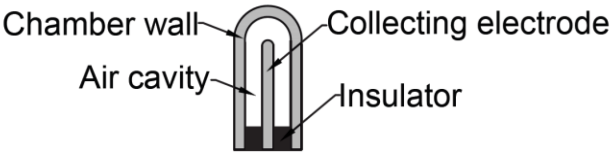

Figure 6: A schematic of a cavity chamber, including a collecting electrode and the insulator between it and the outer electrode (the wall)

4. Cavity theories

Cavity theories can be applied when Bragg-Gray conditions exist. These conditions state that the cavity should be small (compared to the electrons range), so that it does not disturb the fluence of the electrons crossing it (CPE or TCPE) and that the thickness of the wall should be at least equal to the maximum range of secondary electrons released by photons, so that only the electrons crossing the cavity contribute to the absorbed dose.

Under these conditions, the wall is the source of all the secondary electrons depositing energy in the cavity and we can relate the ratio of the doses absorbed to the two media, air and graphite (in the absence of the cavity), to the graphite-to-air mass stopping power ratios, $\boldsymbol{\overline{S}_{c,a}}$:

$$\frac{D_{wall}}{D_{air}} = \frac{\left(\frac{\overline{S}}{\rho}\right)_{wall}}{\left(\frac{\overline{S}}{\rho}\right)_{air}} \tag{5}$$

where the stopping power, $\boldsymbol{S = dE/dx}$, is the average rate of energy loss per unit of path length by a charged particle, and has collision and radiative components, S_{col} and S_{rad}.
Remembering equation (1) we can relate the doses absorbed to the two media and write the dose absorbed to graphite as:

$$D_{wall} = \frac{Q}{m_{air}}\left(\frac{\overline{W}}{e}\right)_{air}\frac{\left(\frac{\overline{S}}{\rho}\right)_{wall}}{\left(\frac{\overline{S}}{\rho}\right)_{air}} = \frac{Q}{m_{air}}\left(\frac{\overline{W}}{e}\right)_{air}\overline{S}_{wall,air} \tag{6}$$

If we remember that, under CPE conditions, we can relate the absorbed dose and the kerma as in (3):

$$K_{wall} = D_{wall}/(1-\overline{g}_{wall}) \tag{7}$$

where g_{wall} is the mean fraction of the energy of the electrons liberated by photons lost in radiative processes in the wall, as defined above.
The kerma can be written as:

$$K = \Psi\left(\frac{\overline{\mu}_{tr}}{\rho}\right) \tag{8}$$

where Ψ is the photon energy fluence and $\bar{\mu}_{tr}$ is the mean mass energy-transfer coefficient. Or in terms of the mean mass energy-absorption coefficient:

$$K = \Psi\left(\frac{\overline{\mu}_{en}}{\rho}\right)\left(\frac{1}{1-\overline{g}}\right) \tag{9}$$

Assuming that the photon fluence is the same in both materials, the kerma ratio for air and graphite is the ratio of the mean photon mass energy transfer coefficients,

$$\frac{K_{air}}{K_{wall}} = (\overline{\mu}_{tr}/\rho)_{air,wall} \tag{10}$$

We can then relate the air-kerma at the reference point in the absence of the chamber with the measured ionizing charge, combining equation 3 and 5:

$$K_{air} = \left(\frac{Q}{m_{air}}\right)\left(\frac{\overline{W}}{e}\right)_{air}\left(\frac{\overline{\mu}_{tr}}{\rho}\right)_{air,wall}\overline{S}_{wall,air}\left(\frac{1}{1-\overline{g}_{wall}}\right) \tag{11}$$

In terms of mass energy absorption coefficients the air kerma is written as:

$$K_{air} = \left(\frac{Q}{m_{air}}\right)\left(\frac{\overline{W}}{e}\right)_{air}\left(\frac{\overline{\mu}_{en}}{\rho}\right)_{air,wall}\overline{S}_{wall,air}\left(\frac{1}{1-\overline{g}_{air}}\right) \tag{12}$$

The air mass $m_{air} = \rho_0 V$, where ρ_0 is the dry air density at the reference temperature and pressure and V is the cavity volume. The charge Q is measured under experimental conditions. This equation gives the air-kerma under ideal conditions. To determine the quantity under real conditions, correction factors must be taken into account.

5. W-value

The determination of the air-kerma by measuring the ionization current requires that the value of the mean energy necessary to produce an ion pair in air, W_{air}, is known. The CCRI(I) recommends a value of W_{air} = 33.97 eV for all air-kerma standards, with a relative standard uncertainty of 0.15% [1]. The value is derived from various sources but some aspects concerned with its determination still need to be clarified. In particular, for stopping powers for air and graphite, any change on their recommended values will affect the recommended value for W_{air}. This is a subject that needs further insight.

Since the uncertainty associated to that the graphite-to-air stopping power ratio is significantly large, the uncertainties of W/e and $\bar{S}_{c,a}$ are expressed as the uncertainty of the product $(W/e).\bar{S}_{c,a}$. Following a 1999 recommendation of the CCRI(I) [2], this product is taken to have a standard uncertainty of 0.11%, where the combined uncertainty of the product is less than the uncertainties of the components because their calculations are not completely independent.

6. Conclusions

Here we presented the working principles of the cavity chambers, and how the cavity chambers could be interpreted in terms of cavity theories. The dose to air can be obtained from the measurement of the ionizing charge in a known mass of air and knowing the value of the mean energy necessary to produce an ion pair in air, W_{air}. Under conditions of charged particle equilibrium, the dose to air can be related to the air-kerma, while cavity theories allow us to relate the dosimetric quantities in two media, which are, in the case of a graphite-walled chamber, the wall material and the air inside the cavity.

References

[1] CCEMRI 1985, Report of the 11th Session (Sèvres: Bureau International des Poids et Mesures), R131–2

[2] CCRI 1999, The value of W/e and its uncertainty, Comm. Cons. Ray. Ionisants 16 145 (Sèvres: Bureau International des Poids et Mesures).

Cavity chamber manufacturing

Margarida Caldeira, IST-LPSR-LMRI

1. Introduction

Most of the ionization produced in the cavity arises from secondary electrons liberated in the surrounding wall, which is obtained if the thickness of the wall is greater than the maximum range of secondary electrons set in motion by photon interaction in the wall material and if the volume of the cavity is not as large as to disturb the electron fluence, with a very low probability of photon interactions inside the cavity. This is to say that the wall is the source of electrons to the gas cavity.

Cavity chambers are usually vented air-filled and graphite-walled. Air is usually used as the cavity material since it allows that the chamber is built with robustness and with a simple design. The venting hole allows the air inside the cavity to be related to the air outside it. The energy required to create an ion pair in air is well-known, with a small relative standard uncertainty, $(W/e)air$ = 33.97JC^{-1} $\pm$0.15%. Finally, since we are considering only two materials, we can choose the wall to be air-equivalent, so that the energy spectrum of electrons liberated in the two media is similar and minimizing the uncertainties of the stopping power and mean mass energy absorption coefficient ratios.

2. Choice of wall material

The condition of air-equivalence ensures that the energy spectrum of electrons liberated in the chamber wall is similar to that in air. This can be achieved if the effective atomic number of the wall material is approximated to that of air.

Since photoelectric effect is highly dependent on Z, the effective atomic number, Z_{eff} is defined as to represent the interaction coefficient for this type of interaction and it can be written as:

$$Z_{eff} = \sqrt[m]{a_1 Z_1^m + a_2 Z_2^m + ...}$$

where a_i are the fractions of electrons existing in the mixture belonging to atoms of atomic number Z_i. m is a value of approximately 3.5 [1], obtaining a value of about 7.8 for the effective atomic number Z_{eff} of air.

Graphite is the most used wall material for cavity chambers, due not only to its atomic number (Z=6), similar to that of air, but also because it is readily available with high purity and known composition, it is dimensionally stable, its machining can be made with high precision and it is also an electrical conductor. For graphite cavity walls, a thickness of 3 mm is sufficient to attend the Bragg-Gray conditions.

3. Choice of Insulators

In the choice of the electrical insulating material, radiation resistance should be taken into account. Usual insulating materials for use in ionization chambers are polystyrene (PS), polyethylene (PE), polytetrafluoroethylene (PTFE, commercial name: Teflon), polymethylmethacrylate (PMMA) or polycarbonate (PC, commercial name: MAKROLON), all with very good electrical insulating characteristics [2]. Even though Teflon is very high resistant to humidity in air, it is very easily damaged by radiation, for doses from approximately 10^4 Gy, so this is an insulator that should be avoided when constructing ionization chambers.

A good solution is provided by cross-linked polystyrene (X-linked PS), since its volume resistivity is almost as good as that for Teflon, and even though its resistance to humidity is not as good, it is very radiation resistant.

4. Cleaning

Electrical leakage is a surface effect that can be reduced if all the surfaces of the insulator are properly cleaned and polished. In particular, humidity, oil skin transferred to the insulator or any kind of dirt (like graphite dust, for example) may be responsible for leakage and affect the measurements.

These problems can be avoided if the insulators are handled with gloves and if the insulators are wiped with pure ethyl or methyl alcohol using a cotton swab and polished. The dusts that can contaminate the surface of the insulators can be blown with a rubber syringe, for example.

Measurements should not be made immediately after this process, due to the triboelectric effect that can produce charges on the surface of the insulator. This effect may take some time to dissipate, during which there will be leakage currents.

The materials used for the cavity chamber built at LMRI were Graphite (Rods available at the laboratory from Carbone Lorraine, now Mersen); Cross-linked polystyrene and Dural/Aluminum, from GoodFellow.

Polishing was made with a polishing product to eliminate scratches and a finishing agent for use after (Altuglas® Polish 1+2). To clean the chamber components we used Isopropyl alcohol (Propanol-2) and distilled water. Dusts were removed with a brush and Propanol-2 (ideally under microscope). The components were dried with nitrogen (to avoid humidity).

5. Cavity chamber design

Cavity chambers used as national standards may have several shapes, for example PTB has cylindrical models, whereas BIPM holds parallel plate chambers. NIST has spherical models, the same as LNHB, that also holds cylindro-spherical ones.

In cylindrical chambers, the effective collecting volume of the cavity is smaller than its geometrical volume, because the conducting surfaces of the chamber (the walls) meet at right angles and in the close vicinity of those corners, in the top and bottom of the chamber, the electric field is approximately null (see figure 1.b). Charged particles generated in those regions will therefore not contribute to the collected ionization current. For cavity chambers with spherical geometry there are no corners between the conducting surfaces (see figure 1.a) and in that case the dead volume is drastically reduced. The electric field inside the cavity chamber can be simulated with finite element calculations.

A spherical-ended cylindrical cavity chamber was built at LMRI, with a geometrical shape similar to that of the cavity chambers from CEA-LNE-LNHB [3].The major difficulty in constructing this kind of chambers is to machine the spherical ends and finding a workshop able to do it with the tolerances that are needed.

The machining of the graphite chamber with spherical ends was carried out in the workshop of LIP (Laboratório de Instrumentação e Física Experimental de Partículas), in

Coimbra. LIP is a national laboratory which goal is the research in the fields of experimental high energy physics and associated instrumentation, with a workshop that is prepared to fulfill the task of building a graphite chamber with these specific characteristics. The workshop is connected to LIP research activities but it also produces work for other university research groups, health institutions and private companies in different areas. It is dedicated to the development and production of prototypes in collaboration with researchers and end users, providing precision engineering to support business activities in the design and production of high quality components. The workshop has extensive experience in manufacturing components for particle physics detectors and it is equipped with advanced mechanical equipment and experienced staff in the design, development and production of components under the most stringent requirements [4].

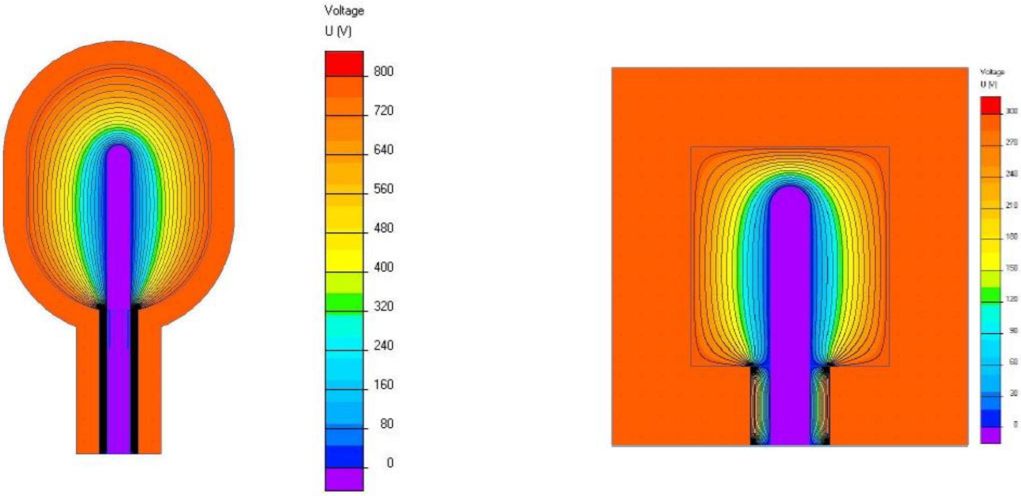

Figure 1: Electric field inside a cylindro-spherical chamber and a cylindrical chamber

The design of the chamber was similar to those from the CEA-LNE-LNHB, with some changes due to the limitations imposed by the material available at the LMRI. Two identical chambers were constructed from graphite rods with 5 cm high and 4.5 cm diameter (see Figure 2).

The other components can also be machined at the Workshop Centre (NOF) at IST, which provides technical support to the experimental research activities at IST and, whenever possible, to outside entities, from the concept to the final product. Its infrastructures are equipped with modern facilities, ranging from numerical control machines to equipment for rapid prototyping polymers. The workshop network is prepared for the manufacture of products in a wide range of materials (Mechanical, Glass, Plastics). It has a metrology laboratory and offers other specific services, such as complete project execution, instrumentation and rental of data acquisition systems to support research [5].

In the chambers neck there are two diametrically opposed venting holes with 1 mm diameter, in order to maintain air pressure equilibrium between the inside and the outside of the chamber. Figure 2.a shows the schematic design with the dimensional characteristics of the graphite chamber that was constructed. The chamber was built in two parts that were joined with a push fit, without any glue or screws. In Figure 2b the two graphite chambers that were machined are presented. The height of the cylinder that composes the middle part of the chamber is 8 mm length. The top and bottom of the chamber are composed of hemispheres with an external diameter of 30 mm. The cavity wall is 3 mm thick, sufficient to maintain CPE in ^{60}Co beams.

Table 1 presents the main characteristics of the chamber.

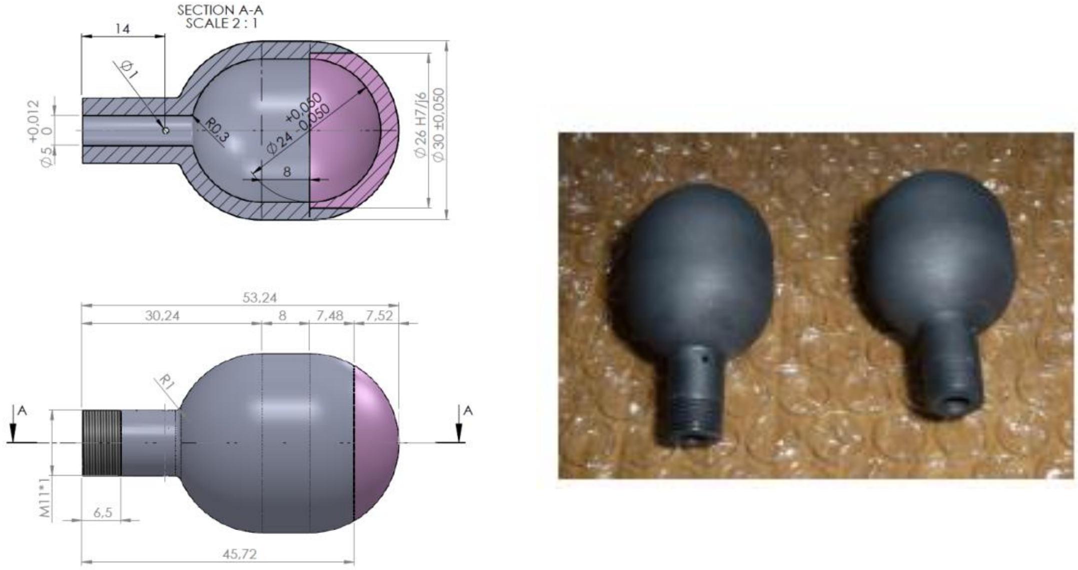

(a) Geometry with dimensions of the graphite chamber;
(b) Cavity chambers constructed at the workshop of LIP-Coimbra

Figure 2: Schematic picture and photographs of the graphite chamber built at the workshop of LIP-Coimbra

Cylindrical with spherical ends graphite cavity standard		
Chamber	Outer height	38 mm
	Outer diameter	30 mm
	Inner height	32 mm
	Inner diameter	24 mm
	Wall thickness	3 mm
Electrode	Diameter	3 mm
	Height	19.74 mm
Volume		11.2 cm^3
Wall	Material	High purity graphite
Insulator		Cross-linked polystyrene
Stem	Material	Aluminum
	Height	270 mm
	Diameter	6 mm

Table 1: Characteristics of the cylindro-spherical cavity chamber

6. Verification of the machining quality of the graphite walls

After the chambers were constructed, their interior was inspected through the observation of radiographs (Figure 3), that were taken at the Department of Radiotherapy and Image of the IPO-Lisboa (Instituto Português de Oncologia de Lisboa). The chambers were rotated to evaluate the machining of their interior in different angles. In particular, we wanted to evaluate the adjustment of the two parts of the chamber, namely if there were any air gaps between them, which could influence the inner volume of the chamber, and the uniformity of the walls thickness.

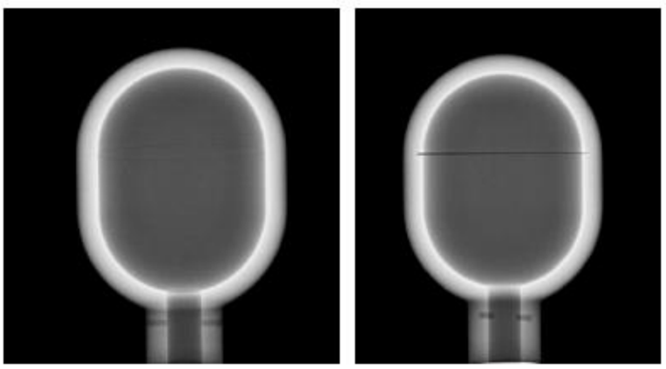

Figure 3: Radiographs of the graphite chamber, with the purpose
to verify the assembling of the two parts and the thickness of the walls

With respect to the thickness of the walls, the results were satisfactory, since it is uniform throughout all the inner surface of the chamber. As for the assembling of the two parts, one of the chambers is well assembled and the other shows a small air gap in the fitting between the two parts of the chamber. Also, it was verified that there are no fractures in the graphite inside the chamber. Given that the quality of the machining was verified, the chamber on the left in Figure 3 was selected to continue the construction of the detector.

Assembling the chamber

The material used as the electrical insulator for the cylindro-spherical chamber is cross-linked polystyrene (X-linked PS), a rigid transparent copolymer, with good electrical properties and dimensional stability and high resistance to radiation. It is easily machined and polished.

There are two groups of insulating parts in the cavity chamber, defined in Figure 4.

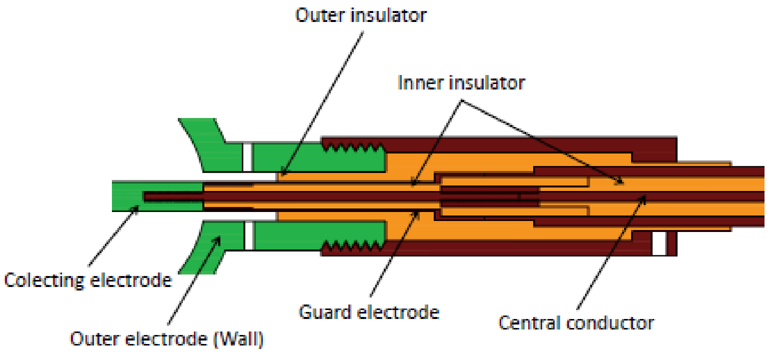

Figure 4: Representation of the assembling of the two groups of insulators and the guard ring

The inner insulator separates the guard ring and the central electrode and extends along the central conductor. The outer insulator separates the chamber's neck (outer electrode) and the guard ring (Figures 5a and 5b). Figures 5c and 5d show a detail of the external insulator and the guard electrode, after assembling. Note the internal insulator that extends the guard ring by a very small distance (0.2 mm, the gap between the guard ring and the central electrode).

The assembling of these components of the chamber has high relevance in the definition of the effective collecting volume. Not only because the volume of the neck of the chamber is defined by length measurements to these components, but also because the position of the guard ring has an important role in the definition of the collecting and non-collecting volumes.

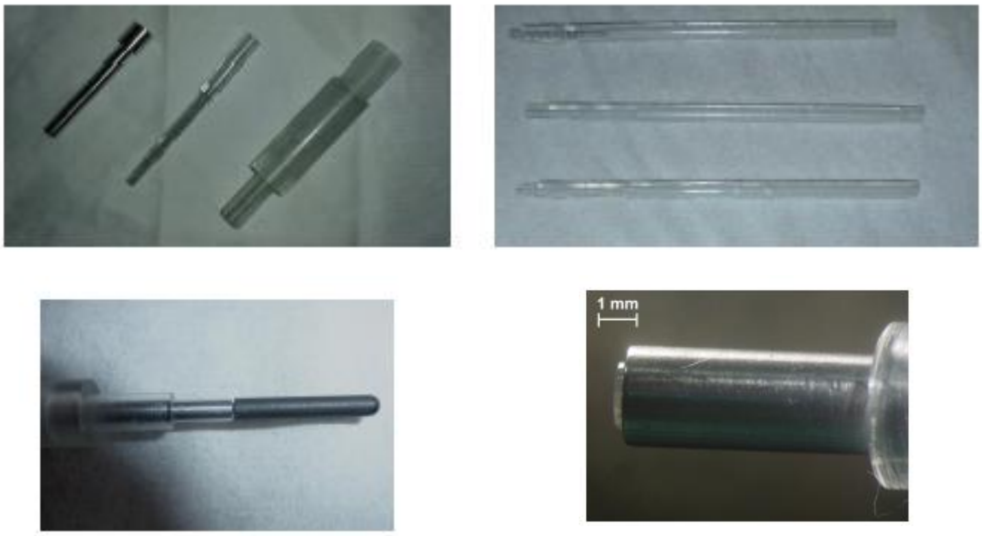

(a) Guard electrode, inner and outer insulators, from left to right (b) Extensions of cross-linked polystyrene that insulate the central electrode(inner insulator) (c) External insulator, guard electrode and collecting electrode (d) Detail of the 0.2 mm gap between the guard ring and the central electrode)

Figure 5: Assembling of the electrical insulators, guard ring and inner electrode in the cavity chamber

The electrical connections between the voltage source and the outer electrode and between the inner electrode and the electrometer are made separately. The inner electrode is connected to an aluminium rod with 1 mm diameter that transports the signal along the interior of the stem (the central conductor in Figure 4). At the end of the stem this rod connects to an SMC coaxial connector that is later connected to the electrometer, Figures 6a and 6b. The high voltage is applied to the wall through an external cable connected to the outer aluminium ring (Figure 6.c) which has also the function of holding all the pieces together. The necessary machining of the aluminium and cross-linked polystyrene pieces was made at IST/CTN workshop.

(a) SMC connector (b) Electrical connections at the end of the stem, for signal transport to the electrometer (c) External cable for the HV transport to the chamber's wall

Figure 6: Electrical connections in the cavity chamber

Before starting the experimental tests, the assembling of the chamber was again verified with radiographs (Figure 7).

The images obtained provided the necessary information in order to correctly position the central electrode, in a first phase adjusting the materials in the chamber's neck so that the central electrode is completely introduced in the chamber's cavity (Figure 7a) and in a second phase centring the inner electrode (Figure 7b). Figure 7c was taken at the LNHB before starting the experimental tests.

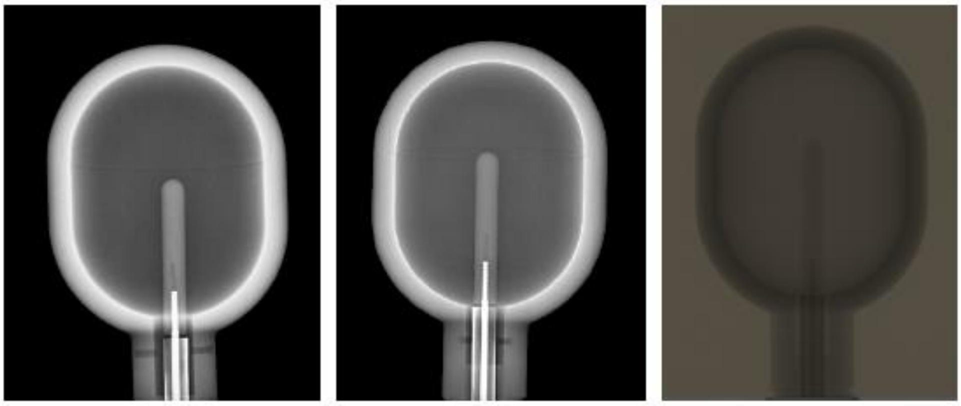

Figure 7: Radiographs of the interior of the assembled chamber. The first two were taken at IPO-Lisboa and the last was taken at LNHB
a) In the first radiograph, the central electrode was not completely introduced in the cavity and there was a deviation of the group "insulators+guard+central electrode" to the side (b) In the second radiograph, the group still needed to be centred (c) Radiograph of the chamber, as it was used for measurements

A simulation of the electric field at the level of the guard ring was made for the cylindro-spherical prototype, using the software QuickField Professional Edition, Figure 8.

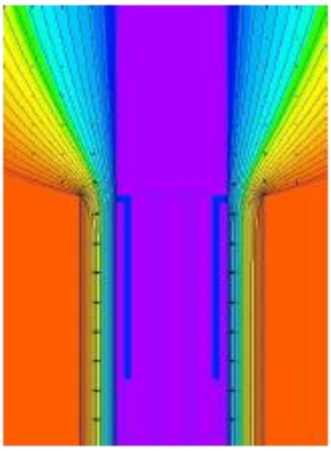

Figure 8: simulation of the electric field at the level of the guard

Due to the evenly distributed electric field that can be observed in Figure 8, unlike for a cylindrical chamber, the effective collecting volume was assumed to be identical to the geometric volume of the air cavity, given that there are no dead volumes.

The figure shows that there is no electric field strength between the insulating material and the guard electrode. Note that the collecting electrode and the guard ring are both grounded, while the high voltage is applied to the outer electrode, i.e., the graphite wall. The air gap 0.1mm thick and 5 mm length separating the top of the guard ring from the insulator reduces surface effects between the two components. These calculations show that the presence of the guard electrode contributes to the definition of the collecting volume.

7. Measurement of the collecting volume of the cavity chamber

Determining the collecting volume is one of the most important aspects related to the construction of air kerma cavity standards, since the collected charge dependents directly of it. Once the geometrical volume is identified as being identical to the effective volume, the next step is to establish a method to calculate the geometrical volume.

The effective collecting volume is defined as the volume inside the cavity where charged particles are generated and collected by the inner electrode, and then measured. Its determination was made according to the method described in [6]. The methodology consists on determining the inner volume of the cavity, V_{int} (Figure 9), to which the volumes of the central electrode, $V_{central}$, and of the chamber's neck, V_{neck}, as well as a small volume below the central electrode, V_0, are subtracted.

The effective collecting volume is hence given by the expression:

$$V_{eff} = V_{int} - V_{central} - V_{neck} - V_0$$

To obtain these volumes, several components of the cavity chamber were measured before assembling the chamber. Through the observation of the electric field simulated inside the chamber using QuickField, Figure 8, the effective collecting volume can be defined as the volume above the plane located at half distance from the bottom of the central electrode and the top of the guard ring (see Figure 6.1), that passes through the edge of the chamber's neck. The approximation is that the central electrode collects the charged particles above that plane and that the guard electrode collects the charges below it. Finally, and according to Figure 8, there is no electric field strength between the inner electrode and the guard ring, so we consider the volume between the central electrode and the guard ring as a non-collecting one.

The inner volume of the graphite chamber (the volume of the cylindro-spherical cavity, including the total length of the neck) was measured using the gravimetric method, at the Laboratory of Volume at the IPQ. The volumes $V_{central}$, V_{neck} and V_0 were obtained by length measurements, performed at the Laboratory of Length, also at the IPQ, using a length scale interferometer.

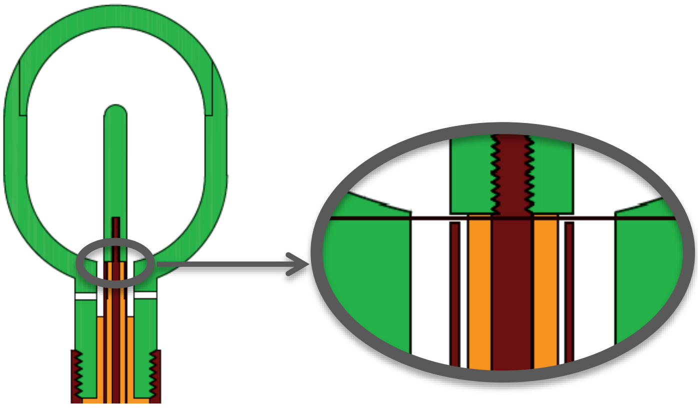

Figure 9: Definition of the effective collecting volume of the cavity chamber, where the chamber's neck volume is defined as the volume below the plane

7.1. Volume measurements: Measurement of V_{int}

The gravimetric method is the standard method used by NMIs and accredited laboratories to calibrate volume instruments, by weighing the contents of a suitable liquid of known temperature and density, usually pure water [7].

The chamber (container) was placed in a recipient with its opening facing upwards. It was weighed while still empty and then filled with distilled water. Given the porous nature of the graphite, it absorbs some water until it reaches a saturation level. For this reason, the method that was adopted consisted in:

1. Weighing the empty, dry chamber
2. Filling the chamber with water
3. Weighing the chamber filled with water
4. Emptying the chamber
5. Re-weighing the empty chamber
6. Repeating steps 2-5 until the measured mass of the empty (wet) chamber is constant.

The effect of water absorption in the graphite walls of the chamber is depicted in Figure 10. The apparent increase of volume is a direct consequence of the increase of the mass of the graphite walls due to water absorption. After the saturation was reached, i.e., when there was no more water absorbed by the graphite walls and hence, the mass of the empty chamber was constant, a sequence of 10 measurements was made in order to determine the inner volume of the chamber.

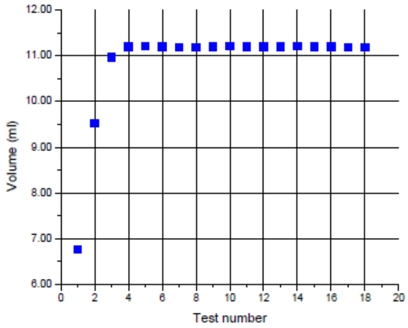

Figure 10: Effect of water absorption by the porous graphite in the measurement of volume

7.2. Length measurements: Measurement of V_0, $V_{central}$ and V_{neck}

All the length measurements were made with the length scale interferometer described in [8]. The basic principle of length measurement using interferometry is the comparison of a length or distance against a known light wavelength.

To determine the volume of the central electrode, $V_{central}$, three sets of measurements were made, to determine its total length, L, its diameter, $\varnothing_2$ and the radius of the hemisphere, R_1.

V_{neck} and V_0 were determined in four stages, by measuring the relations between the lengths of the several components entering the chamber’s neck lengths of the guard and insulators entering the chambers neck (according to [6]).

7.3. Results and discussion

The average inner volume of the cavity, obtained from the average of the 10 measurements, has 11.195 ml, with a standard deviation of the mean of 0.0536% (k=2.22).

The main contribution to the uncertainty in the inner volume of the cavity chamber is the repeatability of measurement. Since the method used to measure the inner volume of the chambers was the same as the method used for the measurements for the LNHB chambers, we made a direct comparison between the relative expanded uncertainties (k=2). We observed that the value of U = 0.05% obtained for the cavity chamber developed at LMRI is within the interval of relative expanded uncertainties obtained for the set of cavity chambers constructed at the LNHB [6], which is between 0.02% and 0.06%.

The major contribution for the volume uncertainty resulting from the length measurements comes from the measurement of the radius of the hemisphere. This was expected, since the measurement of R_1 presented more difficulties that the other measurements, mainly because of a small asymmetry at the interface of the cylinder and the hemisphere composing the central electrode, Figure 11.

The uncertainty (k=2) obtained for the radius of the hemisphere, R_1, was 0.67%, much higher than those obtained for the LNHB chambers (0.06% to 0.13%) [6]. The uncertainty obtained for R_1 was about half the values obtained for the same measurements at the LNHB. As for the length, *L,* of the inner electrode, the relative uncertainties were similar in both cases. The relative uncertainties for the remaining length measures are 3.5 times to 10 times lower than those calculated for the set of chambers from LNHB [6]. These differences are due to the different methods used to measure the lengths and diameters. In fact, the interferometric method allows us to obtain the uncertainty at the thousandth of the millimetre. It proved only to increase the uncertainty for the measurement of the diameter of the hemisphere, due to the reasons described above. The measurements made for the components of the chambers held by LNHB, on the other hand, were made with callipers.

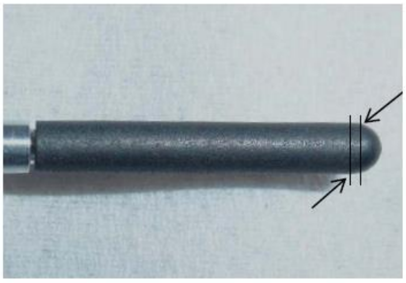

Figure 11: Small asymmetry at the tip of the central electrode that contributes to the increase of the uncertainty associated to the measurement of the radius R_1

The effective collecting volume of the chamber is calculated using the tabulated volumes as in Equation (6.1). The measured value was 10.7058 cm$^{3.}$ The expanded uncertainty for a confidence level of 95% (k=2) is 0.055%. This result agrees with the uncertainties presented for the effective volumes of the six cavity chambers of the LNHB, which vary from 0.03% to 0.08% [6].

Conclusions

The shape of the chamber was chosen so that the geometrical volume would correspond to the collecting one. The material used for the chamber wall was graphite, an air-equivalent material, were CPE can be obtained even in a thin slice of 3 mm. The choice of the insulator (cross-linked polystyrene) was based on its insulating properties in conjunction with its radiation resistance, as well as ability to be machined, cleaned and polished.

The chamber was machined with the desired tolerances and its interior was inspected using radiographs. We could observe that the inner walls were homogeneous, with no cracks and that the two parts that compose it were well fitted.

Before assembling the chamber components, volume and length measurements were made to determine its collecting volume. The results obtained for the associated uncertainty were consistent with those obtained for the volume of chambers with similar shape and volume, providing an indication of its quality.

References

[1] H. Johns, J. Cunningham, The Physics of Radiology, 4th Edition, Charles C Thomas, Springfield IL, 1983.

[2] F. H. Attix, Introduction to Radiological Physics and Radiation Dosimetry, Wiley-VCH Verlag GmbH, Weinheim, Germany, 2007.

[3] F. Delaunay, M. Donois, J. Gouriou, E. Leroy, A. Ostrowsky, New LNHB primary standard for ^{60}Co air kerma, Metrologia 47 (6) (2010) 652.

[4] http://coimbra.lip.pt (Contacts: om-geral@coimbra.lip.pt)

[5] http://nof.tecnico.ulisboa.pt/ (Contacts: nof@tecnico.ulisboa.pt)

[6] E. Leroy, Réalisation et Essais des Chambres de Références Primaires, NT LNHB 07/018A, LNHB (2008).

[7] Guidelines on the Determination of Uncertainty in Gravimetric Volume Calibration, Tech. rep., EURAMET (2012).

[8] J. S. Beers, W. B. Penzes, The NIST length scale interferometer 104 No. 3 (July 23, 1999)

Development of a cavity-ionization chamber at IFIN-HH

Primary standard for air kerma

S. Bercea, D. Dusciac, C. Cenusa, M. Donois, I. Cenusa, A. Ostrowsky, A. Celarel, V. Blideanu, E. Iliescu, J.-M. Bordy

Introduction

The collaboration between IFIN-HH/CMRID and CEA/LNHB in the field of the metrology for dosimetry was intensely developed during the last 10 years. An example of this collaboration is the participation of the two laboratories in several international projects regarding the development of secondary and primary standards for the dosimetry of the environment as well as for medical applications of the ionizing radiation.

This paper deals with the research performed by scientists of CEA-LNHB and IFIN-HH/CMRID in the frame of projects: 14 RPT 04 ABSORB and IFA-CEA Project C4-02 CATRAS.

One of the scientific and technical objectives of the 14 RPT 04 ABSORB Project "Absorbed dose in water and air" is to study the design of cavity chamber primary standards, so that the participating NM/s and D/s seeking to establish a research capability in measuring the air kerma for photon energies such as those of

^{60}Co or/and ^{137}Cs used in radiotherapy. In this way, the participating laboratories will be able to build and operate primary standards with a harmonized target uncertainty budget of 0.5 %, and to elaborate and apply harmonized calibration procedures.

In order to accomplish this task, CMRID from IFIN-HH together with researchers from CEA-LNHB applied for a bilateral cooperation project IFIN-HH/CMRID - CEA/LNHB, Project C4-02 CATRAS ("The development of the traceability of the calibrations in radiotherapy, radiological protection and medical imaging in Romania"). In the framework of this project, a cavity ionization chamber was designed [1].

1. Air kerma measurement

The verification of the components of the cavity ionization chamber included measurements of linear dimensions of pieces provided by the manufacturer, accordingly to the technical specifications shown in Fig. 1 to 6 here below. The preparation of the components included polishing of contact surfaces (polystyrene components), in order to ensure excellent insulation properties.

A cavity-ionization chamber is dedicated to the absolute measurement of the air kerma

(K_{air}) or the air kerma rate ($\dot{K}_{air}$). Therefore, the value of the sensitive volume of the chamber is a quantity involved in the relation used for K_{air}.

The quantity kerma (Kinetic Energy Released in Material) is the sum of the initial kinetic energies of all the ionizing charged particles liberated by uncharged ionizing particles, to a unit of mass of matter [2],

$$K = \frac{dE_{tr}}{dm} \qquad [K] = 1\ \text{Gy} = 1\ \text{J/kg}$$

Where: dE_{tr} is the sum of the initial kinetic energy of all the ionizing charged particles; dm is the mass of matter element, in which the energy was released.

The Absorbed Dose (D) is the mean energy imparted by the radiation to a unit mass of matter [2],

$$D = \frac{d\varepsilon}{dm} \qquad [D] = 1\ \text{Gy} = 1\ \text{J/kg}$$

The absolute measurement of the air kerma (K_{air}) and air kerma rate ($\dot{K}_{air}$), as well as for absorbed dose to air (D_{air}) and absorbed dose to air rate ($\dot{D}_{air}$) can be performed with an ionization chamber of a special type, namely the cavity-ionization chamber.

This is the reason for which, the value of the sensitive volume and its shape and geometry are very important for a correct operation of the detector.

2. Components materials and processing

The cavity ionization chamber designed and manufactured within the CATRAS project has a spherical shape. The chamber's wall is made of graphite. The inner surface of the wall is one of the polarizing electrodes. The chamber's wall is made up of two components (Fig.1) forcedly assembled, and are quite irremovable after assembly (Fig.1). The collecting electrode (Fig.2) is made also from graphite. It is mounted on an aluminum (DURAL) rod, by screw. Components 3, 6, 7, 9 are made of DURAL. Components 4, 5, 8 are made of cross-linked polystyrene. The surfaces of these components (colored in blue) were very polished, in order to reduce, as much as possible, the leakage currents.

The wall material for such a cavity ionization chamber, for air kerma measurement, is graphite. As the mechanical processing of the graphite is a very complicate task, the only company that assumed it was ABT SORIME (France).

The components of the ionization chamber were processed of different materials, according to their role in the chamber assembly.

Therefore, the material for the chamber wall (Fig.1), as well as the central (collecting electrode) (Fig.2) was graphite (carbon Lorraine 5890PT); the insulating components of the chamber (some of them presented in Fig. 4 and Fig. 5) are made of cross-linked polystyrene (provided by CEA-LNHB). The central component (collecting electrode) is installed in a metal stem made of aluminum (DURAL) (Fig.6).

The set-up technology for the ionization chamber had several steps:

1) checking of all the components provided by the manufacturer;
2) technologies for polishing and cleaning of all components;
3) assembling of the components; tests regarding the correct assembling;
4) electrical and radiological tests, to determine some of the parameters of the ionization chamber.

All these operations were performed in the laboratories of CEA-LNHB.

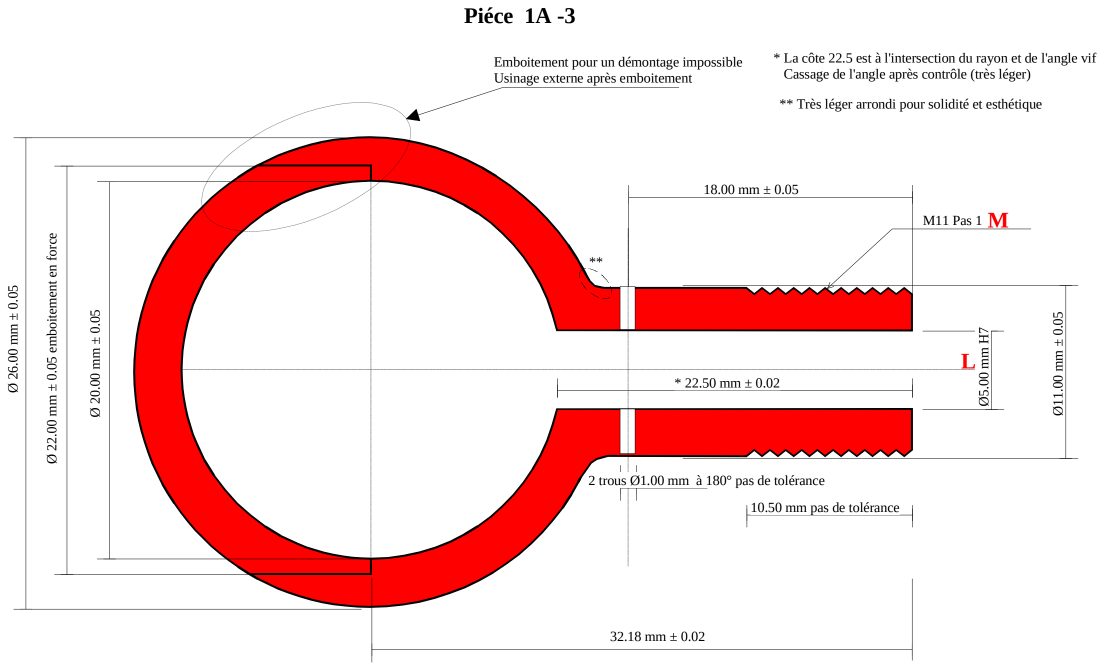

Fig. 1. Component 1A-3: spherical electrode (graphite)

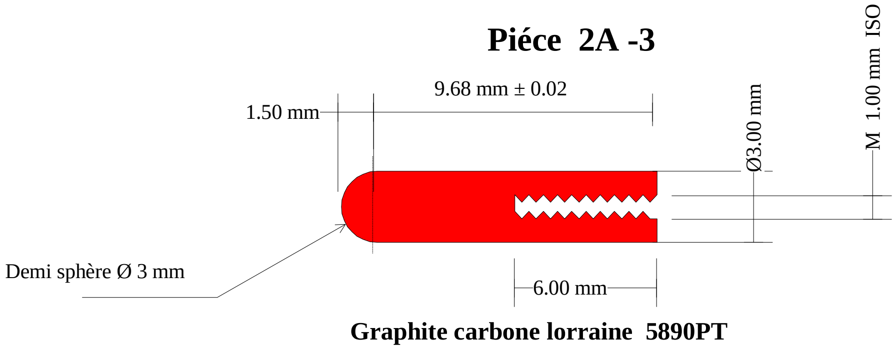

Fig. 2. Component 2A-3: collecting electrode (graphite)

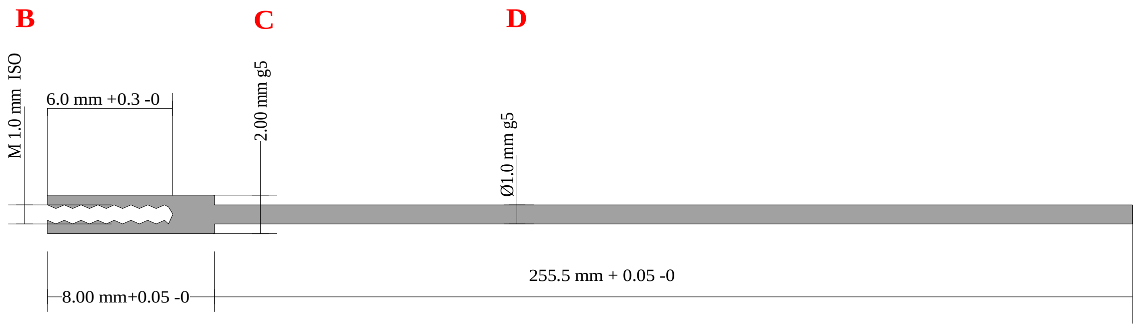

Fig. 3. Component 3 (DURAL)

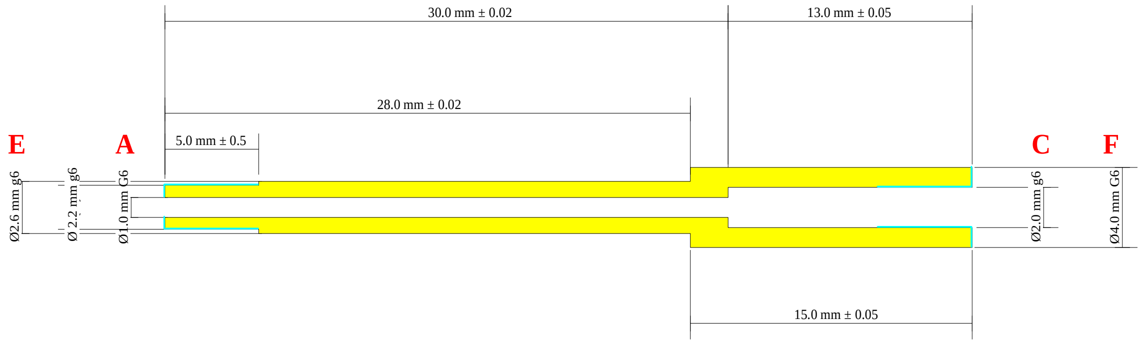

Fig. 4. Component 4 (cross-linked polystyrene)

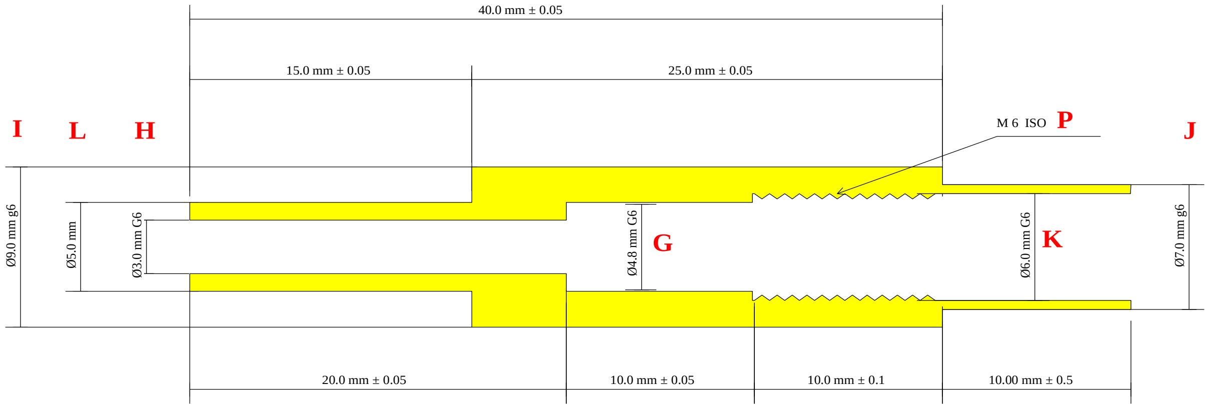

Fig. 5. Component 8 (cross-linked polystyrene)

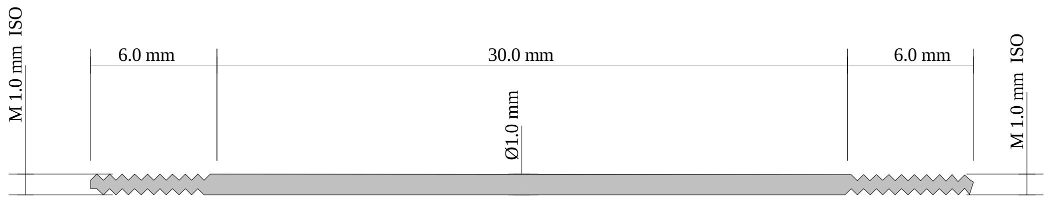

Fig. 6. Metal stem (DURAL)

3. The mounting technology

All the components presented above were assembled in such a way to obtain the cavity ionization chamber (Fig.7). In figures presented here below, the final image of the chamber is shown, having all the components assembled. The order of assembling the components (very important for assembly) was: 3, 3A-3, 4, 5, 6, 7, 8, 2A-3, 9.

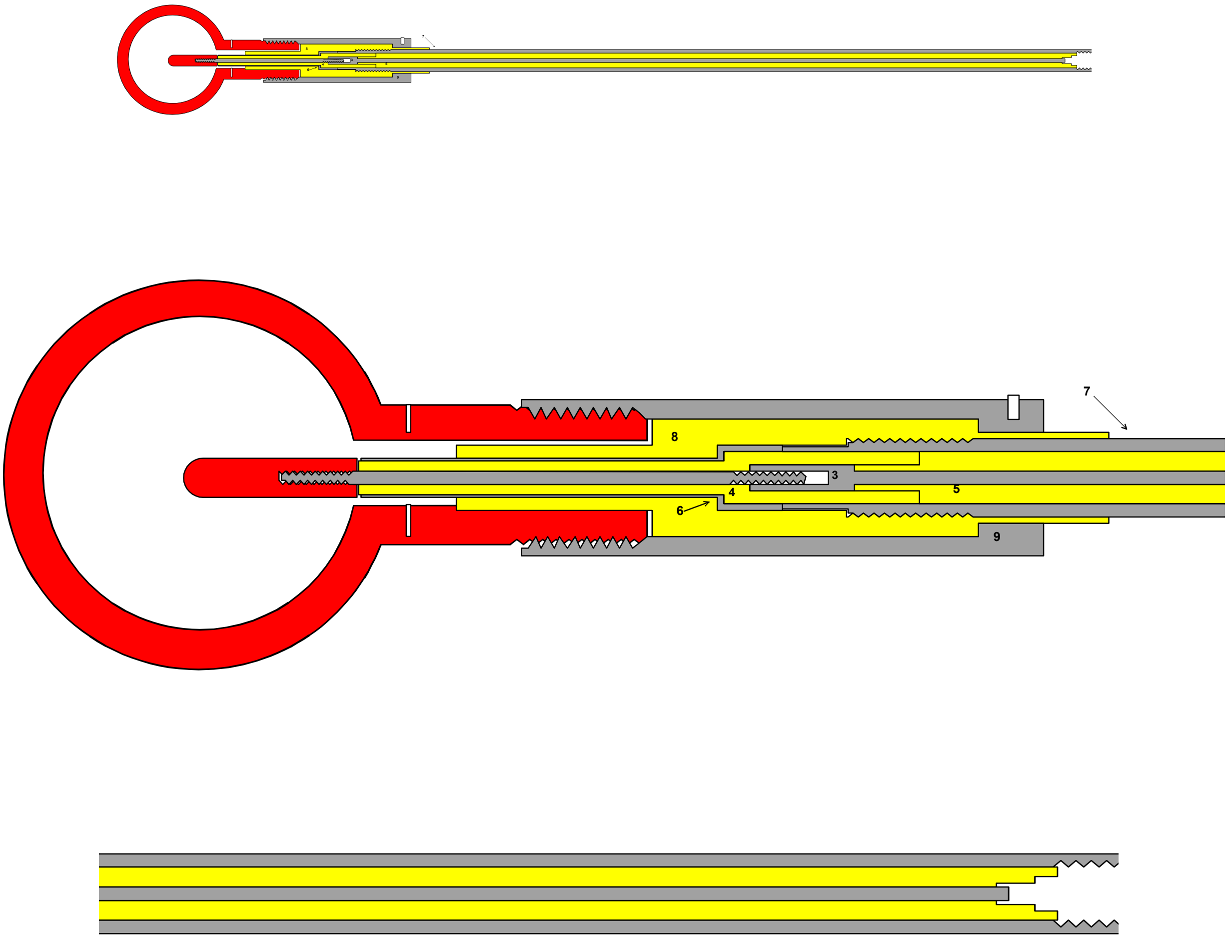

Fig. 7. Assembled ionization chamber (scheme)

In order to check whether the positioning of the components is correct (according to the design), a radiography of the assembly was made. For the radiography, a L 7901-01 HAMAMATSU PHOTONICS X-ray machine was used. (The parameters of the X-ray machine were: U=100kV, I_{max}=250 μA). The image of the chamber was captured by a C7942SK-05 HAMAMATSU PHOTONICS sensor and then, was digitally recorded in a computer.

The first radiography is shown in Fig.8. In this figure, it can be seen that the position of the central electrode is not correct in relation to the spherical cavity (the central electrode does not enter enough into the volume of the chamber). The distance between the correct position and the actual position of the central electrode was of 0.1 mm, in relation to the interior surface of the chamber's wall.

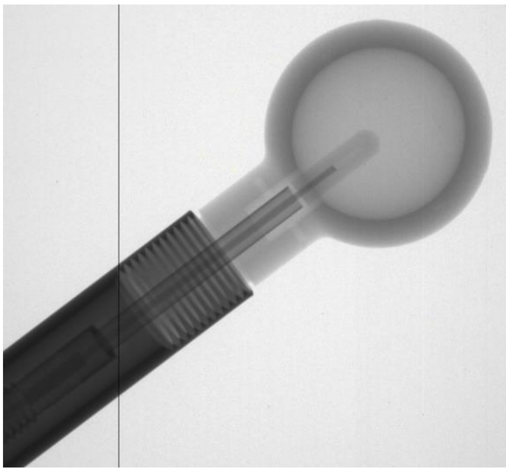

Fig. 8. First version of the assembled ionization chamber (radiography)

In the next stage, the chamber was disassembled. All the pieces made of polystyrene were examined using a microscope, in order to observe if and where, major imperfections exist on their surface and to insist to polish these areas. The conclusion after this examination was that there were no such areas.

The finishing technology had also two stages. In the first stage, a polishing cream with diamond granulates of 6 μm was used. After cleaning with isopropyl alcohol and drying with compressed air, the polishing process continued, by using diamond granulates of 3 μm. All the components made of polystyrene and aluminum were finally cleaned with ultrasound in ultra-pure water and isopropyl

alcohol. Then, the pieces were dried out for 90 min at 60^0C.

The graphite collecting electrode was screwed on the aluminum rod and the electrical contact between the two components was tested using a Fluke 89 multi-meter.

In Fig. 9, a photo of the final assembled ionization chamber is shown.

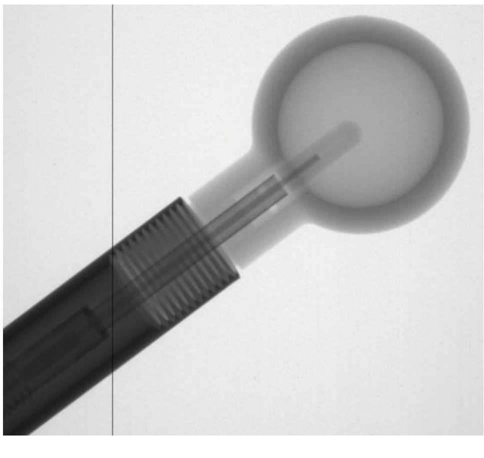

Fig. 9. Final version of the assembled ionization chamber (radiography)

Conclusions

The materials used for manufacturing the components of the cavity-ionization chamber are suitable for the aim of the project.

The technology used assured the necessary quality of the components of the detector, in order to fulfill all the requirements, supposed by its destination as primary standard for air kerma measurements.

Acknowledgement

This work was partly supported by the EMPIR Project 14 RPT 04 ABSORB and partly by the IFA-CEA Project C4-02 CATRAS

References

[1] S. Tuta, S. Bercea, ”Execution and test cavity-ionization chamber for K_{air} – Stage Report, project C4-02 CATRAS”

[2] ICRU Report No. 85: “Fundamental Quantities and Units for Ionizing Radiation (Revised)”, Journal of the ICRU, Volume 11, No 1, 2011

Electrometer Measurement system

Andreas Steurer, Wilhelm Tiefenböck

This chapter presents the technical description of the electrometer measurement system associated with ionization chambers.

There are two different 2-channel electrometer systems for simultaneous measurements (eg. primary standard and monitor). One unit is used for the measurements in the Therapy Level Bunker (Keithley 6517). The other unit is used in the Protection Level Hall (selfmade 2-channel electrometer DCI.2CH).

The BEV Dosimentry Laboratory is using different sets of each 4 Measuring Capacitors (100 pF, 1 nF, 10 nF, 100 nF). The devices to measure the environmental conditions are an absolute barometer DPI141, for each unit a temperature measuring systems with Keithley 2000 multimeter and each 5 sensors PT100 and for each measuring room a humidity measuring system HM30.

A LabView based evaluation software is used. All data (ionization currents, temperature, air pressure, humidity) are collected by the evaluation software. The result which is written to an Excel file is the air density corrected Ionization Chamber Current. If a conversion coefficient is applied the output is the dose rate (corresponding the chosen dose quantity).

The ionization current is evaluated with the loading increase of the measuring capacitor during irradiation and the capacity of the measuring capacitor. Measured is the voltage on the measuring capacitor every second. The mathematical method is a Least Square Fit. The slope of the straight line is a measure for the ionization current.

$$U = k \cdot t + d \tag{1}$$

Meaning of the symbols:

U.......................... Measured voltage on the capacitor

k........................... Slope of the straight line, calculated with Least Square Fit

t .... Measuring time, t = 0 s, 1 s, 2 s, 3 s, ...

d .... Constant, calculated with Least Square Fit

The ionization current is calculated with:

$$I = k \cdot C \tag{21}$$

Meaning of the symbols:

I .... Ionization current

C.......................... Capacity of the measuring capacitor

In Figure 1 an example is given using these date

- Complete measuring time 30 s
- Least Square Fit with 31 measuring points (t = 0 s, 1 s, 2 s, 3 s, ... ,30 s)
- Slope: k = 0,154 48 Vs^{-1}
- C = 1,006 1 · 10^{-9} F
- Resulting ionization current I = 1,554 2 · 10^{-10}

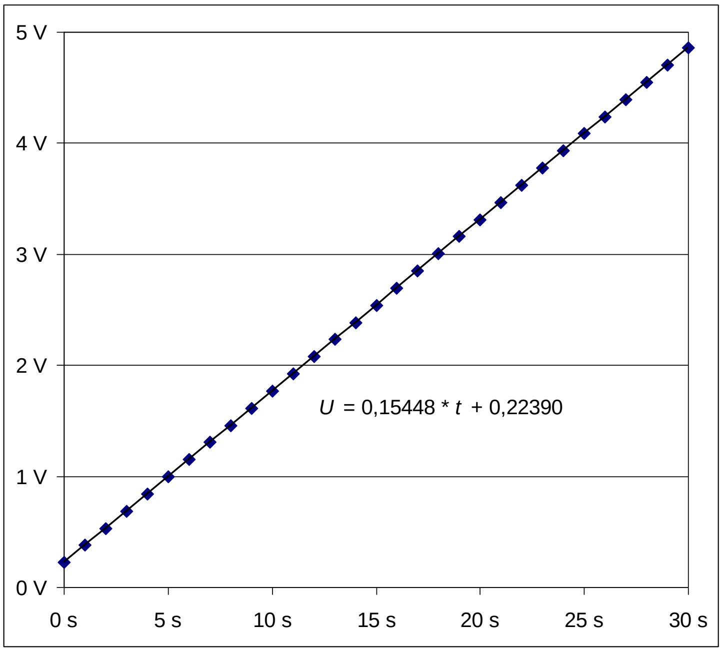

Figure 1 Example for the calculation of the ionization current

As it is shown in Figure 2 the LabView based evaluation software writes all important data into an Excel-sheet. The example shows the output data for a calibration of a Monitor Chamber with a Free Air Ionization Chamber for a Mammography quality (Quantity Air Kerma, air pressure, air temperature near Monitor Chamber and near Free Air Ionization Chamber, air density corrected Ionization currents of the Monitor Chamber and the Free Air Ionization Chamber and finally as the result of the measurement the Calibration Coefficient of the Monitor Chamber and the Air Kerma Rate).

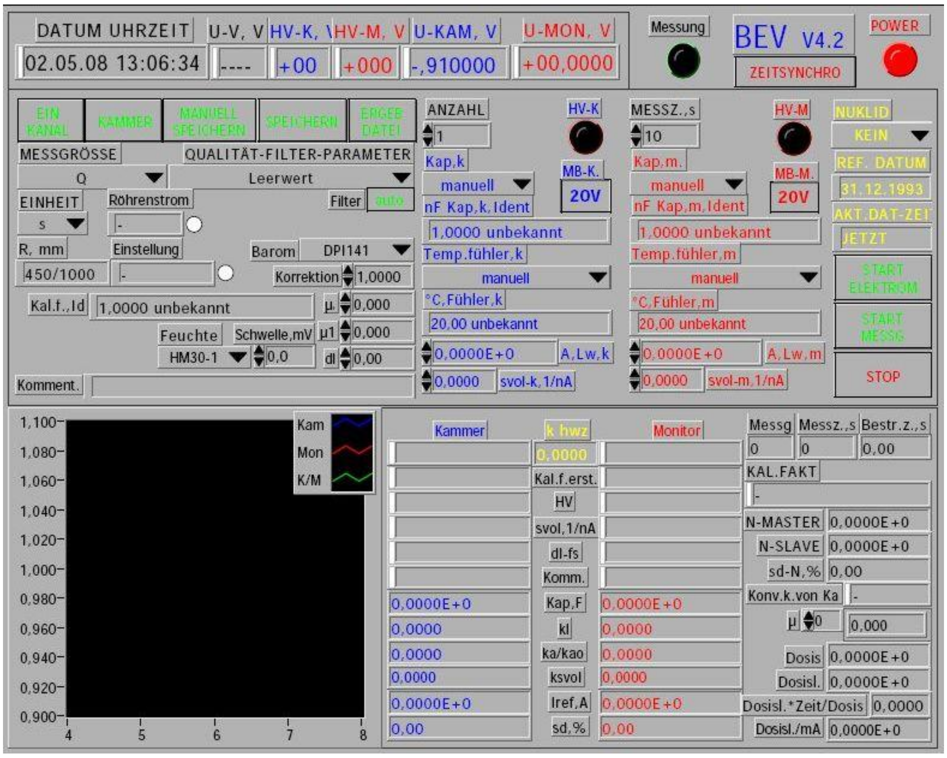

DATUM UHRZEIT 02.05.08 13:06:34
U-V, V ----
HV-K, V +00
HV-M, V +000
U-KAM, V -,910000
U-MON, V +00,0000

MESSGRÖSSE Q
QUALITÄT-FILTER-PARAMETER Leerwert
EINHEIT s
Röhrenstrom -
Filter auto
R, mm 450/1000
Einstellung -
Barom DPI141
Korrektion 1,0000
Kal.f.,Id 1,0000 unbekannt
μ 0,000
μ1 0,000
Feuchte HM30-1
Schwelle,mV 0,0
dl 0,00
Komment.

ANZAHL 1
Kap,k manuell
MB-K. 20V
nF Kap,k,Ident 1,0000 unbekannt
Temp.fühler,k manuell
°C,Fühler,k 20,00 unbekannt
A,Lw,k 0,0000E+0
svol-k,1/nA 0,0000

MESSZ.,s 10
Kap,m. manuell
MB-M. 20V
nF Kap,m,Ident 1,0000 unbekannt
Temp.fühler,m manuell
°C,Fühler,m 20,00 unbekannt
A,Lw,m 0,0000E+0
svol-m,1/nA 0,0000

NUKLID KEIN
REF. DATUM 31.12.1993
AKT.DAT-ZEIT JETZT

Kammer	k hwz	Monitor
	0,0000	
	Kal.f.erst.	
	HV	
	svol,1/nA	
	dl-fs	
	Komm.	
0,0000E+0	Kap,F	0,0000E+0
0,0000	kl	0,0000
0,0000	ka/kao	0,0000
0,0000	ksvol	0,0000
0,0000E+0	Iref,A	0,0000E+0
0,00	sd,%	0,00

Messg 0
Messz.,s 0
Bestr.z.,s 0,00
KAL.FAKT -
N-MASTER 0,0000E+0
N-SLAVE 0,0000E+0
sd-N,% 0,00
Konv.k.von Ka -
μ 0 0,000
Dosis 0,0000E+0
Dosisl. 0,0000E+0
Dosisl.*Zeit/Dosis 0,0000
Dosisl./mA 0,0000E+0

Messung	1
Datum	13. Mär. 14
Uhrzeit	11:09:39
R,mm	332/900
Messgröße	Ka
Konv.koeff.	1
Qual.-Filter	100Mo25Mo30 F10-1
μ0,cm²/g	1,663
μ1,cm^4/g²	0,000
Röhrenstr.,mA	20,7
Einstellung	23,5 kV
Korrektion	1,0000
MB-Kap-K-Id.	20V 216.1-3
Kap-K,F	1,0049E-08
MB-Kap-M-Id.	20V 216.1-4
Kap-M,F	1,0148E-07
Barometer	DPI141
Druck	1008,26 mbar
Hygrometer	HM30-1
Feuchte,%rF	27,0
TK,°C,Id.	20,08 T22
TM,°C,Id.	20,03 T21
kl,K	1,0052
ka/kao,K	0,9999
kl,M	1,0051
ka/kao,M	1,0006
Nuklid	KEIN
Akt.datum	JETZT
Ref.datum	31. Dez. 93
k,hwz	1,0000
Leerw.K,A	2,7660E-14
Leerw.M,A	1,4584E-14
Umax,K,V	3,4907
Iref-K,A	**5,1485E-10**
sdK,%	0,00
svol,k,1/nA	0,0025
ksvol,k	1,0013
Umax,M,V	-7,5576
Iref-M,A	**-1,0926E-08**
sdM,%	0,00
svol,m,1/nA	0,0000
ksvol,m	1,0000
N,Master-Id.	PKM Mammo Mo Mo G4 2E
N,Master	1,6042E+06
N,Slave	**7,5592E+04**
sdS,%	0,00
Q,Dosis	4,9557E-02
Rate	8,2593E-04
Dosisl.*Zeit/Dosis	NaN
Rate/mA	3,9900E-05
Einheit	Gy/s
Messzeit,s	60
Schwelle,mV	0
Bestr.zeit,s	NaN

Figure 2 Program surface and Excel output of the LabView based evaluation software

Electronics associated to the Cavity Chamber

Margarida Caldeira, IST-LPSR-LMRI

1. Introduction

Cavity chambers are ionization chambers based on cavity theories. They may have different shapes (cylindrical, spherical or pancake shaped). The model of the chamber constructed is based on the primary standard from the LNHB, cylindrical with spherical ends, as represented in **Figure 1**. It is a vented air-filled chamber, with its walls made of graphite, with a thickness that allows CPE or TCPE to exist.

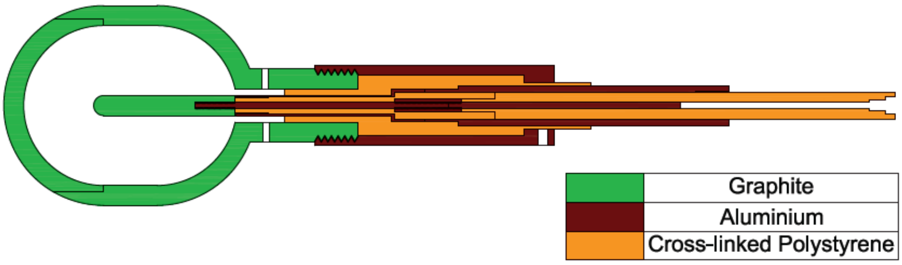

Figure 1: Sketch of the cylindro-spherical cavity chamber

In the choice of the insulating material we took into account its insulating properties, resistance to humidity and to radiation, as well as the ability to be easily cleaned and polished. The cross-linked polystyrene fulfils these requirements.

A guard ring was included, in order to bypass the leakage currents between the outer electrode (the wall) and the inner electrode to ground.

2. Insulators and guard ring assembling

Figure 2 shows a close-up of the neck of the chamber, detailing the insulators and the guard ring.

There are two groups of insulators. The inner insulator separates the guard ring and the central electrode and extends along the central conductor. The outer insulator separates the chamber's neck (outer electrode) and the guard ring.

The inner insulator extends the guard ring by a very small distance (0.2 mm), which is the gap between the guard ring and the central electrode. An air gap of the order of the tenth of the millimeter is introduced between the inner insulator and the guard, extending by a length of 5 mm, in order to reduce surface effects (see Figure 3).

The collecting electrode and guard ring are grounded, while the high voltage is applied to the outer electrode. This is called a grounded input.

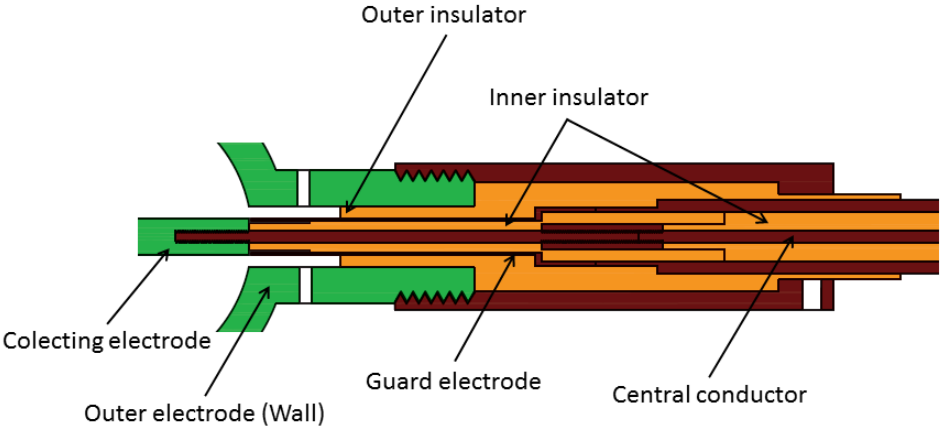

Figure 2: Representation of the assembling of the two groups of insulators and the guard ring

The guard ring is made of Duraluminium and has the same diameter as the central electrode. It has a double role in the construction of the cavity chamber, since it prevents leakages currents to flow from the wall to the central electrode and also defines a separation between collecting and non-collecting volume of the chamber, as we can see in Figure 3.

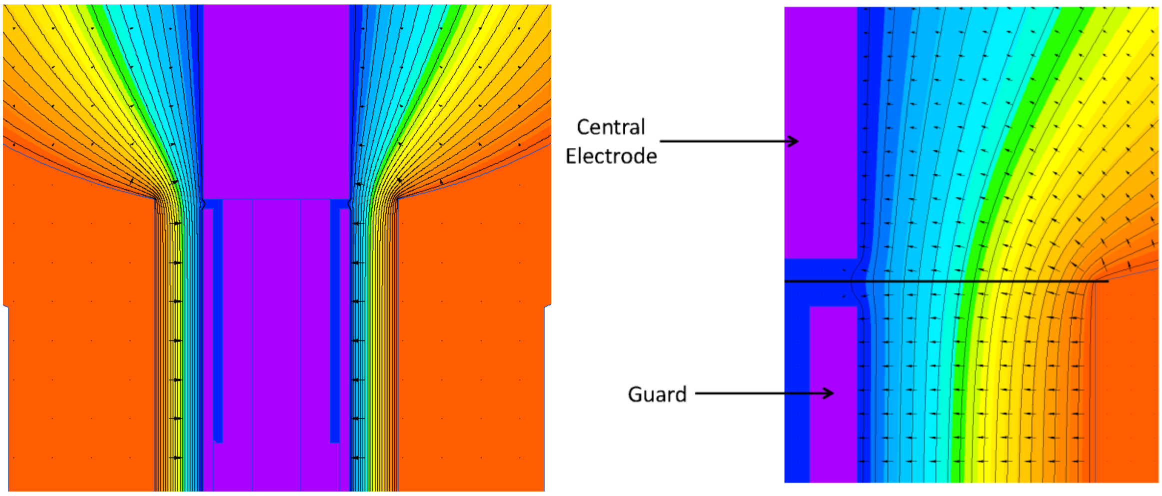

Figure 3: Simulation of the distribution of the electric field inside the cavity chamber, at the level of the neck and detail of the plane at half distance between the central electrode and the guard

Figure 3 shows a detail of the electric field distribution at the level of the chamber's neck. We can observe that there is no electric field strength between the collecting and the guard electrodes, so the volume below the collecting electrode is non-collecting. If we trace a plane at half-distance between the collecting electrode and the guard, passing through the inner edge of the external electrode, we can assume that charged particles above that plane are collected by the central electrode, while charged particles below it are collected by the guard. We also assume that the number of charged particles with the same polarity crossing the plane from one side to the other is the same [1], to ensure equilibrium.

3. **Electrical connections**

The electrical connections between the voltage source and the outer electrode and between the inner electrode and the measuring device are made separately.

The inner electrode is connected to an aluminium rod with 1 mm diameter that transports the signal along the interior of the stem (the central conductor in Figure 1). At the end of the stem this rod connects to an SMC coaxial connector that is later connected to the measuring equipment, Figures 4a and 4b. The high voltage is applied to the wall through an external cable connected to the outer aluminium ring (Figure 4c) which has also the function of holding all the pieces together.

To avoid triboelectric currents generated by charges created between a conductor and an insulator due to friction, the connecting cables should not be kinked, twisted or bended, since it may cause background currents that may persist for hours. Piezoelectric or stored charge effects due to mechanical stress may also occur. To minimize the current due to these effects, it's important to remove mechanical stresses from the insulator and use insulating materials with minimal piezoelectric and stored charge effects. All the insulators must be properly cleaned and polished.

(a) SMC connector

(b) Electrical connections at the end of the stem, for signal transport to the electrometer

(c) External cable for the HV transport to the chamber's wall

Figure 4: Electrical connections in the cavity chamber

4. **Measurements**

Since the amounts of charge collected are very small, an electrometer is used for the measurements. The equipment can be seen as an ultra-high impedance voltmeter, which measures several ranges of charge by means of built-in input capacitors, or several ranges of current using build-in resistors.

The measurements to study the behaviour of the chamber were made in the LMRI ^{60}Co irradiador Eldorado 6 facility, (79.7mGy/min, 18/11/2011), with the collimators set to a 10 x 10 cm field @ 1 m from the source. The high voltage was supplied by a Keithley 247 and the measurements were made with an electrometer UNIDOS from PTW. The humidity, pressure and temperature were always monitored using a hygrometer Rotronic, a barometer Negretti and a thermometer Comark, respectively, and all measurements were corrected for environmental conditions. We also made measurements at the Cobalt-2 and Cobalt-3 installations at LNHB.

After all the components of the chamber were thoroughly cleaned and polished, the chamber was mounted and its behaviour was studied, first making background measurements, then establishing a working voltage and then making stability tests.

4.1. Background measurements

The measured currents that are not produced by radiation in the air cavity must be taken into account. These currents may have origin in triboelectric or piezoelectric effects in the cables, may be radio-induced or may be intrinsic leakage currents. Background is also due to natural radiation, but in this context, this component of the background is negligible.

To quantify theses currents we made measurements before irradiation (intrinsic currents) and immediately after the irradiation (radio-induced currents), always with the HV applied to the chamber's wall.

The background current obtained is represented in **Figure 5**, for the measurements made at the LMRI and at the LNHB.

The background is of the order of 10^{-16} A for the measurements made at LNHB and 10^{-15} A for LMRI, indicating that the chamber is properly assembled and that the insulators are clean and polished, so that there are no impurities affecting the measurements. These values represent about 0.001% of the ionization current and are less than its standard deviation of the mean.

The results also showed that the background currents measured before and after the irradiation of the chamber were similar in magnitude.

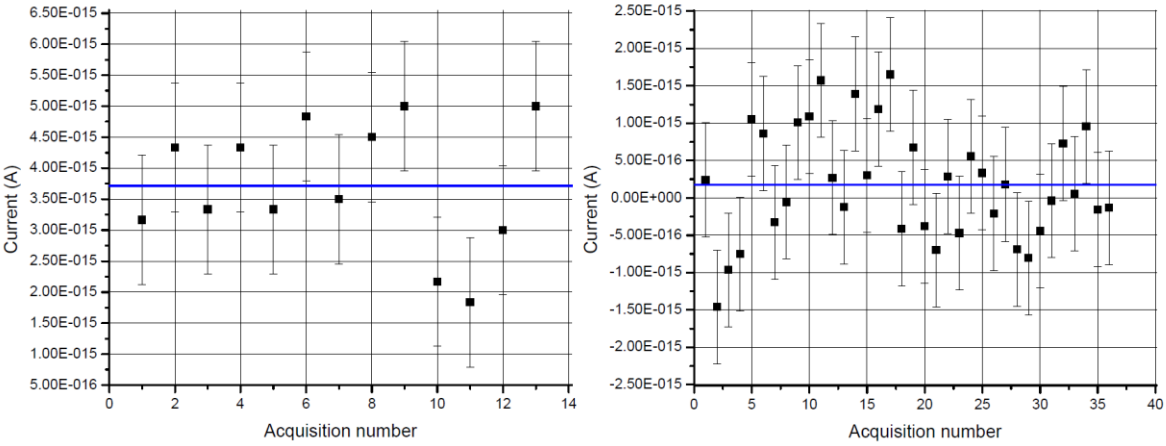

(a) Background current measured at the LMRI

(b) Background current measured at the LNHB

Figure 5: Background measurements for the cavity chamber

4.2. Establishing the working voltage

For the determination of the plateau region of the saturation curve of the chamber, the polarizing voltage was varied from 10 V to 1000 V, for both polarities (Figure 6a) and for two different kerma rates, at LMRI and LNHB (Figure 6b). The results show a well-defined plateau. This indicates that the chamber has no dead volumes in the air that would not contribute to the ionization for low voltages applied, but could contribute for higher voltages. It suggests that the effective collecting volume can be well identified with the geometric volume. Since from HV=600V the ratio $I/I_{800} < 0.1\%$, for the two different kerma rates and for both polarities, the selected working voltage was defined as HV=800V.

4.3. Stability tests

Stability tests were made with a high voltage HV=+800V in both studies. Figures 7a and 7b are representative of the results obtained at LMRI and LNHB respectively. Each point consists in the average of 5 measurements and the uncertainty is the corresponding standard deviation.

No significant variations were observed between each measurement. The maximum deviation from the average was 0.02% for the measurements made at the LMRI and 0.01% for those made at the LNHB.

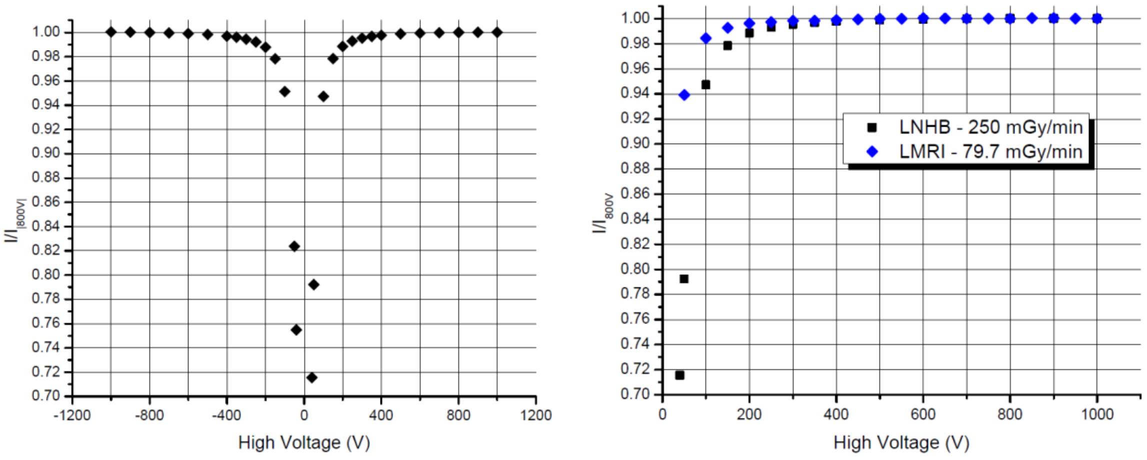

(a) Plateau curves for positive and negative polarity (b) Plateau curves for two different kerma rates

Figure 6: Plateau curves established at LNHB and LMRI

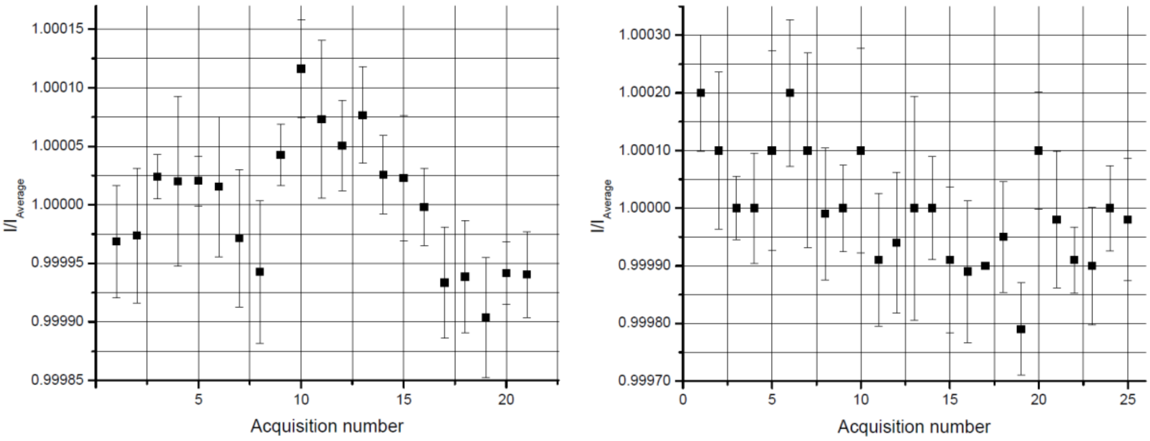

(a) Study of the stability in measured current at the LMRI (b) Study of the stability in measured current at the LNHB

Figure 7: Study of the stability in measured current
using the cylindro-spherical cavity chamber

5. Conclusions

The first tests that were performed, the measurement of the background current, proved that the chamber is well insulated. In fact, the results obtained in the two stages of the study provided us with background currents of the order of 10^{-16} A (at the LNHB) and 10^{-15} A (at the LMRI), which also indicates that the components of the chamber were properly polished and cleaned, leaving no impurities that could affect the measurements because of leakage currents. It is important to mention that the cleaning process of all the components of the chamber had direct consequences in the results obtained. Background measurements made before that process revealed unstable results (drifts) and measurements that could go up to 10^{-13} A.

The tests made for establishing a working voltage showed that a plateau was achieved from a value of applied high voltage of 600 V up to 1000 V. This allowed us to conclude that the developed cavity chamber does not include dead volumes that contribute to the collected charge for increasing values of voltage applied. It is also worth mentioning that the results obtained for positive and negative voltages applied indicated a very low polarity effect.

The chamber also proved to be stable, with no trends and with satisfactory deviations from the average of the measurements: 0.02% for the results at the LMRI and 0.01% for the results at the LNHB.

The results from the experiments made at LMRI and LNHB were compatible, which further validates the results obtained and indicates the possibility of using the constructed chamber as a standard, after it is fully characterized.

References

[1] F. Delaunay, M. Donois, J. Gouriou, E. Leroy, A. Ostrowsky, New LNHB primary standard for ^{60}Co air kerma, Metrologia 47 (6) (2010) 652.

Electrical and radiological tests for the characterization of the cavity-ionization chamber of IFIN-HH

S. Bercea, D. Dusciac, C. Cenusa, M. Donois, I. Cenusa, A. Ostrowsky, A. Celarel, V. Blideanu, E. Iliescu, J.-M. Bordy

Introduction

In order to assure the traceability of measurements in radiotherapy for air kerma, in cooperation with CEA-LNHB, the Collective of Radiation Metrology, Testing and Dosimetry from the "Horia Hulubei" National Institute for R&D in Physics and Nuclear Engineering from Romania, designed and constructed a cavity ionization chamber.

The electrodes of the chamber are made of graphite [1], [2]. The components of the detector and technologies of final processing of these components, as well as of polishing and cleaning are presented in another paper [1]. The aim of this article is to present some of the electrical characteristics of the chamber. Thus, in the present article, we present the work done to determine the following parameters:

1. the leakage current
2. the I-U characteristic curves

1. The ionometric chain

The principal scheme of the ionometric chain is given in Fig. 1:

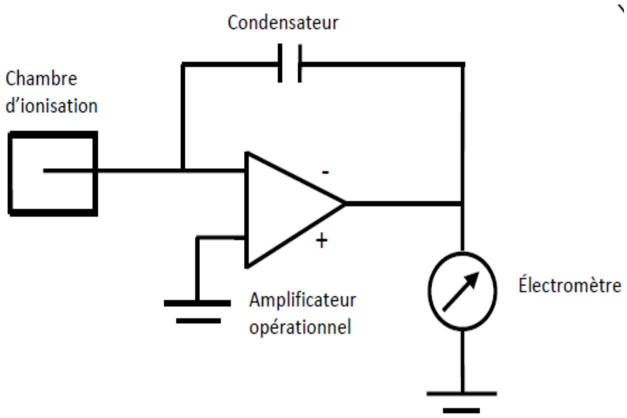

Fig. 1. Scheme of the ionometric chain

The actual measuring system is presented in Fig. 2. This system is a component of the absorbed dose and air kerma primary standard of CEA-LNHB.

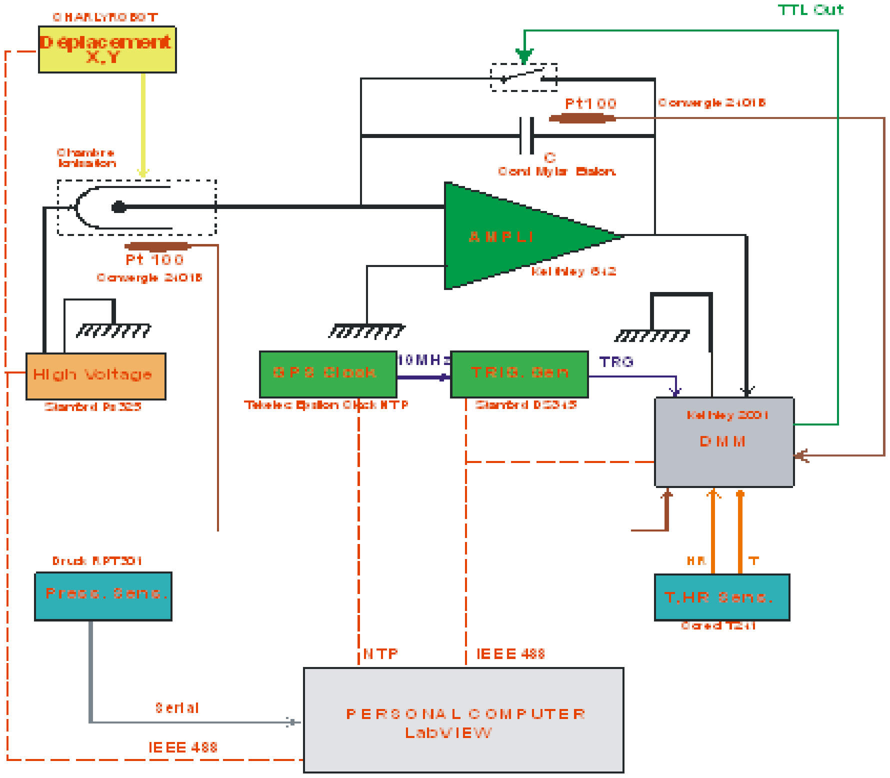

Fig. 2. Measuring system of the absorbed dose and air kerma primary standard of CEA-LNHB

2. Measurement of leakage current

Leakage current is the current provided by the ionization chamber without any radiation field (except the natural radiation background, $K_{back} \approx 10^2$ nGy/h).

The value of the polarizing voltage was U_{pol}=+850 V. After applying the polarizing voltage, we waited for 30 min before starting the measurements, in order to allow the detector to reach a steady state.

Five sets of 30 values were taken for each value of the polarizing voltage. For these measurements, the average value and the extended uncertainty were calculated, for k = 2 (~95% level of confidence). The results for the leakage current, I_{leak} are given in Table 1.

Applied voltage (V)	Leakage current (A)	Extended uncertainty for k=2 (A)
+850 V	-1.27E-15	1.44E-15
-850V	-3.25E-16	8.57E-16

Tab. 1. Leakage current and its extended uncertainty

3. The I-U characteristics of the cavity-ionization chamber

In order to obtain the plateau of the I-U curve, the irradiations were performed with a collimated beam of gamma-ray (Cs-137). The ionization chamber was placed at 2 m from the radioactive source of Cs-137, at 1.5 m from the floor, Fig. 3 shows the ionization chamber placed on the irradiation bench.

Fig. 3. Ionization chamber on irradiation bench

In order to provide an ionization current, the ionization chamber was irradiated at an absorbed dose rate of ~800 mGy/h. The measurement ionometric chain used is the same as the one used to measure the leakage current (Fig.1. and Fig. 2. Here above)/2/.

The polarizing voltage was increased, in steps: 0V, 10V, 20V, 50V, 100V, 200V, 400V, 600V, 800V and 850V. For each value of the voltage, a delay period of 900 s passed between the moment of voltage change and the start of the measurement; 60 values of the ionization current were recorded.

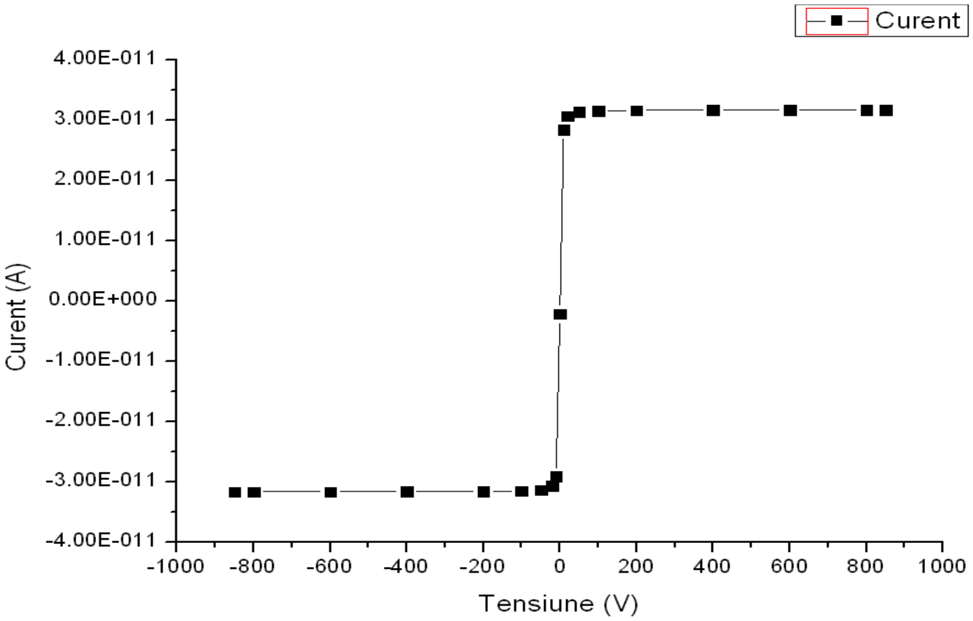

Fig. 4. Current-voltage curve of the ionization chamber

For the plateau of the I-U curve (Fig.4), for negative values of the voltage, the same method was used. The results of the measurements are given in Table 2. From the data of Table 2, one can observe that the ratio of the saturation current (I_{sat}) for the same value of the voltage (I_+/I_-) is 1.00095, i.e. the difference is of 0,095% (~0.1%).

Applied voltage (V)	Measured current (A)	Applied voltage (V)	Measured current (A)
0	-1.9729E-12	0	-2.1528E-12
10	2.8340E-11	-10	-2.9078E-11
20	3.0653E-11	-20	-3.0717E-11
50	3.1362E-11	-50	-3.1359E-11
100	3.1533E-11	-100	-3.1522E-11
200	3.1608E-11	-200	-3.1600E-11
400	3.1639E-11	-400	-3.1641E-11
600	3.1645E-11	-600	-3.1659E-11
800	3.1647E-11	-800	-3.1676E-11
850	3.1645E-11	-850	-3.1677E-11

Tab. 2. Current-voltage values of the ionization chamber

In the same time, the slopes (tg α) of the plateau are also slightly different:

$$\text{tg}\,\alpha_+ = 0,\ \text{tg}\,\alpha_- = 0{,}002\text{V}/200\text{V} = 0{,}001\text{V}/100\text{V} = 10^{-3}\,\text{V}/100\text{V}$$

Conclusions

The results of measurements performed in this first stage, for characterizing the cavity ionization chamber, show that the leakage current and the I-U characteristic are within acceptable limits; this conclusion allows to continue the tests in order to have a complete characterization of the detector.

Acknowledgement

This work was partly supported by the EMPIR Project 14 RPT 04 ABSORB and partly by the IFA-CEA Project C4-02 CATRAS

References

[1] S. Bercea, D. Dusciac, C. Cenusa, M. Donois, I. Cenusa, A. Ostrowsky, A. Celarel, V. Blideanu, E. Iliescu, J.-M. Bordy, "The development of a cavity-ionization chamber as a primary standard for air kerma. Development of a primary standard for K_{air} in IFIN-HH", this proceeding

[2] S. Tuta, S. Bercea, ”Execution and test cavity-ionization chamber for K_{air}- Stage Report, project C4-02 CATRAS”

Cavity chambers

correction factors measurement

Margarida Caldeira, IST-LPSR-LMRI

1 *Introduction*

The air-kerma is given by:

$$K_{air} = \left[\left(\frac{Q}{m_{air}}\right)\left(\frac{\overline{W}}{e}\right)_{air}\left(\frac{\overline{\mu}_{en}}{\rho}\right)_{air,c} \times \left(\frac{\overline{S}}{\rho}\right)_{c,air} / \left(1-\overline{g}_a\right)\right] k_p k_T k_h k_{pol} k_{sat} k_t k_{att} k_d k_{stem} k_{ec} k_{rn} k_{an} k_{wall}$$

where the k_i's are the correction factors. The factors k_p, k_T and k_h correct the measured charge Q for the effects of air pressure, temperature and humidity, respectively, k_{rec} corrects for recombination effects, k_{stem} for chamber stem scattering, k_{wall} for wall effects and k_{an} and k_{rn} for the axial and radial non-uniformity of the beam.

2 *Environmental correction factors*

The determination of the air-kerma requires the measurement of charges liberated per unit mass of dry air. Vented cavity chambers are open to the ambient air, so the mass of air inside the cavity chamber depends on the density of air, and hence, on the environmental conditions: temperature, pressure and humidity. The latter also influences the values of $(W/e)_{air}$ and S_{air} .

For the measurements to be corrected to standard temperature and pressure, for each charge or current measurement, the values of temperature and pressure are recorded. The humidity is also controlled and recorded during this process.

The temperature correction factor, k_T, corrects the measured current for changes in the mass of air contained in the inner volume of the chamber, which may occur due to ambient temperature changes. For an ideal gas, the correction to reference conditions of 20º C (293.15 K) is given by:

$$k_T = \frac{273.15+T}{293.15}$$

where T is the measured temperature in ºC.

The pressure correction factor, k_p, corrects the measured current for the changes in the mass of air contained in the inner volume of the chamber, which may occur due to ambient pressure changes. Assuming an ideal gas, the correction to standard atmospheric pressure (1013.25 hPa) is given by:

$$k_p = \frac{1013.25}{p}$$

where p is the measured ambient pressure in hPa.

Vented ionization chambers are open to ambient air and a correction factor must be included to account for the influence of water vapour, since the humidity in air affects the number of ion pairs created.

The correction factor, k_h, which corrects the measured current for the effect of the variation in vapour quantity of air is, according to ICRU Report 31 [1], k_h=0.997.

This value reports to the current for dry air, at 20º C (293.15 K) and 1 atm, for ^{60}Co beams and it is generally accepted for laboratories with humidity ranging between 20 and 70% and temperatures around 20º C [2].

The uncertainties in the measurement of temperature and pressure are type B uncertainties that take into account the resolution of the equipment and the stated uncertainty in the instruments certificates. The thermometer has a resolution of 0.1 ºC and the stated uncertainty in the measurement range is 0.05 ºC. As for the barometer, the resolution is 0.025 hPa, with a stated uncertainty in the measurement range of 0.19 hPa.

In our measurements, the relative uncertainty in the correction factor associated with temperature was 0.021% and with pressure it was 0.009%. ICRU Report 31 states that for T = 20ºC and p = 1 atm, a correction factor of 0.997 should be considered to account for air humidity. For humidities between 20% and 70%, the deviation varies from 0.9969 and 0.9974, and the uncertainty can be given as 0.029%.

Since the measurements for temperature, pressure and humidity are made outside the chamber, these uncertainties may be multiplied by 2, to account for the differences between the conditions inside and outside the chamber.

3 *Correction factors related to the reference conditions*

3.1 *Attenuation Correction factor*

Since the beam energy fluence attenuation is proportional to the number of air molecules between the source and the ionization chamber, the attenuation correction factor, k_{att} , compensates for the beam attenuation due to the air column between the source and the detector (hence, depending on the source-chamber distance), as a function of pressure and temperature. The correction is given by:

$$k_{att} = \exp\left[\left(\frac{\mu}{\rho}\right)_0 (\rho_0 d_0)\left(\frac{1}{k_{pT}} - 1\right)\right]$$

where d_0 is the distance between the source and the detector, ρ_0 is the air density in reference conditions, $(\mu/\rho)_0$ is the mass attenuation coefficient in air and k_{Tp} is the correction factor for reference temperature and pressure. The value for the mass attenuation coefficient in air, for the Eldorado 6 ^{60}Co beam, $(\mu/\rho)_0=6.0\times10^{-2}$ was taken from **[3]**, considering the average spectrum energy calculated with EGSnrc (1.064 MeV).

The uncertainty associated to the correction for attenuation in air is given by:

$$\frac{u_{k_{att}}}{k_{att}} = (\rho_0 d_0)\sqrt{\left(u\left(\frac{\mu}{\rho}\right)_0\left(\frac{1}{k_{Tp}} - 1\right)\right)^2 + \left(\left(\frac{\mu}{\rho}\right)\frac{1}{k_{Tp}}\frac{u(k_{Tp})}{k_{Tp}}\right)^2}$$

where the estimated uncertainty over $(\mu/\rho)_0$ is 0.1×10^{-2}cm^2/g [4]. The correction factor for environmental conditions varies from 0.994 to 1.006 which in the worst case gives an overall uncertainty of 0.0028%.

3.2 Distance correction factor

The correction factor for the distance, k_d, accounts for the uncertainty in positioning the chamber in terms of distance from the source, which depends on the measurement of the chamber's diameter, the measurement of the source-chamber distance, on the reproducibility of the positioning, orientation of the chamber or on the operator's skills.

The correction factor is given by:

$$k_d = \frac{d_0^2}{(d_0+x)^2}$$

where d_0 is the reference distance and x is the error in positioning. However, since $d_0 >> x$, we consider $k_d=1$. Even though the correction factor related to the measurement of the distance is considered equal to unity, there is an uncertainty associated to it, where the uncertainties associated to the calliper used for the measurement of the diameter of the chamber and to the micrometer used to measure the distance between the source and the chamber, are taken into account. In our case, errors due to operator experience and positioning of the micrometer in the aluminium slab where accounted for as 0.5 mm. The uncertainty due to the displacement, for measurements made at 1m from the source, was given by u_d = 0.029%.

3.3 Correction for source decay

In order to trace the measurements made at a given date to a reference date, a correction factor for source decay, k_t , is introduced:

$$k_t = \exp\left[\frac{\ln 2}{T_{1/2}}\left(t - t_0\right)\right]$$

where t is the date of the measurement, t_0 is the reference date and $T_{1/2}$ = 5.2711 years with an uncertainty of 0.0008 years, is the radioactive half-life, according to Bé [5]. The relative standard uncertainty associated to the source decay is given by:

$$\frac{u_{k_t}}{k_t} = \frac{\ln 2}{T_{1/2}}\sqrt{u_t^2 + \left(\frac{t-t_0}{T_{1/2}}\right)^2 u_{T_{1/2}}^2}$$

where we estimated u_t as 0.010%/minute and $u_{T1/2}$ =0.0008 years is that given by Bé. For our measurements, made over one month, we obtained an uncertainty in the source decay of 0.001%.

4 Electrical correction factors

4.1 Background and leakage current

The measured currents that are not produced by radiation in the air cavity must be taken into account. These currents may have origin in triboelectric or piezoelectric effects in the cables, may be radio-induced or may be intrinsic leakage currents.

To quantify theses currents we made measurements before irradiation (intrinsic currents) and immediately after the irradiation (radio-induced currents), always with the HV applied to the chamber's wall. Results show that the background currents measured before and after the irradiation of the chamber were similar in magnitude and of the order of 10^{-15} A, which represents about 0.001% of the ionization current and is less than its standard deviation of the mean.

All the ionization currents were corrected for background currents, which was taken as the average of the measurements made before and after the chamber irradiation.

4.2 Polarity correction factor

It is very often that the measured signal obtained using a cavity chamber at positive polarity is not equal to that measured at reversed polarity. This polarity effect can be voltage dependent or voltage independent. The voltage independent effects result from radiation interactions that occur in chamber components other than the gas cavity (such as the central electrode or the connecting cables and wires, for example), which produce charges that are non-dosimetric but that influence the result, since they are added or subtracted from the ionization produced in the cavity, depending on the applied polarity. The voltage dependent effects may result from the variation of the effective volume of air inside the chamber, due to the distortion of the electric field lines by space charges or by potential differences between the collecting electrode and the guard ring or to the difference in the collection efficiency of a chamber resulting from the different mobilities of positive and negative ions.

The guard electrode should protect the collecting electrode from ionization signals arising from regions with low or distorted electric fields, but there may be still voltage-dependent polarity effects, as long as the overall impact in the measured signal is not very significant. The impact of the polarity effect is quantified by the polarity correction factor, k_{pol}.

The polarity correction factor is then introduced to account for the effects of applying HV with reversed polarities to the cavity wall. It is determined by measuring the ionization current produced with both positive and negative polarity HV on the chamber's wall. The correction factor is given by:

$$k_{pol} = \frac{|I_V|+|I_{-V}|}{2|I_V|} = \frac{1}{2}\left[1 + \frac{I_{-V}}{I_V}\right]$$

where I_V is the measured current when applying positive HV and I_{-V} is the measured current when applying negative HV. These currents must be corrected for standard values of temperature, pressure and humidity. If the measurements are made consecutively, corrections for decay and attenuation may or may not be applied, since in this case their effect is negligible.

The ionization current was measured with positive polarity ($I_{Vbefore}$) followed by measurements with negative polarity (I_{-V}) and another set of measurements with positive HV (I_{Vafter}), i.e., the current for negative polarity is measured intercalated between two measurements of current with positive polarity, to account for possible drifts in the measurements. The value of I_V in the equation corresponds to the average of $I_{Vbefore}$ and I_{Vafter}. The stabilization time between changes in polarizing voltage was about 10 minutes and to eliminate any accumulated charges the chamber was pre-irradiated before each set of measurements.

The polarity correction factor, k_{pol}, was determined for $|HV| = 800V$, for three different irradiation systems (the Eldorado 6 at the LMRI and the Co-2 and Co-3 at LNHB), at each reference distance. The results are summarized in Table 1.

	Cobalt n.3	Cobalt n.2	Eldorado 6
k_{pol}	1.00030	1.00027	1.00024

Table 1: Polarity correction factors obtained in the three ^{60}Co installations

The small polarity effect is a good indicator for the quality of the chamber, since it suggests that there is no charge production in chamber components other than the cavity and that there is no electric field distortion near the guard ring.

The uncertainty associated to the polarity correction factor is given by:

$$u_{k_{pol}} = \frac{1}{2}\sqrt{\left(\frac{u(I_{-V})}{I_V}\right)^2 + (2k_{pol}-1)^2\left(\frac{u(I_V)}{I_V}\right)^2}$$

I_V and I_{-V} are both corrected for temperature, pressure and humidity. Since the measurements were taken in a short period of time, there was no correction for attenuation and radioactive decay. The value obtained for the relative standard uncertainty associated to the polarity correction factor, u_{kpol}, was 0.027%.

4.3 Recombination or Saturation correction factor

When the cavity chamber is irradiated, some of the charges created in the active collecting volumes are not collected. In fact some of the ions generated inside the air chamber will recombine before reaching the collecting electrode. For this reason, a recombination correction factor, k_{rec}, must be introduced. There are two contributions for this correction factor, the initial and the volume recombinations.

The initial component relates to the recombination of positive and negative ions generated in the same secondary electron path. Since the number of tracks per unit volume of air does not influence the recombination within a given track, this component is independent of dose rate.

Volume recombination refers to ions that are produced in different tracks that meet on their path to the electrodes. In this case, the recombination depends on the ion density and hence, on the dose rate. While the initial recombination is proportional to the inverse of the polarizing voltage, the volume recombination is proportional to the inverse of the square of the polarizing voltage [6]. The contribution of each component varies, depending on the dose rate and on the dimensions of the chamber.

Several methods have been published for the calculation of the recombination correction factor in ionization chambers. The method developed by De Almeida and Niatel [7], as implemented by Boutillon [8], provides an accurate determination of k_{rec} , by determining the chamber response to different polarizing voltages for three or four different air-kerma rates. Ion recombination in ionization chambers has been reviewed by Boag in 1987 **[9]**. However, this theory does not consider polarity effects, so the measured current must be corrected for these effects.

If both components equally contribute, then the correction factor can be written as:

$$k^0_{sat} = \frac{I_\infty}{I_{V_M}} \approx 1 + \frac{A}{|V_M|} + \frac{B}{V_M^2}|I_{V_M}|$$

where:

- A and B are constants for a given combination "ionization chamber + beam"
- V_M is the HV applied to the chamber
- I_M is the current measured when V_M is applied, corrected for polarity effects

The two constants, A and B, are determined by measuring the ionizing currents, I_V and $I_{V/m}$, generated at two different voltages, V and V/m, for different kerma rates, which can be obtained by varying the distance between the detector and the source.

The plot of the ratio $I_V/I_{V/m}$, measured at different distances (kerma rates), as a function of the absolute current, I_V, is a straight line. The function is given by:

$$\frac{I_V}{I_{V/m}} \approx 1 + (m-1)\,\frac{A}{V} + \left(m^2-1\right)\frac{B}{V^2}|I_V|$$

Knowing the slope of the line and the Y-intercept value, it is possible to determine the constants A and B.

The current was measured at three different distances from the source, in three ^{60}Co irradiation systems: the Cobalt-2 (250 mGy/min) and Cobalt-3 (18.257 mGy/min) at LNHB and the Eldorado 6 at LMRI (79.7 mGy/min) at 18/11/2011. The high voltages applied were V = 800V and V/m = 400V (hence, m = 2), for the three cases.

Some of the results for the three experiments are depicted in Figure 1.

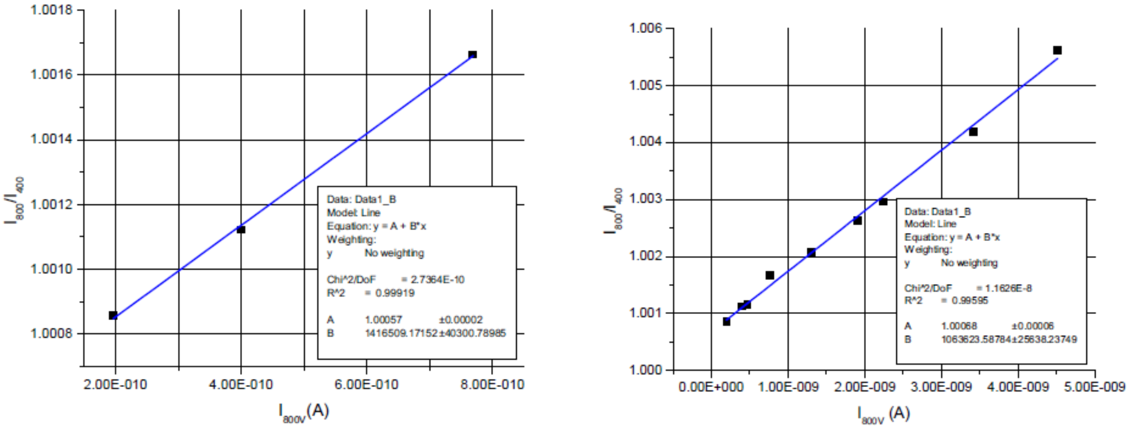

Figure 1: Linear fit of the ratio I_V /$I_{V/m}$ as a function of I_V, for the determination of the constants A and B in the definition of k_{rec}, a) obtained in LMRI; b) for the 3 irradiators

The linear fits allowed us to calculate the slope and the Y-intersect of the curves. From that fits, the constants A and B were determined. The results obtained for the initial and volume recombination for each of the installations individually and for the set of the three (since A and B can be considered constant for different beams, as long as the energy spectrum of the electrons entering the cavity is similar, as for example, beams of the same type of sourceare presented in Table 2.

	I_{800} (A)	I_{800}/I_{400}	Initial Component	Volume component	k_{rec}
Co3	4.51184×10^{-9}	1.00561	1.00062	1.65185×10^{-3}	1.00227
	1.90369×10^{-9}	1.00262	1.00062	6.96972×10^{-4}	1.00132
	4.72200×10^{-10}	1.00120	1.00062	1.72880×10^{-4}	1.00079
Co2	3.41843×10^{-9}	1.00419	1.00071	1.14028×10^{-3}	1.00185
	2.24189×10^{-9}	1.00291	1.00071	7.47828×10^{-4}	1.00146
	1.30022×10^{-9}	1.00206	1.00071	4.33714×10^{-4}	1.00114
ED6	7.68978×10^{-10}	1.00166	1.00057	3.63088×10^{-4}	1.00093
	3.99441×10^{-10}	1.00112	1.00057	1.88604×10^{-4}	1.00076
	1.96516×10^{-10}	1.00085	1.00057	9.27888×10^{-5}	1.00066

Table 2: Results for the recombination correction factor, for the three irradiators, where the initial and volume components are specified.

It can be seen that the initial recombination is independent of measured current for each irradiator (hence, it does not depend on the kerma rate), as follows directly from the expression for the initial recombination, and that the volume recombination depends on the kerma rate. We can also observe that the major contribution comes from the initial component.

The recombination correction factors for the three ^{60}Co beams, for each reference field (Cobalt-2 at 1 m, Cobalt-3 at 0.8 m and Eldorado 6 at 1 m), are presented in **Table 3**.

Beam	Co2	Co3	ED6
d (m)	1	0.8	1
k_{rec}	1.00114	1.00132	1.00076

Table 3: Recombination factors obtained for the three facilities

we write k_{rec} as:

$$k_{rec} = 1 + \frac{x-1}{y^n - x}$$

with $y = \frac{V}{V/m}$ and $x = \frac{I_V}{I_V/m}$, the uncertainty in the recombination correction factor is given by the simplified expression:

$$u_{k_{rec}} = \frac{1}{(y^n - x)^2}\sqrt{(y^n-1)^2 u_x^2 + [n y^{n-1}(x-1)]^2 u_y^2}$$

Where $u_y = y\sqrt{1+y^2}\frac{u(V)}{V_0}$

For our measurements, the value for u_{krec} was 0.018%, where the value has been doubled to account for approximations in the formula.

5 Correction factors related to properties of the chamber

Besides the electrical and environmental conditions, the air-kerma must also be corrected due to characteristics that are inherent to the chamber itself, to account for interactions in the stem, the central electrode and the wall, for example.

5.1 Correction for Stem scattering

When the cavity chamber is irradiated, the radiation field covers part of the stem, contributing to the increase of scattered photons entering the collecting volume and hence, to the increase in the measured ionization current.

Contributions to the chamber response due to these scattered photons are corrected by the stem correction factor, k_{stem}. It can be measured using a dummy stem placed symmetrically opposed to the real chamber stem. The stem correction factor can also be calculated using Monte Carlo simulations. The dummy stem is, ideally, an exact copy of the chamber's stem. However, for this study, this was not the case, since the chamber's neck is 4 mm shorter that the graphite cylinder from the dummy stem. This difference will be taken into account when determining the uncertainty associated to this correction factor. The stem scattering correction is given by the ratio of the ionization current measured without the dummy stem (the usual setup) and the ionization current measured with it:

$$k_{stem} = \frac{I}{I_{+stem}}$$

The experimental setup is presented in **figure 2**.

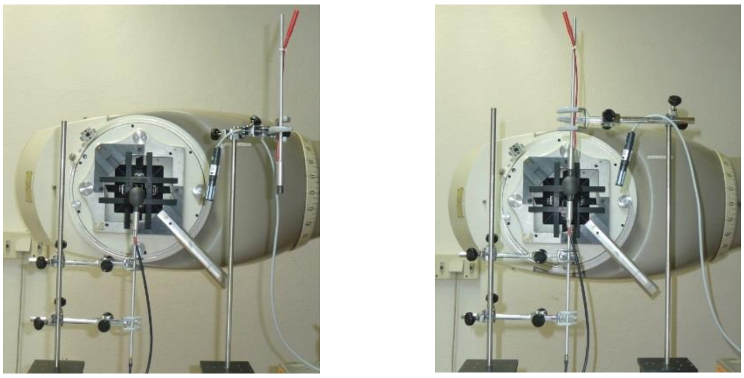

(a) Measurements with no dummy stem (b) Measurements with dummy stem

Figure 2: Experimental setup for the determination of the stem correction factor, k_{stem}

The procedure was to measure the current without the dummy stem, followed by a set of measurements with it and finishing with another set of measurements without the dummy stem. This procedure is to take into account any possible drifts in the measurements. The current I in the equation is given by the average of the two currents measured in the usual setup. The measurements were corrected for environmental conditions. If the measurements are taken in a short period of time, there is no need to correct for attenuation and radioactive decay. As with the previous correction factor determined experimentally, we made measurements in the three ^{60}Co beams.

The experimental results for k_{stem} are presented in **table 4**, where we also include the Monte Carlo result to compare with the measured values.

Beam	Co2	Co3	ED6	MC
d (m)	1	0.8	1	1
k_{stem}	0.9991	0.9992	0.9996	0.9993

Table 4: Stem correction factors obtained in the three different beams

The results obtained in the beams at LNHB were similar. The correction obtained at LMRI is 0.05% smaller than the previous. Taking the average of the 3 results, we obtain k_{stem}=0.9993.

The k_{stem} uncertainty is given by:

$$\frac{u_{k_{stem}}}{k_{stem}} = \sqrt{\frac{1}{I^2} + \frac{1}{\left(I_{stem}\right)^2}}\, u_I$$

The components that contribute to the uncertainty in I are the repeatability in the current measurement and the correction for p, T and h.

The uncertainty associated to the stem correction is then u_{kstem} = 0.055%, where we doubled the uncertainty because the dummy stem is not an exact copy of the chamber's stem.

5.2 Corrections for the central electrode

The perturbation in the measurements due to the presence of the central electrode is taken into account by the correction factor k_{cel}. Given that the wall and the central electrode are made of the same material, we consider k_{cel}=1, according to the methodology adopted by LNHB. A verification was made using EGSnrc.

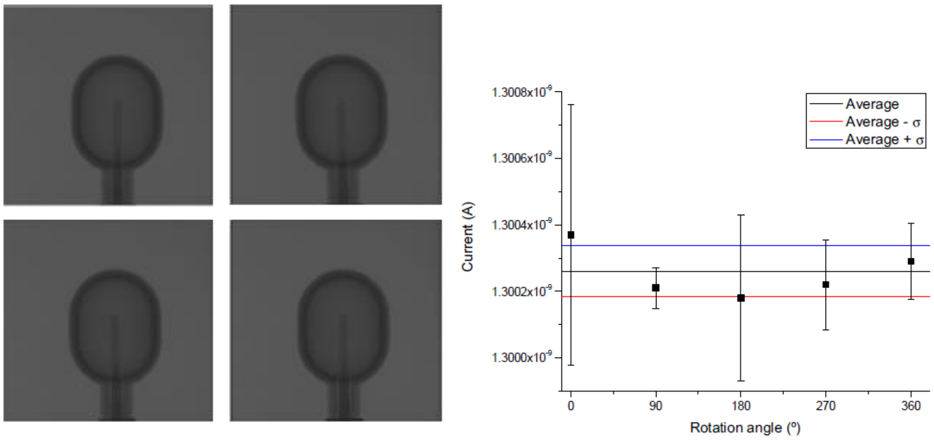

Figure 3 a: Radiographs to observe the central electrode inclination; Figure 3b: Measured current as a function of the rotation angle of the chamber around its axis

Since the radiographs (Figure 3a) showed that there was still a minor inclination of the central electrode, we performed five measurements, rotating the chamber around its axis by angles of 90º, in order to quantify its influence. The results from the measurements, where θ = 0º is the position at which the chamber is usually irradiated, are described in Figure 3b. All the measurements were corrected for standard temperature and pressure, as well as for source decay. The results show that the largest ratio, 0.99985 corresponds to the measurements made at the position θ = 0º and θ = 180º, which indicates that in the chamber's usual irradiation position, the central electrode has a small inclination towards the source direction. In Figure 3b, taking the average of the five measurements, its standard deviation contains the five measured current (within their standard deviations) and it is, in general, smaller than the standard deviation of each individual measurement. For these reasons, no correction factor is considered for the orientation of the central electrode and we take k_{θ} =1.

5.3 Radial non-uniformity

The air-kerma is defined for one point in space. However, the measurements are made using dosimeters with a finite volume. The axial (k_{an}) and radial (k_{rn}) non-uniformity factors are the beam anisotropy correction factors which correct the measured value to that current that would be measured if the beam energy fluence was uniform over the chamber volume and equal to the beam energy fluence at the reference point. Therefore, these correction factors are functions of the current gradient and of the detector's geometry. k_{rn} is obtained from measurements made at the reference plane using a small volume ionization chamber and it is the quantification of the ratio:

$$k_{rn} = \frac{I_{uniforme\ profile}}{I_{measured\ profile}}$$

where $I_{uniforme\ profile}$ is the current obtained if the dose distribution was uniform and equal to the dose at the reference point and $I_{measured\ profile}$ is the current actually measured at the plane perpendicular to the beam, at the reference distance.

The radial non-uniformity correction factor was calculated using the formalism presented by Delaunay [10]. We measured the current at the reference plane (at 1 m from the source), in a 10×10 cm^2 radiation field, using an ionization chamber PTW 23332 with a small volume (0.3 cm^3). For a cylindro-spherical chamber, the profile is measured in the direction of the dosimeter symmetrical axis perpendicular to the beam, so the vertical profile was measured, with the chamber placed horizontally in the radiation field. After the profile of the radiation was determined, it was fitted using a polynomial $f(r) = \sum_{i=0}^{n} \sum a_i r^i$ and then integrated over the height H of the cavity chamber (Figure 4), so that k_{rn} can be written as:

$$k_{rn} = \frac{f(0)\times H}{\int_{-H/2}^{H/2} f(y)dy} = \frac{a_0}{\sum\limits_{i_{pair}} a_i \frac{(H/2)^i}{i+1}}$$

The correction for radial non-uniformity calculated using this formalism gives a value of k_{rn} = 1.0002. The uncertainty for the correction for radial non-uniformity is approximately given by:

$$\frac{u(k_{rn})}{k_{rn}} = \frac{1}{\sqrt{1+1/2n}} \frac{u(I)}{I}$$

The major contribution for the uncertainty is the standard deviation of the current measurements, which is, for the worst case, 0.08%.

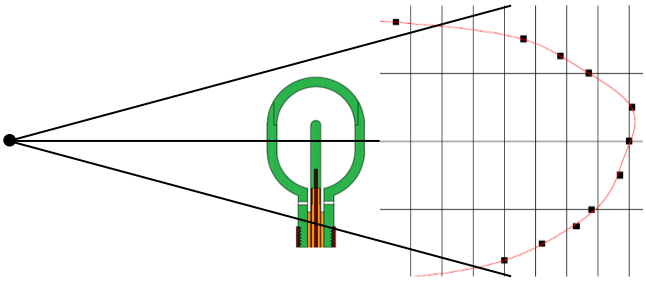

Figure 4: Polynomial fit of the profile over the height of the chamber. The profile corresponds to the profile obtained experimentally over the height of the chamber

6 Conclusions

The results obtained for this cavity chamber in the Eldorado 6 60Co beam are consistent with the correction factors obtained for air-kerma standards for the same radiation.

The small polarity correction factor indicates the good manufacture of the chamber, namely in what concerns the insulation of the signal. This value provides also an indication that there is no field distortion at the level of the guard ring. The measurements made for the calculation of the recombination factor were well fitted using a linear fit, as it was expected.

The values obtained experimentally for the stem correction factor varied from 0.9991 to

0.9996, with an average value of k_{stem}=0.9993. This value could be confirmed using the EGSnrc user code CAVITY.

The variation due to rotation of the chamber and hence, different orientation of the central electrode, is of little importance. The presence of the inner electrode does not affect the measurements, as expected, since it is made of the same material as the walls. This was also confirmed by MC calculations. Taking this into consideration and since the chamber is always irradiated in the same face, the correction factor for the presence of the inner electrode is taken equal to unity.

The radial non-uniformity correction factor is very close to unity, which means that the dose distribution is approximately uniform over the chamber's height for this particular field size.

The results for these correction factors and their associated uncertainties are compatible with the results obtained for cavity chambers with similar design and are, hence, an indication of the quality of the chamber and that it can be considered as a candidate to be a primary standard.

References

[1] Average Energy Required to Produce an Ion Pair, ICRU Report 31, International Comission on Radiation Units and Measurements (1979)

[2] L. Büermann, D. T. Burns, Air-Kerma Cavity Standards, Metrologia 46 (2) (2009), S24

[3] NIST X-Ray and Gamma-Ray Data, http://www.nist.gov/pml/data/xray_gammaray.cfm

[4] F. Delaunay, Une Détermination Simpliste d'Incertitudes Ionométriques de Type B dans un Faisceau de Cobalt-60 ou de Césium-137 - "État de l'Art en Été 2003", NT LNHB 03/29C, LNHB (2005)

[5] M.-M. Bé, V. Chisté, C. Dulieu, E. Browne, C. Baglin, V. Chechev, N. Kuzmenco, R. Helmer, F.Kondev, D. MacMahon, K. Lee, Table of Radionuclides, Vol. 3 . A = 3 to 244 Monographie BIPM-5, 2006

[6] F. H. Attix, Introduction to Radiological Physics and Radiation Dosimetry, Wiley-VCH Verlag GmbH, Weinheim, Germany, 2007

[7] C. de Almeida, M.-T. Niatel, Comparisons Between IRD and BIPM Exposure and Air-Kerma Standards for Cobalt-60 Gamma Rays, Rapport BIPM-1986/12, BIPM (1986)

[8] M. Boutillon, Volume Recombination Parameter in Ionization Chambers, Physics in Medicine and Biology 43 (8) (1998) 2061

[9] J.W. Boag, Ionization Chambers, The Dosimetry of Ionizing Radiation 11 (1987) 169

[10] F. Delaunay, A. Ostrowsky, Some Specific Features of Ionization Chamber Calibrations in Linac X-Ray Beams at the LNE-LNHB, Physics in Medicine and Biology 52 (9) (2007) N207

Cavity chamber

correction factors calculation

Margarida Caldeira, IST-LPSR-LMRI

1. Introduction

Monte Carlo methods are an important tool for the study of radiation transport, with a close connection between the development of these techniques and the need to simulate ionization chamber response accurately, with the attention mostly turned to the development of methods to determine values for stopping powers and for factors that correct for the effects of the wall of the chamber (k_{wall}) and the axial non-uniformity of the beam (k_{an}).

In fact, the use of MC methods in this field has already been extensively validated [1]. In the particular case of the EGSnrc MC code, its use in ionization chamber calculations has been thoroughly benchmarked. It is one of the most used MC codes in medical physics, with a lower energy limit of 1 keV, for photons, and some tens of keV, for electrons, ranging up to some thousand GeV for both charged and uncharged particles. It provides dedicated packages that simulate radiation fields and ion chamber response, for example. In the development of the LMRI cavity chamber, it was the code used to simulate the radiation field and to calculate the physical constants and correction factors that could only be calculated using Monte Carlo. It was used also to validate correction factors obtained experimentally, such as the stem and central electrode correction factors.

2. Simulation of the radiation field

The first step in our MC calculations was the simulation of the experimental radiation field. In order to do that, all the components of the irradiation facility that may have an influence in the spectrum were simulated, namely the finite source and its encapsulation, the collimating system and the trimmer. This task was achieved using the EGSnrc user code BEAMnrc described in **[2]**.

2.1. Modeling the ^{60}Co unit

The irradiation unit Eldorado 6, represented in Figure 1, was modelled according to the sketches in the user's manual and following a similar methodology to that described in [3] and revalidated in [4]. In our particular case, the trimmer was included in the MC simulations, since it is used in the experimental measurements. The highlighted region in Figure 1 corresponds to the components that were simulated in BEAMnrc: the capsule containing the source, the set of collimators (fixed and movable) and the trimmer.

In BEAMnrc, each component of the irradiation facility can be represented as a single component module (CM) that can be regarded as a building block of the irradiator. All of these CMs are re-usable and independent from each other. The simulated Eldorado 6 is composed of 5 CMs, each of which is labelled with a unique identifier, as described in Table 1. The process by which these components are assembled is described in the BEAMnrc user's manual. The CMs are correctly defined when they are assigned with materials defined in PEGS4, the data preparation package. Those materials may already be defined in that pre-processor or the user may create new materials using the same program, which can easily be done using the user interface. The materials used for the simulation of the irradiation facility are defined in the PEGS4 file "gmora.pegs4dat", which is available in the BEAMnrc distribution.

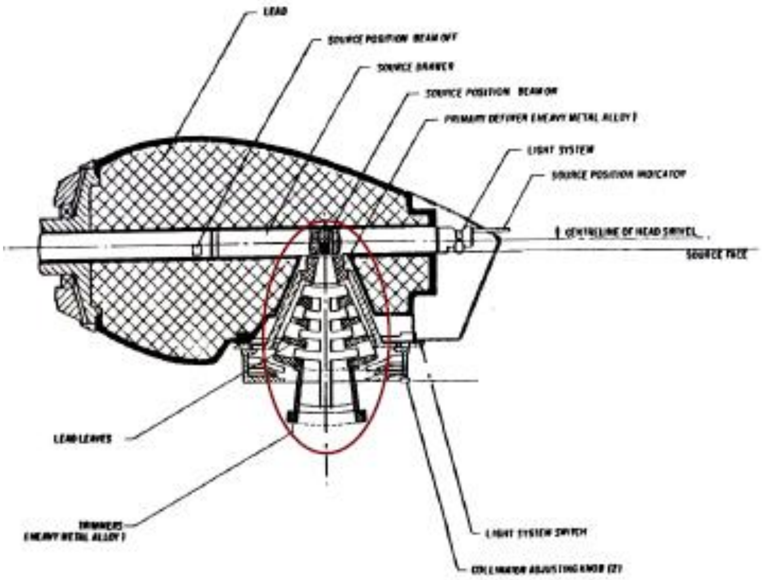

Figure 1: Schematic drawing of the 60Co facility Eldorado 6, highlighting the region to be simulated: source and its encapsulation, collimators and trimmer

Component Module	Identifier	Description
CONESTAK	CAPSULE	Capsule containing the source
PYRAMIDS	PRIMCOLL	Fixed collimator
PYRAMIDS	OUTCOLL	Adustable collimator
PYRAMIDS	TRIMMER	Trimmer bars
SLABS	AIR	Column of air between the trimmer bars and the scoring plane

Table 1: Modules that compose the simulated irradiation facility and corresponding identifiers

Besides a unique PEGS4 designation, each material must be labelled with its density, in units of g/cm3, and a lower and upper energy for photons (AP and UP, respectively), in MeV, as well as for electrons (AE and UE). The parameters AP and AE are the low-energy thresholds for the production of secondary *bremsstrahlung* photons and knock-on electrons, respectively.

Defining AP is simple because we can use a very low value which ensures accurate photon transport, allowing the simulation of all *bremsstrahlung* events as discrete events. The choice of AE, however, demands for a compromise between computer time and accuracy of the simulation, since lower values of AE take more computing time but in general lead to more accurate results. This parameter controls the statistical fluctuations in the electron energy loss and can affect the electron step sizes.

Figure 2 presents the simulation geometry of the Eldorado 6 irradiation system, including the source and housing, as well as the collimating system and trimmer. The figure also indicates the component modules used to build the irradiator and the materials assigned to each of them.

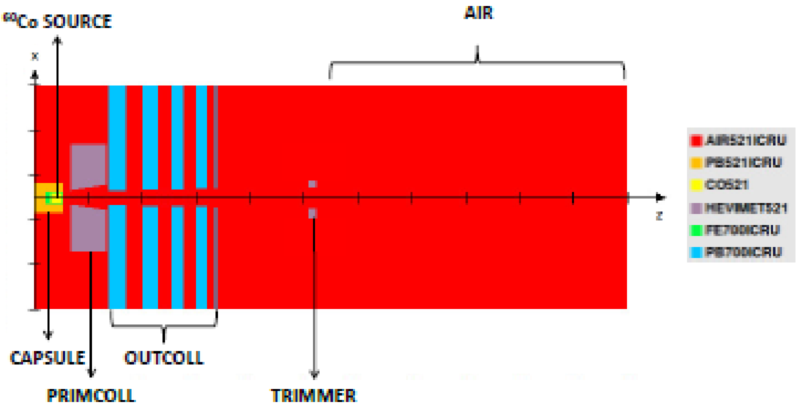

Figure 2: Simulation geometry of the 60Co facility Eldorado 6 and identification of each component module, with a detail of the source capsuling

The source housing used in the Eldorado 6 unit was modelled using a cylindrical geometry, with its symmetry axis coincident with the beam axis. This is obtained using the component module CONESTAK. The source was hence approximated to a uniform cylinder of ^{60}Co with 2 cm diameter, instead of simulating the real source, composed of small pellets. To account for this approximation, the density of the ^{60}Co region was reduced **[3]**. The ^{60}Co cylinder is surrounded by an iron capsule contained in a lead housing 2 cm thick.

For the source input of the BEAMnrc simulation, we used a ^{60}Co spectrum available in the BEAMnrc package, "bareco60.spectrum", which consists in the two lines of 1173.2 keV and 1332.5 keV, contributing with the same intensity. The source is considered to be isotropic and uniform, defined as a vertical ring centred on the Z-axis, with an outer radius of 1 cm, extending through a 2 cm length.

Since the air-kerma is determined for a reference distance of 1 m between the source and the geometrical centre of the chamber, for a 10×10 cm^2 square field, the opening of the outer collimators and of the trimmer, that corresponds to a 10 cm×10 cm square at that distance, was defined based on the method presented in [3] and [4], except that in this case we take into consideration the trimmer bars.

We started by defining a 10 cm×10 cm square in the XY plane located at 1 m from the source. The centres of the source and of the square were set to be coincident. The openings of the outer collimator system and of the trimmer were defined by the straight line that connects the centre of the front face of the source to the point positioned at half the square side at the scoring plane, passing through the inner edge of the trimmer. Then, as the collimating system and the trimmer are adjusted as a single component and are moved about a hinge in the inner edge of the primary collimator entrance, the opening of each collimating leaf is given by the line connecting the hinge to the inner edge of the trimmer.

2.2. Simulation parameters and variance reduction techniques

The simulation parameters were defined so that a phase space output was created at the scoring plane. The simulation result is a phase space file (PHSP file) that contains the relevant information for all particles that cross the scoring plane defined in the input file, such as particle position, direction, charge or energy. This PHSP file can be used as the input source in later simulations using BEAMnrc or any other user code from the EGSnrc system.

Two PHSP files were obtained, one at a scoring plane at 90 cm from the source, for later use in EGSnrc user codes, and one at 100 cm from the source, to determine the 10×10 cm^2

field profile and validate it against experimental results.

The BEAMnrc variable LATCH was enabled, in order to store each particle's history during the simulation. By doing so, we are able to determine the positions where the particles have been created, i.e, in which component it is scattered before it reaches the scoring plane. The LATCH OPTION was then set to 3, in order to record the region numbers where photons interact and the origin of secondary electrons. The simulation was run in parallel, with 10 jobs and 10 chunks per job for 1 × 10^{11} particles.

The global energy cut-offs for the particle transport were set to Global ECUT=0.600 MeV and Global PCUT=0.010 MeV. In order to increase the calculation efficiency, in the source region the values of ECUT were defined to be higher than the global ECUT, so that there was only photon transport in the iron surface in front of the ^{60}Co source.

In order to reduce the computing time, we used the range rejection of electrons, where BEAMnrc calculates the electron range and terminates its history if the particle is unable to leave the present region with enough energy to reach the scoring plane (the range rejection cut-off energy, ECUTRR). If IREJCT_GLOBAL=2, range rejection is performed region-by region and the range rejection cut-off energy is the value of ECUT in the current region. If the range to ECUTRR is less than the perpendicular distance to the nearest region boundary, the history is terminated and the energy is deposited in the current region.

Range rejection of electrons results in an approximation, since the charged particles terminated will not contribute for *bremsstrahlung*. To minimize it, we introduce the input variable ESAVE_GLOBAL defining the maximum charged particle energy (in MeV) at which range rejection is considered. ESAVE_GLOBAL depends on the incident beam energy and the materials that it is passing through. No Russian roulette or *bremsstrahlung* splitting techniques were used and photon forcing was switched off.

The maximum fractional energy loss per step (ESTEPE) was set to the default value, 0.25 (25%). Spin effects were turned on, which is necessary for good backscattering calculations. The photon interaction cross-sections selected to use in the simulation was XCOM, included in the BEAMnrc, which uses the photon cross-sections from Berger and Hubbell. The boundary crossing algorithm used was PRESTA-I and the electron step algorithm was PRESTA-II.

2.3. Interpretation of the phase-space file

To interpret the results, the program BEAMDP (BEAM Data Processor) was used. It is an interactive program that can be used to analyse the BEAMnrc phase-space data files and to derive other information from those files. Among other features, BEAMDP can be used to derive fluence or energy fluence, spectral distributions or XY scatter plots of particles from the PHSP data files. It can also be used to combine phase space files, when the BEAMnrc simulations are run in parallel. We used this feature to combine the 10 PHSP files obtained in the BEAMnrc parallel runs.

3. Modelling the cavity chamber

The EGSnrc package includes a C++ class library (egspp), organized as a main library file and a series of small dynamic shared objects (DSOs), one for each geometry and source type.

Since the EGSnrc C++ class library provides a general purpose geometry package which allows building very complex geometries, it was used to simulate the cavity chamber under study which is cylindrical with spherical ends. This geometry is then used in the input file of the

C++ user code CAVITY, the advanced EGSnrc application used to calculate cavity chamber responses. Except for the calculations where the influence of components of the chamber had to be assessed, the chamber was simulated simply as an air cavity surrounded by the graphite walls, to determine the wall effects. In order to simulate the effects of the stem and of the central electrode, those elements were later added to the geometry definition of the chamber.

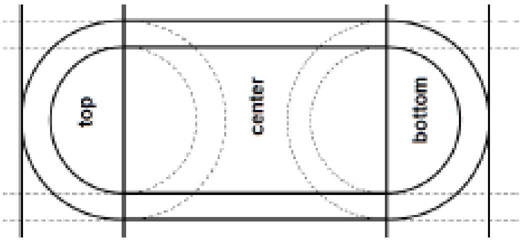

Figure 3: CD geometry used to build the cavity chamber (EGSnrc C++ library class)

The chamber was built using the library *egs_cd_geometry*, which consists of a base geometry (G_B), defining n_B regions, each of which contains other geometries dividing the n_B regions into additional ones. Four vertical planes were defined to form the base geometry, using the library *egs_planes*, which defines 3 regions (see Figure 3). Then two spheres were added to the top and bottom regions using the library *egs_spheres*, dividing that region in two additional regions. Finally, the introduction of two sets of cylinders (using *egs_cylinders*) divides the central region into two more regions. The solid lines in **Figure 3** represent the walls of the simulated chamber.

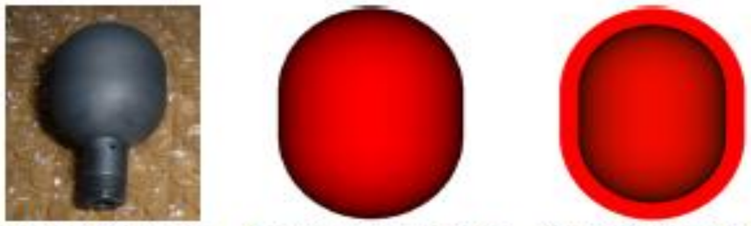

(a) Cavity chamber simulated using EGSnrc

(b) Simulation geometry for the calculation of the wall correction factor, k_{wall}

(c) Cross sectionnal view of the simulation geometry for the calculation of k_{wall}

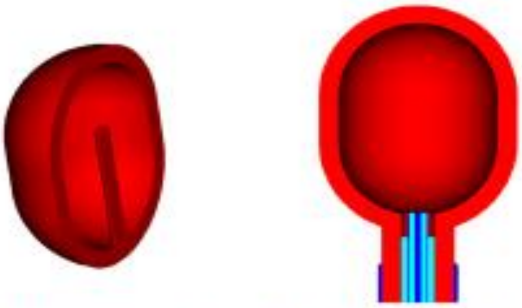

(d) Simulation geometry used to determine the effect of the central electrode

(e) Simulation geometry used to determine the stem correction factor

Figure 4: Simulation models of the cavity chamber.
Red is graphite, dark blue is aluminum and light blue is cross-linked polystyrene.

The source was defined using the library *egs_phsp_source*, where the input source is the realistic phase space file obtained previously using BEAMnrc.

Figure 4.a shows the graphite chamber constructed for the LMRI and Figures 4.b and

4.c represent the EGSnrc model for the k_{wall} calculation. The geometries used to determine the effects of the central electrode and of the stem on the measurement of the air-kerma are depicted in Figures 4.d and 4.e.

For the MC simulations, we used the bulk graphite density obtained by weighting the graphite rod used for the construction of the chamber and measuring its volume. The value obtained was ρ=1.76 g/cm3. The materials used for this set of simulations were defined using the PEGS4 pre-processor. The PEGS4 data file containing the cross section data for the materials used was named cc.pegs4dat.

4. Results: comparison between the experimental and the Monte Carlo profiles

The validation of the PHSP file obtained at the scoring plane using BEAMnrc (1 m from the source, collimators opening corresponding to a 10 cm × 10 cm radiation field) was obtained by comparison with the experimental profiles obtained under the same conditions. The PHSP file obtained by MC calculations was used to construct the vertical and horizontal profiles at the defined scoring plane.

The chamber used to determine the experimental beam profile was a PTW chamber, type 23332, used for the measurement of absorbed dose to water, air-kerma and exposure in ^{60}Co beams, which was selected due to its small volume (since, ideally, the objective is to measure the point ionization current). The experimental vertical and horizontal profiles were determined by moving the small volume chamber to off-centre positions in the interval [-7 cm, 7 cm], in order to obtain the variation of the ionization current over the plane perpendicular to the beam axis. For the horizontal profile the chamber was placed in a vertical position and for the vertical profile the chamber was placed in a horizontal position. The simulated and experimental profiles were compared and the results are represented in **Figure 5**.

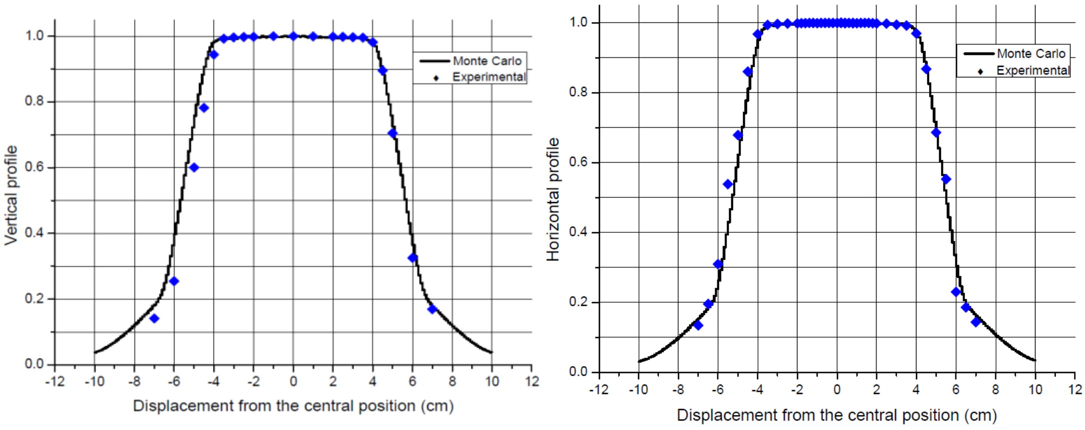

(a) Experimental and MC horizontal profile (b) Experimental and MC vertical profile

Figure 5: Horizontal and vertical profiles obtained experimentally and using Monte Carlo methods

The observation of the figures shows that the experimental and the MC results are in good agreement, hence, the PHSP file obtained using BEAMnrc can be used as the source input in further MC calculations.

Since the IAEA has a phase-space database for external beam radiotherapy where calculations for the Eldorado 6 irradiator are included **[5]**, we compared the spectrum obtained in our BEAMnrc calculations with the validated spectrum in that database. We simulated the radiation field in the same conditions as stated in [**5**]: a 10 cm × 10 cm square field at 80.5 cm from the source, no trimmer included. The results obtained validated our MC simulation of the radiation field for the Eldorado 6 (Figure 6).

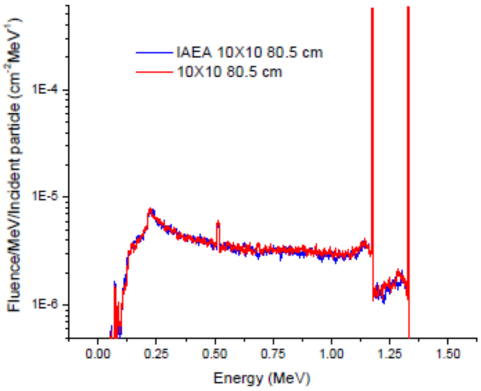

Figure 6: Simulation of the ^{60}Co Eldorado 6 spectrum for a 10×10 cm field at 80.5 cm (calculated and IAEA database for external beam radiotherapy)

5. Air-kerma contributions

5.1. Photon interaction coefficients: determination of g, $(\mu_{en}/\rho)_{a,c}$ and $(\mu_{tr}/\rho)_{a,c}$

The g-value, that quantifies the fraction of the energy transfer lost through radiative processes (*bremsstrahlung*) and consequently dissipated outside the air cavity, and the air to graphite mass energy-absorption coefficient ratio, $(\mu_{en}/\rho)_{a,c}$, contribute to the definition of the kerma. EGSnrc has a user code named 'g', that calculates, for incident photons in a given material, g and the coefficients μ_{tr}/ρ and μ_{en}/ρ. The quantities g_{air} , $g_{graphite}$, $(\mu_{en}/\rho)_{a,c}$ and $(\mu_{tr}/\rho)_{a,c}$ were calculated using that user code.

The calculations were made for air with ρ=1.205×10^{-3} g.cm^{-3} (PESG4 material AIR521ICRU), graphite with ρ=2.265 g.cm^{-3} (PEGS4 material C87ICRU521) and graphite with density ρ=1.70g.cm^{-3} (PEGS4 material 170C521ICRU). The number of particles used for each MC simulation was 1 ×10^{9}. The ^{60}Co spectrum used was that simulated for the Eldorado 6 at LMRI.

We obtained $(\mu_{en}/\rho)_{a,c}$=0.9983, $(\mu_{tr}/\rho)_{a,c}$, =0.9988 (for graphite with ρ=1.70g.cm^{-3}) and g_{air} = 0.0029. The recommended g_{air} for ^{60}Co beams [6] is 0.003. This value was confirmed by Borg et al. [7] that calculated the value as 0.0032 with an uncertainty of 5%. The value for g_{air} obtained from our calculations is below the values that are used by the LNHB (g_{air}=0.0032) and by the LMRI (g_{air}=0.0031). However, the result is consistent with the calculation made by Burns **[8]**, that developed a method to calculate μ_{tr}/ρ for the BIPM ^{60}Co reference chamber using the Monte Carlo code PENELOPE.

Spectrum	$\overline{g}$	$u(\overline{g})$
Mora	0.0029	0.04 %
LMRI	0.0029	0.04 %
2 lines	0.0031	0.03 %

Table 2: Results obtained from the EGSnrc user code 'g'

The correction for radiative losses in air was also calculated using the spectrum obtained by [3] and the ^{60}Co spectrum represented by the two photon lines of 1173.2 keV and 1332.5

keV with equal emission probability. The results are presented in Table 2 and show that the *g*-value given for the two-lines spectrum is 0.0031 whereas for the spectrum of Mora the value is similar to ours: 0.0029.

5.2. Stopping power ratio

Several authors calculated the graphite-to-air stopping power ratio, $S_{c,a}$, for air-kerma standards using different methods and code systems. Regardless the approach used for the calculation, they assume that the electron fluence is not disturbed by the cavity. The graphite-to-air stopping power ratio can be regarded as the ratio of absorbed doses in graphite and in air. For the calculation of those absorbed doses, the spectrum derived from the phase space files generated by the BEAMnrc user code was used as the source file in the CAVITY user code. We ran a simulation for the cavity chamber with the real materials, i.e., graphite wall and air cavity, and another simulation for the cavity chamber filled with air equivalent graphite, i.e., graphite with the same density as air.

The calculation type was set to 'Fano', so that scattered photons are thrown away and the photon attenuation is removed by unweighting and generating a uniform source of electrons throughout the geometry. The simulation was run for 1×10^9 particles.

The Fano theorem states that, for a uniform field of photon beams, the field of secondary radiation is also uniform and independent of density variations throughout the medium and hence it allows to determine the electron fluence in the cavity of a chamber which materials are matched in atomic composition. This means that, under Fano conditions, CPE holds and the dose to a cavity filled with low density wall material (graphite with the density of air) equals the collision kerma in the wall when attenuation and scatter are switched off and the cavity gas has the same dosimetric properties as the wall. The graphite to air stopping power ratio can be written as:

$$s_{c,a} = \frac{D^{Fano}_{cavity,graphite}}{D^{Fano}_{cavity,real}}$$

where $D^{Fano}_{cavity,\ graphite}$ is the dose to the cavity of a graphite equivalent chamber where incident photons that interact in the chamber wall are not attenuated and the scattered photons are discarded. The approach we used to calculate the stopping power ratio is similar to that used by Burns using PENELOPE [8] or by the NPL for the calculation of the stopping power ratio for the air-kerma primary standard for high dose rate ^{192}Ir brachytherapy sources [9] using EGSnrc.

The graphite to air stopping power ratio obtained using the above mentioned method was $S_{c,a}$=1.0014. The type A uncertainty obtained for the stopping power ratio using EGSnrc was 0.1%. The type B uncertainty is taken as that recommended for the product $S_{c,a}W_{air}$, which is 0.11%.

5.3. Correction factors

5.3.1. The wall correction factor

As mentioned before, corrections for wall effects, k_{wall} , are a central subject in the current state of the art of the air-kerma cavity standards. Before 2000, k_{wall} was determined experimentally, by linearly extrapolating the measured results to zero wall thickness. After the limitations of the extrapolation methods were demonstrated and the results for wall correction factors using different MC codes were validated, most of the primary standards laboratories re-evaluated the k_{wall} for their standards**.**

k_{wall} is introduced to take into account the attenuation and scatter in the cavity wall and therefore it is calculated as:

$$A_{wall} = \frac{D_{air}(no\ attenuation,\ no\ scatter)}{D_{air}(attenuation,\ scatter)}$$

where $A_{wall} =,1/k_{wall}$ as defined for the user codes in the EGSnrc system.

The calculations were made using the spectrum derived from the phase space model of the Eldorado 6 ^{60}Co source as the source input for the EGSnrc user code CAVITY. As a scoring option, we selected the calculation type = Awall, which calculates the A_{wall} correction factor in addition to the dose calculation. It gives the ratio of the dose to the cavity accounting for wall scattering and attenuation to the dose obtained when scattered photons are thrown away and the photon attenuation is removed.

The wall correction factor obtained was given as k_{wall}=1.019. The uncertainty of k_{wall} was taken as the type A uncertainty calculated in the MC simulations. The user code was run for 1×10^8 histories, using the photon splitting and the Russian roulette variance reduction techniques. The uncertainty obtained for this number of particles was 0.002%. The results obtained by the CAVITY user code were validated against the code developed at the LNHB for the calculation of the wall correction factor [10], using the same source, geometry and materials as CAVITY. Using this approach, the k_{wall} obtained was 1.019, the same value obtained using CAVITY, with an uncertainty at the k=1 level of 0.0441% for 1×10^8 initial particles.

5.3.2. Correction for axial non-uniformity

The correction for axial non-uniformity, k_{an}, was introduced by Boutillon and Niatel [11] to correct for the axial beam non-uniformity. Disregarding attenuation and scattering, the radiation intensity varies according to the inverse square law. Given that a cavity chamber has a finite volume and is centred at the reference point where the air-kerma rate is to be determined, its response will depend on this distance variation.

k_{an} may be obtained using Monte Carlo simulations. A simple approach which agrees with the analytical theory [12] consists on the ratio of the chamber response per unit primary photon fluence, in the absence of photon attenuation and scattering, for a broad parallel beam to that for a point source (a valid approximation for source sizes much smaller than the measurement distance).

The correction factor can hence be expressed as:

$$k_{an} = \frac{D_{air}(no\ attenuation,\ no\ scatter)^{parallel}}{D_{air}(no\ attenuation,\ no\ scatter)^{divergent}}$$

which represents the relation between the dose contributions due to divergent photons crossing the reference plane at a given point and the corresponding contributions due to parallel photons crossing that point. The ratio of the MC simulations gives a correction factor of k_{an}=1.0002. Both simulations were run for 1×10^9 particles, with an uncertainty of 0.17%. However, it is worth mentioning that the dose gradient on the beam axis can be regarded as linear for small dimension detectors, and in that case, the axial non-uniformity correction factor is equal to unity. The LNHB adopted this approximation that we also follow, so in this case, we assumed that there was no correction for the axial non-uniformity and that there was no uncertainty associated.

5.3.3. Stem and central electrode

The perturbation in the measurements due to the presence of the central electrode is taken into account by the correction factor k_{cel} . Given that the wall and the central electrode are made of the same material, we consider $k_{cel}=1$, according to the methodology adopted by LNHB. A verification was made using EGSnrc. Two simulations were run: one considering the graphite wall and central electrode and another considering only the graphite wall, **Figures 4c** and **4d**. The result obtained for the central electrode correction factor was $k_{cel}=0.9998$, which corresponds to the ratio of the results of the two simulations. We took the option of considering it equal to unity.

The stem correction factor can also be calculated using MC codes running two simulations, one that included the stem and the other that only included the cavity walls, **Figure 4.e**. The radiation field used was that from the LMRI Eldorado 6 simulated using BEAMnrc.

K_{stem} is given by the ratio of the results obtained in the two simulations. The value obtained using MC was compared to the average of the measured values and the results were found to be the same, 0.9993, which was the value we used for this correction factor.

6. Conclusions

The values obtained using MC methods were compared to those calculated for the cavity chambers of LMRI and LNHB. The calculated value for g_{air} is below the value for the graphite chambers of the LMRI (0.0032) and of the LNHB (0.0031). This value, however, is consistent with the value of g_{air} calculated by Burns using PENELOPE, as well as with the result obtained for the graphite cavity standard of ARPANSA, obtained using "g". The same is verified for g_c .

Referring to the results for the mean mass-energy absorption coefficient ratio, the value obtained in our study is 0.9983, while for LMRI the value for $(\mu_{en}/\rho)_{a,c}$ was 0.9985 and for the LNHB it was 0.9988, which represents a difference of 0.02% in the first case and 0.05% in the second. As for the stopping power ratio, $S_{c,a}$, we obtained a value of 1.0014, against 1.0010 obtained for LMRI and 1.0020 for LNHB. These values and their uncertainties, obtained using MC calculations, can be regarded as satisfactory since they are consistent with those expected for primary standards.

The value for k_{wall} was validated against a different method and k_{an} was close to unity, as expected. However, a different MC code should be used for the same calculations, for the sake of robustness of the results.

References

[1] D. W. O. Rogers, Fifty years of monte carlo simulations for medical physics, Physics in Medicine and Biology 51 (2006) R287–R301

[2] D. Rogers, B. Walters, I. Kawrakow, BEAMnrc User's Manual, NRCC Report PIRS-0509(A) revL, NRC, Ottawa, Canada (2013)

[3] G. M. Mora, A. Maio, D. W. O. Rogers, Monte carlo simulation of a typical 60co therapy source, Medical Physics 26 (11) (1999) 2494–2502

[4] B. Muir, G.Xiong, T. P. Selvam, D.W. O. Rogers, 60co phase-space files generated using beamnrc, Tech. Rep. CLRP-Report CLRP-09-01, Physics Department, Carleton University, Ottawa (2009)

[5] Phase-space Database for External Beam Radiotherapy, https://www-nds.iaea.org/phsp/phsp.htmlx

[6] M. Boutillon, g Values from Berger and Seltzer Tables (1982), Comité Consultatif pour les Étalons de Mesure des Rayonnements Ionisants (CCEMRI) Section I/85-18, Bureau International des Poids et Mesures (BIPM), Sèvres

[7] J. Borg, I. Kawrakow, D.W. O. Rogers, J. P. Seuntjens, Monte Carlo Study of Correction Factors for Spencer-Attix Cavity Theory at Photon Energies at or Above 100 keV, Medical Physics 27 (8) (2000) 1804.1813

[8] D. T. Burns, A New Approach to the Determination of Air Kerma Using Primary- Standard Cavity Ionization Chambers, Physics in Medicine and Biology 51 (4) (2006) 929

[9] T. Sander, R. F. Nutbrown, The NPL Air Kerma Primary Standard TH100C for High Dose Rate 192Ir Brachytherapy Source, DQL-RD 004, National Physics Laboratory, NPL (2006)

[10] J. Gouriou, Modélisation à l'aide du Code de Monte Carlo EGSnrc du Facteur de Correction de Perturbation Lie a la Presence de la Paroi en Graphite d'Une Chambre a Ionisation Placée Dans un Faisceau de Cobalt-60, NT LNHB 04/001A, LNHB (2004)

[11] M. Boutillon, M. T. Niatel, A Study of a Graphite Cavity Chamber for Absolute Exposure Measurements of 60Co Gamma Rays, Metrologia 9 (4) (1973) 139

[12] A. F. Bielajew, An Analytic Theory of the Point-Source Nonuniformity Correction Factor for Thick-Walled Ionisation Chambers in Photon Beams, Physics in Medicine and Biology 35 (4) (1990) 517

The Cavity chamber at BEV

Andreas Steurer, Wilhelm Tiefenböck

The paper presents the technical description of the Primary Standards for high energy photon based on cavity chamber including the identification and determination of correction factors.

1 Primary Standards – Air kerma Co-60: 1cm^3 Cavity chamber CC01-125 and CC01-232

1.1 Principle

The air kerma rate under reference conditions for an ideal cavity ionisation chamber is determined by

$$\dot{K}_\mathrm{a} = \frac{I}{\rho_a \cdot V} \cdot \left(\frac{W}{e}\right) \cdot \frac{1}{1-g_\mathrm{a}} \cdot \left(\frac{\bar{\mu}_\mathrm{en}}{\rho}\right)_\mathrm{a,c} \cdot S_\mathrm{c,a} \tag{1}$$

with

$$\left(\frac{\bar{\mu}_\mathrm{en}}{\rho}\right)_\mathrm{a,c} = \frac{\left(\frac{\bar{\mu}_\mathrm{en}}{\rho}\right)_\mathrm{a}}{\left(\frac{\bar{\mu}_\mathrm{en}}{\rho}\right)_\mathrm{c}} \tag{2}$$

and

$$S_\mathrm{c,a} = \frac{S_\mathrm{C}}{S_\mathrm{a}} = \frac{\left(\frac{\bar{S}}{\rho}\right)_c}{\left(\frac{\bar{S}}{\rho}\right)_a} \tag{3}$$

Meaning of the symbols:

I	ionisation current
ρ_a	air density under reference conditions (T_0 = 293,15 K and p_0 = 101,325 kPa)
V	volume of the ionisation camber cavity
$\left(\frac{W}{e}\right)$	ionisation constant for dry air
g_a	fraction of energy lost by bremsstrahlung in air
$\left(\frac{\bar{\mu}_\mathrm{en}}{\rho}\right)_\mathrm{a,c}$	ratio of the mean mass energy absorption coefficients of air and graphite
$\left(\frac{\bar{\mu}_\mathrm{en}}{\rho}\right)_\mathrm{a}$	mean mass energy absorption coefficient of air
$\left(\frac{\bar{\mu}_\mathrm{en}}{\rho}\right)_\mathrm{c}$	mean mass energy absorption coefficient of graphite
$S_\mathrm{c,a}$	ratio of the mean stopping powers of graphite and air
S_c	mean stopping power of graphite
S_a	mean stopping power of air

Using correction factors the air kerma rate real for a real cavity ionisation chamber is determined by

$$\dot{K}_a = \left(I_+ \cdot k_{pT}\right) \cdot \left(\frac{k_{\mathrm{pol}}}{\rho_a \cdot V}\right) \cdot \left(\frac{W}{e}\right) \cdot \frac{1}{1-g_{\mathrm{a}}} \cdot \left(\frac{\bar{\mu}_{\mathrm{en}}}{\rho}\right)_{\mathrm{a,c}} \cdot s_{\mathrm{c,a}} \cdot \prod_i k_i \tag{22}$$

with

$$\rho = \frac{\rho_{\mathrm{a}}}{k_{pT}} \tag{5}$$

$$k_{pT} = k_p \cdot k_T = \frac{p_0}{p} \cdot \frac{T}{T_0} \tag{6}$$

and:

$$k_{\mathrm{pol}} = \frac{I_+ + I_-}{2 \cdot I_+} \tag{7}$$

Meaning of the symbols:

I_+	ionisation chamber current at positive polarising voltage
I_-	ionisation current chamber at negative polarising voltage
k_{pol}	correction factor for polarity of the ionisation chamber voltage
k_{pT}	correction factor to correct the deviation from reference conditions for air density
k_p	correction factor to correct the deviation from reference air pressure (p_0 = 101,325 kPa)
k_T	correction factor to correct the deviation from reference air temperature (T_0 = 293,15 °K)
p	real (measured) air pressure
T	real (measured) air temperature
ρ	real air density

The product of the additional correction factors is:

$$\prod_i k_i = k_{\mathrm{s}} \cdot k_{\mathrm{h}} \cdot k_{\mathrm{st}} \cdot \left(k_{\mathrm{at}} \cdot k_{\mathrm{sc}}\right) \cdot k_{\mathrm{an}} \cdot k_{\mathrm{m}} \tag{8}$$

Meaning of the symbols:

k_{s}	correction factor for recombination losses
k_{h}	correction factor for humidty
k_{st}	correction factor for stem scattering
$\left(k_{\mathrm{at}} \cdot k_{\mathrm{sc}}\right)$	correction factor for wall attenuation and wall scattering
k_{an}	correction factor for axiale non-uniformity
k_{m}	correction factor for radial non-uniformity

1.1.1 Description of the standards type CC01

The primary standards of the BEV to measure air kerma for ^{60}Co gamma radiation and ^{137}Cs gamma radiation are two cylindrical graphite cavity ionisation chambers type CC01-serial numbers 125 and 132 (figure 1 and table 1).

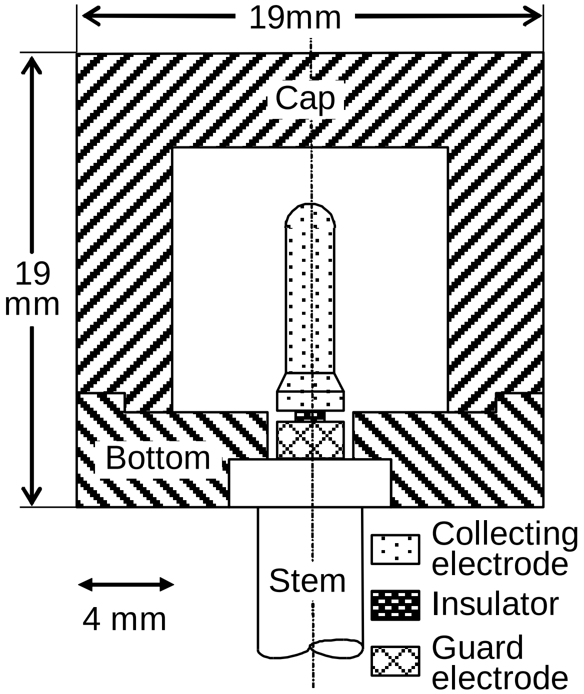

Figure 1 Cross section of ionisation chamber CC01

Parameter	Ionisation chamber	
	CC01-125	CC01-135
Material ionisation chamber	graphite	
Height cylinder	19 mm	
Outer diameter graphite cylinder	19 mm	
Wall thickness chamber	4 mm	
Diameter chamber	11 mm	
Material collecting electrode	Graphit	
Diameter collecting electrode	2 mm	
Nominelle cavity volume	1,0 cm^3	
Graphitdensity, ρ_c	1,72 $g \cdot cm^{-3}$	1,80 $g \cdot cm^{-3}$
Manufacturer of graphite	Ringsdorff	Union Carbide
Material graphite	Ultrapur Graphite EK51	High Purity Moulded Graphite ATJ
Impurity graphite	< 1,5 · 10^{-4}	< 8,0 · 10^{-4}
Real cavity volume, *V*	1,018 7 cm^3	1,017 1 cm^3
Insulator	PTFE Teflon	
Applied Voltage	+ 250 V	
Reference point	Chamber center	

Table 1 Data Ionisation Cavity Chambers CC01-125 and CC01-132

1.1.2 Measuring Conditions

The Reference Conditions for measuring Air Kerma for Co-60 are given in Table 2.

Parameter	Data
Distance source – reference point detector (*SDD*)	1000 mm
Field size	10 cm x 10 cm at *SDD*

Table 2 Reference Condition for measuring Air Kerma for Co-60

1.1.3 Input Data to calculate the Calibration Coefficient

symbol	value	$u_{i,\mathrm{A}}$	$u_{i,\mathrm{B}}$
ρ_a	$1{,}204\,5\ \frac{\mathrm{kg}}{\mathrm{m}^3}$	-	0,01 %
$\left(\frac{W}{e}\right)$	$33{,}97\ \frac{\mathrm{J}}{\mathrm{C}}$	-	0,15 %
g_a for Co-60	0,003 2	-	0,02 %
$\left(\frac{\mu_\mathrm{en}}{\rho}\right)_\mathrm{a,c}$ for Co-60	0,998 5	-	0,05 %
$S_\mathrm{c,a}$ for Co-60	1,001 0	-	0,30 %

Table 3 Physical constants and energy depend data for Co-60

The formula to calculate k_S is:

$$k_\mathrm{S} = 1 + k_\mathrm{init} + k_\mathrm{vol} \cdot |I| \tag{9}$$

Meaning of the symbols:

k_init........................ component of initial recombination to k_s

k_vol........................ component of volume recombination to k_s

I .... actual ionisation current

symbol		Value for Co-60		$u_{i,\mathrm{A}}$	$u_{i,\mathrm{B}}$
		CC01-125	CC01-132		
k_pol		0,999 40	0,999 55	0,02 %	-
k_s	k_init	$2{,}033\,4 \cdot 10^{-3}$	$1{,}788\,4 \cdot 10^{-3}$	0,02 %	0,02 %
	k_vol	$9{,}432\,0 \cdot 10^{5}\ \mathrm{A}^{-1}$	$1{,}045\,1 \cdot 10^{6}\ \mathrm{A}^{-1}$		
k_h		0,997 0	0,997 0	-	0,03 %
k_st		0,999 5	0,999 5	0,02 %	0,02 %
$(k_\mathrm{at} \cdot k_\mathrm{sc})$		1,020 8	1,021 8	0,02 %	0,10 %
k_an		1,000 0	1,000 0	-	0,10 %
k_m		1,000 0	1,000 0	-	0,02 %

Table 4 Correction factors CC01 for Co-60 (Air Kerma)

1.2 Calculation of the Calibration Coefficient

The Calibration Coefficient of the Ionization Chamber in terms of Air Kerma is defined by:

$$N_{K_\mathrm{a}} = \frac{K_\mathrm{a}}{Q} = \frac{\dot{K}_\mathrm{a}}{I} \tag{10}$$

Meaning of the symbols

N_{K_a} .... Calibration Coefficient

K_a, $\dot{K}_\mathrm{a}$ .... Air Kerma respectively Air Kerma Rate

Q, I....................... Loading respectively Current of the Ionization Chamber generated by the irradiation

The Calibration Coefficients of both Ionization Chambers for Co-60 are given in Table 5:

Ionization chamber	N_{K_a} for ^{60}Co
CC01-125	2,828 2 · 10^7 Gy/C
CC01-132	2,835 2 · 10^7 Gy/C

Table 5 Calibration Coefficients for Air Kerma of the BEV Primary Standards for Co-60

Calculating the uncertainty of N_{K_a} one obtains:

symbol	$u_{i,\mathrm{A}}$	$u_{i,\mathrm{B}}$	$u_{i,\mathrm{A}}^2$	$u_{i,\mathrm{B}}^2$
ρ_a	-	0,01 %	-	0,000 1 %^{2}
V	-	0,12 %	-	0,014 4 %^{2}
W/e	-	0,15 %	-	0,022 5 %^{2}
g_a	-	0,02 %	-	0,000 4 %^{2}
$(\mu_\mathrm{en}/\rho)_\mathrm{a,c}$	-	0,05 %	-	0,002 5 %^{2}
$S_\mathrm{c,a}$	-	0,30 %	-	0,090 0 %^{2}
k_pol	0,02 %	-	0,000 4 %^{2}	-
k_s	0,02 %	0,02 %	0,000 4 %^{2}	0,000 4 %^{2}
k_h	-	0,03 %	-	0,000 9 %^{2}
k_st	0,02 %	0,02 %	0,000 4 %^{2}	0,000 4 %^{2}
$(k_\mathrm{at} \cdot k_\mathrm{sc})$	0,02 %	0,10 %	0,000 4 %^{2}	0,010 0 %^{2}
k_an	-	0,10 %	-	0,010 0 %^{2}
k_m	-	0,02 %	-	0,000 4 %^{2}
			$\sum_i u_{i,\mathrm{A}}^2$	$\sum_i u_{i,\mathrm{B}}^2$
			0,001 6 %^{2}	0,152 0 %^{2}
			$U_{N_\mathrm{K}} = \sqrt{\sum_i u_{i,\mathrm{A}}^2 + u_{i,\mathrm{B}}^2} \quad (k=1)$	
			0,39 %	

Table 6 Uncertainty of Calibration Coefficients BEV Primary Standards for Co-60 for Air Kerma

BEV relating Literature

- C. Kessler, P.J. Allisy-Roberts, A. Steurer, W. Tiefenböck, F. Gabris "Comparison of the standards for air kerma of the BEV and the BIPM for ^{60}Co gamma radiation", BIPM.RI(I)_K1_Report, Paris, 2010-01-11.
- C. Kessler, P.J. Allisy-Roberts, A. Steurer, W. Tiefenböck, F. Gabris "Comparison of the standards for air kerma of the BEV and the BIPM for ^{137}Cs gamma radiation", BIPM.RI(I)_K5_Report, Paris, 2010-01-14, Metrologia 47 (2010) p.06007
- PhD Thesis "Primary Standard Dosimetry of High Energy Photon- and Electron Radiation", by DI Andreas Baumgartner, May 2010 (Technical University Wien, Faculty for Physics)

Calibration and Verification at BEV

Andreas Steurer, Wilhelm Tiefenböck

1 Verification (“Eichung”) and Calibration

The BEV – Bundesamt für Eich- und Vermessungswesen (Federal Office of Metrology and Surveying) is the National Metrology Institute (NMI) and National Authority on Legal Metrology in Austria. The dosimetry laboratory of the BEV is a Primary Standard Laboratory for the Dose Quantities Air Kerma (Co-60, Cs-137, several X-Ray-Qualities between 10 kV and 300 kV) and Absorbed Dose to Water (Co-60).

Calibration is well defined in a lot of documents as a comparison of a measuring instrument to be calibrated with a standard (e.g. Primary Standard or Secondary Standard) to ensure the traceability of the measurements done with this measuring instrument.

The result may be a calibration coefficient or a calibration factor or an additive calibration term. From the calibration certificate the user can take the deviation of his measuring instrument from the true value under consideration of a given measurement uncertainty.

Generally a calibration is voluntarily. But in many cases it is mandatory according to the quality management system of to accreditation needs. The calibration is only valid at the time of calibration. The user of the measurement instrument is responsible to apply reasonable re-calibration period.

In Austria verification ("Eichung") is mandatory for measurement instruments, depending on their application as prescribed by the "Maß- und Eichgesetz". A type approval by the BEV of these measuring instruments is required. After a positive type test the measurement instrument – that means, that the measuring instrument complies with the relevant requirements – may be marked by the manufacturer for Verification. With this marking the manufacturer confirms that the measurement instrument is identical in construction to the measurement instrument that was tested in the type approval procedure.

The Verification is carried out by the legal metrology authority (BEV) or authorized verification bodies (authorized by the BEV). The result of the verification is, that the display of the measurement instrument is within defined limits (e.g. interval within ± 5 % of the true value under consideration of a given measurement uncertainty). The verification is valid for the period specified defined by the "Maß- und Eichgesetz" (e.g. 2 years). Then the for subsequent verification is necessary.

According to the "Maß- und Eichgesetz" a Verification is mandatory for measurement instruments (general and in particular – as applicable – also for dosimeters)

- used by authorities an for acts of legal significance
- used in health and environment
- used in safety and traffic

Verification is mandatory for these types of dosimeter

- Therapy Dosimeter for photons and electrons (verification with Co-60, medical physicists are using applicable k_Q-values for his accelerator radiation qualities),
- Diagnostic Dosimeter used for acceptance tests and/or constancy test of diagnostic X-ray facilities,
- Radiation protection Dosimeter for photons (active and passive dosimeter, area dosimeter and personal dosimeter),
- Photon Dosimeter used for individual monitoring.

The type approvals is necessary for Radiation Protection Dosimeter and Dosimeter used for acceptance tests and constancy test in diagnostic radiology. Before the first use a verification is necessary. The Verification period is 2 years.

A special case the procedure for Therapy Dosimeter. These are medical devices with the CE-sign plus for-digit number. No type approval and no verification before the first use are necessary because the type approval and the marketing are replaced by notified body approval. Therefore the first Verification has be done after 2 years. The Verification period is also 2 years.

For a laboratory which is using passive personal dosimeter for individual monitoring the Verification is covered by an authorization of the BEV. The Verification laboratory is kept under surveillance by the BEV (irradiation of TLDs by the BEV, examination by the laboratory, analysis by the BEV).

In Austria the Verification is a sufficient evidence for the traceability. The user of the measuring instrument knows that the display is within defined limits. Nevertheless some user with special accuracy demands additionally are ordering a calibration, especially medical physicists for the calibration of the accelerators.

2 Dosimetry Laboratory

The Dosimetry Laboratory of the BEV is located on the area of Research Center Seibersdorf, ca. 30 km south-east of Vienna. The facilities of the laboratory are 50 % shared with the Secondary Standard and Verification Dosimetry Laboratory of the Seibersdorf Laboratories GmbH.

The radiation facilities of the Dosimetry Laboratory are situated in two irradiation rooms (Figure 1):

- Therapy Level Bunker
- Protection Level Hall

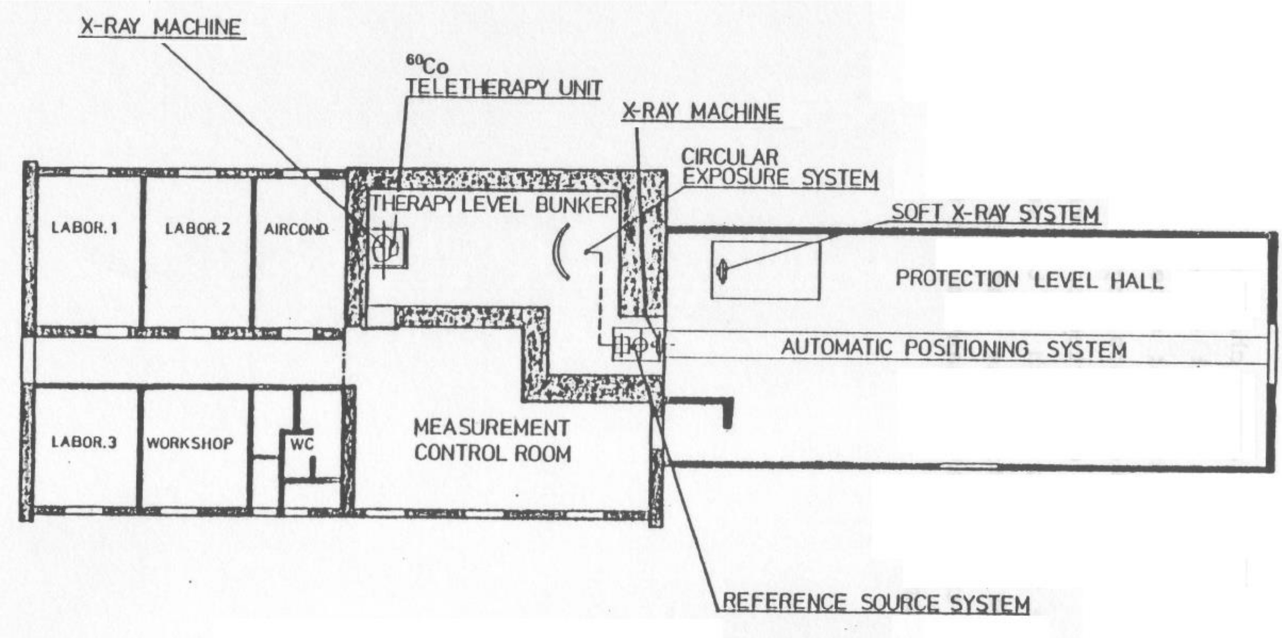

Figure 1 Schematic ground plan of the BEV Dosimetry Laboratory

The irradiation facilities in these rooms are given in Table 1.

Irradiation facility	Intended use	Irraditation room
Co-60 therapy unit Picker	Air Kerma and Absorbed Dose to Water for therapy Co-60 Air Kerma and Radiation Protection Quantities for Co-60 (high doserate)	Therapy Level Bunker
160 kV X-ray generator with 3 tubes (W-Anode, Mo-Anode, Rh-Anode)	Air Kerma for diagnostic qualities (including Mammography)	Therapy Level Bunker
Circlular radiation unit with 4 different sources	Air Kerma and Radiation Protection Quantities for Cs-137	Therapy Level Bunker
Reference radiation unit with 6 different sources	Air kerma and Radiation Protection Quantities for Cs-137 and Co-60	Protection Level Hall
320 kV X-ray generator with W-anode	Air Kerma for medium energy therapy and diagnostic qualities Air Kerma and Radiation Protection Quantities for radiation protection qualities	Protection Level Hall
60 kV X-ray generator with W-Anode and different filter wheels	Air Kerma for low energy therapy and diagnostic qualities Air Kerma and Radiation Protection Quantities for low energy radiation protection qualities	Protection Level Hall

Table 1 Irradiation facilities of the BEV Dosimetry Laboratory

The Primary Standards of the BEV Dosimetry Laboratory are given in Table 2. A detailed description of these Primary Standards are given in this proceeding.

Primary Standard		Intended use
Graphite Calorimeter		Absorbed dose to water Co-60 (Therapy)
1 cm^3 Cavity Ionization Chambers CC01-125 and CC01-132		Air kerma Co-60 (Therapy) and Cs-137 (Therapy, Radiation Protection)
Free Air Ionization Chambers	PKK	Free Air Ionization Chambers of different sizes, related to the different X-Ray sources with different maximum high voltage, Air Kerma (Therapy, Diagnostic, Radiation Protection)
	PKM	
	PKG	

Table 2 Primary Standards of the BEV Dosimetry Laboratory

2.1 Description of the BEV X-ray facilities

The X-ray facilities of the Dosimetry-Laboratory of the BEV are listed in Table 3.

Designation	Manufacturer	Type	High voltage range	X-ray tube(s)	Anode	Anode-angle	Inherent filtration
Low energy X-ray facility	Seifert	Isovolt 3003	1 kV - 60 kV	Machlett OEG 60	W	45 °	1,5 mm Be
Medium energy X-ray facility	Philips	MG 320	14 kV - 320 kV	Philips MCN 321	W	40 °	2,5 mm Be
Diagnostic X-ray facility	Seifert	Isovolt HS 160	5 kV - 160 kV	Isovolt 160 M2/0.4-3.0 / MXR-161	W	20 °	1,0 mm Be
			5 kV - 100 kV	Panalytic PW-2185/00	Mo	20 °	1,0 mm Be
				Panalytic PW-2182/00	Rh	20 °	1,0 mm Be

Table 3 Characteristics of the BEV X-ray facilities

2.1.1 Low energy X-ray facility Seifert Isovolt 3003

2.1.1.1 Provided radiation qualities

The low energy X-ray facility Seifert Isovolt 3003 is used to measure the Air kerma for:

- low energy therapy radiation qualities between 10 kV and 50 kV (TW10, TW25, TW30, TW50, SH50)
- mammography radiation qualities with W-Anode and 60 µm Mo-filter (WMH-Serie) respectively 60 µm Mo / 2 mm Al-filter between 23 kV and 50 kV (WMH-Serie)
- mammography radiation qualities with W-Anode and 40 µm Pd-filter respectively 40 µm Pd / 2 mm Al-filter at 30 kV (WPV30 and WPH30)
- mammography radiation qualities with W-Anode and 50 µm Rh-filter respectively 50 µm Rh / 2 mm Al-filter at 30 kV (WRV30 and WRH30)
- radiation protection qualities N-Series according to ISO 4037-1 between 10 kV and 40 kV (N10 – N40)
- radiation protection qualities H-Series according to ISO 4037-1 between 10 kV and 30 kV (H10 – H30)

2.1.1.2 Setup for measurements

The measurement setup is given in Figure 2.

The main geometric conditions are:

- Focus Detector Distance (*FFD*): 600 mm
- Field size in *FFD*: 10 cm (diameter)

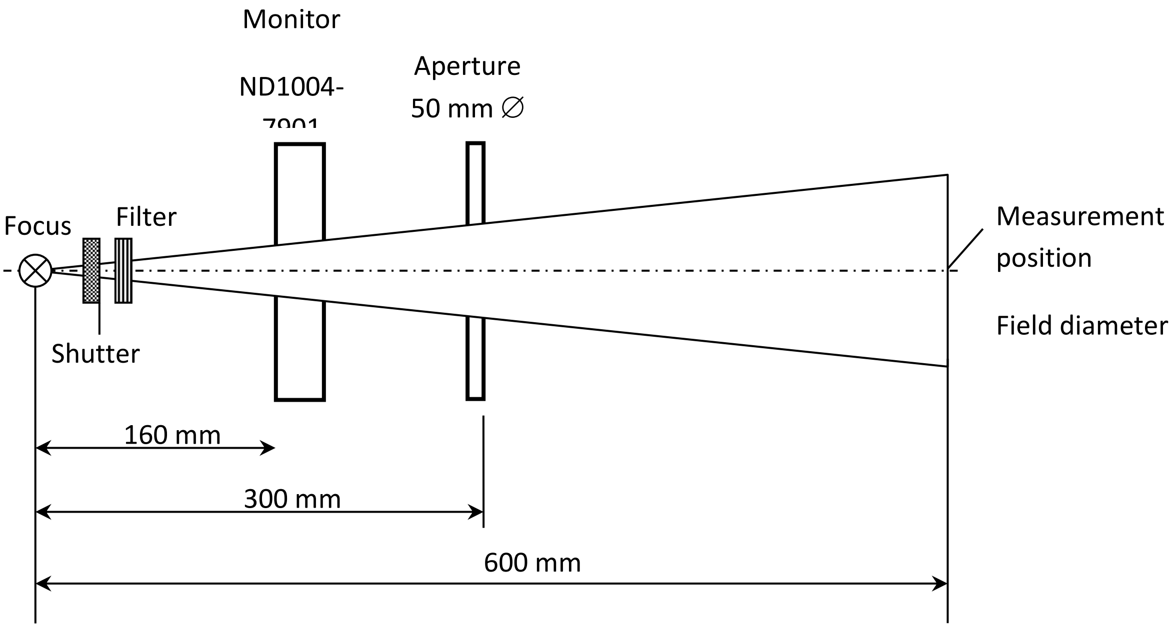

Figure 2 Measurement setup low energy X-ray facility Seifert Isovolt 3003 (schematic)

2.1.2 Medium energy X-ray facility Philips MG 320

2.1.2.1 Provided radiation qualities

The medium energy X-ray facility Philips MG 320 is used to measure the Air kerma for:

- medium energy therapy radiation qualities between 20 kV and 300 kV (TW25, TW30, TW50, SH50, TH70, TH100, TH135, TH 180, TH 250, TH300)
- diagnostic radiation qualities according to IEC 61267 between 30 kV and 150 kV (RQR2 – RQR10, RQR2 – RQR10, RQT8 – RQT10, RQC3, RQC5, RQC8)
- radiation protection qualities N-Series according to ISO 4037-1 between 15 kV and 300 kV (N15 – N300)
- radiation protection qualities W-Series according to ISO 4037-1 between 40 kV and 300 kV (W40 – W300)
- radiation protection qualities H-Series according to ISO 4037-1 between 40 kV and 300 kV (H40 – H300)

2.1.2.2 Setup for measurements

The measurement setup is given in Figure 3.

The main geometric conditions are:

- Focus Detector Distance (*FFD*): 800 mm, 1000 mm, 1350 mm
- Field size in *FFD*: 10 cm, 12 cm, 17 cm (diameter)

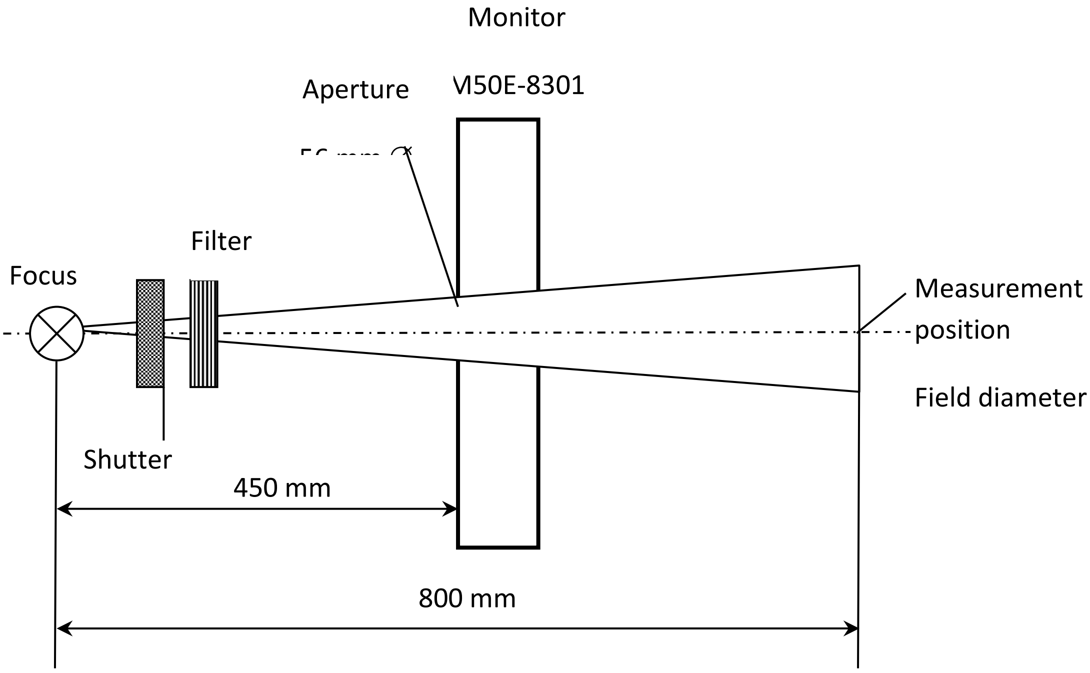

Figure 3 Measurement setup medium energy X-ray facility Philips MG 320 (schematic)

2.1.3 Diagnostic X-ray facility Seifert HS 160

2.1.3.1 Provided radiation qualities

The diagnostic X-ray facility Seifert HS 160 is used to measure the Air kerma for:

- diagnostic radiation qualities according to IEC 61267 between 30 kV and 150 kV (RQR2 – RQR10, RQR2 – RQR10, RQT8 – RQT10, RQC3, RQC5, RQC8)
- several mammograpy radiation qualities between 25 kV and 35 kV as described in Table 4
- dental qualities 8,5 mm Al respectively 8,5 mm Al + 0,5 mm Cu (40 kV, 50 kV, 60 kV, 70 kV, 80 kV, 90 kV, 100 kV)

radiation quality	anode	filter
RQR M1 – M4 (IEC 61267) = MMV25 – MMV35[1)] RQA M1 – M4 (IEC 61267) = MMH25 – MMH35[1)]	Mo	30 µm Mo 30 µm Mo + 2 mm Al
MRV25 – MRV35[1)] MRH25 – MRH35[1)]	Mo	25 µm Rh 25 µm Rh + 2 mm Al
MAV25 – MAV35[1)] MAH25 – MAH35[1)]	Mo	1 mm Al 3 mm Al
RRV25 – RRV35[1)] RRH25 – RRH35[1)]	Rh	25 µm Rh 25 µm Rh + 2 mm Al
RAV25 – RAV35[1)] RAH25 – RAH35[1)]	Rh	1 mm Al 3 mm Al
WMV25 – WMV35[1)] WMH25 – WMH35[1)]	W	60 µm Mo 60 µm Mo + 2 mm Al
WRV25 – WRV35[1)] WRH25 – WRH35[1)]	W	50 µm Rh 50 µm Rh + 2 mm Al
WAV25 – WAV35[1)] WAH25 – WAH35[1)]	W	0,5 mm Al 2,5 mm Al
WAVa25 – WAVa35[1)] WAHa25 – WAHa35[1)]	W	0,7 mm Al 2,7 mm Al
WPV25 – WPV35[1)] WPH25 – WPH35[1)]	W	40 µm Pd 40 µm Pd + 2 mm Al
WSV25 – WSV35[1)] WSH25 – WSH35[1)]	W	50 µm Ag 50 µm Ag + 2 mm Al
[1)] PTB-Code.		

Table 4 Mammography radiation qualities at diagnostic X-ray facility HS 160

2.1.3.2 Setup for key comparison measurements

The measurement setup is given in Figure 4.

The main geometric conditions are:

- Focus Detector Distance (*FFD*): 900 mm
- Field size in *FFD*: 15 cm (diameter)

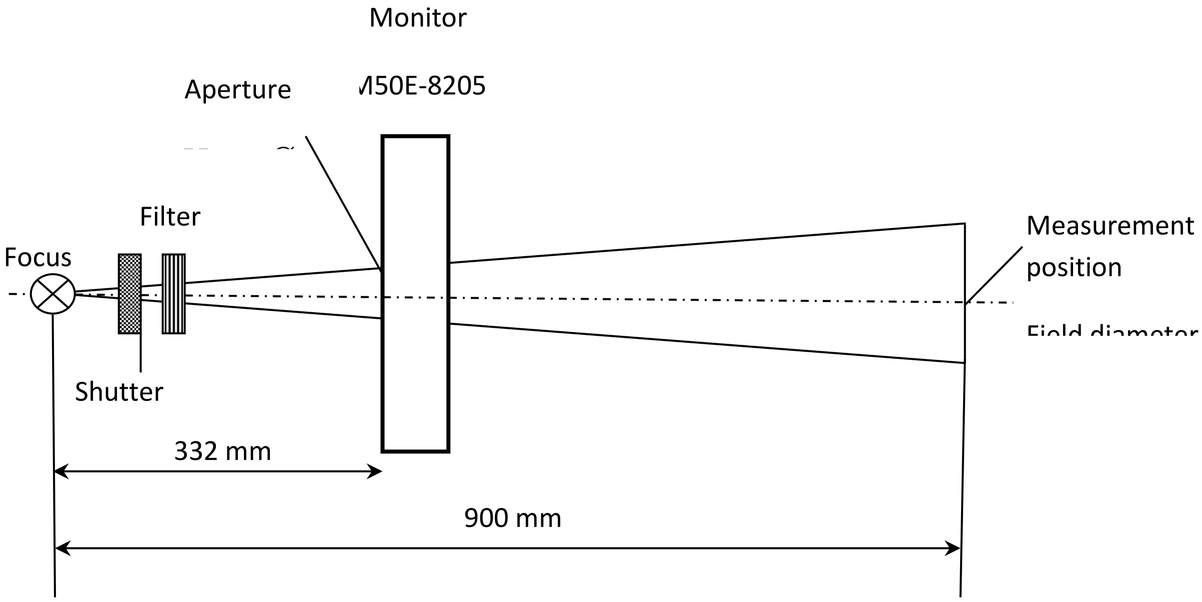

Figure 4 Measurement setup diagnostic X-ray facility Seifert HS 160 (schematic)

2.1.3.3 Spectra measurements

Spectra for the mammography qualities were measured recently wilt a Ge(Li)-detector. As the result of the measurements are raw data a unfolding procedure must be applied using a response matrix which was calculated for this detector with a Monte Carlo method.

The results for the radiation qualities MMV (RQR-M1 – M4) are given in Figure 5.

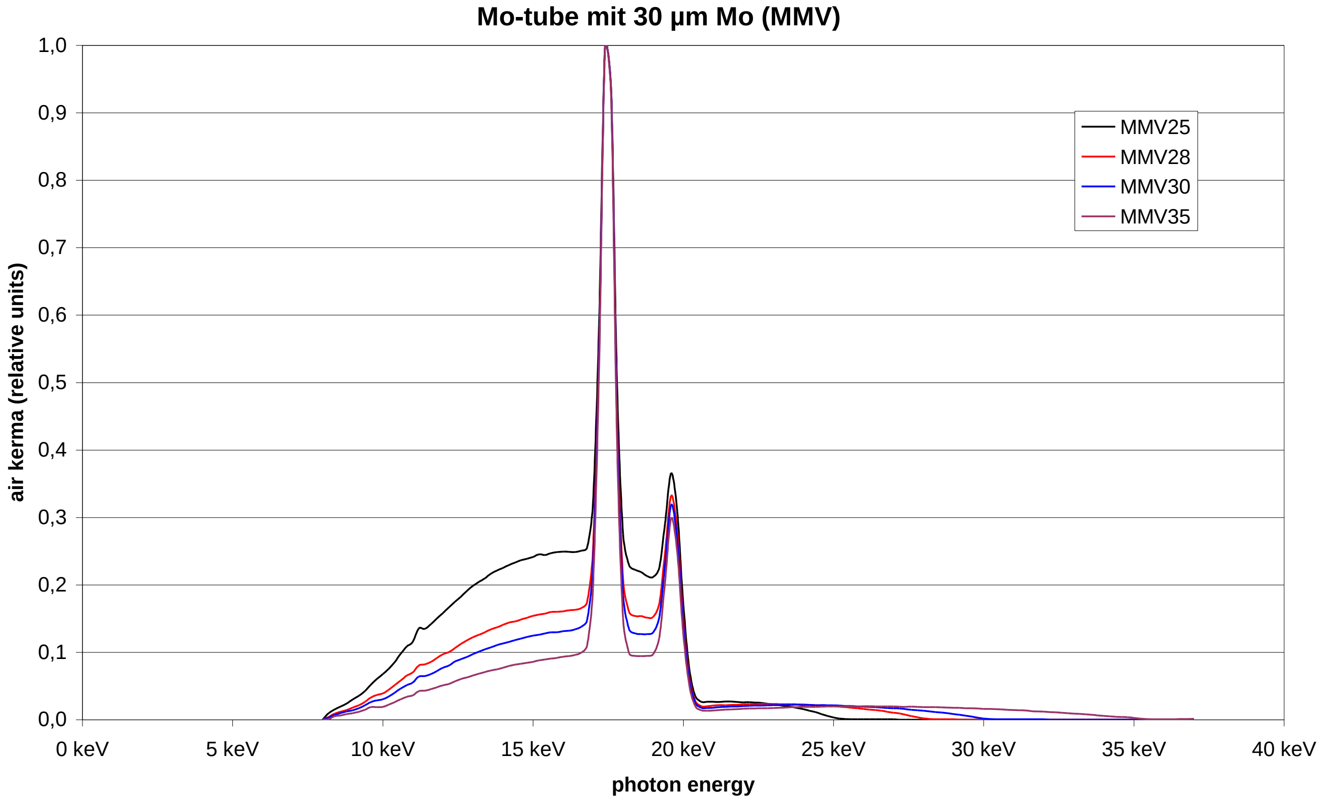

Figure 5 Spectra of the diagnostic X-ray facility Seifert HS 160 with Mo-tube and Mo-filter (radiation qualities MMV25 – MMV35)

The knowledge of the spectra is a precondition to calculate the energy depending data and correction factors to determine the Air Kerma with a Primary Standard.

Using mono energetic data the energy depending data and correction factors are calculated by integrating over the measured spectrum (as described for in section 1.1.2).

2.1.3.4 Half Value Layer measurements

To characterize a radiation quality the measurement of the Half Value Layer is necessary. The measurement setup is given in Figure 6.

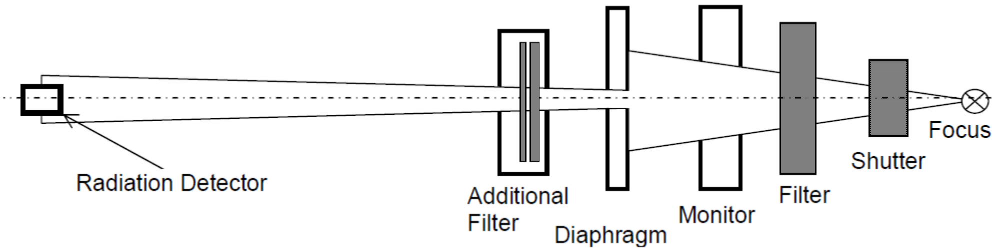

Figure 6 Setup for Half Value Layer measurements

First the ionization current without additional filter is measured. Then additional high pure Aluminium plates of different proper thicknesses are positioned in the beam to receive the Aluminium layer which causes the half value of ionization current using a least square fit.

$$S_x = a \cdot e^{b \cdot x} \qquad (1)$$

Meaning of the symbols:

S_x .... Attenuation ratio of the aluminiujm layer with thckness x in mm

a, b .... Parameter of the least square fit

x........................... thickness of the Aluminium layer

After calculation of the parameters a and b the Half Layer Value is calculated by setting:

$$S_x = 0{,}5 \qquad (2)$$

$$HVL = \frac{1}{b} \cdot \ln\left(\frac{0{,}5}{a}\right) \qquad (3)$$

Meaning of the symbol:

HVL .... Half Value Layer in mm

In Figure 7 one can see the calculation for the Mammography Quality MMV28 (RQR-M2).

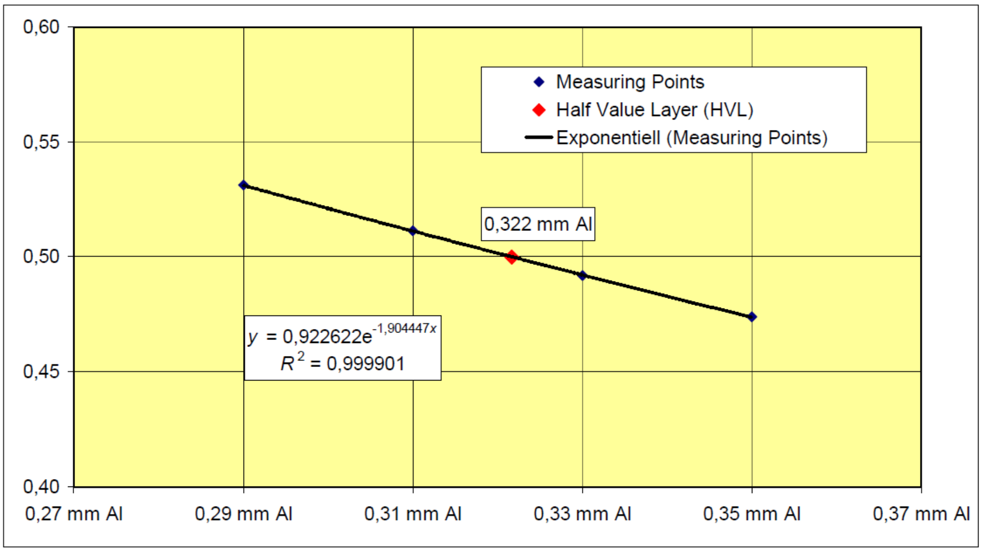

Figure 7 Calculation of the Half Value Layer for the Mammography Quality MMV28 (RQR-M2)

3 Calibration Procedure

A typical calibration setup is given in Figure 8. It shows schematically the geometry of a calibration of a Secondary Standard in an X-ray field in 2 steps.

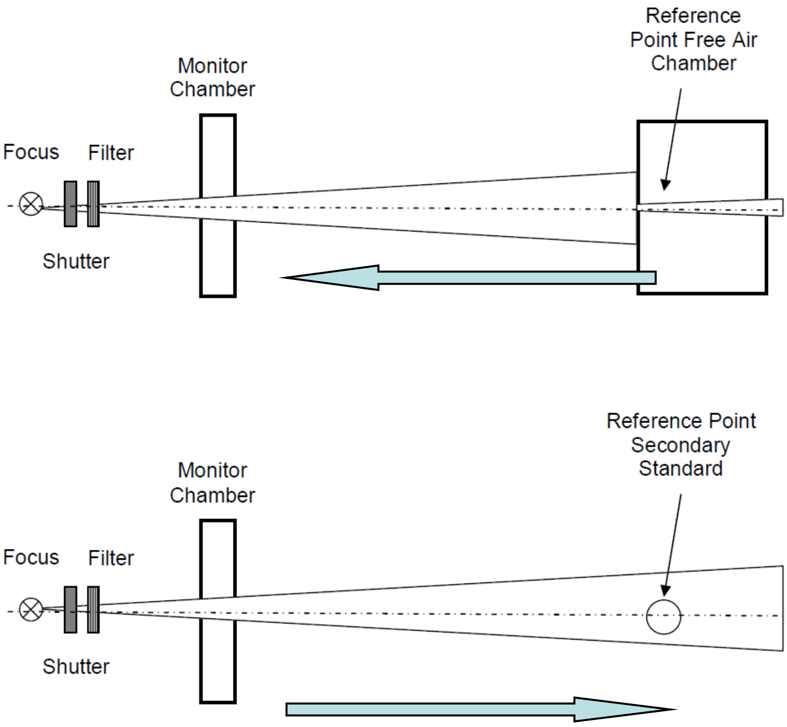

1st step

Calibration of the Monitor with the Primary Standard

2nd step

Calibration of the Secondary Standard with the Monitor

Figure 8 Calibration setup, calibration of a Secondary Standard in an X-ray field

1st step: Calibration of the Monitor Chamber with the Primary Standard

The primary standard is positioned in the radiation field with its reference point on the beam axis in the specified Focus-Detector-Distance (*FDD*). The air kerma rate is determined by the primary standard P.

$$\dot{K}_a = I_{\mathrm{P}} \cdot N_{\dot{K}_a,\mathrm{P}} \tag{4}$$

Meaning of the symbols:

$\dot{K}_a$ .... Air Kerma Rate

I_{P}.......................... Ionization Current Primary Standard (air density corrected)

$N_{\dot{K}_a,\mathrm{P}}$ .... Calibration Coefficient Primary Standard P (Gy/C)

The value of the air kerma rate is related to the ionization current of the Monitor Chamber M:

$$I_{\mathrm{M}} \cdot N_{\dot{K}_a,\mathrm{M}} \cdot \left(\frac{k_{\mathrm{a}}}{k_{a0}}\right)_{\mathrm{MP}} = \dot{K}_a \tag{5}$$

Meaning of the symbols:

I_{M} .... Ionization Current Monitor Chamber (air density corrected)

$\left(\frac{k_{\mathrm{a}}}{k_{a0}}\right)_{\mathrm{MP}}$ .... Correction of Air Attenuation between M and P to reference air density

The Calibration Coefficient of the Monitor Chamber M in Gy/C is calculated with:

$$N_{\dot{K}_a,\mathrm{M}} = \frac{I_{\mathrm{P}}}{I_{\mathrm{M}} \cdot \left(\frac{k_{\mathrm{a}}}{k_{a0}}\right)_{\mathrm{MP}}} \cdot N_{\dot{K}_a,\mathrm{P}} \tag{6}$$

Meaning of the symbol:

$N_{\dot{K}_a,\mathrm{M}}$ .... Calibration Coefficient Monitor Chamber M (Gy/C)

2nd Step: Calibration of the Transfer Standard (Secondary Standard) with the Monitor Chamber

The primary standard is replaced by the Transfer Standard T with its reference point on the beam axis in the specified *FDD*.

Now the air kerma rate is determined by the Monitor Chamber M:

$$\dot{K}_a = I_{\mathrm{M}} \cdot \left(\frac{k_{\mathrm{a}}}{k_{a0}}\right)_{\mathrm{MT}} \cdot N_{\dot{K}_a,\mathrm{M}} \tag{7}$$

The value of the air kerma rate is related to the ionization current of the transfer standard T:

$$I_{\mathrm{T}} \cdot N_{\dot{K}_a,\mathrm{T}} = \dot{K}_a \tag{8}$$

Meaning of the symbol:

I_{T}.......................... Ionization Current Transfer Standard (air density corrected)

The calibration coefficient of the Transfer Standard T in Gy/C is calculated with:

$$N_{\dot{K}_a,\mathrm{T}} = \frac{I_\mathrm{M} \cdot \left(\dfrac{k_\mathrm{a}}{k_{a0}}\right)_\mathrm{MT}}{I_\mathrm{T}} \cdot N_{\dot{K}_a,\mathrm{M}} \tag{9}$$

Meaning of the symbols:

$N_{\dot{K}_a,\mathrm{T}}$ .... Calibration Coefficient Transfer Chamber T (Gy/C)

$\left(\dfrac{k_\mathrm{a}}{k_{a0}}\right)_\mathrm{MT}$ .... Correction of Air Attenuation between M and T to reference air density

Typical Uncertainty Budgets for the 2 steps are given in Table 5 and Table 6.

Input quantity	Symbol	$u_{i,\mathrm{A}}$	$u_{i,\mathrm{B}}$	$u_{i,\mathrm{A}}^2 + u_{i,\mathrm{B}}^2$
Calibration coefficient of the primary standard (Example: PKM for Mammography)	$N_{\dot{K}_a,\mathrm{P}}$	-	0,35 %	0,122 5 $\%^2$
Ionization current of the primary standard	I_+	0,03 %	0,05 %	0,003 4 $\%^2$
Air density correction factor	k_pT	-	0,01 %	0,000 1 $\%^2$
Attenuation correction factor	$\dfrac{k_\mathrm{a}}{k_{a0}}$	-	0,10 %	0,010 0 $\%^2$
Recombination correction factor	$k_\mathrm{s,vol}$	0,02 %	0,05 %	0,002 9 $\%^2$
Position of the primary standard	$\left(\dfrac{r_\mathrm{r}}{r_\mathrm{n}}\right)_\mathrm{P}^2$	-	0,04 %	0,001 6 $\%^2$
Ionization current of the monitor chamber	I_M	0,03 %	0,05 %	0,003 4 $\%^2$
Air density correction factor monitor chamber	$k_{pT,\mathrm{M}}$	-	0,01 %	0,000 1 $\%^2$
Attenuation correction between monitor chamber and primary standard	$\left(\dfrac{k_\mathrm{a}}{k_{a0}}\right)_\mathrm{MP}$	-	0,04 %	0,001 6 $\%^2$
Calibration coefficient of the monitor chamber	$N_{\dot{K}_a,\mathrm{M}}$	$u_{N_{\dot{K}_a},\mathrm{M}} = \sqrt{\sum_i \left(u_{i,\mathrm{A}}^2 + u_{i,\mathrm{B}}^2\right)} =$		0,382 %

Table 5 Uncertainty calculation for step 1 of the calibration procedure (calibration coefficient monitor chamber)

Input quantity	Symbol	$u_{i,\mathrm{A}}$	$u_{i,\mathrm{B}}$	$u_{i,\mathrm{A}}^2 + u_{i,\mathrm{B}}^2$
Calibration coefficient of the monitor chamber (result in Table 5)	$N_{\dot{K}_a,\mathrm{T}}$	-	0,38 %	0,146 0 $\%^2$
Ionization current of the monitor chamber	I_M	0,03 %	0,05 %	0,003 4 $\%^2$
Air density correction factor monitor chamber	$k_{pT,\mathrm{M}}$	-	0,01 %	0,000 1 $\%^2$
Attenuation correction between monitor chamber and transfer standard	$\left(\frac{k_\mathrm{a}}{k_{a0}}\right)_\mathrm{MT}$	-	0,04 %	0,001 6 $\%^2$
Ionization current of the transfer chamber	I_T	0,03 %	0,05 %	0,003 4 $\%^2$
Air density correction factor monitor chamber	$k_{pT,\mathrm{T}}$	-	0,01 %	0,000 1 $\%^2$
Position of the primary standard	$\left(\frac{r_\mathrm{r}}{r_\mathrm{n}}\right)_\mathrm{T}^2$	-	0,04 %	0,001 6 $\%^2$
Calibration coefficient of the monitor chamber	$N_{\dot{K}_a,\mathrm{T}}$	$u_{N_{\dot{K}_a},\mathrm{T}} = \sqrt{\sum_i \left(u_{i,\mathrm{A}}^2 + u_{i,\mathrm{B}}^2\right)} =$		0,395 $\%^2$
		$U_{N_{\dot{K}_a},\mathrm{T}} = 2 \cdot u_{N_{\dot{K}_a},\mathrm{T}} =$		0,79 %

Table 6 Uncertainty calculation for step 2 of the calibration procedure (calibration coefficient transfer chamber)

The CEA LIST LNE-LNHB water calorimeter

Benjamin Rapp – CEA LIST (LNE) LNHB

1. *General overview*

The last generation of water calorimeter of LNHB was built taking into consideration the experience of other metrology laboratories and our own experience in water calorimetry for measurements in high-energy photon beams [1][2][3]. Thus, the calorimeter was designed to operate at 4 °C, the temperature of the maximum density of water, to minimize convective currents inside the water volume used for measurements. The inner part of the water calorimeter consists of a 30×30×35 cm^3 radiotherapy water phantom built with PMMA of 15 mm thickness, and filled with demineralized water. Some pictures of the calorimeter can be seen in Figure 1.

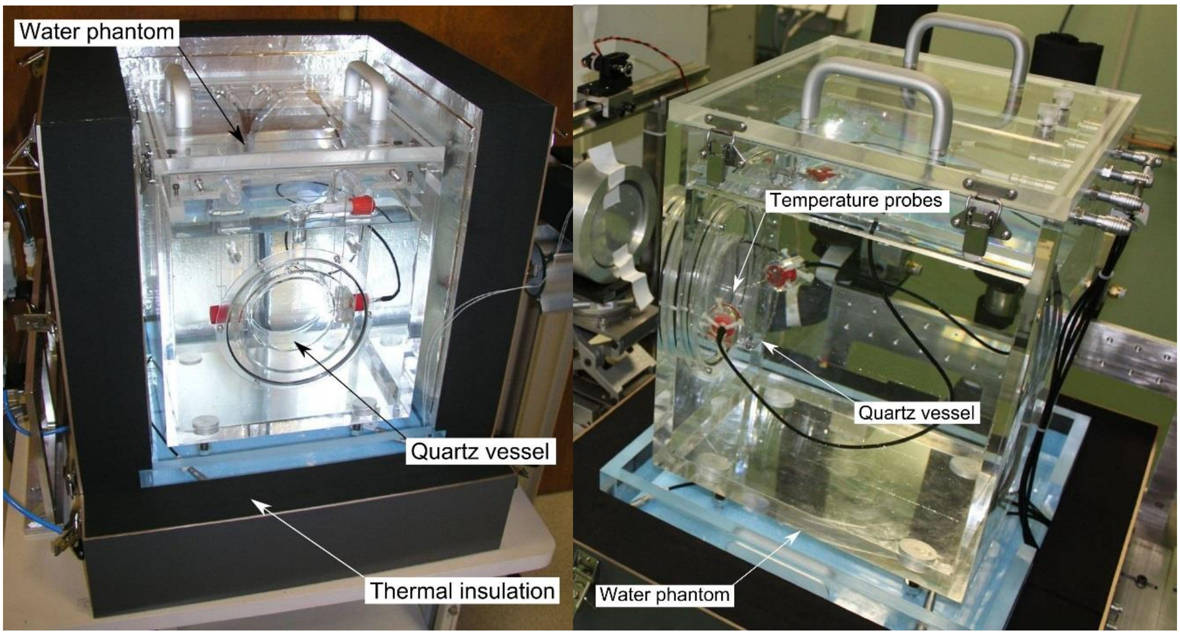

Figure 1 : Front view (on left) and side view (on right) of the water calorimeter.

The temperature rise is measured by two thermistor probes, placed inside a cylindrical quartz vessel filled with high-purity water. This quartz vessel can be inserted in the front face of the water phantom (for measurements at low depth in water) or placed at any depth in the water phantom. In both cases, the calorimeter is suitable for use with horizontal beams only. To insert the quartz vessel in the front face of the water phantom, the vessel is sealed in a PMMA ring with a silicon joint. This ring is fixed with screws to the front face of the water phantom, and sealed with a rubber joint around it. A schematic horizontal section of the calorimeter centered on the quartz vessel is shown in Figure 2. Detailed drawings of the calorimeter and its components are given in annex.

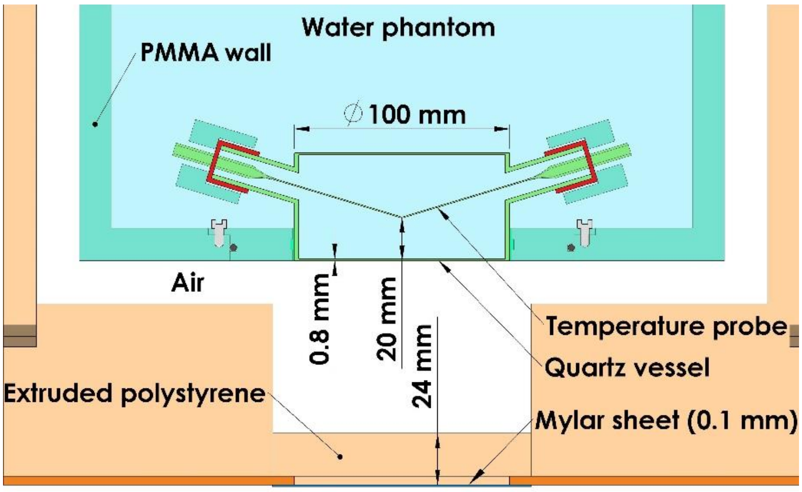

Figure 2: Schematic horizontal section of the water calorimeter.

The temperature of the water phantom is regulated (at 4 °C) by a cold air circulation inside a 20 mm gap between the phantom and the thermal enclosure. The thermal enclosure, that is needed to insulate against ambient temperature fluctuations, consists of a thick layer (80 mm) of extruded polystyrene inside a PVC box of 4 mm thickness. There is a window of 12 × 12 cm^2 area in the thermal enclosure with a reduced thickness of materials on the beam axis (24 mm of extruded polystyrene slab and a Mylar sheet of 0.1 mm).

2. *Air regulation system of the new calorimeter*

The thermal regulation of water calorimeters can be done with a circulation of water or air. Water circulation is generally preferred because the thermal transfers between the water phantom and the circulating water are more efficient than with air, and the thermal regulation of water is easier and more direct. But calorimeters with a system of water regulation are heavy and difficult to carry to different places. No water circulation must be present in the beam path because of the absorption and scattering induced. The absence of a cooling medium, in front of the measurement point, results in a thermal leakage demanding a large thermal insulation in the beam path.

Until now, air-regulated calorimeters have a large air gap around the water phantom. This large air gap between the thermal enclosure and water phantom is maintained at 4 °C by circulating in a secondary water-to-air heat exchanger. Some rotating fans are used inside the thermal enclosure to force air circulation and then obtain a temperature as homogeneous as possible.

In our new calorimeter, the option of air regulation was chosen. But instead of having a finite volume of cold air inside the thermal enclosure and trying to regulate its temperature by using rotating fans and water-to-air heat exchangers, we decided to inject a strong flow of cold air at constant temperature into the calorimeter and let it escape naturally by some openings in the thermal enclosure. This allows a more compact and transportable instrument.

A strong flow of cold air is generated by a commercial vortex tube fed with compressed air and connected to a pressure regulator (see the principle diagram of the system in Figure 3, and a general view of the system in Figure 4).

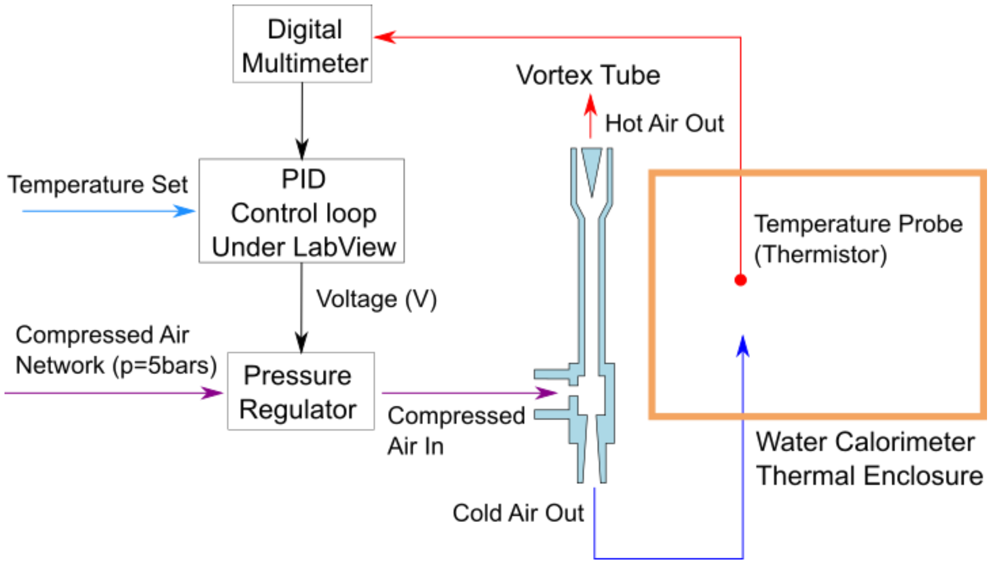

Figure 3: Principle diagram of the air regulation system.

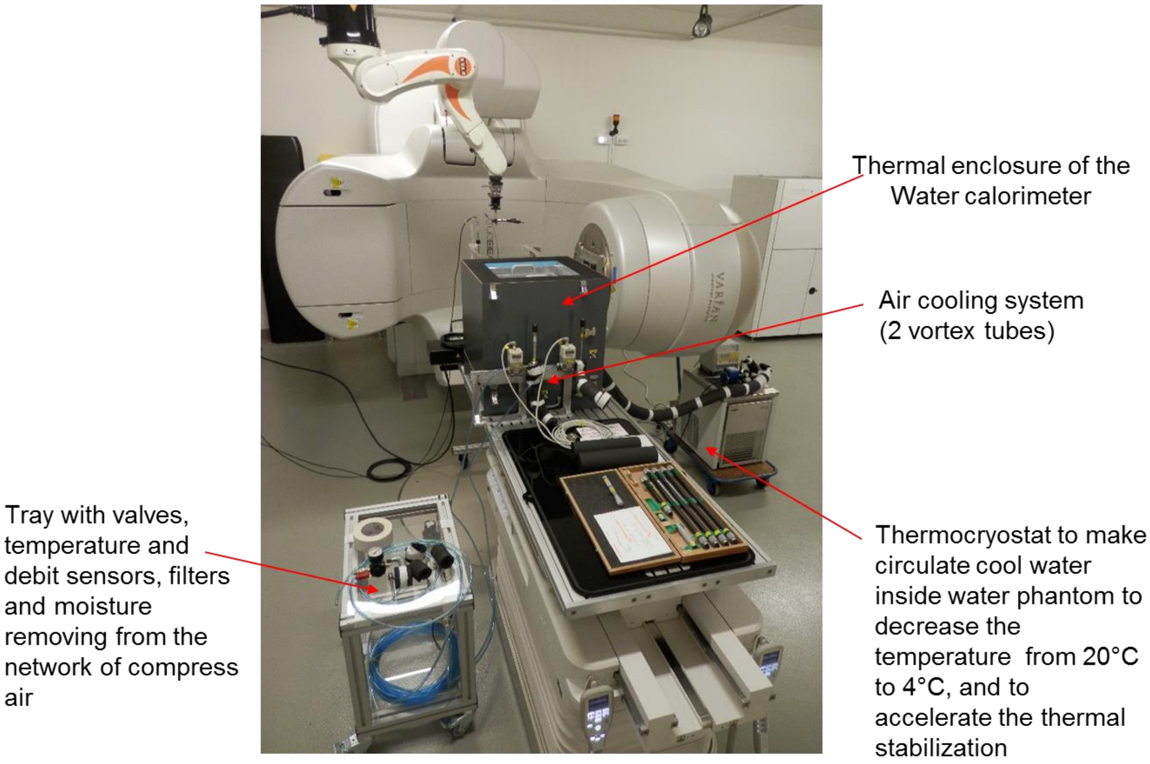

Figure 4: Water calorimeter air regulation system.

The compressed air is supplied by an industrial distribution network, at a pressure of 7 bar and at ambient temperature. The regulator is part of a PID control loop, programmed with the LabView programming environment, in which the process variable is the temperature measured inside the calorimeter thermal enclosure by a thermistor. Two of these systems are used to inject cold air underneath the water phantom and inside the entrance window of the calorimeter. With this system the temperature of air around the water phantom is maintained in a stationary state around 4 °C. The temperature measurements, made with small thermistors in different locations inside the thermal enclosure, showed the existence of a vertical temperature gradient. However, by adjusting regulation parameters, a stable temperature close to 4 °C was obtained inside the quartz vessel. The temperature measurement showed a maximum drift of 20 μK min^{-1} over a long period of time (several weeks) (Figure 5). During our previous studies with the water calorimeter in high-energy photon beams, we observed that

the influence of a thermal drift lower than 50 μKmin^{-1} on the measured temperature rise is negligible. For comparison, the minimum temperature rise measurable is around 300 μK.
To accelerate the initial temperature stabilization of the water calorimeter, a pump is used to make circulating the water of the phantom inside a thermal exchanger. With this system, the temperature of 4°C is reach in 5 hours (Figure 6).

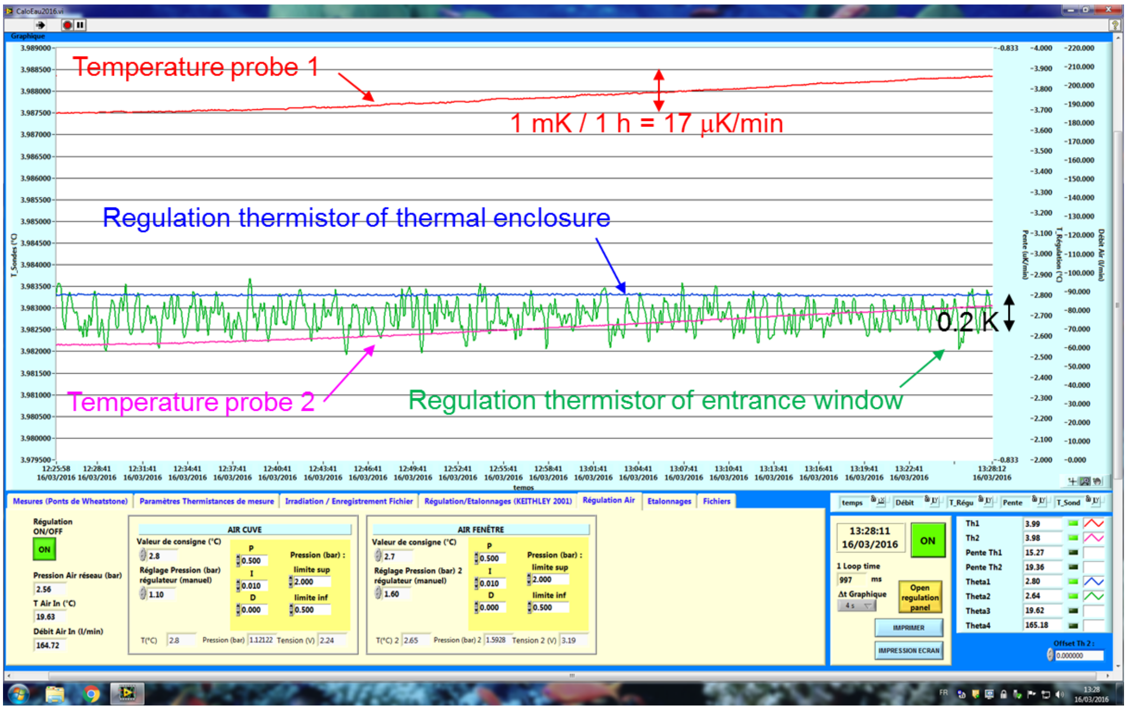

Mesures (Ponts de Wheatstone) | Paramètres Thermistances de mesure | Irradiation / Enregistrement Fichier | Régulation/Etalonnages (KEITHLEY 2001) | Régulation Air | Etalonnages | Fichiers

Régulation ON/OFF: ON
Pression Air réseau (bar): 2.56
T Air In (°C): 19.63
Débit Air In (l/min): 164.72

AIR CUVE
Valeur de consigne (°C): 2.8
Réglage Pression (bar) régulateur (manuel): 1.10
P: 0.500
I: 0.010
D: 0.000
Pression (bar) : limite sup: 2.000
limite inf: 0.500
T(°C): 2.8
Pression (bar): 1.12122
Tension (V): 2.24

AIR FENÊTRE
Valeur de consigne (°C): 2.7
Réglage Pression (bar) 2 régulateur (manuel): 1.60
P: 0.500
I: 0.010
D: 0.000
Pression (bar) : limite sup: 2.000
limite inf: 0.500
T(°C) 2: 2.65
Pression (bar) 2: 1.5928
Tension 2 (V): 3.19

13:28:11 16/03/2016
ON
1 Loop time: 997 ms
Δt Graphique: 4 s
Open regulation panel
IMPRIMER
IMPRESSION ECRAN

Th1: 3.99
Th2: 3.98
Pente Th1: 15.27
Pente Th2: 19.36
Theta1: 2.80
Theta2: 2.64
Theta3: 19.62
Theta4: 165.18
Offset Th 2 : 0.000000

Figure 5: Stability of temperature inside the calorimeter thermal enclosure.

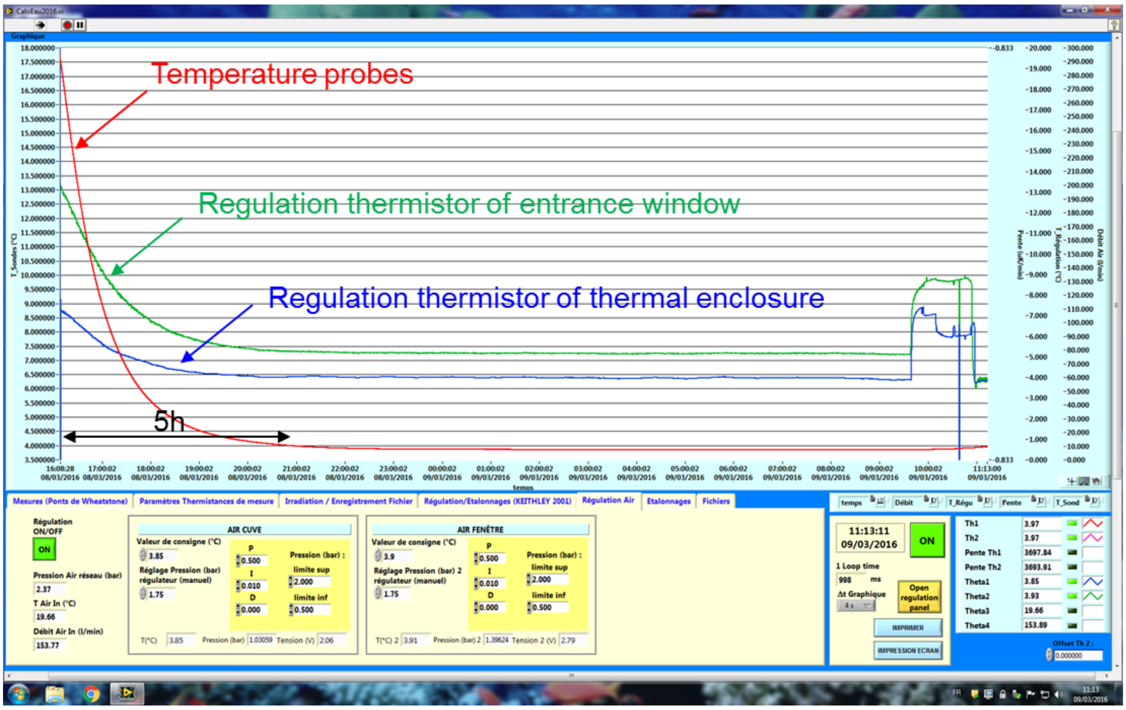

Mesures (Ponts de Wheatstone) | Paramètres Thermistances de mesure | Irradiation / Enregistrement Fichier | Régulation/Etalonnages (KEITHLEY 2001) | Régulation Air | Etalonnages | Fichiers

Régulation ON/OFF: ON
Pression Air réseau (bar): 2.37
T Air In (°C): 19.66
Débit Air In (l/min): 153.77

AIR CUVE
Valeur de consigne (°C): 3.85
Réglage Pression (bar) régulateur (manuel): 1.75
P: 0.500
I: 0.010
D: 0.000
Pression (bar) : limite sup: 2.000
limite inf: 0.500
T(°C): 3.85
Pression (bar): 1.03059
Tension (V): 2.06

AIR FENÊTRE
Valeur de consigne (°C): 3.9
Réglage Pression (bar) 2 régulateur (manuel): 1.75
P: 0.500
I: 0.010
D: 0.000
Pression (bar) : limite sup: 2.000
limite inf: 0.500
T(°C) 2: 3.91
Pression (bar) 2: 1.39624
Tension 2 (V): 2.79

11:13:11 09/03/2016
ON
1 Loop time: 998 ms
Δt Graphique: 4 s
Open regulation panel
IMPRIMER
IMPRESSION ECRAN

Th1: 3.97
Th2: 3.97
Pente Th1: 3697.84
Pente Th2: 3693.91
Theta1: 3.85
Theta2: 3.93
Theta3: 19.66
Theta4: 153.89
Offset Th 2 : 0.000000

Figure 6: Initial temperature stabilization of the water calorimeter.

3. *Quartz vessel*

The quartz vessel is of cylindrical shape with a diameter of 10 cm and a thickness of 5 cm. Its front and back parallel faces are made up of quartz sheets of 0.8 mm thickness. Quartz was chosen to avoid contamination of high-purity water inside the vessel. In order to perform measurements at low depth in water (typically 2 cm for medium-energy x-rays), the quartz vessel is inserted in the front wall of the water phantom. Two probes are placed inside a quartz vessel to measure the temperature (Figure 7).

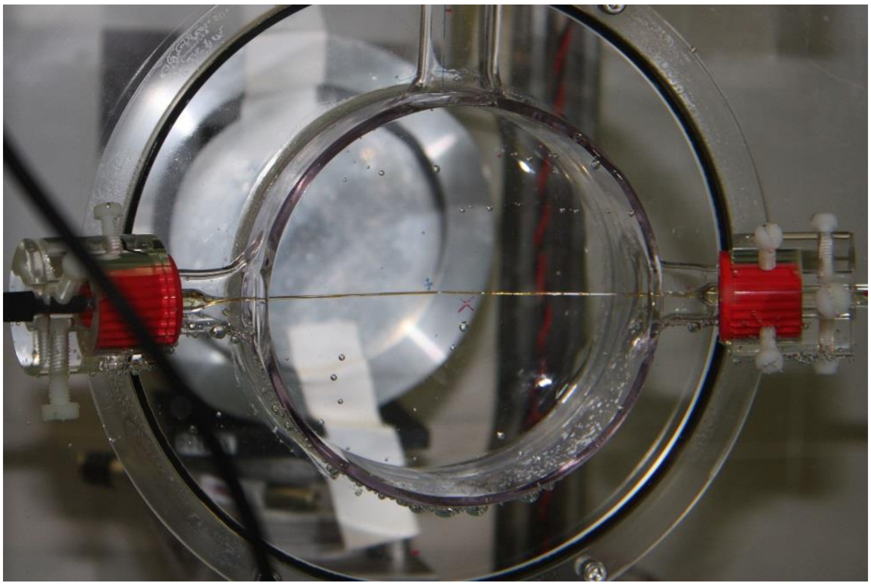

Figure 7: View of the quartz vessel with 2 temperatures probes, embedded in front the PMMA phantom of the water calorimeter.

With this design, measurements can be performed at a depth down to 0.5 cm in water from the surface of the water phantom. The only limitations are the thickness of the front face of the quartz vessel and a direct contact to be avoided between the temperature probe and the quartz vessel front face. Until now, in other primary standard dosimetry laboratories, low-depth measurements were achieved by using the free surface of water on the top of water phantom, for vertical beams only (for example, the McGill University water calorimeter developed to operate in electron beams). Our calorimeter design allows us to perform measurements at low depth in water in horizontal beams, which is generally more common.

The quartz vessel is filled with high-purity water saturated with N_2 gas, and pre-irradiated at several hundreds of grays, in order to control the heat defect of water. The high-purity water is produced with a MILLIPORE MILLIQ A10 filtration system feed with distillated water. A special apparatus made of quartz has been built for gas saturation of water, and to fill the quartz vessel (see Figure 8).

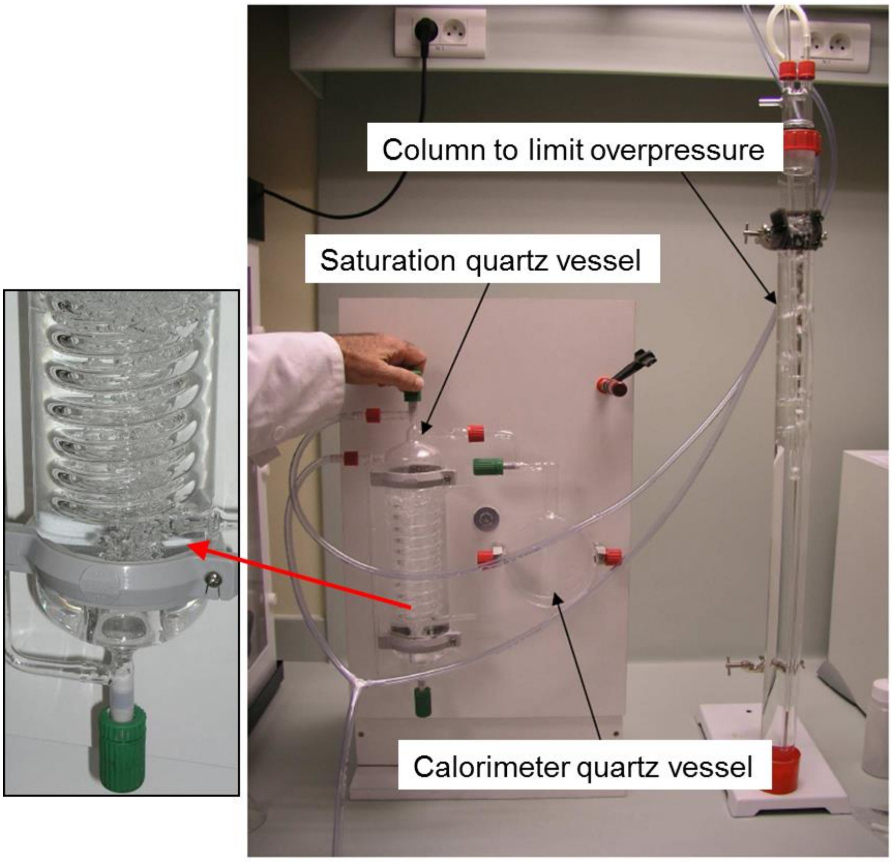

Figure 8: View of the system used to fill quartz vessel with high-purity water saturated with nitrogen gas.

4. *Temperature probes*

A temperature probe (see Figure 9) consists of a sealed quartz capillary of 0.6 mm outer diameter with a negative-temperature-coefficient (NTC) thermistor inside. The NTC thermistor (BR11KA432J reference produced by General Electric) is glass-encapsulated and has a nominal resistance of 4300 Ω at 25 °C (or ~ 9300 Ω at 4 °C) and a diameter of 0.28 mm. The thermistor is connected to a cable through Pt/Ir wires (ø 0.05 mm) electrically insulated with Kapton tubes (ø 0.18 mm). The capillary is filled with an epoxy resin under vacuum to avoid air bubbles.

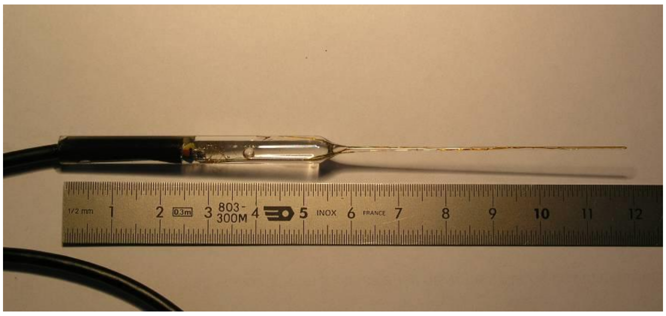

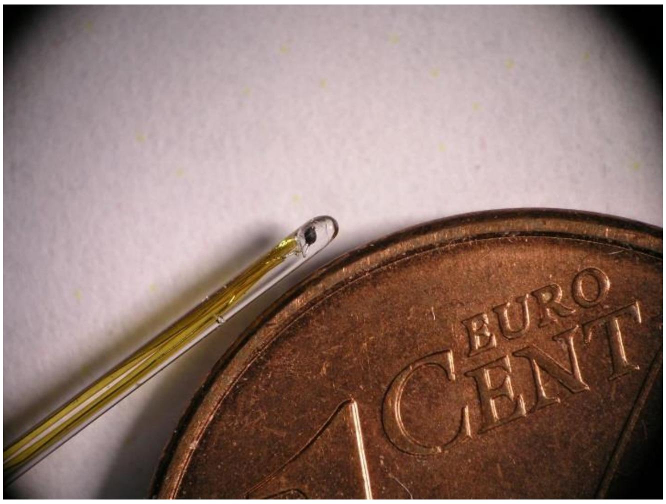

Figure 9: Full view (top) and view of the thermistor (bottom) of a temperature probe.

5. Temperature probes calibration

The calibration of the temperatures probes is done by comparison with a standard platinum resistance thermometer (SPRT), itself calibrated by the French primary metrology laboratory for temperature measurements (LNE-LCM). For calibration, the probes are immersed in water in a deep calibration bath (LAUDA Cooling thermostat) with a high temperature homogeneity and stability. The temperature of the bath is changed in steps from 1 to 8 °C. The thermistor equation is used over this range of temperature for fitting the measured resistance of the thermistor, as a function of the bath temperature given by the SPRT:

$$R = R(T_0)e^{\beta\left(\frac{1}{T}-\frac{1}{T_0}\right)}$$

With $R(T_0)$ the resistance at temperature $T0$ and β the material constant of the thermistor. An example of calibration curve is given in Figure 10. The final relative uncertainty on the temperature rise measurement resulting from this calibration is estimated to 0.1%. The calibration of the temperature probes is done with the electronics also used for calorimetry measurements. In this way, the Wheatstone bridges and voltmeters used for readout do not need to be calibrated.

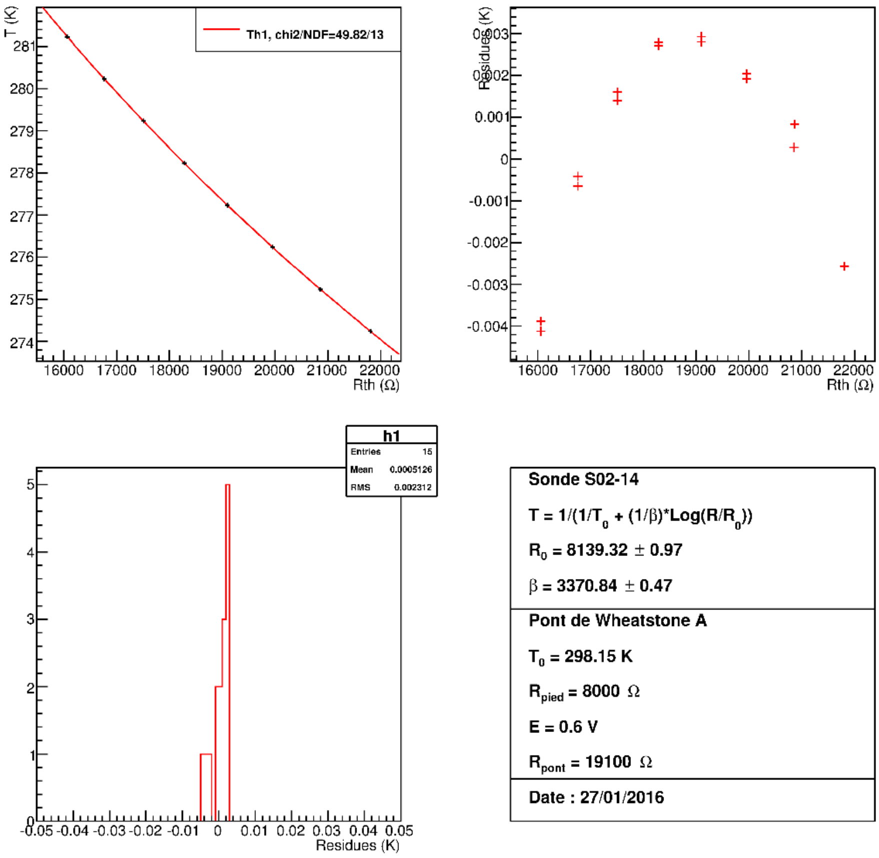

Figure 10: Example of a calibration curve obtained for a temperature probe.

6. Water calorimeter electronics

The resistances of the thermistors of the two temperature probes are measured by two dc Wheatstone bridges built with high-precision resistors of 8000Ω, connected to a precision voltmeter. The bridges are used near equilibrium without re-balancing after each irradiation; instead the bridge equation is applied to calculate the resistance of the thermistors. Each temperature probe is calibrated with its own bridge and voltmeter, so the parameters of the bridge need not be known accurately. DC Wheatstone bridges have been chosen deliberately instead of ac bridges. The dc bridges can be noisier than the ac ones, but their calibration is easier and more stable. Moreover, no further calibration is needed during the measurement process. A LabView program is used to read the voltmeters used in the Wheatstone bridges and in the calorimeter temperature regulation system (Figure 11).

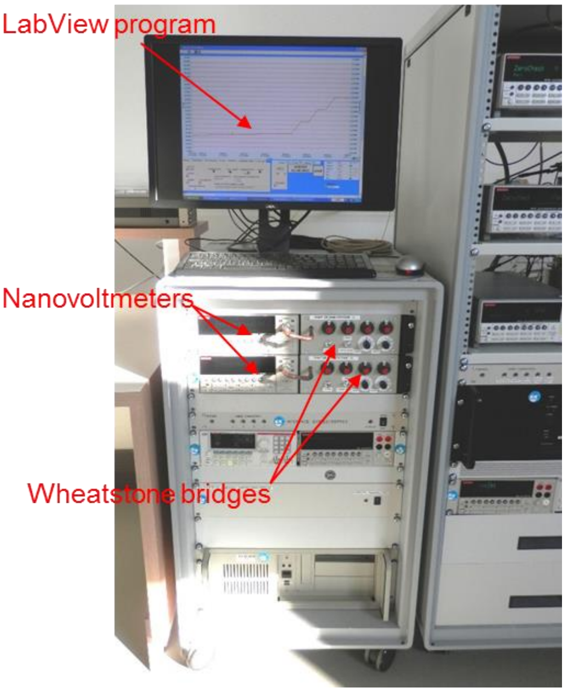

Figure 11: Water calorimeter electronics.

7. *Positioning of temperature probes in water*

The positioning of temperature probes inside the quartz vessel can be performed only after filling the vessel with ultra-pure water. So only an optical method can be used. For this task, a long working-distance microscope objective is placed on the head of a video camera mounted on a motorized micro-metric translation stage (see Figure 12). The working distance of this objective (distance between the front end of objective and the surface to observe) is 34 mm in air, and the depth of field is 14 μm.

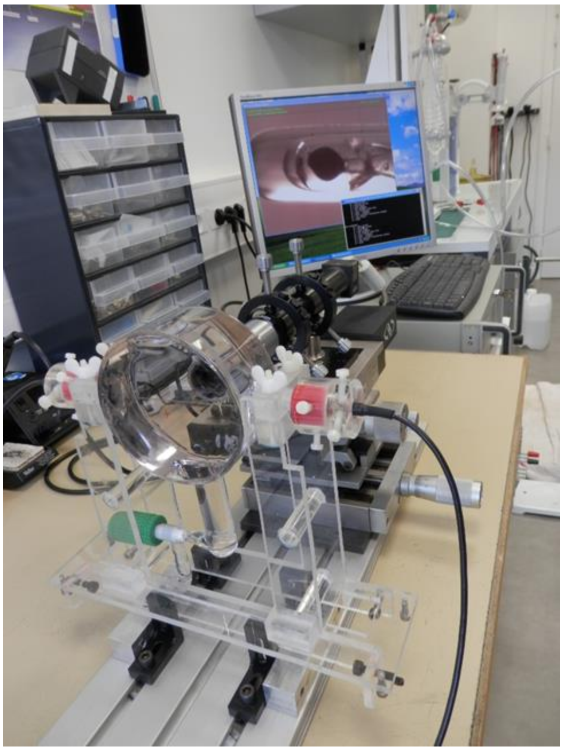

Figure 12: View of the system for measuring the depth of thermistors inside quartz vessel.

A distance measurement is obtained from the translation stage by focusing alternatively on the thermistor bead of the temperature probe and the external surface of the quartz vessel.

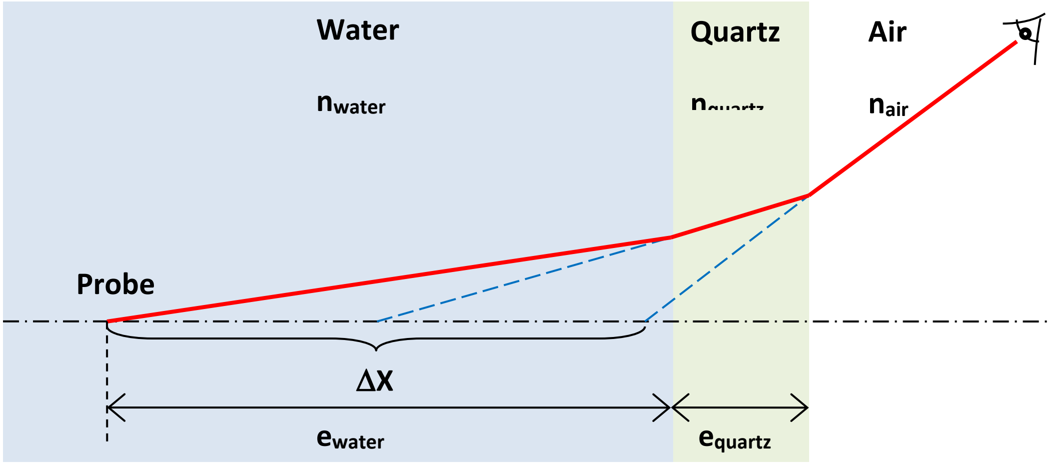

This measurement has to be corrected for the refraction of light in water and quartz to obtain the real depth of the thermistor in the quartz vessel:

$$\Delta X = e_{water}\left[1-\frac{n_{air}}{n_{water}}\right] + e_{quartz}\left[1-\frac{n_{air}}{n_{quartz}}\right]$$

The absolute accuracy of the motorized micro-metric translation stage was measured by the supplier (Newport Corporation), and is lower than 10 μm. The relative standard uncertainty on the distance measurement with this optical system was estimated at 50 μm. The accuracy has been checked with glass plane plates used as windows in optical systems. These plane plates are made up of an optical glass with a well-known refraction index. The thickness of the plane plates (10 and 20 mm) were measured with the optical system, and compared with measurements made with a calibrated micrometer. The measurements were compatible taking into consideration the relative standard uncertainty of the optical system. So, with such a device, the depth in the quartz vessel of the thermistor of the temperature probe can be measured with a relative standard uncertainty of 50 μm (k = 1).

8. Measurement principle and correction factors

The absorbed dose to water (D_w) is determined from the temperature rise measurement by the following equation:

$$D_w = C_p \Delta T (1-h)^{-1} k_p k_c k_\rho k_d$$

Where C_p is the specific heat capacity of water at 4 °C, _T is the measured temperature rise under irradiation, h is the water chemical heat defect, k_p is the radiation field perturbation correction factor, k_c is the thermal conduction correction factor, k_ρ is the density of water correction factor and k_d is the depth-in-water correction factor. The specific heat capacity of water at 4 °C has been taken as 4204.8 J kg^{-1} K^{-1}. This value is calculated from a polynomial equation given in the *Journal of Physical and Chemical Reference Data*. This polynomial equation is based on a set of experimental data published in 1939 by Osborne. The relative uncertainty of this set of data is not well documented, but is estimated to be between 0.01 and 0.02% in the *Journal of Physical and Chemical Reference Data*. So, the relative uncertainty on the specific heat capacity of water has been enlarged to 0.1%.

a. Temperature rise measurement (ΔT)

The low thermal diffusivity of water allows the measurement of a local temperature rise over a timescale of a few minutes. The choice of the irradiation time is a compromise between a good signal-to-noise ratio and a minimization of thermal transfer effects on the temperature rise measurement. The irradiation scheme is a sequence of three irradiations of 4 min, followed by a pause time of 1.5 h to allow the cone of heat produced by irradiation in water to vanish. The temperature rise (ΔT) is determined by an extrapolation to mid-irradiation of the linear fits of the temperature drift before and after irradiation. An example of temperature rise measurement for the ISOH300 x-ray beam is given in Figure 13.

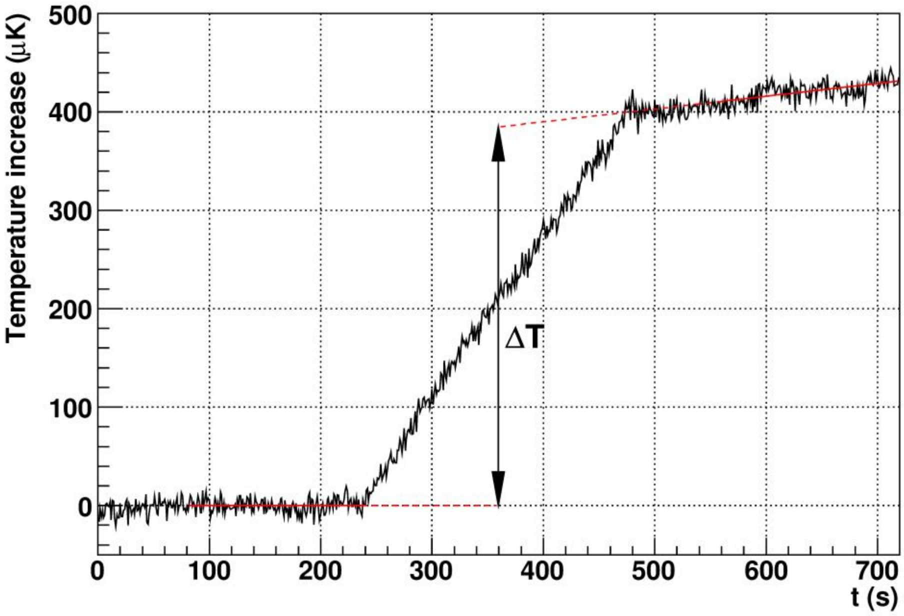

Figure 13: Example of temperature rise measurement for the ISOH300 x-ray beam.

The data obtained immediately after the irradiation stop are not taken into account because this period is sensitive to the thermal effect caused by the temperature probes.

The value of temperature rise (ΔT) changes with the delay of post-irradiation measurements chosen after the irradiation stop. The thermal conduction correction factor (k_c) also varies with the delay of post-irradiation measurements (from 10 s to 80 s), because it is calculated by applying the same extrapolation method. This effect is including in the calculation of the uncertainty of the thermal conduction correction factor.

b. Thermal conduction correction factor (k_c)

The thermal transfers in water occur by conduction and convection, but natural convective thermal transfers are minimized by operating at 4 °C at the maximum density of water. Then, a correction factor denoted by k_c, taking into account thermal transfers by conduction, is applied to the measurements. To evaluate this correction factor a Monte Carlo simulation of the heat deposition in the water phantom by radiation is combined with the calculation of the heat transfers by conduction in the calorimeter with a finite-element code (COMSOL).

The thermal effects of the quartz vessel and the temperature probes are calculated separately with the finite-element code. Since their dimensions are two orders magnitude different, it is difficult to match the mesh elements at the boundary of the quartz probe with the mesh elements in the water inside the quartz vessel.

The geometry used in the finite-element code for calculating the effect of the quartz vessel is exactly matching the one used in the Monte Carlo code for energy deposition calculation. The energy deposition by all particle sources and by unit of volume, in the water phantom and the quartz vessel, is recorded in each voxel of a rectangular and cylindrical mesh grid. A text file is filled with these values interpolated on a rectangular grid that can be used by the COMSOL code. In this code, this file is used as a heat source (function of space coordinates) for thermal transfer calculations. The temperature curve is given by the temperature drift with time inside the quartz vessel.

To calculate the effect of temperature probes with the COMSOL code, the geometry used includes the last centimeter of the end of a probe and a small volume of water around it. It's not possible to record, in the Monte-Carlo code, the energy deposition in each voxel of a fine mesh grid covering the temperature probes, because the size of the voxels needed would be too small to cover the geometry of the thermistor bead or quartz capillary. Instead the averaged energy deposition in each volume, at the end of the modeled thermistor probe, is recorded separately.

The temperature curves of the quartz vessel and temperature probe are combined together, and the temperature rise $(\Delta T)_{\text{quartz vessel \& probes}}$ for each of the irradiation steps is calculated and compared to the temperature rise $(\Delta T\ )_{\text{water}}$ obtained from the temperature reference curve. The temperature rise is calculated using the same method as experimentally (extrapolation of linear fits to mid-irradiation) with the same parameters (same delay for post irradiation measurements). For the quartz vessel, the reference temperature curve is obtained by a simulation with the thermal conduction of materials equal to zero, and for temperature probes by a calculation with quartz material replaced by water. The thermal conduction correction factor (k_c) is the ratio between the calculated temperature rise $(\Delta T)_{\text{quartz vessel \& probes}}$ and $(\Delta T\ )_{\text{water}}$ for each of the consecutive irradiation steps. An example of simulated temperature curves for the ISOH300 x-ray beam is given in Figure 14.

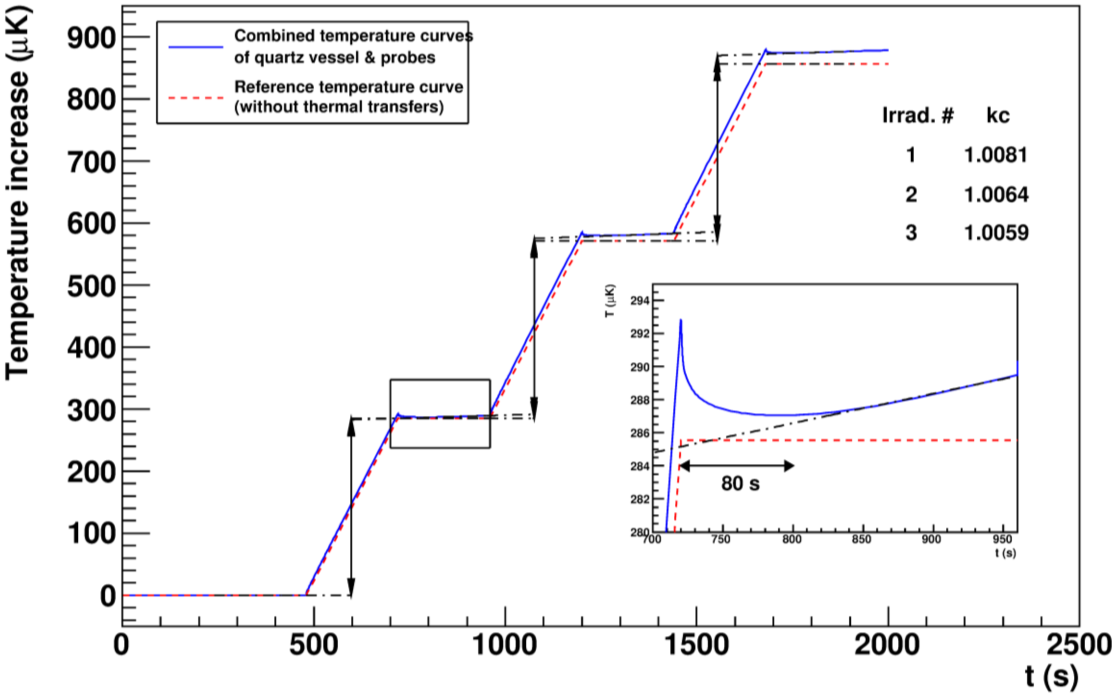

Figure 14: Thermal conduction correction factor for the ISOH300 beam calculated from the combined temperature curves of the quartz vessel and probes, for a sequence of three irradiations of 4 min. In the zoomed figure, one can see the peak which occurs after the irradiation stop, and which is the effect of the temperature probes.

The effect of the temperature probes is visible as a peak which occurs after the irradiation stop. The intensity of the peak is more important for low-energy x-ray beams. The intensity of the peak decreases fast (after 10 to 20 s), but a local minimum can be seen on the temperature curve around 40 to 60 s after the irradiation stop. It corresponds to the transition between the tail of the temperature peak after the irradiation stop (due to the thermal effect of probe vanishing), and the increasing thermal effect of the quartz vessel. To minimize the effect of temperature probes on the thermal conduction correction factor and the measured temperature rise, it was chosen to perform post-irradiation linear fits with the values obtained later than 80 s after the irradiation stop. Moreover, the exact geometry and material composition of temperature probes are not well known.

c. Radiation field perturbation correction factor (k_p)

The radiation field is perturbed by the calorimeter non-water materials. The perturbation comes first from the thermal enclosure, and particularly from the insulating materials inside the calorimeter window. The second perturbation is due to the quartz vessel and the temperature probes.

The perturbation factor due to the thermal enclosure is determined by both ionization chamber measurements and Monte Carlo simulations. An ionization chamber is placed at the same depth in water as the temperature probes inside the water phantom used for ionization chamber calibration of the water phantom of the calorimeter. The radiation field perturbation factor due to the thermal enclosure is then measured as the ratio between the current given by the ionization chamber measured with and without the front part of the thermal enclosure. Monte Carlo simulations were done to check this value. There was good agreement with the measurements for medium-energy x-ray beams around 250 and 300 kV or high energy photons beams, but discrepancies at lower energies are observed, because the commercial polystyrene contains a proportion of 0.8 to 4% in mass of bromine due to the addition of fire retardants.

The perturbation of the radiation field by the quartz vessel can be determined also by both ionization chamber measurements and Monte Carlo simulations. A small volume ionization chamber is placed in a water phantom, and measurements are performed with and without the quartz vessel surrounding the ionization chamber. The effect of temperature probes is much smaller than the one of the quartz vessel and was neglected (the measurement or simulation of this effect is particularly difficult because of the small size of the probes).

The uncertainties on the radiation field perturbation are the type A uncertainties on the ratio of currents measured by the ionization chamber, or the type A uncertainties given by the Monte Carlo code.

d. Water chemical heat defect (h)

All the energy deposited by radiation in water is not converted into heat; this effect is called the heat defect of water h. The heat defect of water depends on the content of gases dissolved in water, impurities and the type of radiation. For high-purity water saturated with an inert gas such as nitrogen or argon, in the absence of a gas volume, a stationary state is reached after a small accumulated dose, and the heat defect measured and predicted by radiolysis models is zero. If a gas volume is in contact with water, then there is an accumulation inside the gas volume of the volatile compounds such as O_2 and H_2 that are either initially present in water or produced in water by radiolysis. And the continuous transfer of these gases between the gas volume and the water changes the heat defect. In our case, the quartz vessel is filled with high-purity water saturated with N_2 gas (see Figure 13), and a pre-irradiation of the water vessel at several hundred grays is done to stabilize the heat defect before measurements. In high-energy photon or electron beams, for which the linear-energy transfer (LET) is low (0.2 keV μm^{-1}), the heat defect of ultra-pure water saturated with N_2 gas is zero. In medium-energy x-ray beams, the LET is between 2 and 6 keVμm^{-1} for an x-ray energy of 200 and 50 keV, respectively. Simulations of the water radiolysis were done for such an LET and the value of the heat defect is found endothermic ($h > 0$) and between 0.02% and 0.1% (for ultra-pure water perfectly saturated with N2 gas, and without any impurities). Similar calculations based on real measurements of the dissolved oxygen concentration and organic carbon impurities also allowed us to estimate the uncertainty on the heat defect of water. The value obtained is about 0.3% and is in agreement with those used by other metrology laboratories. So the heat defect of water for medium-energy x-rays was taken as zero with a 0.3% relative standard uncertainty.

e. Density of water correction factor (k_ρ)

The density of water changes between 4 °C (temperature of calorimetric measurements) and 20 °C (reference temperature for ionometric measurements). So the measured absorbed dose to water must be corrected for this effect. For this the dose gradient at the depth of measurement in water, for the different reference beams, must be known. It is obtained from the central axis depth dose profile in water calculated with a Monte-Carlo code.

f. Depth-in-water correction factor (k_d)

The depth in water of temperature probes is measured by the optical system already described and can be slightly different from the target value. Then, the measured absorbed dose to water is corrected (k_d depth-in-water correction factor) for this depth difference by using the value of the dose gradient obtained from a Monte Carlo simulation.

9. Uncertainty budget for the absorbed dose to water measured by water calorimetry in medium-energy x-ray beams

The absorbed dose rate to water was measured for six medium-energy x-ray beams at LNHB [3][4][5]. The depth in water phantom is of 2 cm and the source-detector distance is of 53 cm. The average number of measurements performed for each of the six beams is about 100. The statistical uncertainty on the temperature rise ranges from 0.24% to 0.40%. An example of uncertainty budget for the ISOH300 x-ray beam is given in Tableau 1. The final combined relative standard uncertainty for the six beams ranges from 0.49% (for CCRI250) to 0.72% (for RQR6). It is worth noting that the two predominant uncertainty components (except ΔT measurement reproducibility) are those related to the heat defect of water and the radiation field perturbation correction factor. An international comparison of primary absorbed dose to water standards in the medium-energy X-ray range was done for 4 CCRI beams and gave similar results [6].

Tableau 1: Uncertainty budget for the absorbed dose rate to water D_W measurement in the ISOH300 x-ray beam.

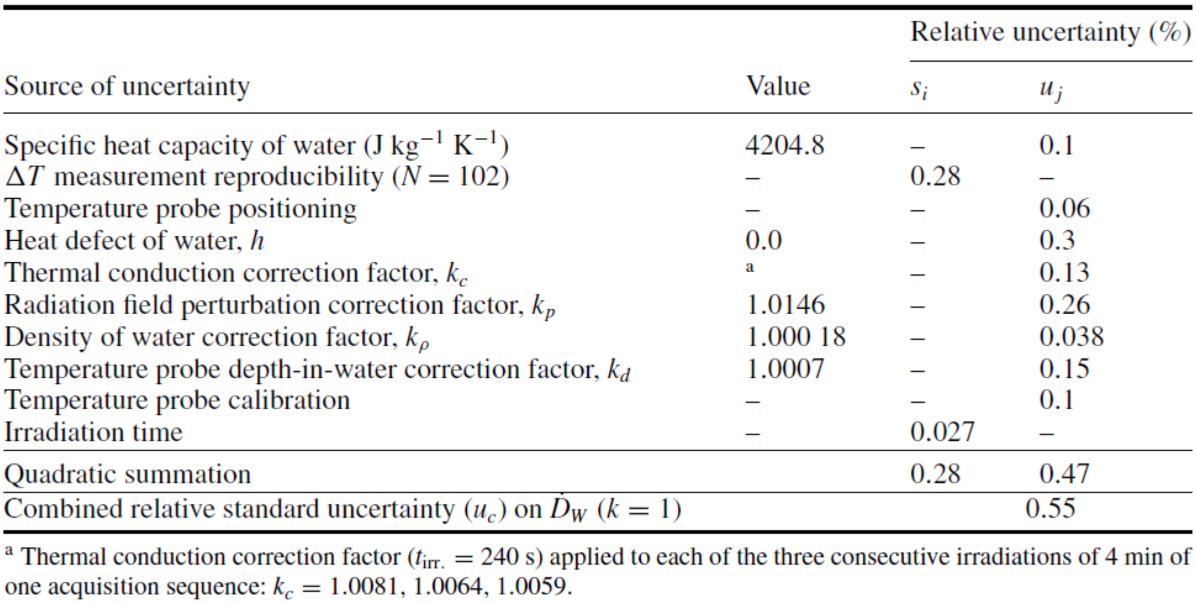

Source of uncertainty	Value	Relative uncertainty (%)	
		s_i	u_j
Specific heat capacity of water (J kg^{-1} K^{-1})	4204.8	–	0.1
ΔT measurement reproducibility ($N = 102$)	–	0.28	–
Temperature probe positioning	–	–	0.06
Heat defect of water, h	0.0	–	0.3
Thermal conduction correction factor, k_c	[a]	–	0.13
Radiation field perturbation correction factor, k_p	1.0146	–	0.26
Density of water correction factor, k_ρ	1.000 18	–	0.038
Temperature probe depth-in-water correction factor, k_d	1.0007	–	0.15
Temperature probe calibration	–	–	0.1
Irradiation time	–	0.027	–
Quadratic summation		0.28	0.47
Combined relative standard uncertainty (u_c) on $\dot{D}_W$ ($k = 1$)		0.55	

[a] Thermal conduction correction factor ($t_{\mathrm{irr.}} = 240$ s) applied to each of the three consecutive irradiations of 4 min of one acquisition sequence: $k_c = 1.0081, 1.0064, 1.0059$.

10. Uncertainty budget for the absorbed dose to water measured by water calorimetry in a ^{60}Co beam

The water calorimeter has been used in the LNHB ^{60}Co beam [2][8]. The measurements were carried out under the following conditions: a source-detector distance of 1 m and a depth in the water phantom of 5 cm (4.6 cm of water + 0.4 cm of PMMA – thickness of the phantom window). The water absorbed dose rate of the source during measurements is about 0.4 Gy/min. The uncertainty budget is given in Tableau 2.

Tableau 2: Uncertainty budget for the absorbed dose rate to water D_W measurement in the LNHB 60Co beam.

Source of uncertainty	Value	Relative uncertainty	
		100 si	100 uj
Temperature probe calibration	-	0.10	
Temperature probe positioning	-		0.10
Specific heat of water ($J.Kg^{-1}.K^{-1}$)	4204.8		0.10
Thermal conduction correction factor k_c	*		0.10
Radiation field perturbation correction factor k_p	1.0033	0.10	
Heat defect of water h	0		0.30
Density of water correction factor $k\rho$	1.00032	0.01	
ΔT measurement reproducibility (N=584)	-	0.12	
Quadratic summation		0.19	0.35
Combined relative standard uncertainty on D_w		**0.39**	

** Thermal conduction correction factor ($t_{irr.}$= 240 s) :*
k_c = 1.0043, 1.0012, 1.0004, 0.9997

11. *Uncertainty budget for the absorbed dose to water measured by water calorimetry in high energy accelerator photon beams*

The absorbed dose rate to water was measured in the 6 MV, 12 MV and 20 MV linac high energy photons beams of the LNHB Saturne 43 accelerator [7]. The reference point for the Dw determination is at 10 cm depth along the beam axis in a cubic water phantom of side length 30 cm, at a source-detector distance of 1 m. The dose rate of the beam is about 1.7 Gy/min. The thermal conduction correction factor (k_c) range from 0.994 to 1.004. The radiation field perturbation factor (k_p) is about 1.001 for quartz vessel and about 1.003 for water calorimeter thermal enclosure. The uncertainty budget is given in Tableau 3.

Tableau 3: Estimated uncertainty contributions for absorbed dose to water calibration factor in the 6 MV, 12 MV and 20 MV accelerator photon beams using the LNHB water calorimeter.

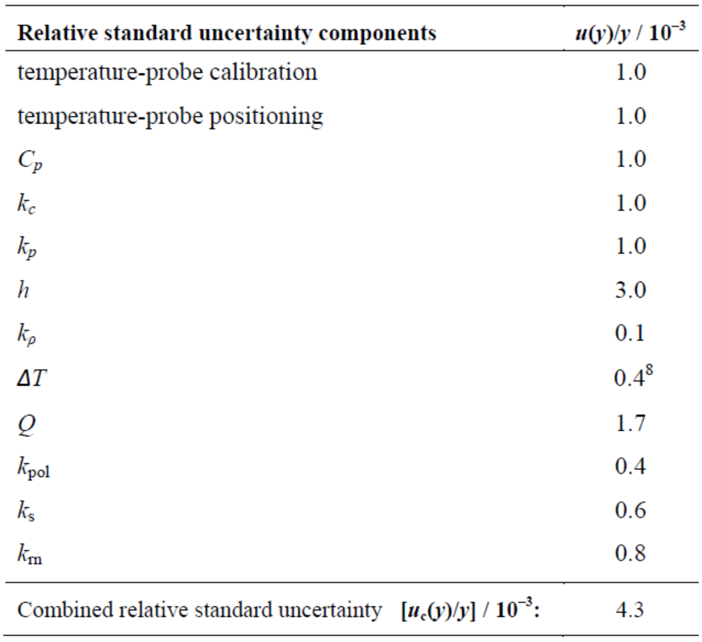

Relative standard uncertainty components	$u(y)/y$ / 10^{-3}
temperature-probe calibration	1.0
temperature-probe positioning	1.0
C_p	1.0
k_c	1.0
k_p	1.0
h	3.0
k_ρ	0.1
ΔT	0.4[8]
Q	1.7
k_{pol}	0.4
k_{s}	0.6
k_{m}	0.8
Combined relative standard uncertainty **[$u_c(y)/y$] / 10^{-3}:**	4.3

References

[1] Rapp B, Development of a water calorimeter for dosimetry at LNE-LNHB, Rev. Fr Metrologie **24** (2010-4) 3–8

[2] Rapp B, The LNE-LNHB water calorimeter: measurements in a ^{60}Co beam *IDOS: Proc. Int. Symp. On Standards, Applications and Quality Assurance in Medical Radiation Dosimetry (IAEA Proceedings Series STI/PUB/1514) (Vienna, 9–12 Nov. 2010)* vol 1 p 67

[3] B Rapp, N Perichon, M Denoziere, J Daures, A Ostrowsky and J-M Bordy, The LNE-LNHB water calorimeter for primary measurement of absorbed dose at low depth in water: application to medium-energy x-rays, Phys. Med. Biol. **58** (2013) 2769–2786

[4] Perichon N, Rapp B, Denoziere M, Daures J, Ostrowsky A and Bordy J-M, Comparison between absorbed dose to water standards established by water calorimetry at the LNE-LNHB and by application of international air-kerma based protocols for kilovoltage medium energy x-rays, Phys. Med. Biol. **58** (2013) 2787

[5] Rapp B, Absorbed dose to water standards established by water calorimetry at the LNE-LNHB for medium energy X-ray, Rev. Fr Metrologie **35** (2014-3) 15–23

[6] L. Büermann, A. S. Guerra, M. Pimpinella, M. Pinto, J. de Pooter, L. de Prez, B. Jansen, M. Denoziere and B. Rapp, First international comparison of primary absorbed dose to water standards in the medium-energy X-ray range, EURAMET.RI(I)-S13 - Final report dated 2016-02-18, Metrologia **53** (2016)Tech. Suppl. 06007

[7] S. Picard, D. T. Burns, P. Roger, F. Delaunay, J. Gouriou, M. Le Roy, A. Ostrowsky, L. Sommier, D. Vermesse, Key comparison BIPM.RI(I)-K6 of the standards for absorbed dose to water of the LNE-LNHB, France and the BIPM in accelerator photon beams, Metrologia 2013 **50** Tech. Suppl. 06015

[8] C. Kessler, D.T. Burns, F. Delaunay, M. Donois, Key comparison BIPM.RI(I)-K4 of the absorbed dose to water standards of the LNE-LNHB, France and the BIPM in ^{60}Co gamma radiation, Metrologia 2013, **50**, Tech. Suppl. 06019

Annex: Drawings of water calorimeter components

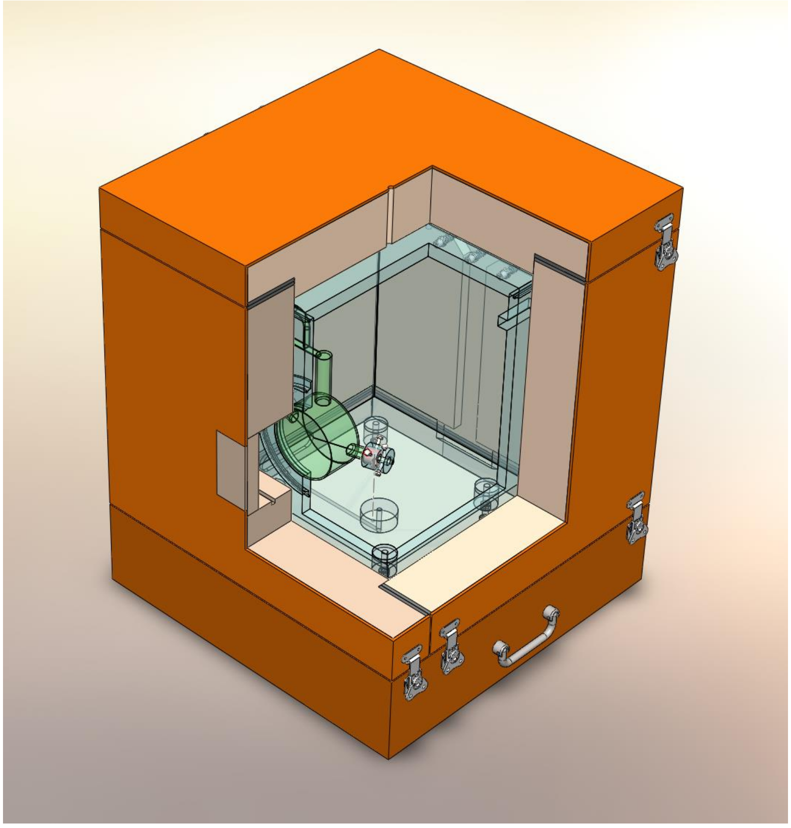

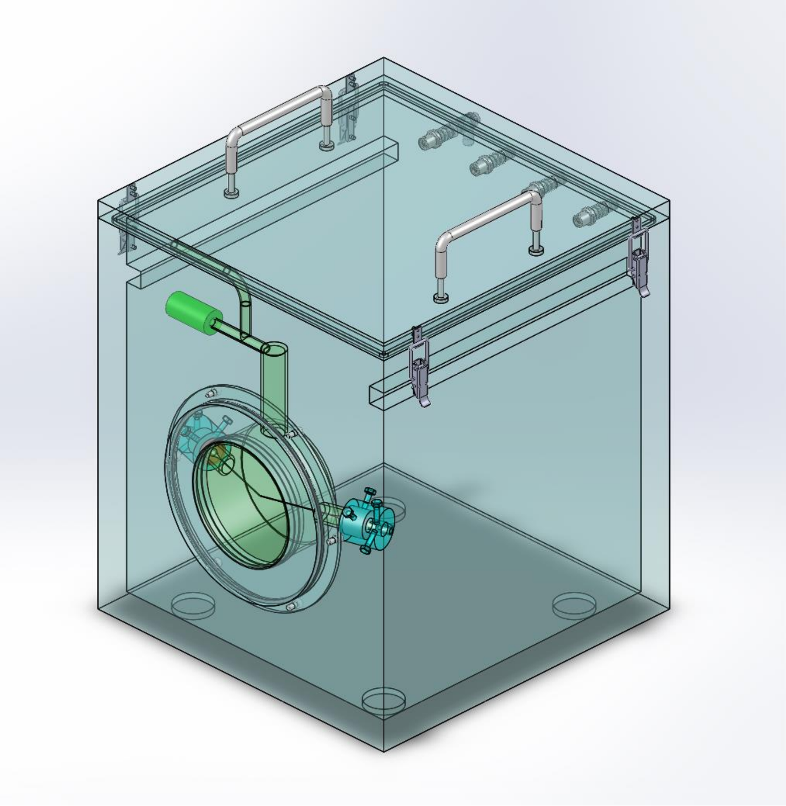

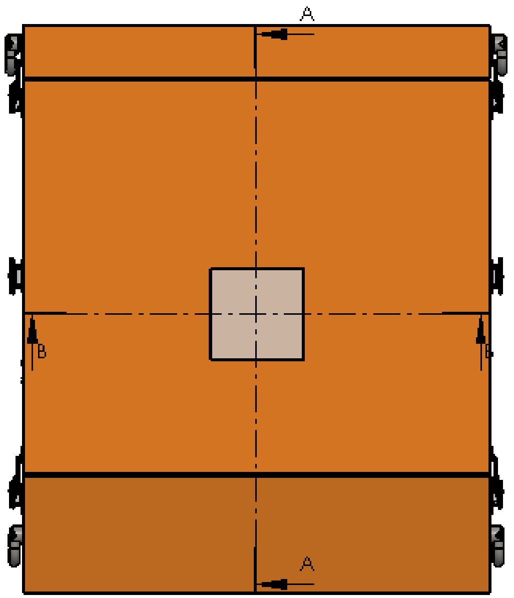

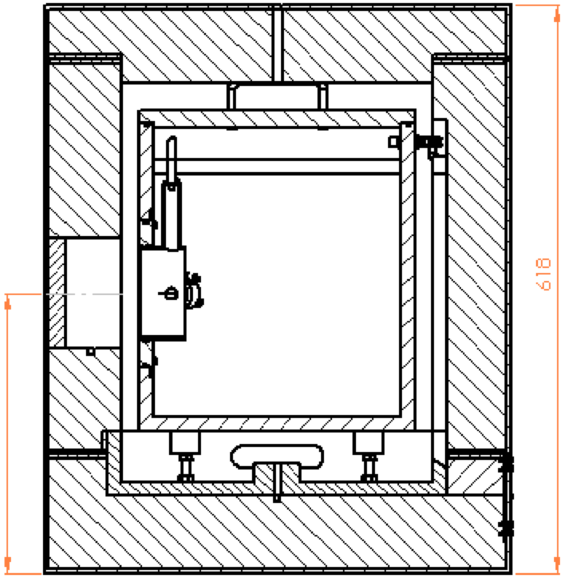

COUPE A-A
ECHELLE 1 : 5

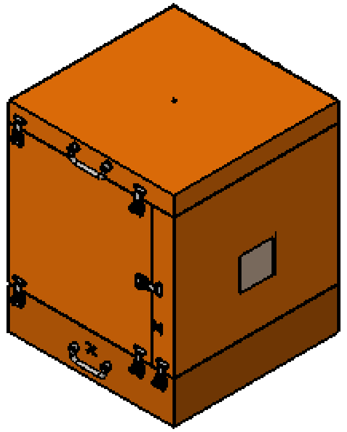

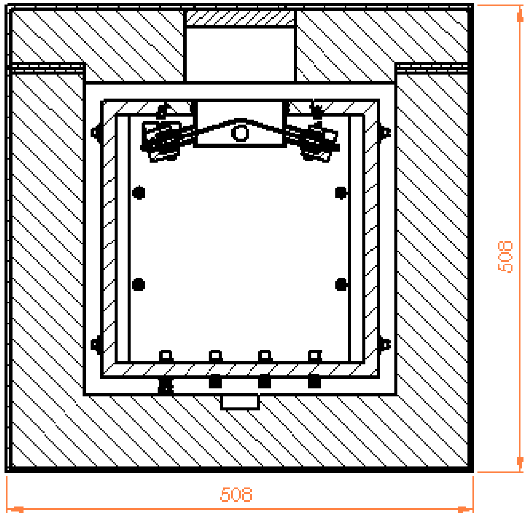

COUPE B-B
ECHELLE 1 : 5

SAUF INDICATION CONTRAIRE: LES COTES SONT EN MILLIMETRES ETAT DE SURFACE: TOLERANCES: LINEAIRES: ANGULAIRES:	FINITION:	CASSER LES ANGLES VIFS	NE PAS CHANGER L'ECHELLE	REVISION	
	NOM	SIGNATURE	DATE	TITRE:	Vue générale
AUTEUR	E. RAPP		10/05/2010		
VERIF.					
APPR.					
FAB.					
QUAL.				MATERIAU:	No. DE PLAN: Divers — A3
				MASSE:	ECHELLE:1:10 — FEUILLE 1 SUR 1

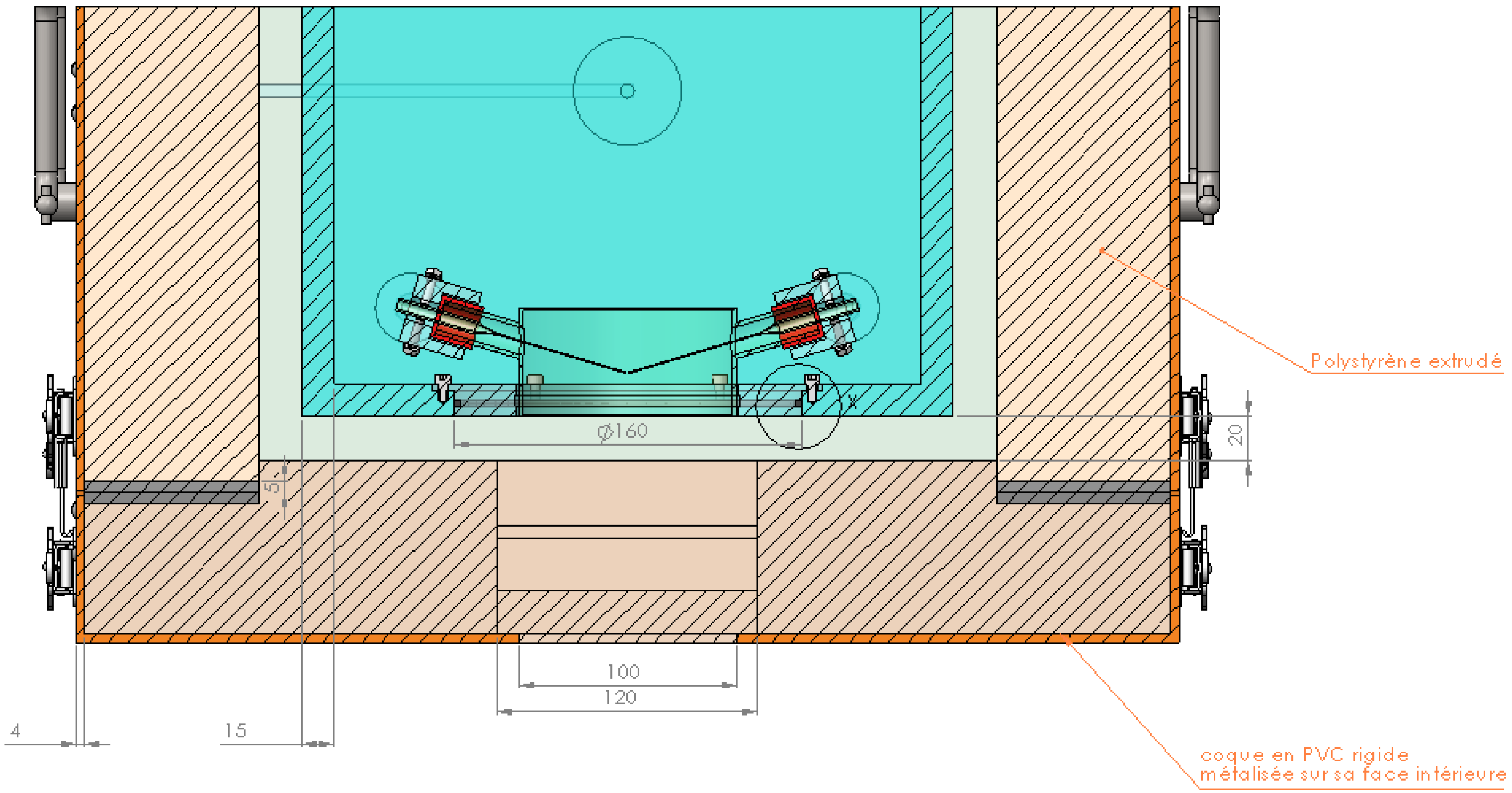

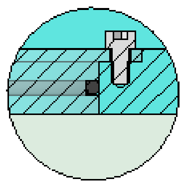

DÉTAIL X
ECHELLE 1 : 1

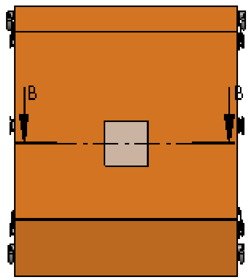

COUPE B-B
ECHELLE 1 : 2

SAUF INDICATION CONTRAIRE:
LES COTES SONT EN MILLIMETRES
ETAT DE SURFACE:
TOLERANCES:
LINEAIRES:
ANGULAIRES:

FINITION:

CASSER LES
ANGLES VIFS

NE PAS CHANGER L'ECHELLE

REVISION

	NOM	SIGNATURE	DATE
AUTEUR	E RAPP		10/05/2010
VERIF.			
APPR.			
FAB.			
QUAL.			

MATERIAU:

MASSE:

TITRE:

Vue générale (coupe)

No. DE PLAN

Divers

A3

ECHELLE:1:10

FEUILLE 1 SUR 1

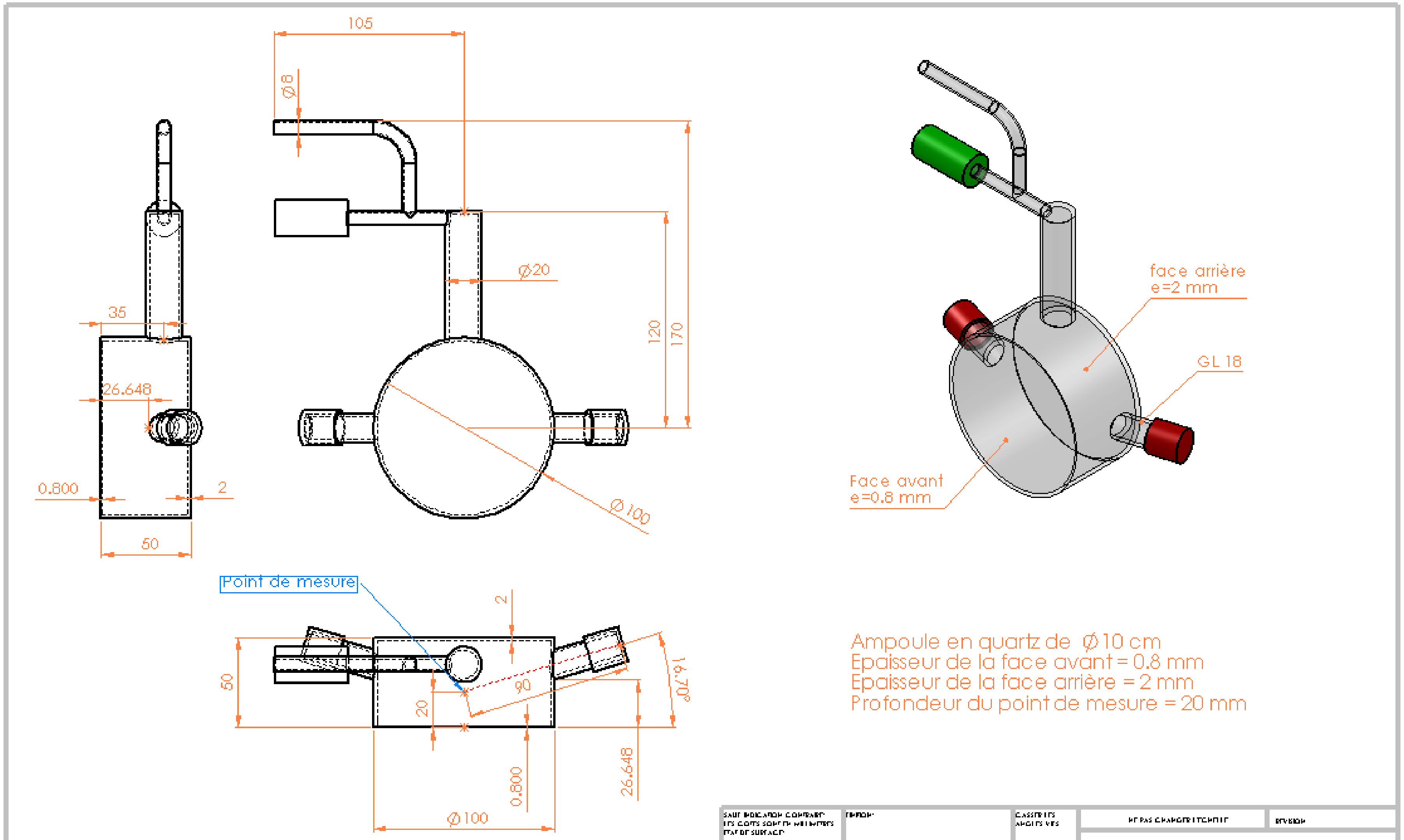

Ampoule en quartz de Ø10 cm
Epaisseur de la face avant = 0.8 mm
Epaisseur de la face arrière = 2 mm
Profondeur du point de mesure = 20 mm

SAUF INDICATION CONTRAIRE:
LES COTES SONT EN MILLIMETRES
ETAT DE SURFACE:
TOLERANCES:
LINEAIRES:
ANGULAIRES:

FINITION:

CASSER LES
ANGLES VIFS

NE PAS CHANGER L'ECHELLE

REVISION

	NOM	SIGNATURE	DATE
AUTEUR	I RAPP		[illegible]2010
VERIF			
APPR			
FAB			
QUAL			

MATERIAU:
Quartz

MASSE:

TITRE:
Ampoule en quartz
Ø10 cm, N°1

No. DE PLAN
Ampoule

A3

ECHELLE:

FEUILLE 1 SUR 1

Quartz capillary

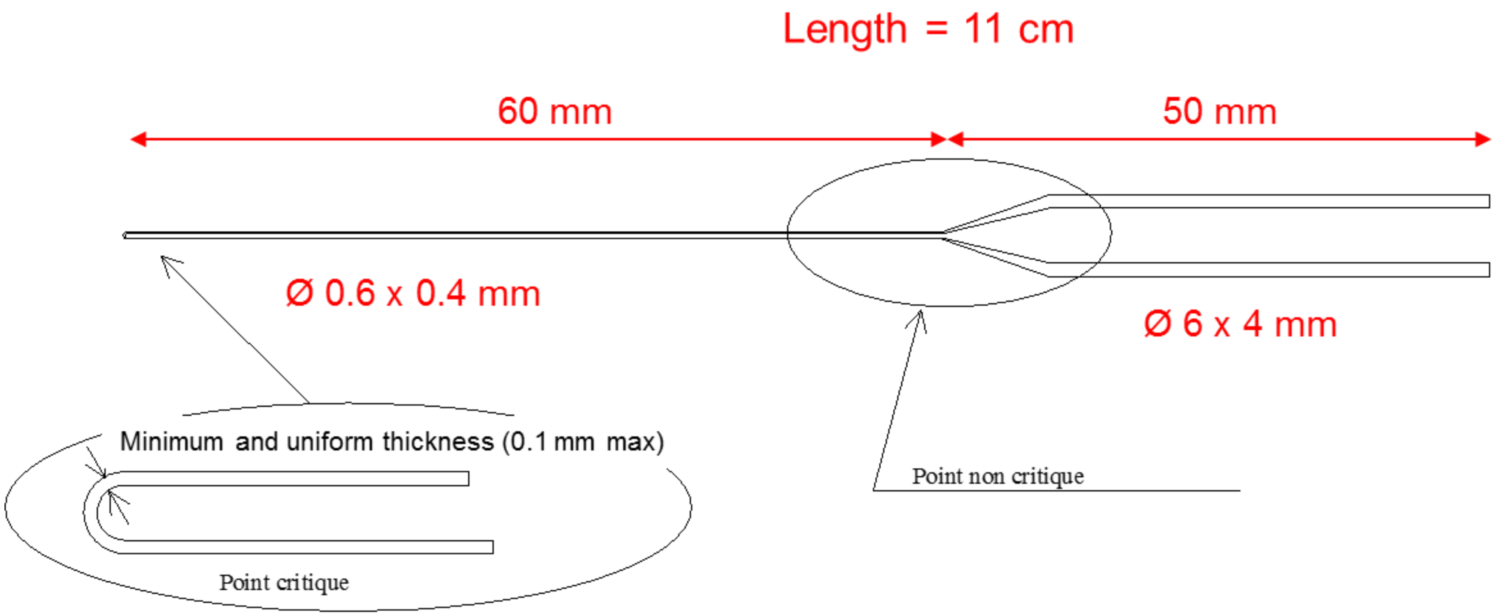

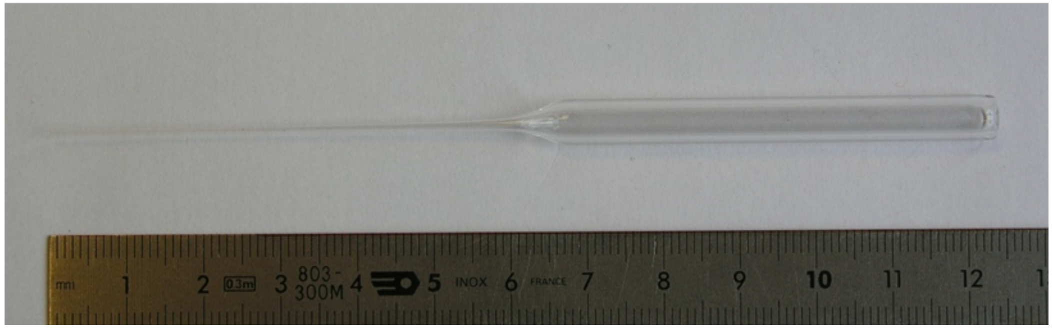

The Graphite calorimeter of the BEV

Andreas Steurer, Wilhelm Tiefenböck

This paper presents the technical description of the Primary Standard for absorbed dose to water based on a graphite calorimeter including the identification and determination of correction factors.

1 Primary Standards - Absorbed Dose to Water Co-60: Graphite Calorimeter

1.1 Principle

Absorbed Dose means the absorption of energy which means increasing of temperature. Therefore the direct measurement of absorbed dose is the measurement of this temperature increase.

One can measure the temperature increase directly in water with a Water Calorimeter.

Alternatively one can measure the temperature increase in graphite to get Absorbed Dose to Graphite with a Graphite Calorimeter. Subsequently in a second step a conversion from Absorbed Dose to Graphite to Absorbed Dose to Water must be done.

The BEV Primary Standard for Absorbed Dose to water is a Graphite Calorimeter. The temperature increase is measured with thermistors within the Graphite Calorimeter which are integrated in a Wheatstone Bridge to measure the change of their resistance.

1.1.1 Design of the Graphite Calorimeter

The Austrian Primary Standard of Absorbed Dose to Water is a graphite calorimeter. It was developed in the Austrian Research Center Seibersdorf based on the design by Domen and is in operation since 1983. The calorimeter is designed for quasi-adiabatic and quasi-isothermal mode of operation. The hardware including all measuring thermistors still works properly.

Recently the calorimeter was refurbished with a complete check of the graphite calorimeter hardware components and the measurement electronics and the revision and replacement of hardware components. In addition a new LabView based evaluation program including linear and non-linear drift was developed. Extensive Penelope based Monte Carlo calculations were done to verify and re-evaluate correction factors. It can be used for all modes of operation and electrical calibrations. Finally a verification of calorimeter response for complete temperature working range was done.

The conversion from absorbed dose to graphite to absorbed dose to water is done by two methods based on the scaling theorem. These methods are conversion by calculation and conversion with an ionization chamber.

To realize a proper radiation field the BEV dosimetry laboratory is equipped with a Picker therapy unit which was recently reloaded was a 185 TBq Co-60-source. The reference value for absorbed dose to water is 12,134 6 mGy/s (reference date: 31.12.2013, reference conditions: 1 m distance from focus, 5 g/cm^2 water depth, 10 cm x 10 cm field size). A study on the determination and verification of photon fluence spectra from this teletherapy unit based upon Monte Carlo simulations with PENELOPE and MCNP was done. These energy spectra were used in this study for the determination of the graphite calorimeter correction factors.

Figure 1 gives a schematic representation of the BEV graphite calorimeter main components. The “core” is the innermost body in which the absorbed dose is determined. It is a graphite disc 20 mm in diameter and a thickness of 2.75 mm. The core is enclosed in the “jacket” and this is enclosed in the “shield”. They are thermally isolated from each other by 0.5 mm vacuum gaps and mylar coatings. The shield is mounted in the “medium” which is thermo-regulated and therefore stabilizes to the working temperature at about 27 °C. The graphite calorimeter bodies are mounted in a Polymethylmethacrylate (PMMA) vacuum chamber which is enclosed by the graphite phantom, the outermost part of the graphite calorimeter. The graphite phantom consists of graphite plates of different thicknesses supported by a wooden frame. The mass densities of the graphite plates are well known to enable depth dose measurements.

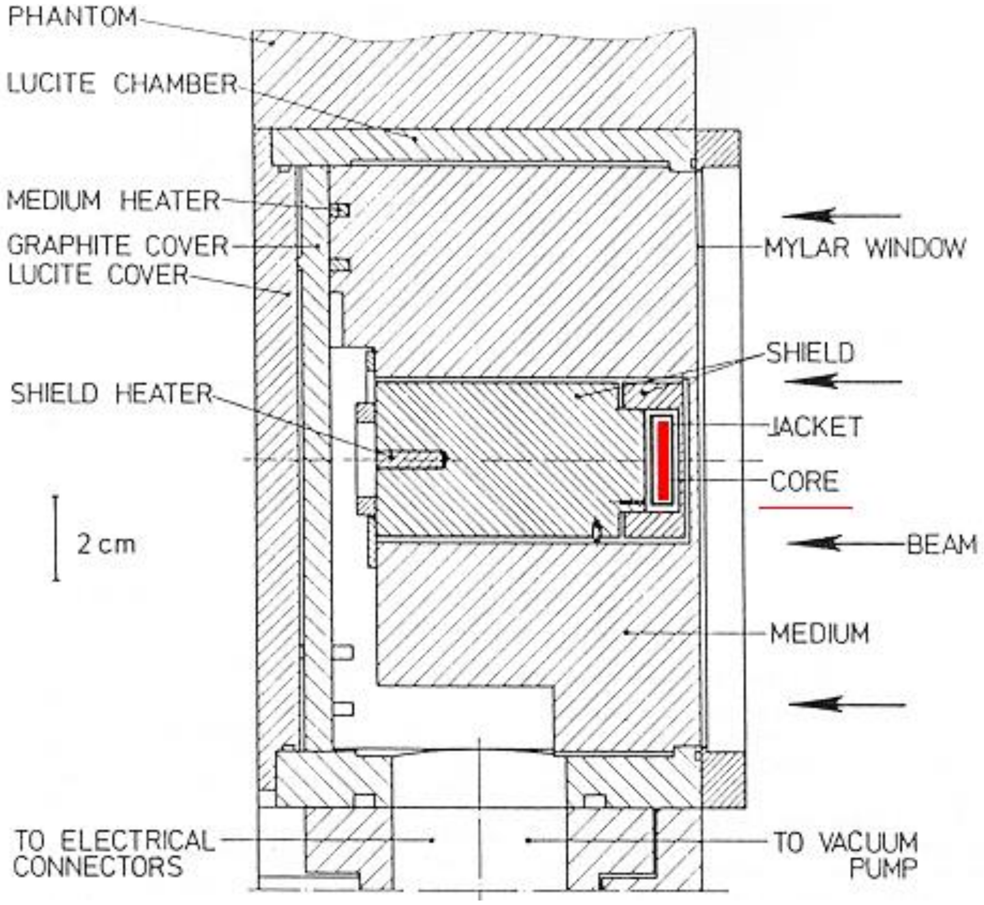

Figure 1 Schematic construction of the BEV Graphite Calorimeter

1.1.2 Measuring Conditions and Scaling theorem

The Reference Conditions for measuring Absorbed Dose to Water for Co-60 are given in Table 1.

Parameter	Data
Distance source – reference point detector (*SDD*)	1000 mm
Reference water depth	5 g/cm^2
Field size	10 cm x 10 cm at *SDD*

Table 1 Reference Condition for measuring Absorbed Dose to Water for Co-60

To allow the conversion from Absorbed Dose to Graphite to Absorbed Dose to Water the so called Scaling Theorem is used. That means:

Assuming, that all photon interactions occur by Compton scatter. If:

- Two blocks of different materials are irradiated by the same photon beam emitted by a point source.
- All dimensions are scaled in the inverse ratio of the electron densities of the two media.

Then:

- The energy spectra of the primary and scattered photons and their distribution in angle at the corresponding scaled points of measurement will be the same.

The determined Scaling Factor for water depth 5 g/cm^2 is

$$SF = 1{,}563 \tag{1}$$

Meaning of the symbol:

SF........................	Scaling Factor

As the distance between the source and the graphite phantom must be scaled with this factor it is important to know the virtual point source position accurately. Therefore measurements in different distances for extrapolation are necessary.

First one assumes a nominal distance between the source and the detector (ionization Chamber). Then one varies the distance. For every distance the Ionization current is measured. Using Lease Square Fit one can calculated the correction difference between the assumed distance and real distance between virtual point source position and the detector. The example shows (Figure 2) a difference of 17,59 mm. The means that the virtual point source position is 17,59 mm closer as assumed. The formula for the Least Square Fit is:

$$R = k \cdot \frac{1}{\sqrt{I}} + B \tag{2}$$

Meaning of the symbols:

R..........................	Assumed distance between source and detector in mm
k...........................	Constant
I	Measured Ionization Current for every assumed distance
B..........................	Calculated correction difference between the assumed distance and real distance with Least Square Fit in mm

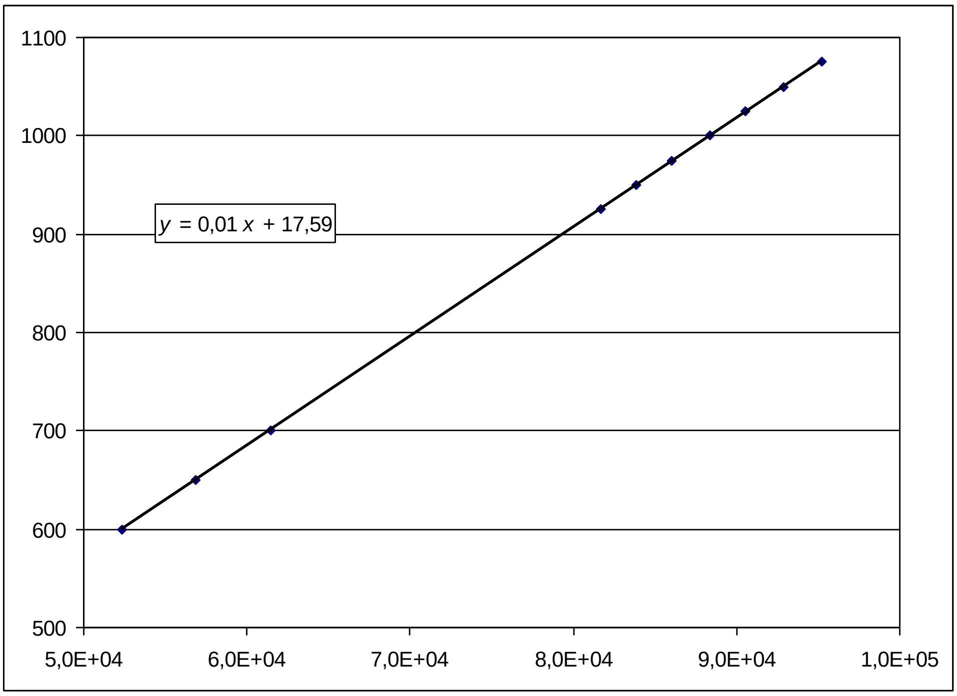

Figure 2 Measurement of virtual point source position of the Co-60 source

Also the graphite depth must be scaled. The water depth of 5 g/cm^2 corresponds to a graphite depth of 5,556 g/cm^2. This is an important parameter for the construction of the graphite phantom.

1.1.3 Determination of Absorbed Dose to Water

1.1.3.1 Operation modes to determine Absorbed Dose to Graphite

The graphite calorimeter allows determination of absorbed dose to graphite with a quasi-adiabatic or a quasi-isothermal operation mode. The Absorbed Dose to Graphite reference value is the mean value of the results of both methodes.

Quasi-adiabatic mode

In the quasi-adiabatic mode the temperatures of the different graphite calorimeter bodies are enhanced by the irradiation. The temperature rise of the core is measured over the response of the core thermistor resistances. To obtain an equivalent temperature rise in all bodies additional electrical heating is required, particularly in the shield.

The Absorbed Dose to Water determined using the quasi-adiabatic mode is calculated with:

$$D_{\mathrm{g,adiabat}} = \frac{1}{m_{\mathrm{c}}} \cdot K_{\mathrm{ad}} \cdot k_1 \cdot k_{\mathrm{gap}} \cdot k_{1/2} \cdot k_{\mathrm{stab}} \qquad (3)$$

$$K_{\mathrm{ad}} = \left(\frac{\Delta R}{R} + k_2 \cdot \Delta U \right) \qquad (4)$$

Meaning of the symbols:

$D_{\mathrm{g,adiabat}}$	Absorbed dose to Graphite, determined with the quasi-adiabatic mode in Gy
m_{c}	Core mass in g
K_{ad}	Correction factor for quasi-adiabatic operation
k_1	Temperature-dependent quasi-adiabatic calibration factor in mJ/%
k_{gap}	Correction for the effect of the vacuum gaps
$k_{1/2}$	Normalisation factor for the reference date

k_{stab} .... Considers the long-term stability of the dose rate

$\frac{\Delta R}{R}$ .... Change in resistance of the thermistors in %, measured with a Wheatstone Bridge

k_2 .... Chart-calibration factor in %/V

ΔU .... Temperature drift correction (difference in voltage) in V

Quasi-isothermic mode

In the quasi-isothermal mode of operation the temperatures are held at a constant equilibrium temperature throughout the measurement. In order to achieve this temperature equilibrium all graphite calorimeter bodies are continuously heated electrically during pre- and post-irradiation intervals with a heating power close to the expected irradiation power. Consequently electrical heating is switched off during irradiation, because it is replaced by the heat produced by the beam.

The evaluation of the quasi-isothermal measurements is is calculated with:

$$D_{\mathrm{g,isotherm}} = \frac{1}{m_{\mathrm{c}}} \cdot \left[P_0 \cdot t_{\mathrm{h,off}}\right] \cdot k_{\mathrm{iso}} \cdot k_{\mathrm{gap}} \cdot k_{1/2} \cdot k_{\mathrm{stab}} \qquad (5)$$

$$k_{\mathrm{iso}} = 1 + k_1 \cdot \left(\frac{\Delta R}{R} + k_2 \cdot \Delta U\right) \cdot \frac{1}{P_0 \cdot t_{\mathrm{h,off}}} \qquad (6)$$

$$\frac{\Delta R}{R} = 0 \text{ (isothermic mode: no change of balance resistor)} \qquad (7)$$

Meaning of the symbols:

$D_{\mathrm{g,\ isotherm}}$ .... Absorbed dose to Graphite, determined with the quasi-isothermic mode in Gy

P_0 .... Heating power (close to the expected irradiation power) before and after irradiation in W

$t_{\mathrm{h,off}}$ .... Time during which the electrical heaters are switched off (ideally, when it equals the irradiation time t) in s

k_{iso} .... Corrections factor for the quasi-isothermic operation mode

1.1.3.2 Conversion modes to determine Absorbed Dose to Water

There are two methods to convert the Absorbed Dose to Graphite Reference value into Absorbed Dose to water. The Absorbed Dose to Water reference value is the mean of the results of both methods.

Method 1: Conversion by calculation

$$\dot{D}_{\mathrm{w,Method\,1}} = \dot{D}_{\mathrm{g}} \cdot \left(\frac{R_{\mathrm{g,eff}}}{R_{\mathrm{w,eff}}}\right)^2 \cdot \left(\frac{\bar{\mu}_{\mathrm{en}}}{\rho}\right)_{\mathrm{w,g}} \cdot \beta_{\mathrm{w,g}} \cdot k_{\Delta\mathrm{air}} \cdot k_{\mathrm{gs}} \cdot k_{\mathrm{g,c}} \cdot k_{\mathrm{depth}} \cdot k_{\mathrm{front}} \qquad (8)$$

Meaning of the symbols:

R_{g} .... scaled distance to calorimeter

R_{w} .... distance to the reference point in water phantom

$\left(\frac{\bar{\mu}_{\mathrm{en}}}{\rho}\right)_{\mathrm{w,g}}$ .... ratio of the average mass energy absorption coefficients of water and graphite

$\beta_{\mathrm{w,g}}$ .... ratio of the absorbed dose to collision kerma of water and graphite

$k_{\Delta\mathrm{air}}$ .... difference in air attenuation at the corresponding measurement distances as required for compliance with the scaling theorem.

$k_{\mathrm{g,c}}$ .... scaling correction: deviation of the graphite phantom dimensions, both in size and shape, from the exact scaling requirements

$k_{\mathrm{g,c}}$ .... correction for the effective graphite calorimeter measurement depth

k_{depth} .... considers depths in graphite and in water

k_{front} .... considers the front wall of the water phantom

Method 2: Conversion by Ionization Current measurement

The used Ionization Chamber is CC01-105 which is the same type as shown in Figure 1.

$$\dot{D}_{\mathrm{w,Method\ 2}} = \dot{D}_{\mathrm{g}} \cdot \frac{I_{\mathrm{w}}}{I_{\mathrm{g}}} \cdot \left(\frac{\overline{\mu}_{\mathrm{en}}}{\rho} \right)_{\mathrm{w,g}} \cdot \frac{1}{k_{\mathrm{gi}}} \cdot \beta_{\mathrm{w,g}} \cdot p_{\mathrm{w,g}} \cdot k_{\mathrm{ps}} \cdot k_{\mathrm{g,c}} \cdot k_{\mathrm{depth}} \cdot k_{\mathrm{front}} \tag{9}$$

Meaning of the symbols:

Q_{g} .... measured ionization chamber current in graphite phantom (scaled distance)

Q_{w} .... measured ionization chamber current in water phantom (reference distance)

k_{gi} .... correction for the difference between the effective ionisation chamber measuring depth and the required scaled reference depth in the graphite phantom.

$p_{\mathrm{w,g}}$ .... replacement correction factor, accounts for the replacement of water by graphite in the volume of the entire chamber CC01-105

k_{ps} .... correction that accounts for the 1.5 mm of PMMA around the CC01-105 chamber.

k_{depth} .... considers the chamber position in graphite and in water

1.1.4 Values of correction factors

The values of selected correction factors are given in Table 2

Correction factor	Symbol	value
correction for the effect of the gaps	k_{gap}	1,006 1
air attenuation correction	$k_{\Delta\mathrm{air}}$	0,997 1
scaling correction	k_{gs}	0,999 8
replacement factor	$p_{\mathrm{w,g}}$	1,015 0
correction for the envelope of the chamber	k_{ps}	1,000 6
interpolation on depth dose curve	k_{gc}	0,988 6
	k_{gi}	0,991 3

Table 2 Correction factors for the operation of the Graphite Calorimeter

1.1.5 Monte Carlo Calculation of the Co-60 spectrum

An important requirement for calculating correction factors is the knowledge of the spectrum. The spectrum of the BEV Teletherapy Source was calculated with Penelope Monte Carlo Calculation (Figure 3). The spectrum was verified with depth dose measurements (Figure 4).

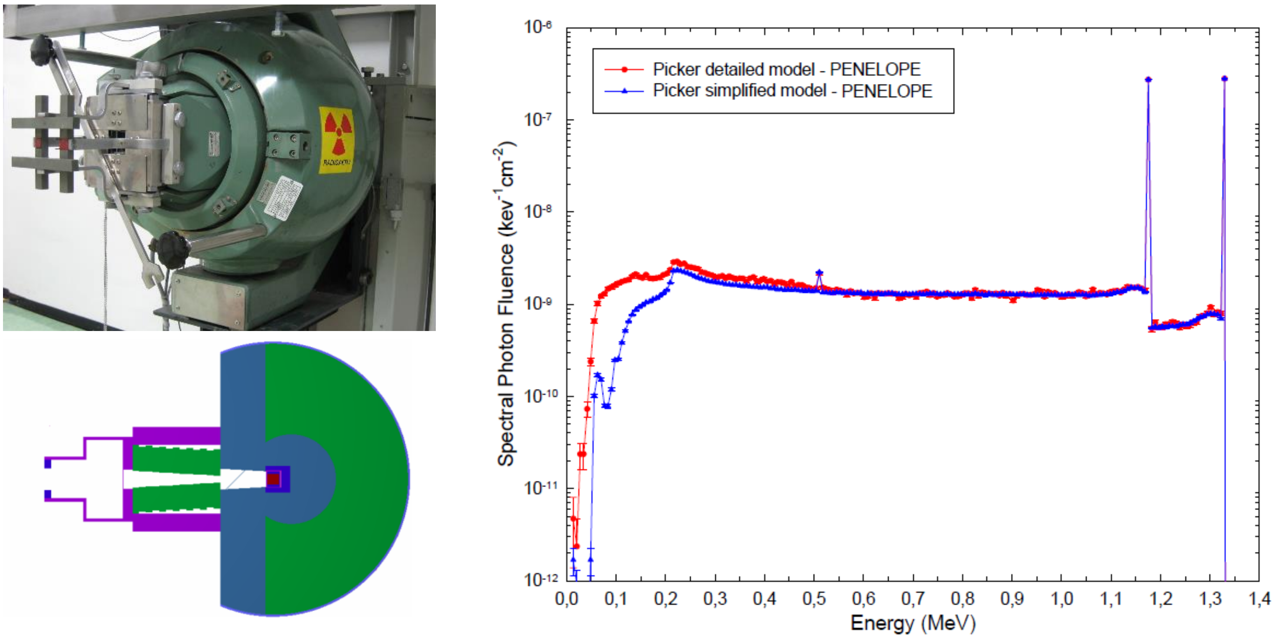

Figure 3 Determination of the Co-60 source spectrum

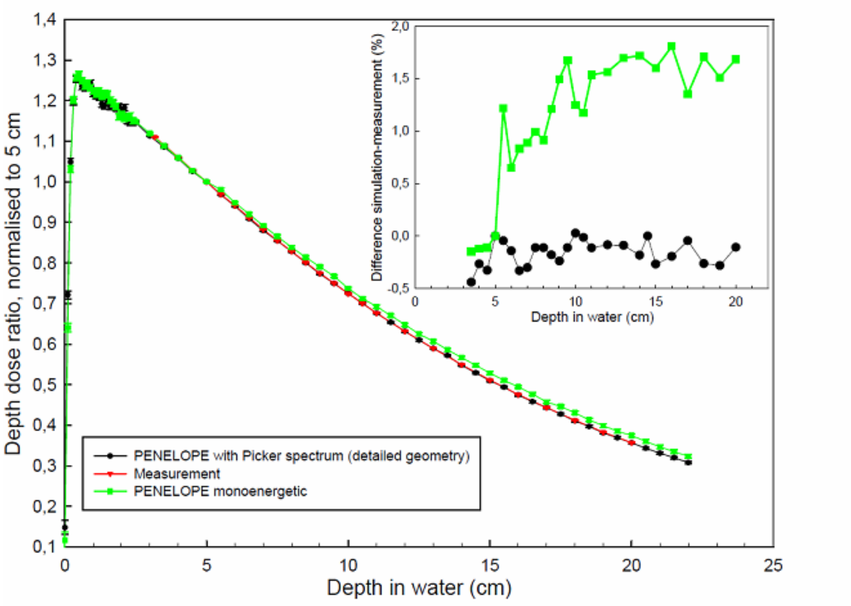

Comparison of the PENELOPE simulated and measured depth-dose curves.

Figure 4 Verification of the calculated spectrum

1.1.6 Results and uncertainty

A new Co-60 source with the nominal activity of 185 TBq (reference date 31.12.2013) was installed 2014. The reference value measured with the graphite calorimeter in terms of Absorbed Dose Rate to Water is 12,134 6 mGy/s (reference date 31.12.2013) with a standard uncertainty of 0,38 %.

It is calculated as the mean of both measerrment methods and both conversion methods.

The uncertainty is determined by the two steps as described in Table 3 and Table 4:

X_i	quasi-adiabatic Method			quasi-isothemic Method		
	$u_{X_i,\mathrm{A,r}}$	$u_{X_i,\mathrm{B,r}}$	$u^2_{X_i,\mathrm{r}}$	$u_{X_i,\mathrm{A,r}}$	$u_{X_i,\mathrm{B,r}}$	$u^2_{X_i,\mathrm{r}}$
m_c	0 %	0,12 %	0,014 4 $\%^2$	0 %	0,12 %	0,014 4 $\%^2$
k_ad	0,05 %	0 %	0,002 5 $\%^2$	-	-	-
k_1	0,02 %	0,15 %	0,022 9 $\%^2$	-	-	-
k_gap	0 %	0,15 %	0,022 5 $\%^2$	0 %	0,15 %	0,022 5 $\%^2$
$k_\mathrm{g,c}$	0 %	0,03 %	0,000 9 $\%^2$	0 %	0,03 %	0,000 9 $\%^2$
k_HWZ	0 %	0,02 %	0,000 4 $\%^2$	0 %	0,02 %	0,000 4 $\%^2$
ΔU	0,02 %	0 %	0,000 4 $\%^2$	0,02 %	0	0,000 4 $\%^2$
k_stab	0 %	0,12 %	0,014 4 $\%^2$	0	0,15 %	0,022 5 $\%^2$
P_0	-	-	-	0	0,03 %	0,000 9 $\%^2$
$t_\mathrm{h,off}$	-	-	-	0,03 %	0,01 %	0,001 0 $\%^2$
k_iso	-	-	-	0	0,12 %	0,014 4 $\%^2$
t	0 %	0,03 %	0,000 9 $\%^2$	0 %	0,03 %	0,000 9 $\%^2$
Y_i	$\dot{D}_\mathrm{g,adiabat}$	$\sum_{i=1}^{n} u^2_{X_i,\mathrm{r}}$:	0,064 9 $\%^2$	$\dot{D}_\mathrm{g,isotherm}$	$\sum_{i=1}^{n} u^2_{X_i,\mathrm{r}}$:	0,063 9 $\%^2$
		$u_\mathrm{C,r} = \sqrt{\sum_{i=1}^{n} u^2_{X_i,\mathrm{r}}}$:	0,255 %		$u_\mathrm{C,r} = \sqrt{\sum_{i=1}^{n} u^2_{X_i,\mathrm{r}}}$:	0,253 %

Table 3 Standard Uncertainty Absorbed Dose Rate to Graphite

X_i	Method 1			Method 2		
	$u_{X_i,\mathrm{A,r}}$	$u_{X_i,\mathrm{B,r}}$	$u_{X_i,\mathrm{r}}^2$	$u_{X_i,\mathrm{A,r}}$	$u_{X_i,\mathrm{B,r}}$	$u_{X_i,\mathrm{r}}^2$
$\left[\left(\frac{R_\mathrm{g}}{R_w}\right)^2\right]$	0 %	0,2 %	0,040 0 %^{2}	0 %	0,1 %	0,010 0 %^{2}
$\left(\frac{\overline{\mu}_\mathrm{en}}{\rho}\right)_\mathrm{w,g}$	0 %	0,1 %	0,010 0 %^{2}	0 %	0,1 %	0,010 0 %^{2}
$\beta_\mathrm{w,g}$	0 %	0,1 %	0,010 0 %^{2}	0 %	0,1 %	0,010 0 %^{2}
$k_{\Delta\mathrm{air}}$	0 %	0,03 %	0,000 9 %^{2}	-	-	-
k_gs	0 %	0,02 %	0,000 4 %^{2}	-	-	-
k_depth	0 %	0,1 %	0,010 0 %^{2}	0 %	0,07 %	0,004 9 %^{2}
k_front	0 %	0,05 %	0,002 5 %^{2}	0 %	0,05 %	0,002 5 %^{2}
$\left(\frac{I_\mathrm{w}}{I_g}\right)$	-	-	-	0,05 %	0,05 %	0,005 0 %^{2}
k_gi	-	-	-	0 %	0,03 %	0,000 9 %^{2}
$p_\mathrm{w,g}$	-	-	-	0 %	0,2 %	0,040 0 %^{2}
k_ps	-	-	-	0 %	0,05 %	0,002 5 %^{2}
Y_i	Con-versions factor Method 1	$\sum_{i=1}^{n} u_{X_i,\mathrm{r}}^2$:	0,073 8 %^{2}	con-versions factor Method 2	$\sum_{i=1}^{n} u_{X_i,\mathrm{r}}^2$:	0,075 8 %^{2}
		$u_\mathrm{C,r} = \sqrt{\sum_{i=1}^{n} u_{X_i,\mathrm{r}}^2}$:	0,272 %		$u_\mathrm{C,r} = \sqrt{\sum_{i=1}^{n} u_{X_i,\mathrm{r}}^2}$:	0,275 %

Table 4 Standard Uncertainty Conversion from Absorbed Dose Rate to Graphite into Absorbed Dose to water

1.1.7 Transfer of Absorbed Dose to Water to an Ionization chamber

After determination of the Absorbed Dose to Water value for calibration purposes an Ionization chamber is positioned in the water phantom under Reference Conditions. The ionization current is measured.

The Calibration Coefficient of the Ionization Chamber in terms of Absorbed Dose to Water is defined by:

$$N_{D_\mathrm{w}} = \frac{D_\mathrm{w}}{Q} \tag{10}$$

Meaning of the symbols

N_{D_w} .... Calibration Coefficient

D_w .... Absorbed Dose to Water

Q.......................... Loading of the Ionization Chamber generated by the irradiation

2 BEV relating Literature

- Leitner A., Witzani J.: The Realization of the Unit of Absorbed Dose at the Austrian Dosimetry Laboratory Seibersdorf, OEFZS–4740, Februar 1995
- Witzani J., Duftschmid K.E., Strachotinsky Ch. & Leitner A.: A Graphite Absorbed-Dose Calorimeter in the Quasi-Isothermal Mode of Operation, Metrologia 20, 73-79 (1983), Springer-Verlag
- Baumgartner A., Steurer A., Tiefenböck W., Gabris F. Maringer F.J., Kapsch R.P. & Stucki G.: "Re-evaluation of correction factors of a primary standard graphite calorimeter in ^{60}Co gamma ray beams as a basis for the appointment of the BEV absorbed dose rate to water reference value", Radiation Protection Dosimetry (2010), pp. 1-10
- C. Kessler, P.J. Allisy-Roberts, A. Steurer, A Baumgartner, W. Tiefenböck, F. Gabris "Comparison of the standards for absorbed dose to water of the BEV and the BIPM for ^{60}Co gamma radiation", BIPM.RI(I)_K4_Report, Paris, 2010-04-28, Metrologia 47 (2010) p. 06017

Introduction to uncertainty budget and GUM method

JM Bordy - CEA LIST (LNE) LNHB

Introduction

This paper is intended to give an overview of the expression of uncertainty in measurement applied to calibration for ionizing radiation. Most of the information are taken from the GUM and a few internet websites.

I - Distribution laws (Binomial, Poisson, Normal)

The likelihood of an event E occurring is: $P(E) = \frac{\text{Number of events considered outcome E}}{Number\ of\ total\ events}$

For ionizing radiations purposes, the event, E, is for example the disintegration of a nuclide or the interaction of a radiation with a target (nucleus or electron). In such a case the probability is governed by the binomial law, that is to say the nuclide either decays or does not, the radiation either impinging with a target or does not. In other words, the event of interest either occurs or does not.

The binomial random variable probability is given by $P(x) = \frac{\mathrm{n!}}{\mathrm{x!(n-x)!}} p^x (1-p)^{n-x}$

- n is the number of trials
- x is the number of successes
- p is the probability event of interest occurs on any one trial

The binomial law can be approximated by a Poisson law for which an event can occur 0, 1, 2, … times in an interval. The average number of events in an interval is designated, µ. The probability of observing k events in an interval is given by the equation:

$$P(k\ events\ in\ interval) = \frac{\mu^x \mathrm{e}^{-\mu}}{\mathrm{x!}}$$

- µ is the average number of events per interval
- x takes discrete values 0, 1, 2, …

One can note that µ is the only one parameter required to describe the probability mass function for a Poisson distribution, as a consequence the average values of a Poisson distribution is equal to its variance. The Poisson distribution is not symmetric but when µ increased the Poisson distribution becomes more and more symmetric around µ and can be approximated by the normal law which is given by:

$$p(x) = \frac{1}{\mathrm{s}\sqrt{2\pi}} e^{\left(\frac{(x-\mu)^2}{2s^2}\right)}$$

- µ is the average values of the distribution
- s is the standard deviation of the distribution

The Normal law needs two parameters, the average values and the variance. If the two parameters are equals and µ is large then the Normal law is a good symmetric approximation of the Poisson Law.

Therefore, under know conditions, the normal law can be use to describe the radioactive phenomenon's.

II – Systematic and random "errors"

The error of the result of a measurement may often be considered as arising from a number of random and systematic effects that contribute individual components of error to the error of the result.

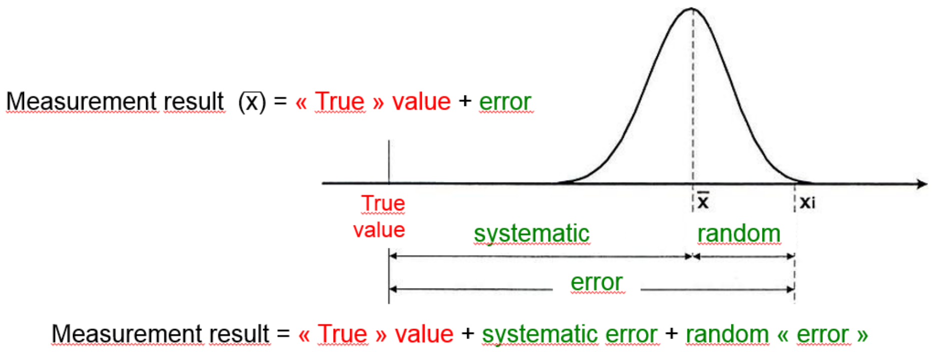

The systematic error is a mean that would result from an infinite number of measurements of the same measurand carried out under repeatability conditions minus a true value of the measurand.

The random error is the result of a measurement minus the mean that would result from an infinite number of measurements of the same measurand carried out under repeatability conditions.

The goal is to avoid systematic errors and to estimate the random « errors » to get a result as close as possible of the « true » value.

III - Practical example (Calibration for Ionizing radiation)

Prior to the calculation of the uncertainty budget, one has to establish a mathematical model. This model is an equation such as $Y=f(X_1, X_2, \dots X_i, \dots X_n)$, where X_i represent the contribution of the influence quantities.

Let's take the example with Y as the air kerma measured with an open ionizing chamber (IC). This IC is put in front of the radiation beam at a distance, d, from the radiation source. The raw signal of the IC need to be corrected for environmental conditions: temperature, pressure, humidity. The raw current is derived for the charge collected on the electrodes of the IC during time intervals, t.

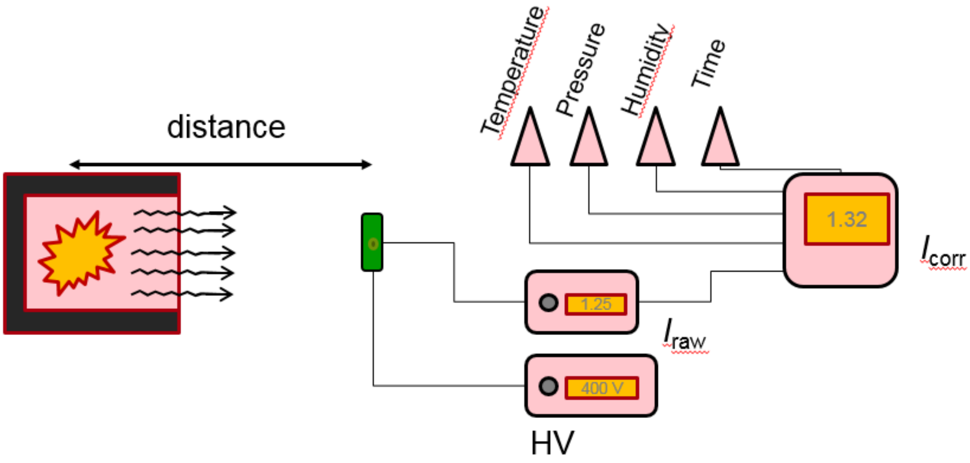

The air kerma is obtained through the calibration factor in reference conditions of the IC, N_{ka}, according to the model of equation 1. Therefore at the point of test the air kerma is:

$$K_a = N_{ka}\, I_{corr} = N_{ka}\, (I_{raw} - I_0)\, \Pi_i\, k_i \qquad (1)$$

Where $\Pi_i\, k_i$ is the product of the correction coefficients, i.e. for temperature pressure … but also for the saturation and the polarization effects. They are the influence quantities.

All the terms of this equation have an associated uncertainty, u, which have to be combined to derive the uncertainty associated with the measured air kerma value.

IV – Standard combined uncertainty (sandwich law)

For a given model $Y=f(X_1, X_2, \ldots X_n)$, the combined standard uncertainty, $u_c(Y)$, is the square root of the combined variances, $u^2_c(Y)$. it is calculated using the following formulae, known as the sandwich law.

$$u_c^2(Y) = \sum_{i=1}^{n} \left[\frac{\partial f}{\partial X_i}\right]^2 u^2(X_i) + 2 \sum_{i=1}^{n-1} \sum_{j=i+1}^{n} \frac{\partial f}{\partial X_i} \frac{\partial f}{\partial X_j} u(X_i, X_j)$$

This formulae has two terms. The last one is the covariance term, it takes into account, if any, the correlation between the quantities X_i. The covariance of two random variables is a measure of their mutual dependence. This covariance is difficult to evaluate. Nevertheless, it can be estimated by $s(X_1, X_2)$, where $X_1$and X_2 two correlated quantities, for which *n* independent pairs of simultaneous observations $X_{1,i}$ and $X_{2,i}$ of X_1 and X_2 can be measured.

$$s(X_1, X_2) = \frac{1}{\mathrm{n}-1} \sum_{n-1}^{n} (X_{1,i} - \overline{X_1})(X_{2,i} - \overline{X_2})$$

If there is no correlation the standard uncertainty associated with Y is therefore:

$$u_c\ (Y) = \sqrt{\sum_{i=1}^{n} \left[\frac{\partial f}{\partial X_i}\right]^2 u^2(X_i)}$$

Two cases are of particular interest when using the sandwich law, they are the sum (and subtraction) and the product (and division). Thus if:

Y = A + B or Y = A – B then $u^2_c(Y) = u^2(A) + u^2(B)$

Y = A B or Y = A / B then $\frac{u_c^2(Y)}{Y^2} = \frac{u^2(A)}{A^2} + \frac{u^2(B)}{B^2}$

V – Evaluation of the standard uncertainties (types A and B evaluation)

There is not always a simple correspondence between the classification into categories A or B and the previously used classification into random and systematic “error”; both can be of type A or B.

Type A: When repeated observation are possible, X_1, X_2, …, X_n, the measurement standard uncertainty is obtained using the experimental standard deviation (on the distribution of the results).

$$s(X_i) = \sqrt{\frac{\sum_{i=1}^{n}(X_i - \overline{X})^2}{n-1}}$$

If a measurement laboratory had limitless time and resources, it could conduct an exhaustive statistical investigation of every conceivable cause of uncertainty, for example, by using many different makes and kinds of instruments, different methods of measurement, different applications of the method, and different approximations in its theoretical models of the measurement. The uncertainties associated with all of these causes could then be evaluated by the statistical analysis of series of observations and the uncertainty of each cause would be characterized by a statistically evaluated standard deviation. In other words, all of the uncertainty components would be obtained from Type A evaluations. Since such an investigation is not an economic practicality, many uncertainty components must be evaluated by whatever other means is practical. In this case type B evaluation can be used.

Type B: the standard uncertainty is evaluated by scientific judgement based on all of the available information on the possible variability of X_i

- Previous measurement data;
- Experience with or general knowledge of the behaviour and properties of relevant materials and instruments (sensitivity …);
- Manufacturer's specifications (resolution …);
- Data provided in calibration and other certificates;
- Uncertainties assigned to reference data taken from handbooks (nuclear data …).
- The worker itself (e.g. distance …)
- …/…

The figure hereafter shows a few examples of distribution shape. One can see that, depending on the shape of the distribution, the relationship between the standard deviation and the full width of the distribution is not the same. The rectangular distribution is of particular interest since in most of the cases, the shape of the distribution for type B evaluation is not known a priory and because the standard deviation for this shape is conservative compared to the other distributions, σ = a / √3. Therefore, if the shape of the distribution for a given quantity is not known, one has to use a conservative evaluation of the standard deviation that is to say considering the rectangular distribution. Thus, the uncertainty for this quantity will be overestimate.

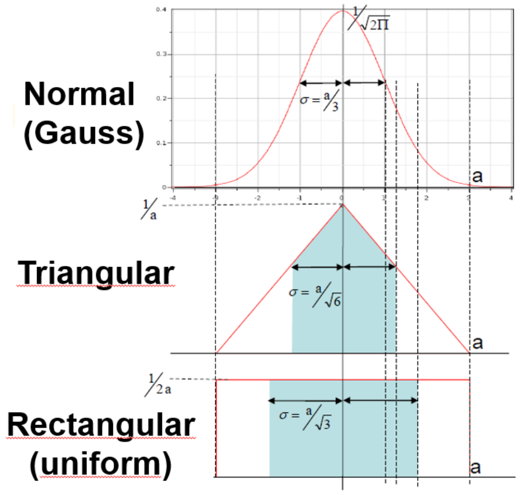

VI - The central limit theorem

This theorem shows that when a mathematical model is used, the distribution law of Y, obtained from at least three non correlated variables/quantities, X_i, having about the same weight, can be approximate by the normal law.

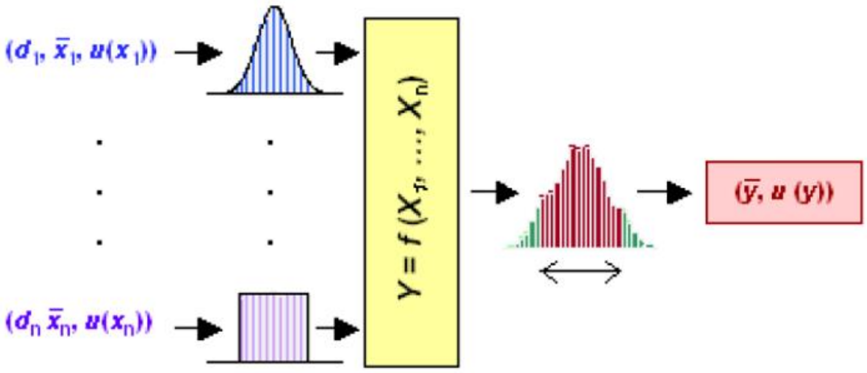

VII - Expanded uncertainty (coverage factor, confidence interval)

One of the key features of the normal law is that for the normal distribution the values less than one standard deviation away from the mean account for 68.27% of the set; while two standard deviations from the mean account for 95.45%; and three standard deviations account for 99.73%.

The expanded uncertainty symbol is, U. The coverage factor, k, correspond to the number of standard deviation used to define the confidence interval. Therefore, using the same model as before, $U(Y) = k\ u_c(Y)$

And thus, the confidence is an interval is defined as: $[\mu - U(Y)\ ,\ \mu + U(Y)]$ or $[\mu - k\ u_c(Y)\ ,\ \mu + k\ u_c(Y)]$

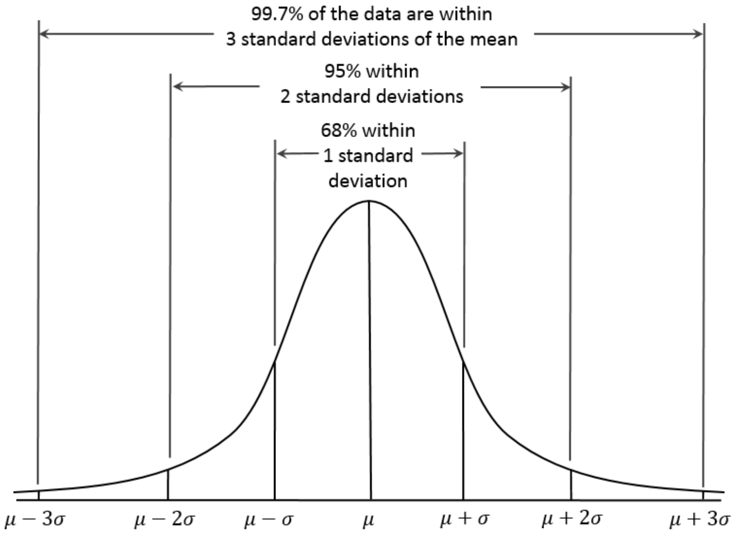

ÉDITÉ PAR
LA DIRECTION DES SYSTEMES
D'INFORMATION

CEA / SACLAY 91191 GIF-SUR-YVETTE CEDEX FRANCE